

Dynamical properties of water and of the LiCl solution, investigated by inelastic scattering of synchrotron radiation and visible light

Silvia C. Santucci

▶ **To cite this version:**

Silvia C. Santucci. Dynamical properties of water and of the LiCl solution, investigated by inelastic scattering of synchrotron radiation and visible light. Condensed Matter [cond-mat]. Université Joseph-Fourier - Grenoble I, 2010. English. NNT : . tel-00526125v3

HAL Id: tel-00526125

https://theses.hal.science/tel-00526125v3

Submitted on 5 Nov 2010

HAL is a multi-disciplinary open access archive for the deposit and dissemination of scientific research documents, whether they are published or not. The documents may come from teaching and research institutions in France or abroad, or from public or private research centers.

L'archive ouverte pluridisciplinaire **HAL**, est destinée au dépôt et à la diffusion de documents scientifiques de niveau recherche, publiés ou non, émanant des établissements d'enseignement et de recherche français ou étrangers, des laboratoires publics ou privés.

UNIVERSITÉ DE GRENOBLE
ÉCOLE DOCTORALE de PHYSIQUE

THÈSE

Pour obtenir le grade de

DOCTEUR DE L'UNIVERSITÉ DE GRENOBLE

Spécialité Physique de la Matière Condensée et du Rayonnement

Arrête ministériel : 7 Août 2006

Présentée et soutenue publiquement par

Silvia SANTUCCI

le 12 Juillet 2010

Propriétés dynamiques de l'eau et de la solution LiCl-6H_2O, étudiées par diffusion inélastique du rayonnement synchrotron et de la lumière visible

---

Thèse dirigée par Jean-François LEGRAND

JURY

M. Thierry DOMBRE	Professeur, Université Joseph Fourier, Grenoble	Président
M.me Christiane ALBA-SIMIONESCO	Directeur de Recherche, Laboratoire Léon Brillouin, Saclay	Rapporteur
M.me Pascale ROY	Directeur de Recherche, Synchrotron Soleil, Saint Aubin	Rapporteur
M. Daniele FIORETTO	Professeur, Università degli Studi di Perugia	Examinateur
M. Serge PEREZ	Directeur de Recherche, ESRF, Grenoble	Examinateur
M. Jean-François LEGRAND	Professeur, Université de Strasbourg	Examinateur

Thèse preparée au sein des laboratoires:

European Synchrotron Radiation Facility, 6 Rue Jules Horowitz, 38000, Grenoble, France
Elettra Synchrotron, Area Science Park, S.S. 14, Km 163.5, 34100 Basovizza, Trieste, Italie
Dipartimento di Fisica, Università degli Studi di Perugia, Via Pascoli 06100, Perugia, Italie
dans l'École Doctorale de Physique

Acknowledgements

I am grateful to my supervisor Jean-François Legrand for having proposed the subject of LiCl aqueous solutions, which is now experiencing renewed interest in many laboratories in Europe. This thesis has been a highly demanding work, partly intersected with other scientific projects. With respect to this, I am grateful to Jean-François for having kept his role of supervisor with immutable interest, availability, trust and wiseness. I am grateful to Claudio Masciovecchio, responsible of the IUVS beamline in Trieste, to Daniele Fioretto, responsible for the GHOST group of optical spectroscopies of the Physics Department of Perugia University and to Giulio Monaco, beamline scientist of the ID16 beamline at the ESRF, for the strong support I have received in their laboratories. I acknowledge the suggestion of water as a scientific subject and I am grateful for the large possibility to perform experiments, for the illuminating discussions on many aspects of science and life and for the success that our efforts have obtained, by publishing several times on high quality journals. I am grateful to Gabriele Viliani of the University of Trento for supporting this project and for illuminating discussions.

I am grateful to all the people i have had the luck to work with, in the three labs: Alessandro Gessini and Silvia Di Fonzo in Trieste, Lucia Comez, Filippo Scarponi and Silvia Corezzi in Perugia, Roberto Verbeni in Grenoble. From all of them i have learnt a lot and this work could not have been possible without their contribution.

I want to thank all the technicians of the workshops in Perugia University and Elettra synchrotron for the efficient building of custom sample holders.

I want to thank the whole Lilit group and the whole OM group of Dan Cojoc in IOM-TASC, in Trieste, for the time spent together as friends and colleagues and for letting me use the cleanroom to prepare the samples of superpure water.

I am grateful to the SAXS group in Elettra synchrotron for the support with their chemical laboratory, especially to Barbara Sartori for her accurate assistance.

I am grateful to all my present colleagues of the ID13 beamline of the ESRF, especially to Christian Riekel and Manfred Burghammer for the wise and generous encouragement they have given me in the last efforts of submitting my thesis.

I am grateful to Christiane Alba-Simionesco and Pascale Roy for carefully reviewing this manuscript and to the whole committee for the interesting final discussion.

During the development of this work I have had the luck to meet many young scientists from all around the world who have enchanted me with the richness of their lives. I am particularly grateful to Silvia Tacchi of Perugia University and to Véronique Siegler, Kristine Niss, Silvia Imberti and Laure Libralesso for the nice friendship we have established during the HERCULES course.

I am grateful to my family and friends, which indirectly shared the workload, for the joy and humor they have brought into the difficulties and successes of this work.

Last but not least, I am grateful to my darling Sebastian, who shares with me the good and the weird times of life, for his precious support and for his serene and constant encouragement in finalizing the thesis submission.

Introduction (Français)

Depuis l'antiquité, l'eau est probablement la substance qui a été la plus étudiée[1]. L'intérêt scientifique qu'elle suscite est multiple: l'eau est essentielle pour la vie et fondamentale pour l'activité humaine. L'eau est le composé le plus abondant sur la terre et ses propriétés physiques anomales par rapport à celles des autres liquides garantissent l'existence de l'écosystème de notre planète [2].

Le diagramme de phases de l'eau stable et métastable est surprenant [3]. Dans plusieurs expériences réalisées au cours des années depuis 1820, l'eau à pression atmosphérique a été surfondue jusqu'à la limite $T_H = 235$ K, connue maintenant pour être la température de nucléation homogène de la glace [4]. L'eau est un mauvais candidat à la vitrification. L'hyper trempe de gouttelettes microniques nécessite une vitesse de refroidissement de 10^5 K/s. Les phases vitreuses de l'eau ont été obtenues par évaporation sous vide sur une plaque froide, pour la glace de basse densité; ou par compression de la phase cristalline à des températures bien inférieures à T_H, pour la glace de haute densité [3]. Une troisième forme de glace amorphe (de très haute densité) a été obtenue par chauffage isobare de la phase de haute densité [5]. Ainsi la température de transition vitreuse de l'eau $T_g = 136$ K a fait l'objet de controverses passionnés [3, 6]. Quoi qu'il en soit, il subsiste un intervalle de température qualifié de *no man's land*, entre T_H and T_g, dans lequel aucune phase amorphe de l'eau (liquide ou vitreuse) n'a jamais été observée. C'est dans cet intervalle de température inaccessible que l'on s'attendrait à observer des divergences dans la chaleur spécifique, la compressibilité isotherme, le coefficient de dilatation la viscosité et les temps de relaxation [4]. En effet toutes ces propriétés qui ont été mesurées au maximum jusqu'à T_H peuvent être extrapolées par une loi de puissance qui tend vers l'infini à $T_S = 228$ K, 7 degrés en dessous de T_H [4].

De nombreuses interprétations ont proliféré sur ces propriétés de l'eau surfondue et différents diagrammes de phase ont été proposés à partir de considérations dynamiques ou thermodynamiques [7]. Aucune de ces théories n'explique l'ensemble de la phénoménologie de l'eau, ni n'est supportée par des évidences expérimentales. Les prédictions de la Théorie du Couplage de Modes (MCT) [8], développée à l'origine pour fournir une description dynamique de la transition de verres fragiles, ont montré qu'elles rendaient bien compte des simulations de dynamique moléculaire de l'eau surfondue [9, 10, 11, 12, 13, 14]. Dans la formulation simplifiée de la théorie MCT, la transition vitreuse est associée à un gel des fluctuations de densité à longue portée caractérisant la relaxation structurale. Cette formulation exacte prédit un temps de relaxation structurale divergeant, suivant une loi de puissance, à la température T_c. Dans une formulation plus avancée le gel de la relaxation apparait comme un artefact qui disparait lorsque les quantités de mouvement des particules sont prises en compte [15]. La température T_c correspond alors à un changement de régime dynamique et elle conserve sa signification pour interpréter la dynamique lente, au dessus de T_c, quand le effets de hopping sont négligeables. La théorie MCT permet des prédictions très précises qui peuvent être confrontées aux études expérimentales des propriétés dynamiques.

L'un des principaux objectifs de ce travail a été de comparer les prédictions de la Théorie de Couplage de Modes avec les résultats des études de relaxation structurale de l'eau liquide et surfondue. En confirmant la validité de cette interprétation dynamique, on pourrait en déduire, de façon plus générale, que : (i) si la théorie MCT, développée pour des liquides simples, réussit à décrire un système aussi compliqué que l'eau, cela supporte l'idée d'un comportement assez universel des liquides dans un large domaine de surfusion [11]. (ii) la théorie MCT prédisant une

transition purement dynamique à $T_c \approx T_S$,un mécanisme dynamique peut aussi être invoqué pour expliquer la divergence apparente des propriétés physiques, sans nécessité d'introduire une singularité thermodynamique.

Le point de vue dynamique adopté par la théorie MCT s'intéresse à l'étude de la fonction de corrélation des fluctuations de densité et à une phénoménologie de relaxation qui en découle. Quand une perturbation est exercée sur un fluide, le retour à l'équilibre est piloté par des processus de relaxation qui évoluent dans le système. Dans une description macroscopique, la diffusion, l'écoulement visqueux et la conduction thermique sont les caractéristiques du transport dissipatif et en l'absence de perturbations extérieures les fluctuations spontanées suivent les memes lois de dissipation que les perturbations d'origine externe [16].

Du point de vue expérimental, **les techniques de diffusion inélastique** sont bien adaptées pour caractériser la dynamique des systèmes désordonnés sur une gamme de fréquences étendue [17, 18]. Le *facteur de structure dynamique*, transformée de Fourier de la fonction d'auto-corrélation de la densité, peut être mesuré par diffusion inélastique de rayonnement dans la gamme de fréquence du GHz au THz. Le spectre du rayonnement diffusé est caractérisé par des pics représentatifs d'un échange d'énergie avec les modes acoustiques créés ou anihilés dans le milieu diffuseur. En fonction de la longueur d'onde incidente et des limites de l'instrument, différentes techniques donnent à des domaines complémentaires en énergie h et en vecteur de diffusion Q, comme le montre la Figure 1.

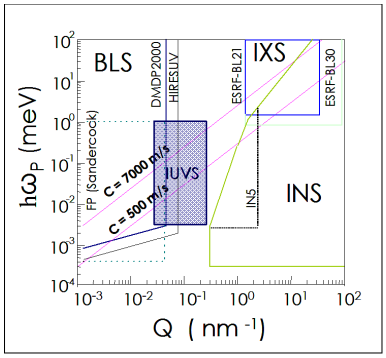


Figure 1: Gammes d' énergie h et de vecteur de diffusion Q sondés par différentes techniques de diffusion inélastique de rayonnement. Les principales utilisées dans ce travail sont la diffusion Brillouin de la lumière visible (BLS), la diffusion inélastique du rayonnement ultraviolet (IUVS) réalisée sur le nouvel instrument du synchrotron Elettra, ainsi que la diffusion inélastique des rayons X (IXS) réalisée à l'ESRF.

Pour étudier un mécanisme de relaxation dans une certaine gamme de temperature (ou de pression), il faut choisir la technique expérimentale qui donne *la meilleure sensibilité* dans la gamme désiré des temps de relaxation τ. Cela implique de sonder les modes acoustiques de fréquence angulaire $\omega \approx 1/\tau$

Avant ce travail les techniques BLS et IXS étaient les deux seules techniques de diffusion inélastique du rayonnement électromagnétique et les résultats obtenus antérieurement sur la dynamique relaxationelle de l'eau suggéraient une sensibilité accrue, à basse température dans la gamme mésoscopique des échanges d'énergie de 10 μeV à 1 meV, et des vecteurs de diffusion de 0.02 à 0.2 nm^{-1}: En effet, la meilleure sensibilité de la technique IXS est obtenue au dessus de 1 nm^{-1} [19]. Et aux petits vecteurs Q, la technique BLS est adaptée à la relaxation de l'eau bien en dessus de la limite de surfusion que l'on peut atteindre au laboratoire [20].

Le développement de la ligne de lumière IUVS au synchrotron Elettra de Trieste [21], [22], a rendu possible d'étudier la dynamique relaxationnelle de l'eau surfondue. Par IUVS, nous avons mesuré le facteur de structure dynamique de l'eau liquide normale et surfondue, pour la première fois jusqu'à 253 K. Comme l'eau a été le premier système étudié par IUVS, nous avons aussi utilisé la technique BLS pour obtenir des données de référence pour la nouvelle ligne. Cela a permis d'étendre le domaine des fréquences mesurées à trois décades et l'ensemble des spectres IUVS et BLS a été analysé simultanément à l'aide d'un simple formalisme d'hydrodynamique

généralisée (avec introduction de fonctions mémoire)[16, 17]. Nous avons ainsi obtenu l'évolution en température de la relaxation structurale de l'eau à différentes valeurs de Q de 0.02 à 0.1 nm^{-1}. Ces observations ont été confrontées avec succès aux prédiction de la théorie MCT [23]. La comparaison de nos résultats avec ceux des expériences d'IXS réalisées indépendamment [19] a confirmé la fiabilité des mesures d'IUVS et leur contribution originale pour l'étude de la relaxation structurale de l'eau surfondue. De plus, les caractéristiques de cette relaxation structurale ont mis en évidence des éléments discriminants dans la controverse sur l'origine de la dispersion acoustique de l'eau dans la gamme du THz [24, 25].

La solution LiCl-6H_2O. Comme la température de solidification de l'eau peut être abaissée par addition de sel, une autre approche peut permettre d'étendre le domaine de surfusion de l'eau : par dilution progressive de solutions aqueuses on peut envisager d'extrapoler leurs propriétés de relaxation au cas de l'eau pure. Comme première étape dans cette direction, nous avons étudié, avec les outils décrits ci-dessus, la dynamique relaxationnelle de la solution LiCl-6H_2O. En effet, les solutions LiCl-RH_2O (où R désigne le rapport molaire solvant/soluté) présentent un intéressant diagramme de phase [26]. Pour R = 6, toute cristallisation est évitée jusqu'à basse température et une transition vitreuse est observée à $T_g = 135$ K. Nous avons exploré les propriétés dynamiques de cette solution dans une large gamme de fréquence, par spectroscopie de corrélation de photons et par les techniques BLS, IUVS et IXS. Ces études confirment les propriétés de relaxation structurale de la solution et montrent de fortes similitudes avec les propriétés de l'eau pure dans un domaine de température où celles-ci semblent diverger [27].

Structure du document. **Le chapitre 1** présente la problématique scientifique de ce travail et décrit en particulier les propriétés anomales de l'eau surfondue. Les résultats obtenus par simulation de dynamique moléculaire sont analysées en regard des prédictions de la théorie MCT. La controverse sur l'origine du *"second son"* observé à haute fréquence dans l'eau liquide est discutée en termes de relaxation structurale et la discussion met en évidence le besoin d'études de diffusion inélastique dans la gamme de l'ultra violet. Enfin, l'exposé des propriétés des solutions aqueuses de LiCl vient compléter la présentaion des objectifs de ce travail.

Le chapitre 2 aborde l'approche méthodologique qui est basée sur l'étude du facteur de structure dynamique. Du point de vue théorique, les simulations de dynamique moléculaires prédisent un comportement du facteur de structure dynamique comparable avec celui déduit de la théorie MCT. Et du point de vue des expériences, le facteur de structure dynamique mesuré sur une large gamme de fréquence est analysé à l'aide d'un formalisme hydrodynamique qui permet la comparaison avec les prédictions théoriques

Dans le **chapitre 3** sont décrits les instruments utilisés et en particulier la ligne de lumière IUVS construite auprès du synchrotron Elettra. Sont aussi présentées des descriptions plus courtes de l'interféromètre de Fabry-Perrot utilisé en diffusion Brillouin et de la ligne de lumière ID16 de l'ESRF.

Dans les **chapitres suivants (4, 5)**, sont détaillées les expériences réalisées, et l'analyse des résultats obtenus dans l'eau surfondue puis dans la solution LiCl-6H_2O.

La **discussion finale** reprend l'ensemble des résultats obtenus et met en évidence des points de comparaisons intéressants entre les deux systèmes.

La liste des publications réalisées au cours de ce travail, à travers de multiples collaborations, est donnée dans l'**annexe A**.

Et l'**annexe B** présente des résultats obtenus par l'auteur sur un sujet un peu différent qui concerne l'analyse de la largeur de raie des phonons détectés dans une expérience de photoémission par rayonnement synchrotron [28].

Introduction

Since the antiquity [1] water is probably the most studied substance ever. The interest of science towards this substance is manyfold: water is ubiquitous, essential to life and fundamental in human activity. Water is the most abundant compound on Earth and its physical properties, anomalous with respect to other liquids, guarantee the existence of the ecosystem on our planet [2].

The phase diagram of stable and metastable water is puzzling [3]. In several experiments performed along decades at least since 1820, bulk water at ambient pressure has been supercooled, down to the limit $T_H = 235$ K, now known as its homogeneous nucleation temperature [4]. Water is a bad glass former. The hyperquenching of micron sized droplet has been realized at a cooling rate of 10^5 K/s. Glassy phases of water have been obtained by in-vacuum evaporation onto a cold plate (low density glass) and by pressurization of the crystalline phase (high density glass), at much lower temperatures than T_H [3]. A third form of glass (very high density glass) has been realized from the isobaric heating of the high density glass [5]. The glass transition temperature of water, $T_g = 136$ K, has been subjected to fervid dispute [3, 6]. Nevertheless, there is a puzzling gap between T_H and T_g, called *no-man's land*, where bulk *non-crystalline* water (liquid or glass) has never been observed. Just within this no-man's land, a diverging behavior has been inferred of properties such as the isobaric specific heat, the isothermal compressibility, the isobaric expansion coefficient, the shear viscosity and relaxation times [4]. All these properties, which have been measured, at maximum, down to T_H, can be interpolated by a power-law which tends to infinity at $T_S = 228K$, seven degrees below T_H [4].

A number of interpretations have been proliferating of the divergences in supercooled water and the intricate phase diagram, based either on thermodynamic or dynamic considerations [7]. None of the theories fully explains the entire phenomenology of water and none of them is fully supported yet by experimental evidences. The predictions of mode coupling theory (MCT) [8], originally developed to provide a dynamical viewpoint of the glass transition of fragile glass-formers, have been shown to apply to the dynamics of supercooled water, through molecular dynamics simulations (MD) [9, 10, 11, 12, 13, 14]. In the idealized formulation of MCT, the glass transition is associated to a purely kinetic blockage of the long range density fluctuations related to the structural relaxation. In this exact formulation the structural relaxation time is expected to follow a power law which diverges at a temperature T_c. The ideal MCT can be considered as a first order approximation in a more complex scheme [15] where the kinetic transition is an artifact of the approximations involved and disappears when couplings with particle momenta are taken into account. The concept of T_c retains the meaning of crossover temperature between two different dynamic behaviors and the prediction of the ideal MCT can be used to interpret the slow dynamics above T_c, when hopping effects are negligible. MD simulations of water dynamics have expressed a diverging power law for the temperature dependence of the structural relaxation time of water, where T_c is expected to be very close to T_S [11]. A good point of MCT is the ability to state very precise predictions which can be compared to the experimental determination of dynamical properties.

The investigation of the structural relaxation of liquid and supercooled water and the comparison to MCT predictions has been one of the main aims of the present work. Indeed the validity of the dynamic interpretation brings some general implications: *(i)* if MCT, which had been developed for simple liquids, is also successful in describing a complicated molecular system

like water, the existence of a universality in the self and collective behavior of liquids under deep supercooling is supported [11]. *(ii)* MCT predicts a purely dynamic transition at $T_c \approx T_S$. As a consequence, a purely dynamic mechanism can also be invoked to explain the apparent divergences of the physical properties, with no need for thermodynamic singularity.

The dynamical viewpoint adopted by MCT, is concerned with the study of the correlation functions of density fluctuations and with the relaxational phenomenology, which is intrinsically connected to them. When a perturbation is exerted on a fluid, the disturbance is damped by relaxation processes which evolve inside the system. In a macroscopic description, diffusion, viscous flow and thermal conduction are the macroscopic transport phenomena which play the dissipative role. In the absence of any external perturbation, spontaneous microscopic fluctuations always occur in a system which are dissipated in the same way as the external perturbance [16].

On the experimental side, **inelastic scattering** techniques are well assessed for the characterization of the dynamics of disordered systems over a wide dynamic regime [17, 18]. The *dynamic structure factor*, the Fourier transform of the mass density autocorrelation function, can be measured through inelastic scattering of radiation in the GHz to THz frequency domain. The excitation spectra are characterized by intensity peaks due to energy exchange between the incident probe and the acoustic modes of the investigated system. Depending on the incident wavelength of choice and on the instrumental limits, different techniques can access different region of exchanged energy ($\hbar\omega_P$) and momentum (Q), as shown in the diagram of Figure 2.

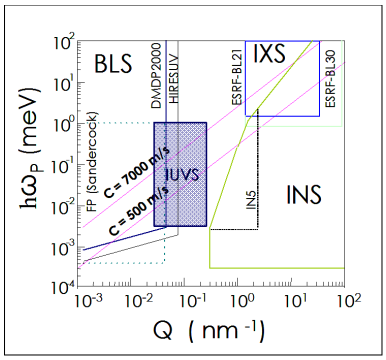


Figure 2: Exchanged (probed) energy $\hbar\omega_P$ and momentum transfer Q accessible by various technique for inelastic scattering. Mainly concerned with the present work is the new inelastic ultra violet scattering technique (IUVS). The first results ever published by any IUVS experiment are reported here, which, for instrumental construction, could not have been obtained by means of the other techniques for inelastic scattering. Other techniques of our interest are Brillouin light scattering (BLS) of visible light, and inelastic X-rays scattering (IXS) which is performed at synchrotron radiation sources.

To study a relaxation process in a certain temperature (and/or pressure) region, the opportune technique has to be chosen which fulfills the *best sensitivity condition* to the process in that temperature region. The eligible technique should be able to probe acoustic modes of angular frequency ω_P comparable to the reciprocal evolution time of the relaxation process, $1/\tau$.

Before the present work BLS and IXS were the two techniques available for inelastic scattering of radiation. BLS and IXS investigations of water dynamics had inferred that the best sensitivity condition to the relaxational dynamics of water would have been achieved by a technique which can probe the so-called *mesoscopic region* of exchanged energy and momentum which lies from 10 μeV to 1 meV and from 0.02 and 0.2 nm^{-1}. Indeed the best sensitivity of IXS to the relaxational dynamics of water is achieved at above 1 nm^{-1} [19]. At low Qs, BLS matches the relaxation of water well below the supercooling limit that is reachable in normal laboratory conditions [20].

The development of the IUVS beamline in Elettra synchrotron in Trieste [21], [22] [1]

[1] Underlined references have been co-authored by the author of the present manuscript.

has made it possible to investigate the relaxational dynamics of supercooled water. We have measured the dynamic structure factor of liquid and supercooled water by IUVS for the first time, down to 253 K. Since water has been the first system investigated by IUVS, we have also performed BLS measurements to get reference data for the new beamline. This has extended the investigated domain to a 3 decades wide frequency window. We have analyzed IUVS and BLS spectra simultaneously, in the framework of simple hydrodynamics and generalized hydrodynamics (with the introduction of the formalism of memory funcions) [16, 17]. As a result, we have obtained the characterization of the temperature evolution of the structural relaxation of water at different Q values, between 0.02 and 0.1 nm^{-1}. Our determinations have been successfully compared to the predictions of MCT [23]. The comparison of our investigations to results from IXS measurements, which had been performed and analyzed independently [19], has given confirmation of the reliability of IUVS experiments and of the unique role of IUVS, among other inelastic scattering techniques, in the investigation of the relaxational dynamics of supercooled water. Moreover, the characterization of the structural relaxation of water has brought discriminating evidences to the dilemma about the physical origin of the so called *fast sound* of water in the THz regime [24, 25].

The aqueous solution LiCl-6$\mathbf{H_2O}$. As the freezing point of water can be lowered by the addition of salt, another route to the properties of deeply supercooled water is the use of aqueous solutions under progressive dilution. By diluting a solution one can think to extrapolate the properties of the solvent. A first step in this direction has been done in the present work by characterizing the relaxational dynamics of the aqueous solution LiCl-6H_2O. The solutions LiCl-$R$$H_2O$ (where R is the solvent/solute molar ratio) offer actually an interesting phase diagram scenario. When $R \geq 6$ [26] the melting point decreases on reducing R and at $R = 6$ crystallization is just avoided down to $T_g = 135$ K, where the glass transition occurs. Adding water, the melting point increases. We have performed a wideband characterization of the $R = 6$ solution by photon correlation spectroscopy, BLS, IUVS and IXS techniques. The investigations have revealed the onset of the structural relaxation of the solution, as an interesting coincidence, in the same temperature domain at which the properties of water seem to diverge [27].

Structure of the document.

In Chapter 1 the scientific background is outlined. The diverging properties of supercooled water are introduced. MD simulations of supercooled water dynamics and their connection to the prediction of MCT are illustrated. The dilemma about the physical origin fast sound, which is strictly concerned with the the relaxational dynamics of water, is reported. The need for IUVS investigations of the structural relaxation of supercooled water is pointed out. The route of dilution of LiCl solutions is also introduced. Finally, the aims of the work are defined.

In chapter 2 the methodological approach adopted in the present work is described. The dynamic structure factor is the central quantity of our investigation. On the theoretical and computational side, molecular dynamics simulations of the dynamic structure factor have expressed well defined predictions about the relaxational dynamics of supercooled water, compatible with MCT. On the experimental side, we measure the dynamic structure factor by inelastic scattering experiments. Analyzing the measured intensity in the framework of simple and generalized hydrodynamics, we obtain the dynamical properties of water which we compare to the theoretical predictions.

Chapter 3 is a description of the instrumentation utilized. The beamline for inelastic ultra violet scattering in Elettra synchrotron is discussed in more detail. A shorter description is also given of the Fabry-Perot interferometer used for BLS measurements and of the ID16 beamline of the ESRF.

In Chapter 4 and Chapter 5 experiments, elaborations and results are reported and discussed, about water and the LiCl-6H_2O solution, respectively.

Final Remarks. The results obtained about the relaxational dynamics of water and of the solution LiCl-6H_2O are finally compared and interesting coincidences are highlighted .

Appendix A. the publications aroused by the present thesis work are listed in Appendix A. Co-authored works, performed in the laboratories attended during the development of the present work, are also mentioned.

Appendix B. In parallel to the present work, the Author has developed the elaboration of an experiment of synchrotron X-ray photoemission spectroscopy (XPS) which has lead to the proposition of a method to perform surface calorimetry. This method relies on the phonon broadening of bulk and surface photoemission peaks. Since phonon modes are nevertheless concerned with the present work and also in virtue of the interesting results obtained (published in [28]), this extra-topic is discussed here.

Résumé du Chapitre 1

Dans le Chapitre 1, nous présentons le contexte scientifique de ce travail et ses objectifs. Après une rapide présentation des propriétés fascinantes de l'eau, nous montrons que certaines de ses propriétés thermodynamiques et de transport présentent un comportement critique dans la phase surfondue qui peut être qualifié d'anomal par rapport au comportement de la plupart des liquides dans les mêmes conditions. Cependant la divergence de ces propriétés est interrompue par la cristallisation et il existe donc pour l'eau amorphe un intervalle de température qualifié de *no man's land* o ù toute tentative d'investigation s'avère impossible. C'est le domaine dans lequel devraient se produire les divergences attendues, ce qui a prêté matière, depuis des décennies, à de nombreuses controverses sur la vitrification de l'eau et sur l'interprétation des propriétés dynamiques et thermodynamiques associées. Des simulations de dynamique moléculaire ont fourni une description numérique de la relaxation structurale de l'eau, en bon accord avec le scénario proposé par la théorie du couplage de modes (MCT) Dans ce travail nous avons cherché à comparer les propriétés de relaxation de l'eau surfondue aux prédictions théoriques et numériques. De plus, comme la vitesse du son est intrinsèquement associée à la dynamique des liquides, nous avons pu contribuer à la discussion sur l'origine du *second son* dans l'eau. La diffusion inélastique de l'ultra violet est une technique de choix pour sonder la dynamique de l'eau surfondue. Une seconde voie consiste à diluer des solutions aqueuses pour extrapoler les propriétés de l'eau pure. Nous nous sommes engagés dans cette direction en étudiant la dynamique de la solution LiCl-6H_2O qui vitrifie sans cristalliser avec une température de transition vitreuse proche de celle attendue pour l'eau.

Chapter 1

Why Water

Abstract

In this chapter, the scientific background of the present work is drawn, together with its aims and expectations. A short overview about the fascinating properties of water is drafted. Some thermodynamic and transport functions of water exhibit, in the supercooled phase, a dramatic increase, anomalous with respect to the behavior of most liquids at the same thermodynamic conditions. The divergences seem to occur in the no-man's land of water, where any attempt to supercool bulk samples has been inconclusive. The physical origin of the divergences and the controversial behavior of water as a glass forming system are being matter of lively discussions since decades and thermodynamic and dynamical interpretations have been proposed. Molecular dynamics simulations have provided a well defined numerical description of the structural relaxation of water, in good agreement with mode-coupling theory (MCT) scenario. In this work we have meant to provide an experimental comparison to the relaxational properties of supercooled water to the numerical and theoretical predictions. Moreover, since sound velocity is intrinsically connected with the dynamics of liquids, we have faced the dilemma about the physical origin of *fast-sound*. Inelastic ultra violet scattering is the technique of choice to probe the dynamics of supercooled water. A second route is the dilution of aqueous solution to extrapolate the properties of the pure solvent. A first step in this direction has been done in this work by studying the dynamics of the LiCl-$6H_2O$ solution, which is a good glass-former whose glass transition temperature coincides with the one of water.

1.1 Importance of water

The motivation for the enormous interest of science towards water is comprehensively multiplex: water is ubiquitous in nature and essential to life. Indeed, water is the most abundant compound on earth (seventy percent of our planet is covered by oceans) and it is also the only substance which may be found in nature in the three states solid, liquid and gas, at ordinary temperature and pressure.

Any living tissue is mainly composed of water [2], cells, organs and microorganisms are constantly bathed in aqueous environment: without water, the four major classes of biological reactions -oxidations, photosynthesis, hydrolysis and condensation [29]- would not take place, with the consequence that biological systems would not function and life as we know would have not been originated. Water has unique hydration properties towards biological macromolecules (in particular proteins and nucleic acids) that determine their three-dimensional structures, and hence their functions in solution. This hydration forms gels that can reversibly undergo the gel-sol phase transitions that underlie many cellular mechanisms. Water ionizes and allows easy proton exchange between molecules, so contributing to the richness of the ionic interactions in biology [2].

Water is often called the *universal solvent* [2]. Due to its polarity, high dielectric constant and small size, water is particularly efficient to solve polar and ionic compounds and salts. A large

variety of chemical reactions take place in water or in aqueous mixed solvents. The interaction of water with clays, surfactants and metal surfaces is important in oil recovery, mining, catalysis, corrosion, inhibition and other technologically important concerns [2].

Water possesses strongly polar Hydrogen bonds which are responsible for a striking set of physical and chemical properties [2]. Throughout decades, different depictions of water structure have been proposed, based on different Hydrogen bonding coordination number, from clathrate to linear chains. However, the question "how is water structured, at molecular level?" is still debated, despite the massive efforts expressed in this sense.

Since water is so common, it is often regarded as a "typical" liquid. On the contrary, no other molecular liquid with as many nonstandard properties as water is known. According to W. Luck [2] "Life would not be possible on our planet without these anomalous properties of water". Supporting Luck's point of view, a much earlier and very detailed description of the way the various properties of water make it uniquely suitable for supporting biological life had been published in 1913 by L. J. Henderson [2].

The heat capacity of water is much higher than the value expected through contributions from various degrees of freedom using ordinary consideration. This fact, together with high thermal conductivity and high water content in organisms, contributes to thermal regulation and prevents local temperature fluctuations. The high latent heat of evaporation gives living tissues resistance to dehydration. In seas and oceans, the large heat capacity allows them to act as heat reservoirs, such that sea temperatures vary only a third as much as land temperatures and so moderate our climate (e.g. the Gulf stream carries tropical warmth to northwestern Europe). The compressibility of water reduces the sea level by about 40 m giving us 5% more land. Water's high surface tension plus its expansion on freezing encourages the erosion of rocks to give soil for our agriculture.

The molar volume at 1 Atm pressure and 273 K decreases from 19.66 cm^3 for ice to 18.02 cm^3 for liquid water. Contraction (-8 % volume) on melting is relatively rare among substances. As the liquid is further heated, it continues to contract until a density maximum is achieved at $\approx$ 277 K [2]. This anomalous phenomenon disappears at a sufficiently high pressure, where the temperature dependence of the volume becomes "normal". This density maximum together with the low ice density results in (i) the necessity that all of a body of fresh water (not just its surface) is close to 4° C before any freezing can occur, (ii) the freezing of rivers, lakes and oceans is from the top down, so permitting survival of the bottom ecology, insulating water from further freezing, reflecting back sunlight into space and allowing rapid thawing, and (iii) density driven thermal convection causing seasonal mixing in deeper temperate waters carrying life-providing oxygen into the depths.

Water at not too high pressure possesses a negative coefficient of viscosity below about 20° C [2]. This means that an increase in the pressure gives a lower viscosity, in an anti-intuitive behavior. With increasing pressure, cold water molecules move faster but hot water molecules move slower. Effectively, amongst the anomalies of water, are notable the opposite properties of hot and cold water, with the anomalous behavior more accentuated at low temperatures where the properties of supercooled water often diverge from those of hexagonal ice. As cold liquid water is heated it shrinks, it becomes less easy to compress, its refractive index increases, the speed of sound within it increases, gases become less soluble and it is easier to heat and conducts heat better. In contrast as hot liquid water is heated it expands, it becomes easier to compress, its refractive index reduces, the speed of sound within it decreases, gases become more soluble and it is harder to heat and a poorer conductor of heat. Hot water freezes faster than cold water and ice melts when compressed except at high pressures when liquid water freezes when compressed.

If the properties of liquid water in the normal liquid range are eccentric, they become exceedingly so below the equilibrium freezing point, in the metastable supercooled range. This is the subject of the next section.

A note about bibliography

A very good resource about water, always kept up to date, is the website of Prof. Martin Chaplin of London South Bank University: *Water Structure and Behavior* at the URL **http://www.lsbu.ac.uk/water/**, where about 1600 references are collected, including some results of the present work.

1.2 The supercooled state of water at ambient pressure

The schematic diagram in Fig. 1.1 maps the temperature ranges of stability of water at atmospheric pressure. The stability domain of liquid water is between 373 and 273 K. From top to bottom of the temperature scale, T_B is the normal boiling point, above which superheating has been realized, up to 553 [30]. The onset of anomalies has been observed in sound velocity (333 K), isothermal compressibility (319 K), shear viscosity (293 K), and in density, which has its maximum value at $T_{MD} = 277$ K [4, 31].

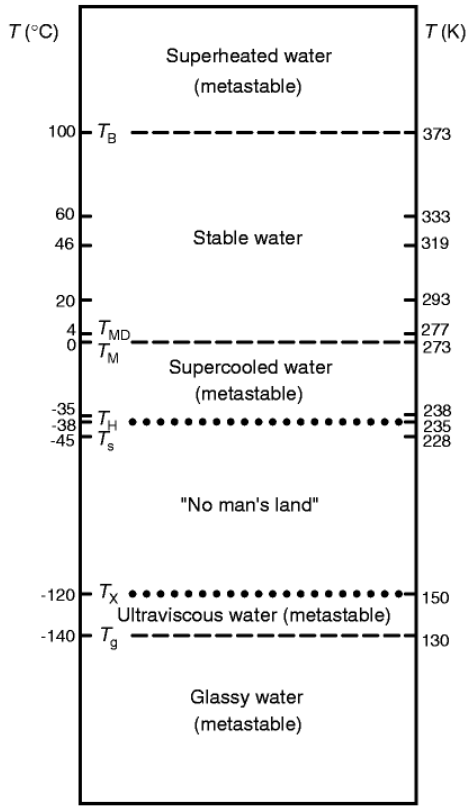


Figure 1.1: Thermodynamic regions of phase stability of water at P = 1 Atm, adapted from Ref. [3]. See text.

Below the equilibrium freezing point, $T_M = 273$ K, the supercooled metastable phase has been realized in bulk water down to the temperature of homogeneous nucleation $T_H = 235 \pm 1$ K (-38° C) [4]. In cloud chambers three degree of supercooling have been gained, down to 232 ± 1 K (-41° C). Non-bulk water confined in ≈ 1 nm diameter pores, can be supercooled down to 200 K [32]. Indeed, the interval between T_H and $T_X = 150$ K, temperature when cubic ice I_c is stable phase, is often referred as *no-man's-land*, because the direct observation could not be performed of bulk supercooled water, regardless of whether one attempts to enter the no man's land by cooling further a supercooled sample or water or by heating the glass, which tends unavoidably to crystallize to cubic ice above T_X. Due to polyamorphism of water, the glass transition temperature itself is ill defined. Since a long time it has been stated that T_g should be ≈ 136 K (hyperquenching glass transition) [33] even though other studies are more in favor of the reassignment to 165 K (calorimetric glass transition) [34, 35]. Very recently, the values 210 K [36] and 228 K [37] have also been proposed for T_g.

1.2.1 Puzzling properties of supercooled and glassy water

It is just in the supercooled range and into the no-man's land that the thermodynamic properties of water show or are expected to show the most pronounced anomalies. In Figures 1.2 and 1.3 the temperature dependence of density, thermal expansion coefficient, isothermal compressibility and molar heat of water (dotted plots) are compared to the behavior of most liquids (red lines).

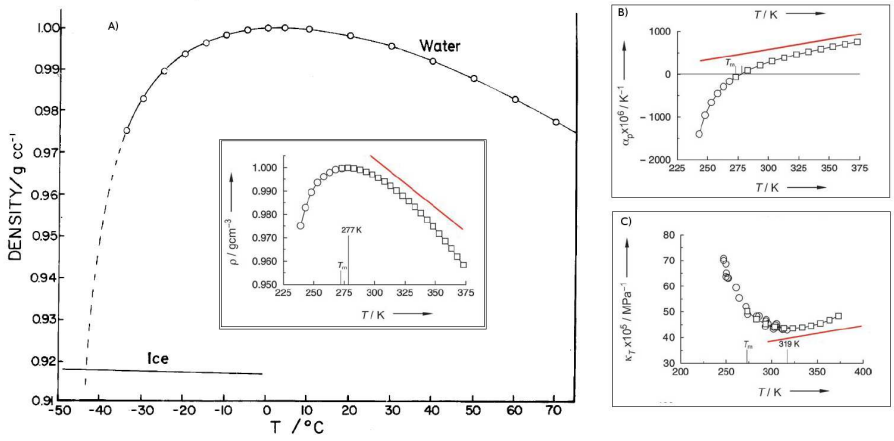


Figure 1.2: A schematic comparison of the temperature dependence at ambient pressure of density ρ (panel A), and its derivatives: the thermal expansion coefficient α_P (panel B) and the isothermal compressibility κ_T (panel C). Red lines represents the behavior of simple liquids. The density has a maximum at 277 K and seems to tend to the density of ice I at $T_S = 228$ K. The derivatives of density exhibits apparent divergences towards T_S while most liquids follow almost linear trends.

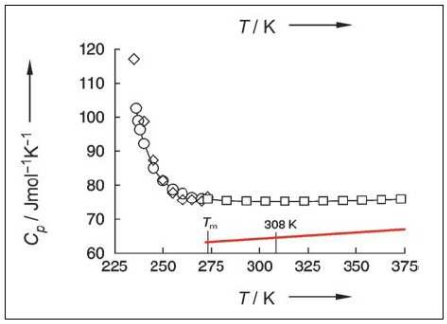


Figure 1.3: Molar heat of water as a function of temperature at ambient pressure (dotted line), compared to the linear trend of other liquids (red line)

Density

The density of bulk water has been measured from 373 K to 239 K [4]. The limit of 239 K has been reached in capillaries of $\approx 10\ \mu$ diameter, the thinnest size at which the properties of capillary water are the same than in bulk [4]. The density show two noticeable features: a maximum at $T_{MD} = 277$ K and an apparent (extrapolated) "decay" to the density of ice I at $T_S \approx 228$K, which actually has not been observed because of crystallization. Since ice I has the most open structure as possible, for a system of four coordinated molecules, this extrapolation has made to propose that a kind of structural rearrangement of hydrogen bonding coordination [4].

Apparent divergences at T_S

The isothermal expansion coefficient $\alpha_P = (\partial ln(v)/\partial T)_P$, the isothermal compressibility $\kappa_T = -(\partial ln(v)/\partial P)_T$ (where v is the molar volume) as well as the isobaric heat capacity at constant pressure C_P, and also transport properties like shear viscosity and self-diffusion coefficient, have revealed, in the supercooled phase, a dramatic increase as a function of decreasing temperature which has been all well accounted for, in all cases, by the same power law [4]

$$y(T) \propto \left(\frac{T_S}{T - T_S}\right)^{\gamma_y} \tag{1.1}$$

which diverges towards $T_S = 228 \pm 3$ K (-45° C), nine degrees below T_S. As T_S is located 7 degrees below T_H the divergence is called "apparent" or "inferred". If the limiting temperature T_S is common to all the properties, the γ_y exponent is instead characteristic of the physical quantity. It is in any case found to be greater than unity and varying in the range $1.5 \div 1.8$.

Derivatives of density

It is straightforward to observe that the marked increase in $\alpha_P = (\partial ln(v)/\partial T)_P$ and $\kappa_T = -(\partial ln(v)/\partial P)_T$, the derivatives of density, reflect the change in slope below T_{MD}. A more exhaustive explanation is given if pressure comes into play [1].

Molar Heat

In Figure 1.3, the molar heat of water measured by standard calorimetry as a function of temperature is reported, together with measurements performed in water emulsions down to T_H. Values at lowest temperatures have been measured using emulsion samples, as reducing sample dimensions avoids sample freezing [4].

If C_P seems to diverge towards 228 K (-45 ° C), this does not occur in C_V, because of a compensation that may be realized by the following relationship:

$$C_V = C_P - VT\frac{\alpha_P^2}{\chi_T} \tag{1.4}$$

[1] The identity which relates the locus of temperatures at which the density is maximum at fixed pressure (water locus of density maxima, also referred to as the temperature of maximum density, TMD) to the temperature dependence of the isothermal compressibility κ_T [38] is

$$\left(\frac{\partial \kappa_T}{\partial T}\right) = \frac{v^{-1}(\partial^2 v/\partial T^2)_{P,atTMD}}{(dP/dT)_{TMD}} \tag{1.2}$$

α and κ_T are related by the identity

$$\left(\frac{\partial \kappa_T}{\partial T}\right)_P = \left(\frac{\partial \alpha}{\partial P}\right)_T \tag{1.3}$$

As the density decreases below T_{MD} with the decreasing temperature, the thermal expansion coefficient α_P becomes negative. It follows from Eqs. (1.2) and (1.3) that the magnitude decrease of the (negative) thermal expansion coefficient upon isothermal compression and the increase in isothermal compressibility upon isobaric cooling are inseparable from the existence of the negatively sloped TMD locus (in the T-P plane [7]), as it has been measured for water [39].

Shear viscosity

The viscosity of a liquid is a macroscopic measure of its resistance to flow. The shear viscosity of water $\eta_s(T)$, is reported in Figure 1.4 in Angell-plot format ($\lg \eta_s$ versus $1/T$). The viscosity has been measured down to 238 K by means of various techniques, among which is capillary viscosimetry. The experimental curve cannot be fit by an Arrhenius curve. Viscosity has been interpolated by the diverging power law of Eq. 1.1, with an exponent $\gamma_y = 1.55$ [4].

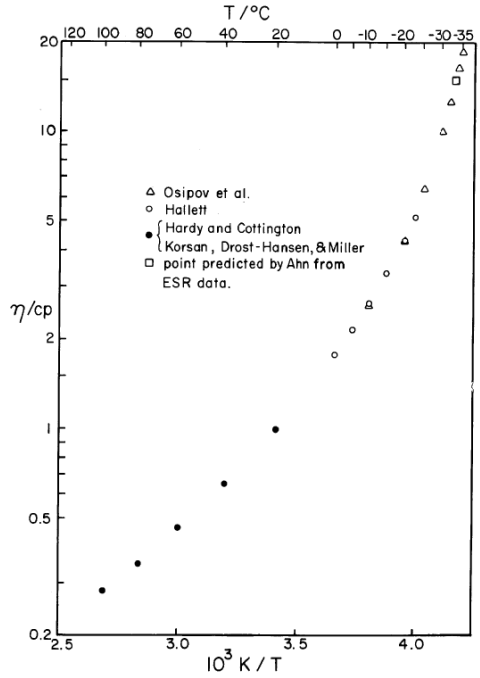


Figure 1.4: Angell plot of viscosity of water. (Picture from [4]).

An enhancement of the viscosity upon cooling is usually one of the immediate fingerprints of the glass transition. The good glass-forming systems, upon sufficiently fast cooling below the melting point, bypass nucleation and hold in the metastable supercooled liquid phase. Upon further cooling, at some point the viscosity undergoes an increase of several decades in few degrees, a sign that the system is not anymore ready to flow and, in correspondence to the glass transition temperature T_g the glassy phase is obtained. At that point the viscosity will have reached a constant value (typically 10^{13} Poise) which does not change any longer upon further cooling. Such an increase in viscosity is accompanied by other phenomena, like a peak in the heat capacity in correspondence of T_g and the discontinuity in the volume and in the expansion coefficient (See *e.g.* Ref. [40]).

As one can appreciate in Figure 1.4, freezing occurs before enough data are collected to ascribe the phenomenology of water to glass transition. Indeed, the allocation of this substance among glass forming systems is controversial for more than one reason.

1.2.2 Water as a glass-former

Water is quite a bad glass former. Hyperquenched glass of micron sized droplet has been realized at a cooling rate of 10^5 K/s [42]. At lower cooling rates and for larger samples crystallization

always intervenes. Moreover, the same way this substance is polymorphic (it owns at least 12, possibly 15, forms of ice) this substance is also poly-amorphic, having its glasses been realized in different forms, reason why there is not an agreement about T_g.

Glasses of water are classified as low density and high density amorphous phases, LDA and HDA. LDA has been realized by vapor deposition onto a cold surface [43] and by hyperquenching of micron-sized droplets [44, 45, 46]. LDA transforms into a highly viscous liquid when heated above $\approx$ 130 K, which defines the experimentally known value of T_g. HDA has been realized by pressurizing hexagonal ice, I_h below 150 K [47, 5, 48] and, independently, by bombarding an ice-I_h layer with an electron beam. When compressed further, at low enough temperatures, HDA transforms in a high density crystalline ice [48, 49]. If HDA is warmed to $\approx$ 115 K, it suddenly expands to LDA. The transition HDA-LDA is reversible [50, 51] as HDA can be obtained by compressing LDA. A third form of glass, the very high density amorphous phase (VHDA), has been realized from the isobaric heating of the high density glass [5].

Such a complex behavior is concerned from far with the problematic we have at ambient pressure in moderately supercooled water. This is resumed in section 1.3.3.

1.3 Interpretation: the dynamic viewpoint of mode coupling theory

Theoretical and experimental efforts of scientists have been devoted along decades to understand the origin of the puzzling phase diagram of water and the apparent divergences. Several models which have been proposed to explain the anomalous properties of water are reviewed in Ref. [7]. Among the most debated interpretations are the presence of a retracing spinodal line [52, 53, 54], the occurence of a liquid-liquid transition and the existence of a second critical point [55, 56, 57, 58, 59, 60, 61, 62, 63] or, oppositely a singularity-free scenario [64, 65, 66, 67, 68, 69, 70, 71, 72] with a possible fragile-to-strong transition [6]. Until now, none of the theories can fully explain the entire phenomenology of water and none of them is fully supported yet by experimental evidences.

Beyond these interpretations, a considerable computational work [9, 10, 11, 12, 13, 14] based on molecular dynamics simulations (MD) with the SPC/E model of water [73] has shown that supercooled water exhibits slow dynamics in the supercooled region, consistent with the predictions of the idealized mode-coupling theory (MCT) [74], which can explain the anomalies of water from a dynamical viewpoint, without resorting to any thermodynamic anomaly.

Originally developed to provide a dynamical viewpoint of the glass transition of fragile glass-formers [8, 74, 75], MCT provides an accurate description of the temporal evolution of correlation functions of the mass density. In the idealized formulation, the glass transition is associated to a purely dynamical structural arrest of the long range density fluctuations related to the structural relaxation. The structural relaxation time is expected to follow a power law which diverges at a temperature T_c. Below T_c the correlation functions no longer decay to zero and the system undergoes a transition from ergodic to non-ergodic regime. This idealized formulation of MCT can be considered as a first order approximation in a more complex scheme [15] where the blockage is an artifact of the approximations involved and disappears when couplings with particle momenta are taken into account. In the complete scheme, the coupling between density and momentum fluctuations, not taken into account in the so-called idealized mode-coupling theory, restores the ergodicity below T_c. The concept of T_c retains the meaning of crossover temperature between two different dynamic behaviors and the prediction of the ideal MCT can be used to interpret the slow dynamics above T_c, when hopping effects are negligible, e.g. in the moderately supercooled regime of water.

The main implication of MCT is that this theory assigns a purely dynamical origin to the anomalies of supercooled water. No thermodynamic singularity is invoked to explain the slowing down of structural relaxation. An avoided dynamic transition where the system would become non-ergodic is rather thought to underlie the experimental observations of slow dynamics in supercooled

water.

1.3.1 MCT statements

MCT for supercooled liquids moves its steps from the cage-effect modeling. The particles are localized in cages formed by their neighbors. Only a part of the configuration space is available for motion, while a major one is excluded due to the strong short range repulsive potentials [2]. Migration of molecules in normal liquids is possible only because the neighboring particles are not fixed but move out of the way: the neighbors can move because their neighbors move, etc. In a complete equivalence, which applies for every particle, the cage-forming particles exhibit the same dynamics as those which are trapped in the cages and all fluctuations have to be treated on the same level. In the supercooled phase or in dense liquid regime a particle trapped in a cage can migrate only through the rearrangement of a *large* number of particle surrounding it and a strong coupling exists between the motion of the single particle and the density fluctuations in the fluid. In dense or supercooled liquids the *structural or alpha- relaxation* is the cooperative rearrangement of large complexes of molecules. Upon lowering the temperature or increasing the density, a rapid increase in the local order surrounding the particle arises, leading to a substantial increase of the relaxation time.

MCT predicts the evolution of any correlator that has a nonzero overlap with density [16], such as, e.g., the density itself, the current density, and the tagged particle density. The quantity of our interest is the so called intermediate scattering function, $F(Q,t)$ that is, the (Q,t)-th component of the density-density correlation function $G(r,t) = \rho^{-1}\langle\rho(r,t)\rho(0,0)\rangle$, [16] (See Chapter 2):

$$F(Q,t) = N^{-1}\langle\rho(Q,t)\rho(Q,0)\rangle = \int drG(r,t)\exp(-iQ\cdot r) \tag{1.5}$$

where

$$\rho(Q) = \int dr\rho(r)\exp(-iQ\cdot r) \tag{1.6}$$

The zero-time value of F i s the static structure factor

$$S(Q) = N^{-1}\langle\rho(Q,0)\rho(Q,0)\rangle \tag{1.7}$$

Central to the theory is an equation for the normalized $F(Q,t)$, that is for $\phi(Q,t) = F(Q,t)/S(Q)$, whose solution will yield the time evolution of density fluctuations. Without loss of generality, it is correct the use of a generalized Langevin equation for $\phi(Q,t)$

$$\ddot{\phi}\,(Q,t) + \Omega_Q^2\gamma_Q\,\dot{\phi}\,(Q,t) + \Omega_Q^2(t)\phi(Q,t) + \Omega_Q^2\int_0^t dt' m_Q(t-t')\,\dot{\phi}\,(Q,t') = 0 \tag{1.8}$$

where $m(Q,t)$ is the *memory function* (see Chapt. 2), $\Omega_{\mathbf{Q}}^2\gamma_{\mathbf{Q}} \equiv \nu_0$ is a damping constant and $\Omega_{\mathbf{Q}}$ is a characteristic phonon frequency, given by

$$\Omega_Q^2 = (Qv)^2/S(Q), \qquad v = (RT/M)^{1/2} \tag{1.9}$$

where R is the constant of gases and M is the molar mass.

The initial conditions for this equation are:

$$\phi(Q,0) = 1, \qquad \dot{\phi}\,(Q,0) = 0 \tag{1.10}$$

The unknownness about the behavior of the system is moved into the memory function $m(Q,t)$.

The fundamental statement of MCT is posed at this point, as a feedback mechanism is introduced into memory function: the memory $m(Q,t)$ itself is considered as a functional of $\phi(Q,t)$

[2] It is an essential problem of a theory of liquids to include this fact and obtain its implications on measurable quantities. Cohen and Turnbull modified the transition state theory for particle diffusion by accounting for the difference between free and total volume. Thereby they arrived at the Vogel-Fulcher law [76]

$$m(Q,t) = m(\phi(Q,t)) \tag{1.11}$$

which Götze denotes symbolically as

$$m(Q,t) = v_1\phi(Q,t) + v_2\phi(Q,t)^2 \tag{1.12}$$

Equation (1.11) is the main point of this approach and expresses the coupling between the mode $\phi(Q,t)$ and its memory $m(Q,t)$, which gives the name to the theory. The underlying idea can be understood intuitively as follows. If we choose as memory function the viscosity, η, of the system, the viscosity itself exerts a control on the relaxation time. In fact, the relaxation of fluctuating stresses contains structural rearrangements which are strongly inhibited if the viscosity gets high. That causes a dependence on η of the relaxation time τ such that $\tau \to \infty$ for $\eta \to \infty$. This can be understood as *(i)* the relaxation occurs primarily through diffusive motion across the cages; *(ii)* diffusivity is inversely proportional to viscosity; *(iii)* viscosity is proportional to relaxation time. These relations define a nonlinear feedback mechanism for the viscosity.

Details about the solving of Eq.(1.8) may be found in [77]. The ideal MCT predicts the existence of a two-step relaxation scenario for $\phi(t)$ which is represented schematically in Figure 1.5. Above T_c (panel a)) the so called beta-relaxation occurs at shorter correlation (decay from the first to the second plateau) and then the so called alpha-relaxation, at long correlation times (decay from the second plateau to zero).

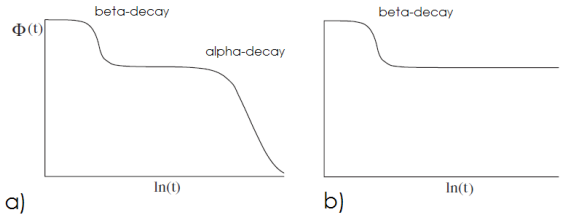


Figure 1.5: a) ergodic (supercooled) regime for $T > T_c$. Both beta- and alpha processes occur. The correlation of density fluctuations vanishes on a finite timescale. b) In the glassy non-ergodic phase below T_c the idealized MCT foresees the blockage of the long range and long time density fluctuations forbids the time decay of the corresponding correlations. Only fast processes are present.

The second intermediate plateau is the so called non-ergodicity factor f, as for T $< T_c$ the blockage of the long range fluctuations occurs which brings the system in a non-ergodic glassy phase. Only the energy activated molecular processes occur in the system (panel b)). The beta relaxation may be fitted as $f + At^{-a}$, the alpha-relaxation as $f - Bt^{-b}$. The exponents a and b are not independent but related through the relationship $\Gamma(1-a)^2/\Gamma(1-2a) = \Gamma(1+b)^2/\Gamma(1+2b)$, where Γ is the Euler's gamma function.

The structural (or alpha) relaxation time has a power law dependence on temperature

$$\tau(T) \propto |T - T_c|^{-\gamma} \tag{1.13}$$

where $\gamma = 1/2a + 1/2b$.

In the long time limit, as an analytical solution for ϕ cannot be given, it has been shown numerically that $\phi(t)$ follows a Kohlrausch-William-Watts (KWW) stretched exponential form:

$$\phi(t) \propto exp^{-(t/\tau)^\beta} \tag{1.14}$$

The ideal MCT can be considered as a first order approximation in a more complex scheme [15] where the kinetic transition is an artifact of the approximations involved and disappears when couplings with particle momenta are taken into account. Nevertheless, the concept of T_c retains the meaning of crossover temperature between two different dynamic behaviors and the prediction

of the ideal MCT can be used to interpret the slow dynamics above T_c, when hopping effects are negligible.

1.3.2 MD simulations

Molecular dynamics simulations have been performed of the intermediate scattering function $F(Q,t)$ of water at T = 207 up to 285 K, in a time range from 1 fs to 10 ns and wavevectors between 0.3 and 80 nm^{-1} [9, 10, 11, 12, 13, 14][3].

In agreement with the MCT predictions, all the correlators show a two-step decay process (See figure 1.6).

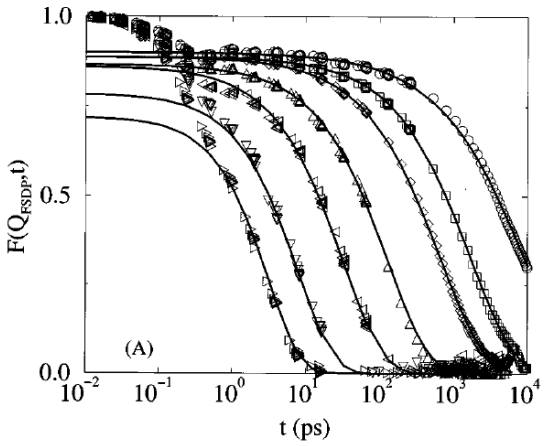


Figure 1.6: Correlators calculated by MD simulations of water dynamics at Q = 18 nm^{-1}, and temperatures from 207 K (circles), 210 K (squares), 213 K (diamonds), 225 K (top-up triangles), 238 K (top-down triangles), 238 K (top-left triangles) 258 K (top-down triangles), 285 K (top-right triangles). (Figure adapted from F. Sciortino et al, Phys. Rev. E. 56, 5397 (1997).)

The second decay process, from the non-ergodicity parameter to zero, to has been clearly identified with the alpha-relaxation process. It is characterized by the higly stretched-exponential behavior of Eq. (1.14). The stretching coefficient β is Q-dependent (see figure 1.7). The stretching is more prominent at high Qs ($\beta = 0.5 \pm 0.1$) and becomes minor at low Qs ($\beta = 0.7 \pm 0.1$).

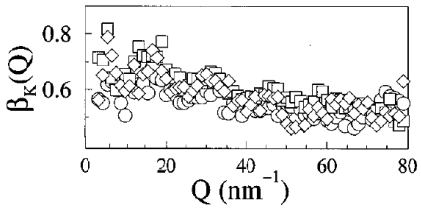


Figure 1.7: Stretching exponent β calculated by MD simulations, as a function of Q and at temperatures between 200 K and 225 K (Figure adapted from F. Sciortino et al, Phys. Rev. E. 56, 5397 (1997).)

[3]Molecular dynamics simulations have been performed on a system of N = 216 molecules of water at constant volume. The total volume of 216 molecules if the density is 1 g cm^{-3} corresponds to a cube of side $\approx$ 1 to 2 nm. The molecules interact with the extended simple point charge (SPC/E) potential with boundary conditions [73] which treats a single water molecule as a rigid set of point masses with an OH distance of 0.1 nm and an HOH angle equal to the tetrahedral angle 109.47 °. The Coulomb charges are placed on the atoms and their magnitudes are q_H = 0.4238 times the electron charge and q_O = -2q_H . Oxygen atoms interact via a Lennard-Jones potential with the values of σ = 0.316 56 nm and ϵ = 0.650 17 kJ mol^{-1}.[11]

The structural relaxation time follows an apparent power law divergence according to Eq. (1.13), towards a T_c which is located at about 50 K below the maximum density temperature which, at ambient pressure, will locate the divergence in the $\approx$ 220 - 230 K interval, that is, close to the temperature T_S where the thermodynamic properties seem to diverge. The γ exponent of the power law for $\tau(T)$ is $\gamma = 2.7$.

1.3.3 Implications

There are several reasons for an experimental test of MCT.

The results of MD simulations with the SPC/E potential express impressively well defined predictions, in agreement with MCT, which call for experimental evidences. Indeed, the intermediate scattering function, or, equivalently, the dynamic structure factor, is the quantity measured by experiments of inelastic scattering of radiation. The fact that MCT, which has been developed for simple liquids, may succeed in describing such a complicated molecular system, strongly supports the existence of a universality in the self and collective behavior of liquids under deep supercooling [11].

It has been generally found that the T_c of the idealized version of MCT T_c is higher than the real glass transition T_g [78]. The ergodicity of the system below T_c is taken into account when the correlation with the momenta are included [7, 11]. Nevertheless, for the temperature regime below T_c, theoretical viewpoints like the Adam-Gibbs theory come usually into play more reliably [79]. The critical temperature T_c retains then the meaning of a dynamical change in the system investigated.

Tt is worth mentioning the liquid-liquid phase transition hypothesis, which also arose from molecular dynamics simulations of the structure and equation of state of supercooled water.

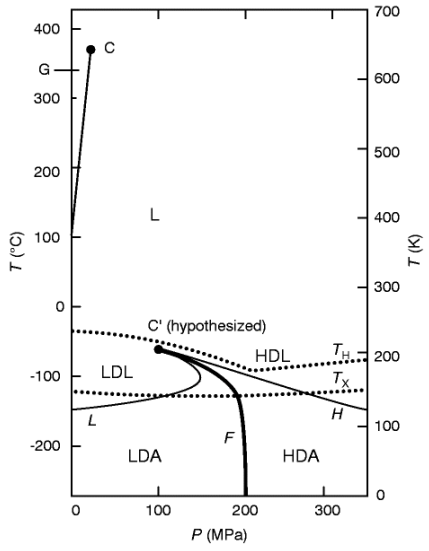


Figure 1.8:

This model hypothesizes the existence of a second critical point, $T'_{cr} \approx 220$ K, $P'_{cr} \approx 100$ MPa and $\rho'_{cr} \approx 1$ g/cm^3 below which the liquid phase separates into two distinct liquid phases: a low-density liquid (LDL) phase at low pressures and a high-density liquid (HDL) at high pressure. Water near the known critical point [4] is a fluctuating mixture of molecules whose local structures

[4]The known critical point has coordinates $T_{cr} = 647$ K, $P_{cr} = 22$ MPa and critical density $\rho_{cr} = 0.328$ g cm^{-3}. Below this point, the high-pressure and high-temperature liquid phase separates into two distinct fluid phases: a low-density gas phase at low pressure and a higher-density liquid phase at high pressure.

resemble the liquid and gas phases. Similarly, water near the hypothesized second critical point is a fluctuating mixture of molecules whose local existence of two distinct liquid phases and, therefore, of a liquid-liquid transition line between these two liquids. Even if our target has been limited to the investigation of the supercooled phase at ambient pressure, our attention is brought on the closeness of T_S, T_c and T'_{cr}. If a second critical point exists, it would influence the whole phase diagram, not only the local region around it.

1.4 The dynamical approach can solve the dilemma of *fast-sound*

Since the dynamical properties of a liquid are intrinsically related to speed of sound, the characterization of the structural relaxation of supercooled water is expected to provide evidences able to discriminate about different interpretations of the phenomenon of *fast-sound*. Indeed, the existence in water of acoustic-like modes which propagate at about 3200 m/s, a value close to the speed of sound in ice and roughly twice than that of ordinary sound in the liquid, has been assessed since decades. These modes had been first hypothesized by molecular dynamic (MD) simulations and then revealed by inelastic scattering of neutrons (INS) and X-rays (IXS), at wave vectors higher than 1 nm^{-1} (See the reviewing paper Ref. [80] and references therein). In Figure 1.9 the data of the dispersion relations (energy $h\nu$ of the detected/calculated modes as a function of the respective momentum transfers Q) of water at 293 K and ambient pressure are reported. Measurements and simulations have been lead at Qs ranging from 1 to 12 nm^{-1}.

The whole scenario of Figure 1.9 identifies two limiting speeds of sound evaluated according to the relationship $C = h\nu/Q$: at low momenta, the value $c_0 = 1500$ m/s, well known from ultrasonic measurements at KHz frequencies [139], is given by the slope of the lower straight line. At high Q's, the speed of sound $c_\infty = 3200$ m/s is the slope of the higher straight line.

Two phenomenological models aim at the interpretation of the complete set of data reported in Figure 1.9 :

1. The visco-to-elastic transition picture, in the framework of generalized hydrodynamics [16],
2. The opticlike-acoustic modes interaction interpretation [92]

1. According to the works in Refs. [19, 90, 91], developed in the framework of generalized hydrodynamics, when the frequency of the acoustic modes excited by the incoming radiation (or neutrons) is low enough (-or if, given a fixed frequency, the temperature is high enough-) for the molecular rearrangements which give rise to the structural relaxation to follow the acoustic modes, the structural relaxation itself will not affect the acoustic modes. This limiting regime system is called *viscous* or *relaxed*. The speed of sound is named c_0. At higher and higher momentum transfers -or frequency- the relaxation becomes less and less able to follow the acoustic modes. The acoustic modes at a frequency comparable to the reversed relaxation time, can exchange energy with the relaxation and the so-called *apparent* speed of sound $C = h\nu/Q$ increases (See Chapters 2 and 4). At higher Qs, given that the temperature is not changed, the modes will be too fast to interact with the molecular reorganizations of the structural relaxation. The system is told to be in the *unrelaxed* regime or to give an *elastic* response. The speed of sound is in its high frequency limit, denoted c_∞.

In Fig. 1.10 the speed of sound $C(Q)$ measured by IXS reveals the transition of the system from the viscous to the elastic regime at 293 K. The value $c_0 = 1500 m/s$ has been measured by ultrasound techniques. The transition is not complete due to the resolution limits of IXS and has been measured down to $Q \approx 1$ nm^{-1}. As a function of increasing momentum transfer, $C(Q)$ grows up to the limiting value $c_\infty = 3200 m/s$.

2. The interaction-model [92], conceived in conceptual agreement with the hydrodynamics of disparate-mass fluid mixtures [85], is based on the hypothesis that an interaction occurs between a dispersive-acoustic mode and an optic-like (non dispersive) mode, which have the same symmetry and cross at $Q \approx 3$ nm^{-1}. The modes are depicted in Figure 1.11 over the experimental dots, together with the hypothesized interaction function.

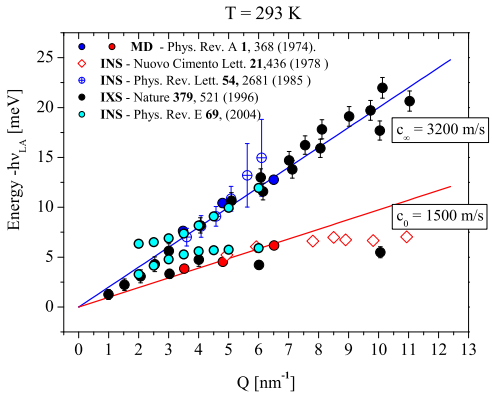


Figure 1.9: Dispersion relation of water at 293 K and ambient pressure, as calculated by MD simulation and measured in IXS and INS experiments (dots). The slopes of the two lines are the two limiting values of speed of sound in these condition of temperature and pressure: $c_0 = 1500$ m/s and $c_\infty = 3200$ m/s. The first indication for the presence of the high-frequency sound mode was given in 1974 by MD simulations [81]. A decade later, inelastic neutron scattering experiments on D_2O provided the first experimental evidence for a collective mode having a speed of ≈ 3300 m/s in the $Q = 3.5 \div 6$ nm^{-1} region [82]. In the same years, the term *fast-sound* was introduced to indicate a high frequency ($\omega/2\pi \approx 10^{13}$ Hz) and high Q's ($\approx 1 \div 6$ nm^{-1}) density wave, that was calculated by MD [83] and detected by INS [84] in binary mixtures with large mass difference, like metallic alloys and rare-gas mixtures. This fast mode was inferred to be propagated by the lighter component of the mixture alone [85]. Moreover, MD simulations suggested a bifurcation from *normal* to *fast* sound regime at wave vectors approaching some nm^{-1} [86]. The denotation *fast-sound* was progressively extended to the high-frequency sound found in water [87] when MD studies attributed its propagation to the librational motion of hydrogen atoms [88].

The non-dispersive mode is characterized by a Q-independent energy $\hbar\omega_0$. The energy of the dispersive acoustic mode is linearly dependent on Q like $\hbar\omega_a = \hbar c_\infty Q$, where c_∞ is the slope of the curve. The two modes $\omega_0(Q)$ and $\omega_a(Q)$ are hypothesized to interact at $Q \approx 1$ nm^{-1}. The interaction term $\beta(Q)$, is defined to be maximum where the modes cross and to be extinguished at high Qs. It is thus shaped as:

$$\beta(Q) = \beta_0 Q e^{-\lambda Q} \tag{1.15}$$

$\beta(Q)$ is linear at low Q's and decays exponentially at high Q's. The interacted modes result [92]:

$$\omega_\pm^2(Q) = \frac{\omega_a^2 + \omega_0^2 \pm \sqrt{(\omega_a^2 - \omega_0^2)^2 + 4\beta^2}}{2} \tag{1.16}$$

In figure 1.11 the non interacted modes, the interaction term and the interacted modes ω_+ and ω_- are shown as a function of Q. Slow and fast sound in this viewpoint are associated to the low frequency and high frequency slopes of ω_- and ω_+, respectively. An important difference with respect to the viscoelastic picture is that no relaxation and *no transition* between the two modes is involved.

The intriguing point is that both models can interpret reasonably well the high frequency data even though they are based on basically different background hypotheses. Indeed, the interaction model hypothesizes a linear dependence of $\beta(Q)$ just around $Q \approx 0.1$ nm^{-1}, a dynamical region where experimental evidences for water dynamics are lacking. Actually the Q-region around 0.1 nm^{-1} is exactly the one we want to investigate, in order to characterize the relaxational dynamics.

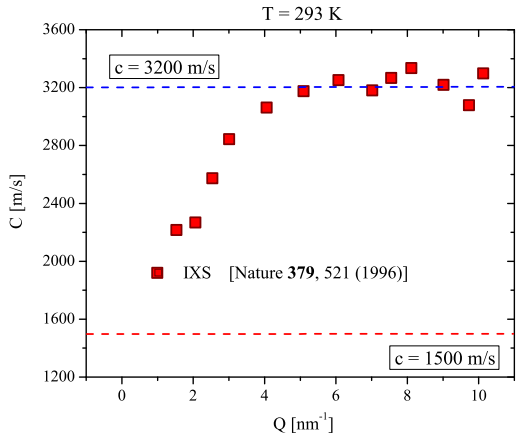


Figure 1.10: Apparent speed of sound at 293 K and ambient pressure calculated from the IXS data according to $C(Q) = h\nu_{LA}(Q)$. According to hydrodynamics, the evident transition between the low and high speed limits is due to competing timescales of acoustic phonons and of structural relaxation. At low frequencies the system is relaxed and the flow is viscous, phonons are slow enough that the relaxation can "accord" on their frequencies. Figure adapted from [80]

This region is meaningful because the symmetry rules decouple the longitudinal from the transverse variables in the generalized Langevin equations of hydrodynamic [16], i.e., the pure longitudinal and transverse modes may be detected separately.

1.5 Need for inelastic ultra violet scattering

Before the development of the present work, the dynamic structure factor of water had been measured down to 273 K by inelastic X-ray scattering [19] and down to 250 K by Brillouin light scattering [20]. These works had inferred that the relaxation of supercooled water is characterized by a timescale of 1-10 ps, which escapes the energy-momentum dynamical windows probed by these techniques. Beyond that, a previous optical Kerr effect (OKE) experiment [93] pointed toward a MCT-based interpretation of the dynamics in liquid water. This experiment indicated the existence of a well defined stretching of the measured correlation functions. Nevertheless the OKE technique does not probe directly the central quantity of MCT, i.e. the density-density correlation function $F(Q,t)$. Moreover it has been demonstrated [94] that care must be taken in making a quantitative comparison between OKE data and MCT predictions. With respect to this, a direct determination of $F(Q,t)$ or of its Fourier transform the dynamic structure $S(Q,\omega)$, is highly desirable.

A unique technique for measuring the dynamic structure factor of supercooled water is expected to be inelastic ultra violet scattering (IUVS) at "mesoscopic" energy and momenta, i.e., between those probed by BLS and IXS. This is expressed in more detail in Chapter 3. The beamline 10.2 in the Elettra synchrotron of Trieste, first instrumentation ever built to perform IUVS experiments can actually span such a mesoscopic region, as the momentum transfers probed can range around 0.1 nm^{-1} and the exchanged energies between $\approx$ 10 to 100 microelectronvolts (See Chapter 3).

Inelastic ultra violet scattering has been utilized for the first time ever, to study the dynamics of supercooled water. As the 10.2 beamline was new and also to get information in a larger frequency window, we have performed BLS reference measurements too.

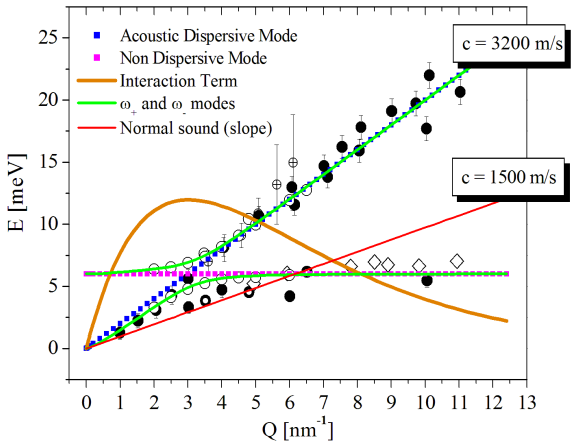


Figure 1.11: Dispersion relation of Figure 1.9 with the two modes of interaction-model superimposed. Dotted lines are the non-interacted modes. Continuous green lines are ω_- and ω_+ interacted modes of Eq. (1.16). The orange line represents the interaction term of Eq. (1.15). Figure adapted from Ref. [92].

1.6 Why LiCl-6H_2O

We have performed a wideband investigation of the dynamics of the LiCl-6H_2O (See Chapter 5). The motivations are introduced in the following sections.

1.6.1 The untrivial supercooling of water

The early studies of supercooled water, since 1837, were more challenged by the understanding of supercooling limit than by the measuring of the physical properties of water themselves [95]. The attempts to reach the lowest degree of supercooling of water severely tested the experimental skills of generations of investigators, who run into the ambiguity of sample-dependent and vessel-dependent freezing points. While it is easy supercool water down to 263 K, below this temperature the freezing point becomes more and more unpredictable. Theoretical studies of nucleation of water, now supported by molecular dynamics simulations, were developed in parallel to the experiments since 1870 [96]. It was stated that the disperse particulates present in water, as well as the protuberances on the walls of vessels, provide centers of nucleation and trigger the formation of ice at a foreign surface, the *heterogeneous nucleation*. The lowest temperature ever reached by supercooled water in a test-tube is 243 $\pm$ 1 K, but this limit showed scarce reproducibility, even under accurate cleaning procedure of samples and tubing. It was shown that a successful way to the homogeneous nucleation of water is the isolation of water by any kind of solid boundaries and the realization of samples as smaller as possible, to diminish the probability of nucleation. Homogeneous nucleation was observed in cloud chambers and emulsions [97].

A common statement from these early investigations is that water in volumes of 10^{-9} cm^3, corresponding to a 10 μ diameter droplet, freezes at $T_H = 235$ K, for a period of observation of 1 - 100 s, irrespectively of whether its environment is a glass wall, oil or other molecular liquid film or a nitrogen gas blanket. The value T_H is now commonly assumed as the homogeneous nucleation temperature of water.

In Figure 1.12 the data collected along decades about heterogeneous and homogeneous nucleation point of water are reported, as a function of the equivalent radius of the sample volume (See Ref. [4] and references therein).

The dotted lines over Figure 1.12 warn us about the fact that, due to the use of samples of 1 mm to 1 cm diameter, which are mandatory in non micro-focused scattering techniques, the heterogeneous nucleation could limit the supercooling at $\approx$ 248 K. Indeed in the present work, even

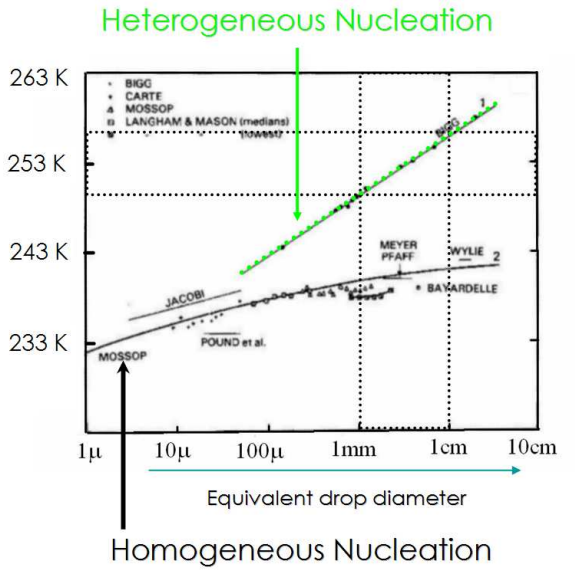


Figure 1.12: Heterogeneous and homogeneous nucleation temperatures of water as a function of the equivalent droplet diameter of the sample investigated. Heterogeneous nucleation is due to particulates suspended in the samples or on the wells of the holder. Homogeneous nucleation can be obtained in condition of extreme cleanliness and/or in very small samples. The vertical dotted lines mark the size limit of the sample we can use in inelastic scattering experiments and, consequent to the intersection with the heterogeneous and homogeneous nucleation curve, the horizontal lines give an idea of the supercooling expectations. This figure has been adapted from Ref. [4].

with the purest water available in the smallest samples possible, we have reached a supercooling of 251 K, which has anyway been useful to assess most of our targets. Indeed with $\approx$ 20 K of supercooling we have nevertheless shown the possibilities the new IUVS technique, tested MCT predictions and shed light on the dilemma about *fast-sound*.

1.6.2 Diluting the solutions to reach the solvent

To characterize the dynamics of further supercooled *bulk* water, an indirect route is the investigation of aqueous solutions under progressive dilution, to overtake the problem of freezing. A first step in this direction has been done in the present work by investigating the dynamics of the aqueous solution LiCl-6H_2O.

The solutions LiCl-$R$$H_2O$ (where R is the solvent/solute molar ratio) offer actually an interesting phase diagram scenario (See figure 1.13 [98]).

The LiCl-$R$$H_2O$ solutions at thermodynamic equilibrium may form three crystalline hydrates, for R =2, 3, 5. An eutectic point exists for the $R \approx 7$ solution at T_e = 199 K, where the liquid separates into ice microcrystals and R=5 hydrate microcrystals. The non-equilibrium aspect of the phase diagram was first studied in 1960 [99]. A glass transition occurs for all the $R > 3$ solutions. In any case, T_g is located around 140 K, close to the value of pure water. Furthermore, in the vicinity of R=6, no additional thermal anomaly is observed above the glass transition, indicating that the supercooled liquid below T_e is stable down to T_g. Diluting the solution at $R \geq 6$ [26] the melting point increases and tends to the point of the pure solvent. In this sense, a first step to the pure solvent has been the characterization of the R = 6 solution. We have measured the dynamic structure factor of the liquid and glassy phases of the solution LiCl - 6H_2O by means of inelastic scattering of radiation in the visible, UV and X-ray range, from 1 GHz to 10 THz and by means of photon-correlation spectroscopy, from 0.01 Hz to 20 KHz. The measurements were performed in a broad temperature range between 353 K and 80 K. Our data (See Chapter 5) show

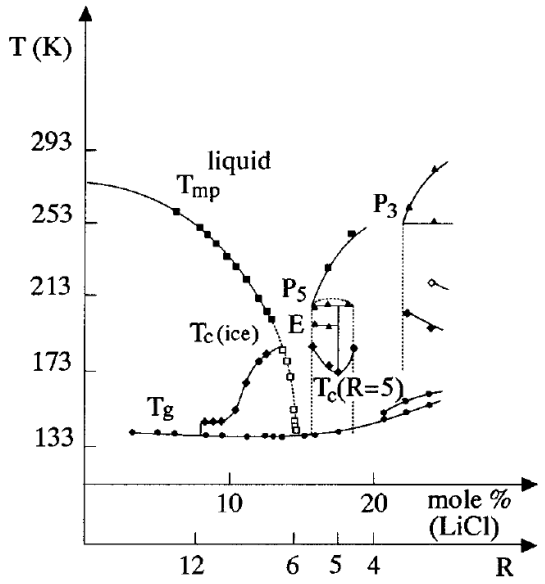


Figure 1.13: Phase diagram of the LiCl-RH$_2$O solutions (see text)

that a single relaxation process, which, at high temperatures, has features similar to those of the single relaxation of pure water, starts to differentiate into two relaxations, structural ($\alpha-$) and secondary ($\beta-$), upon cooling below $\sim$ 220 K. On cooling the system below this temperature, the relaxation strengths reveal an uncommon behavior with respect to most glass forming systems: the β relaxation is the continuation of the single process existing at high temperature and an onset occurs for the α- from the β-process.

The $R = 6$ solution shows interesting coincidences with the phenomenology of the pure solvent: the onset of the $\alpha-$ relaxation occurs close to the T_S of water. Moreover, an interesting correspondence has been found between the values of the high frequency sound velocity of the solution and of the solvent. These aspects are discussed in Chapter 5 and in the Conclusions.

1.7 Expectations for the present work

In summary, the aim of the present work is the characterization of the structural relaxation of supercooled water by the novel technique IUVS at the novel beamline 10.2 in Elettra synchrotron. Test BLS measurement will be a reference for IUVS and will also enlarge the investigated frequency domain. The feasibility of IUVS measurements at the new beamline will be shown and, regarding the dynamics of supercooled water, also the uniqueness of IUVS technique. The dynamic structure factor measured by inelastic scattering experiments in the low Q regime will be analyzed in the framework of generalized hydrodynamics. The temperature dependence of the relaxation parameters will be compared to the theories. The structural relaxation time and stretching will be compared to MCT predictions, in order to bring a piece of information about possible interpretations of the apparent divergences in supercooled water. The speed of sound will allow to ascertain the physical origin of *fast sound*. The dynamics of the aqueous solution LiCl-H$_2$O will be characterized in a frequency window of 5 decades by BLS, IUVS and IXS experiments. This investigation will be not only a characterization for the solution but also a first step towards the approach to properties of pure bulk water through the properties of its solutions progressively diluted.

Résumé du Chapitre 2

Dans ce chapitre, nous décrivons l'approche méthodique adoptée pour l'étude de la dynamique des liquides. La fonction centrale est le facteur de structure dynamique $S(Q, \omega)$ qui est la double transformée de Fourier de la fonction d'autocorrélation de la densité $G(r, t)$. Ces deux fonctions contiennent la même information sur la dynamique d'un liquide et du point de vue théorique on peut les calculer à partir d'hypothses microscopiques. Expérimentalement, on peut mesurer $S(Q, \omega)$ et $G(r, t)$ lors d'expériences de diffusion inélastique ou de spectroscopie de corrélation de photons. Leur analyse dans un formalisme d'hydrodynamique ou d'hydrodynamique généralisée fournit les caractéristiques de la dynamique relaxationnelle du systme étudié. La confrontation avec la théorie est réalisée à un niveau phénoménologique en comparant les paramtres de relaxation déterminés expérimentalement est ceux résultant de prédictions théoriques.

Chapter 2

The dynamic structure factor

Abstract

In this chapter the methodological approach adopted in the investigation of the dynamics of liquids is described. The central entity of interest is the dynamic structure factor, $S(Q,\omega)$, the Fourier transform of the mass density autocorrelation function $G(r,t)$. Both quantities include, equivalently, all the information about the dynamics of a liquid. From a theoretical viewpoint, they may be predicted starting at microscopic assumptions. On the experimental side, $S(Q,\omega)$ and $G(r,t)$ can be measured through inelastic scattering experiments or photon correlation spectroscopy. The analysis of the measured $S(Q,\omega)$ and $G(r,t)$ in the framework of hydrodynamics or generalized hydrodynamics gives access to the features of the relaxational dynamics of the investigated system. The comparison of experiments and theory is made at the *phenomenological* - or intermediate - level, i.e., between the relaxational parameters experimentally determined and the corresponding results of theoretical predictions.

2.1 Methodological approach to the liquid state

A liquid appears like a shapeless object, little compressible and ready to flow. When X-rays are scattered from a liquid, there are no sharp Bragg reflections, demonstrating that its atoms or molecules lack the long range order. Due to the translational and rotational degrees of freedom, relaxation processes occur into a liquid, over timescales and lengthscales which may be spread over decades, depending on the kind of process and the thermodynamic conditions.

Relaxation processes aim at the restoration of an equilibrium condition after an external perturbations or a spontaneous fluctuations has occurred. Disturbances are damped by dissipation phenomena like diffusion, viscous flow and thermal conduction. If reasonably small, external applied perturbations are dissipated in the same way as spontaneous fluctuations, what luckily makes it possible the study of the response of the system. By inducing perturbations at different frequencies and momenta, we may get information on the corresponding dynamics of the unperturbed system at different timescales and lengths. This is expressed by the fluctuation-dissipation theorem [100] and is the premise for investigations based on radiation-matter interaction.

From a theoretical viewpoint, the response of a fluid to an applied perturbation is formalized in three complementary cases [16]: *(i) the hydrodynamic regime*, at low frequency and momentum. The fluctuations in the liquid evolve so slowly, and over a spatial extension so much large, with respect to the time and length scales of the applied perturbation (i.e. frequency and wavelength of an incident wave), that the system can be considered as a continuum in local thermodynamic equilibrium. In this regime the system is characterized on the macroscopic level by thermodynamic bulk quantities, while microscopic information can be obtained only indirectly. *(ii) The molecular dynamics limit*, at high frequency and momentum. Molecular dynamics is concerned with the relation between molecular interactions and atomic motions on the one hand, and macroscopic properties of the fluid on the other. Molecular dynamics provides the framework for extending

hydrodynamic calculations to spatial and time variations comparable to the collision mean free path and mean time between collisions. In this region the local structure of the fluid, the existence of short-range ordering, has to be considered along with high-frequency behavior such as molecular relaxation. (iii) The *generalized hydrodynamic regime*, between these two limits. When the condition of slow variations of the applied perturbation with respect to the fluctuations timescale starts not being fully satisfied, the behavior of the fluid deviates from the predictions of hydrodynamics in a subtle and gradual manner. It is hence appropriate to extend the hydrodynamic description by retaining the basic structure of the equations but replacing the thermodynamic derivatives and transport coefficients by functions which can vary in space or in space and time. The phenomenology of a relaxation process characterized by a timescale that matches the reverse frequency of certain acoustic modes falls into de domain of generalized hydrodynamics.

The approach of hydrodynamics and generalized hydrodynamics is based on *time correlation functions*. A time correlation function is the thermodynamic average of the product of two dynamical variables, each expressing the instantaneous deviation of a property from its equilibrium value, at particular points in space and time. The average is carried out over the phase coordinates of all the molecules in the fluid with an equilibrium ensemble as the weighting function. A time correlation function is therefore a function of space and time, and it describes the thermal fluctuations which occur spontaneously in the equilibrium system.

The central entity of interest is the dynamic structure factor, $S(Q,\omega)$, the Fourier transform of the mass density autocorrelation function $G(r,t)$. Both quantities include all the information about the dynamics of a liquid. From a theoretical viewpoint they may be predicted, starting at microscopic assumptions. On the experimental side, they can be measured through inelastic scattering experiments ($S(Q,\omega)$) or photon correlation spectroscopy ($G(r,t)$). Comparison of the measured values to the theoretical predictions gives account for the basis of the theory itself.

2.2 Density autocorrelation function and dynamic structure factor

The Density-density correlation function

The number density of a system of volume V composed by N molecules is defined by [16]:

$$n(\mathbf{r},t) = \frac{1}{\sqrt{N}} \sum_{l=1}^{N} \delta(\mathbf{r} - \mathbf{R}_l(t)) \tag{2.1}$$

Here, δ is Dirac Delta function and $R_l(t)$ is the position occupied by the l^{th} particle at time t. The average density is $\langle n(\mathbf{r},t)\rangle = sqrtN/V$ and it is assumed to be constant. Density fluctuations are the instant deviations from the average value:

$$\delta n(\mathbf{r}',t) = n(\mathbf{r},t) - \langle n(\mathbf{r},t)\rangle \tag{2.2}$$

The density-density space-time correlation function is:

$$G(|\mathbf{r}|,t) = V < \delta n(\mathbf{r}',0)\delta n(\mathbf{r}'',t) >= \frac{V}{N}\left\langle \sum_{l'l''} \delta(\mathbf{r}' - \mathbf{R}_{l'}(0))\delta(\mathbf{r}'' - \mathbf{R}_{l''}(t)) \right\rangle - \frac{N}{V} \tag{2.3}$$

The ultimate questions that hydrodynamics is purposed to solve concern the causes of correlations of density fluctuations and the characterization of the processes that make them to occur.

The intermediate scattering function

The intermediate scattering function is the space-only Fourier transform of $G(\mathbf{r},t)$, a convenient quantity in general discussions and actual calculations. It is defined as

$$F(\mathbf{Q},t) = \langle \delta n^*(\mathbf{Q},0)\delta n(\mathbf{Q},t)\rangle = \langle n^*(\mathbf{Q},0)n(\mathbf{Q},t)\rangle - \frac{(2\pi)^3 N}{V}\delta(\mathbf{Q}) \tag{2.4}$$

where

$$n(\mathbf{Q},t) = \frac{1}{\sqrt{N}}\sum_i e^{i\mathbf{Q}\cdot\mathbf{R}_l(t)} \tag{2.5}$$

and $\delta n(\mathbf{Q},t)$ is the Q^{th} component of the fluctuation of $n(\mathbf{r},t)$. Since the thermal average is defined with respect to a time independent ensemble, $F(\mathbf{Q},t)$ is stationary, that is, its dependence on time is across the time interval.

The dynamic structure factor

The space-time Fourier transform of $G(\mathbf{r},t)$ is the dynamic structure factor:

$$S(\mathbf{Q},\omega) = \int_V d\mathbf{r}\int_{-\infty}^{+\infty} G(\mathbf{r},t)e^{i(\mathbf{Q}\cdot\mathbf{r}-\omega t)}dt = \int_{-\infty}^{+\infty} e^{-i\omega t}F(\mathbf{Q},t)dt \tag{2.6}$$

The static structure factor

The equal-time or static structure factor is

$$S(Q) = F(Q,t=0) = \langle \delta n^*(\mathbf{Q},0)\delta n(\mathbf{Q},0)\rangle \tag{2.7}$$

which describes the average equilibrium distribution of molecular separations in fluids through the relationship

$$F(Q,0) = 1 + \frac{N}{V}\int d^3 r e^{i\mathbf{Q}\cdot\mathbf{r}}[g(r)-1] \tag{2.8}$$

where $g(r)$ is the equilibrium pair distribution function

$$g(r) = \left(\frac{V}{N}\right)^2 \sum_{l'l''}\langle \delta(\mathbf{r}-\mathbf{R}_{l'})\delta(\mathbf{R}_{l''})\rangle \tag{2.9}$$

that is measurable by X-rays and neutron diffraction experiments. $S(Q)$ is related to $S(Q,\omega)$ through the relationship

$$S(Q) = \frac{1}{2\pi}\int_{-\infty}^{\infty} S(Q,\omega)d\omega \tag{2.10}$$

Indeed the value of $S(Q)$ is the area below the spectrum of $S(Q,\omega)$ and can be used in experimental determinations to normalize the measured $S(Q,\omega)$ to its pure value. In the low frequency limit $S(Q)$ is proportional to the isothermal compressibility $\chi_T = 1/\rho(\partial\rho/\partial p)_T$ through the relationship:

$$\lim_{Q\to 0} S(Q) = \frac{NK_BT\chi_T}{V} \tag{2.11}$$

where K_B is the Boltzmann constant and T the temperature.

$S(Q)$ and spectral momenta

In the limit of short times and high frequencies, the intermediate scattering function can be expressed as a Taylor series as a function of time:

$$F(Q,t) = \omega^0(Q) + i\omega^1(Q)t - \omega^2(Q)\frac{t^2}{2!} - i\omega^3(Q)\frac{t^3}{3!} + ... \tag{2.12}$$

where the coefficients of the expansion, called spectral momenta, are given by [16, 102]:

$$\omega^n(Q) = \int_{-\infty}^{+\infty} \omega^n S(Q,\omega)d\omega \tag{2.13}$$

With respect to this, $S(Q)$ is the 0-th spectral moment of $F(Q)$. In principle, the time dependence of $F(Q,t)$ can be obtained from the knowledge of the ω^n coefficients, and hence the $S(Q,\omega)$. Unfortunately, the expressions of the high order spectral momenta are very complicated and unusable in practice [16],[103, 104, 105, 106]. Nevertheless, this expression states that the spectral moment are not supposed to diverge.

2.3 The dynamic structure factor in the hydrodynamic limit

In the hydrodynamic regime an exact expression can be obtained for $S(Q,\omega)$ at low Qs and low ω that depends on time-averaged purely macroscopic quantities [16, 17]. Q and ω denote the Q-th the ω-th Fourier components of the perturbation. Any information about microscopic structure and dynamics is lost. The fluid is ideally divided in elements, of mass M and volume V and confined within a surface S, large enough with respect to the intermolecular distance to be considered continuous but small enough for the value of state variables to be uniquely defined. The tractation is based on classical conservation laws of mass, momentum and energy.

Mass Conservation. As the fluid is a continuum, with respect to the perturbation lengthscale, the use of the particle density $n(\mathbf{r},t)$ is better replaced by the use of the local mass density $\rho(\mathbf{r},t)$ which is defined through the integral relationship:

$$M(t) = \int_V \rho(\mathbf{r},t)d\mathbf{r} \tag{2.14}$$

The conservation of the mass is expressed by the continuity law:

$$\frac{\partial\rho(\mathbf{r},t)}{\partial t} + \nabla\cdot\mathbf{j}^M = 0 \tag{2.15}$$

where $\mathbf{j}^M(\mathbf{r},t) = \rho(\mathbf{r},t)\mathbf{v}(\mathbf{r},t)$ is the mass current density.

Momentum Conservation. The element of volume is subject to mechanical action (stress) from the surrounding elements. Stresses are due to hydrostatic pressure , p, and to dilatational and shear solicitations (stress tensor π_{ij}). The Cauchy law of motion, for the tensorial stress-strain relation is:

$$\rho\frac{dv_i}{dt} = \frac{\partial}{\partial r_j}[-p\delta_{ij} + \pi_{ij}] \tag{2.16}$$

The symmetric stress tensor is

$$\pi_{ij} = [2\eta_s + \eta_d\delta ij]\Delta_{ij} \tag{2.17}$$

where the coefficients η_s and η_d are, respectively, the shear and dilatational viscosity and Δij is the deformation rate tensor defined as

$$\Delta_{ij} = \frac{1}{2}\left(\frac{\partial}{\partial r_j}v_i\frac{\partial}{\partial r_i}v_j\right) \tag{2.18}$$

Along the diagonal of π_{ij}, the viscosity is expressed by$\eta_l = 2\eta_s + \eta_d$ (longitudinal viscosity).

Combining the the Cauchy law with the Eqs. (2.17) and (2.18), one gets the vectorial Navier-Stokes equation, which expresses the momentum conservation law:

$$\rho\frac{\partial}{\partial t}\mathbf{v} = -\rho(\mathbf{v}\cdot\nabla)\mathbf{v} - \nabla p + \eta_s[\nabla^2\mathbf{v} + \nabla(\nabla\cdot\mathbf{v})] + \eta_d\nabla(\nabla\cdot\mathbf{v}) \tag{2.19}$$

Energy Conservation. If e denotes the internal energy per unit mass, the conservation equation requires that any change in e be balanced by thermal reaction of the system and mechanical dissipation [16]:

$$\rho\frac{de}{dt} = (-p\delta_{ij} + \pi_{ij})\Delta_{ij} - \frac{\partial}{\partial r_i}j_i^e = -p\frac{\partial}{\partial r_i}v_i + \phi_\eta - \frac{\partial}{\partial r_i}j_i^e \tag{2.20}$$

where $\mathbf{j}_i^e$ is the energy flux and $\phi_\eta = \pi_{_{ij}}\Delta_i j$ is the viscous dissipation.

Hydrodynamic equations in terms of transport coefficients

The conservation three laws govern the motion of the fluid. The equations can be rewritten as function of the variables ρ, T and $\mathbf{v}$. Transport coefficients such as the kinematic shear viscosity, $\nu_s = \eta_s/\rho$, the kinematic dilatational viscosity $\nu_d = \eta_d/\rho$, and the isothermal conductivity κ_T, which is defined by the Fourier law $\nabla\mathbf{j}_e = -\kappa_T\nabla^2 T$, work as parameters,.

By changing the variables we obtain:

$$\frac{\partial}{\partial t}\rho + \nabla\cdot(\rho\mathbf{v}) = 0 \tag{2.21}$$

$$\frac{\partial}{\partial t}\mathbf{v} + (\mathbf{v}\cdot\nabla)\mathbf{v} + \frac{c_0^2}{\gamma}\left(\frac{\nabla\rho}{\rho} + \alpha_P\nabla T\right) - \nu_s[\nabla^2\mathbf{v} + \nabla(\nabla\cdot\mathbf{v})] - \nu_d\nabla(\nabla\cdot\mathbf{v}) = 0 \tag{2.22}$$

$$\frac{\partial}{\partial t}T + \mathbf{v}\cdot\nabla T + \frac{(\gamma-1)}{\alpha_P}\nabla\cdot\mathbf{v} - \frac{\kappa_T\nabla^2 T + \phi_\eta}{\rho C_V} = 0 \tag{2.23}$$

Here, $\gamma = C_P/C_V$ is the ratio of specific heats at constant pressure and volume, $c_0 = (\partial p/\partial\rho)_s^{1/2}$ is the sound velocity at constant entropy (adiabatic), $\alpha_P = \rho(\partial V/\partial T)_p = -\rho^{-1}(\partial\rho/\partial T)_p$ is the expansion coefficient at constant pressure and ϕ_η accounts for the increase of entropy due to viscous dissipation. Such a rephrasing will enhance the experimental accessibility of the $S(Q,\omega)$, as the thermodynamical properties can be measured apart by complementary experiments.

Small fluctuations and hydrodynamic modes

Equations (2.21), (2.22), (2.23) hold for a continuous medium, locally homogeneous, isotropic, viscous and thermally conducting. Under these conditions the equations are exact and, in principle, a purely formal exact solution can be given. Nevertheless, we are dealing with small fluctuations systems at equilibrium, not solicited by external variation of mass, force and energy (no sources or wells). Without loss of generality, a perturbation analysis is convenient, to linearize the equations. We rewrite the variables for the respective fluctuations around their equilibrium values. We introduce the substitutions $\rho = \rho_0 + \delta\rho$ where $\rho_0 = \langle\rho(\mathbf{r},t)\rangle$; $T = T_0 + \delta T$, being $T_0 = \langle T(\mathbf{r},t)\rangle$; $\mathbf{v} = \delta\mathbf{v}$, being $\mathbf{v}_0 = \langle\mathbf{v}(\mathbf{r},t)\rangle = \mathbf{0}$. The result is a linear system of the equations (here omitted, see Ref. [16]) where no product is involved between the variables $\delta\rho$, δT and $\mathbf{v}$. To rephrase the problem for our specific problems, a new set of variables is chosen, still statistically independent, instead of $(\delta\rho, \delta T, \mathbf{v})$. The equations are rewritten in terms of the set $(\delta s, \delta p, w, \mu_1, \mu_2)$, respectively entropy fluctuation, pressure fluctuation, and longitudinal current and transverse current components. We remark that the $Ql \ll 1$ assumption holds, where Q denotes the Q-th Fourier component of the perturbation and l is the mean free path [16]. The longitudinal current is defined as $w = \rho_0\nabla\cdot\mathbf{v}$ and is the parallel component, $j_{\parallel}^M$, of the mass current $\mathbf{j}^M$, with respect to the Q-vector direction. The transverse components are defined as $\mu_i = \rho_0(\nabla\wedge\mathbf{v})_i$, $i = 1, 2$, and are the and the normal components, $(j_{\perp}^M)i$, $i = 1, 2$, of the mass current respect the Q-vector direction. Thermodynamic

and transport coefficients are implied, as a consequence of the equation of state and of the Fourier law: γ, α_P and c_0, as well as the thermal diffusivity, $D_T = \kappa_T/(\rho_0 C_P)$, the kinematic shear viscosity $\nu_s = \eta_s/\rho_0$ the bulk kinematic viscosity $\nu_b = \eta_b/\rho_0$ and the longitudinal kinematic viscosity $\nu_l = \eta_l/\rho_0$ where $\eta_l = 2\eta_s + \eta_d = \frac{4}{3}\eta_s + \eta_b$ (being η_b the bulk viscosity).

The solutions for the obtained equations is more conveniently obtained in the Laplace-Fourier space Laplace-Fourier space, (ς, Q).

$$\widetilde{\delta x}_Q(\varsigma) = \int_0^\infty dt e^{-\varsigma t} \int_{-\infty}^{\infty} \delta x(\mathbf{r}, t) e^{i\mathbf{Q}\cdot\mathbf{r}} d\mathbf{r} \tag{2.24}$$

where $\varsigma = \epsilon + i\omega$ is the complex Laplace variable.

At this point it is worth reporting the set of linearized equations in matrix format, which becomes the the starting point for the analysis of hydrodynamic modes:

$$(\widetilde{\delta p}_Q(\varsigma), \widetilde{w}_Q(\varsigma), \widetilde{\delta s}_Q(\varsigma), \widetilde{\mu}_{1,Q}(\varsigma), \widetilde{\mu}_{2,Q}(\varsigma))\mathbf{M} = (\delta p_Q(0), w_Q(0), \delta s_Q(0), \mu_{1,Q}(0), \mu_{2,Q}(0)) \tag{2.25}$$

Where $\mathbf{M}$ is the matrix of coefficients. The determinant D of the system is:

$$\begin{bmatrix} [\varsigma + (\gamma-1)D_T Q^2] & c_0^2 & \rho_0 \alpha_P^{-1}(\gamma-1)D_T Q^2 & 0 & 0 \\ -Q^2 & [\varsigma + (\nu_l Q^2)] & 0 & 0 & 0 \\ \rho_0^{-1}\alpha D_T Q^2 & 0 & [\varsigma + D_T Q^2] & 0 & 0 \\ 0 & 0 & 0 & [\varsigma + \nu_s Q^2] & 0 \\ 0 & 0 & 0 & 0 & [\varsigma + \nu_s Q^2] \end{bmatrix} \tag{2.26}$$

The lower 2×2 right minor yields two degenerate roots:

$$\varsigma_{1,2} = -\nu_s Q^2 \tag{2.27}$$

which correspond to two transverse shear modes, completely decoupled from the rest of the matrix and which do not propagate. Their existence cannot be detected experimentally in a simple isotropic fluid.

The analysis of (2.26) reduces to solving the remaining 3×3 top-left minor. Introducing the reduced parameters $a = D_T Q/c_0$, $b = \nu_l Q/c_0$ and the reduced variable $z = \varsigma/(c_0 Q)$ yields [16]

$$z^3 + z^2(\gamma a + b) + z(1 + \gamma a b) + a = 0 \tag{2.28}$$

A perturbational solution is justified in the hydrodynamic regime, as the long wavelength condition makes that a and b are small. [1]

Up to the first order in a and b, i.e., to the order Q^2, we find three longitudinal modes which characterize the fluid dynamics in the hydrodynamic regime [16]:

$$\varsigma_0 = -D_T Q^2 \tag{2.29}$$

and

$$\varsigma_\pm = \pm i c_0 Q - \Gamma Q^2 \tag{2.30}$$

where

$$\Gamma = \frac{1}{2}[\nu_l + (\gamma - 1)D_T] \tag{2.31}$$

The real root (2.29) corresponds to a thermal diffusivity mode, due to entropy fluctuations at constant pressure. These fluctuations do not propagate and give rise to a purely diffusive effect.

[1] Even if an exact solution is formally possible, in a typical case of light scattering, which is the appropriate probe for measuring fluctuations in the hydrodynamic regime, a perturbation calculation is of order here whose solutions are more meaningful from a physical point of view. Indeed, for light scattering experiments Q is of the order of 10^5 cm^{-1} and $c_0 \approx 10^5$ cm/s. Thus a and b are of the order 10^{-2} to 10^{-3}

The two conjugate solutions (2.30) are due to two propagating longitudinal modes arising from pressure fluctuations at constant entropy (adiabatic). These are the longitudinal acoustic (LA) modes, which propagate at the adiabatic sound velocity, c_0, and whose lifetime (damping coefficient) is given by Γ/Q^2. The LA modes and the thermal diffusive mode are coupled through the $(1,3)$ and $(3,1)$ matrix elements. If we neglect this coupling, which is weak for ordinary fluids in the hydrodynamic limit, the matrix of coefficients (2.26) can be depicted schematically as in Fig. 2.3. We count, totally, five decoupled modes: two propagating LA modes (pressure fluctuations at constant entropy), a non-propagating longitudinal entropy mode associated to thermal diffusion (entropy fluctuations at constant pressure) and two non-propagating transverse shear modes, decoupled from density fluctuations (shear viscosity modes).

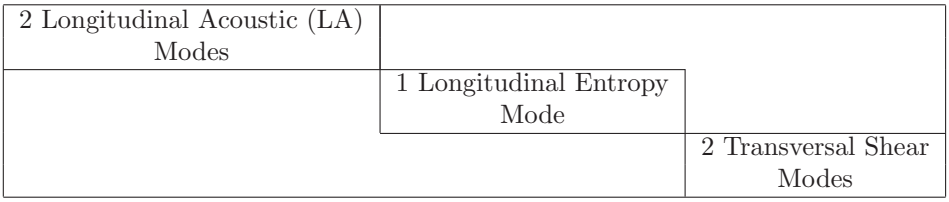


Figure 2.1: *Schematization of the determinant in Eq.(2.26) in the hydrodynamic approximation*

Autocorrelation function of the density fluctuations: the Rayleigh-Brillouin spectrum

Now the density-density correlation function can be calculated. The linearized hydrodynamic system of equations can be solved with respect to $\delta\rho(Q,\varsigma)$. It can be demonstrated [16] that the solution is given by the 3×3 upper minor of the determinant in Eq. (2.26). The correlation function results:

$$\langle\delta\rho^*(Q,0)\widetilde{\delta\rho}(Q,\varsigma)\rangle = \frac{(\varsigma+\nu_l Q^2)(\varsigma+\gamma D_T Q^2)+(1-\gamma^{-1})c_0^2Q^2}{(\varsigma-\varsigma_0)(\varsigma-\varsigma_+)(\varsigma-\varsigma_-)}\langle\delta\rho^*(Q,0)\delta\rho(Q,0)\rangle \tag{2.32}$$

where ς_0 and $\varsigma_\pm$ are the solutions of the dispersion relation, given in Eqs. (2.29) -(2.31).

The quantity $\langle\delta\rho^*(Q,0)\delta\rho(Q,0)\rangle$ is the *static structure factor* $S(Q)$, the Fourier transform of the density autocorrelation function at time zero, which describes the average distribution of molecular separations in the fluid. The result in Eq. (2.32) is correct up to order Q^2. Passing from Laplace to Fourier space and neglecting the $\propto Q^4$ terms with respect to the $\propto Q^2$ ones, the Rayleigh-Brillouin spectrum is obtained after some straightforward algebra [16]:

$$\begin{aligned}
\frac{S(Q,\omega)}{S(Q)} &= 2Re\lim_{\epsilon\to 0}\frac{\langle\delta\rho^*(Q,0)\widetilde{\delta\rho}(Q,\varsigma=\epsilon+i\omega)\rangle}{\langle\delta\rho^*(Q,0)\delta\rho(Q,0)\rangle} = \\
&= \left(\frac{\gamma-1}{\gamma}\right)\left(\frac{2D_TQ^2}{\omega^2+(D_TQ^2)^2}\right)+ \\
&+ \frac{1}{\gamma}\left[\frac{\Gamma Q^2}{(\omega+c_0Q)^2+(\Gamma Q^2)^2}+\frac{\Gamma Q^2}{(\omega-c_0Q)^2+(\Gamma Q^2)^2}\right]+ \\
&+ \frac{Q}{\gamma c_0}\left[\Gamma+(\gamma-1)D_T\right]\left[\frac{(\omega+c_0Q)}{(\omega+c_0Q)^2+(\Gamma Q^2)^2}-\frac{(\omega-c_0Q)}{(\omega-c_0Q)^2+(\Gamma Q^2)^2}\right]
\end{aligned} \tag{2.33}$$

This result yields the shape of the spectrum measured by light scattering spectroscopy from a simple monatomic liquid. A summarizing representation is given in Fig. 2.2.

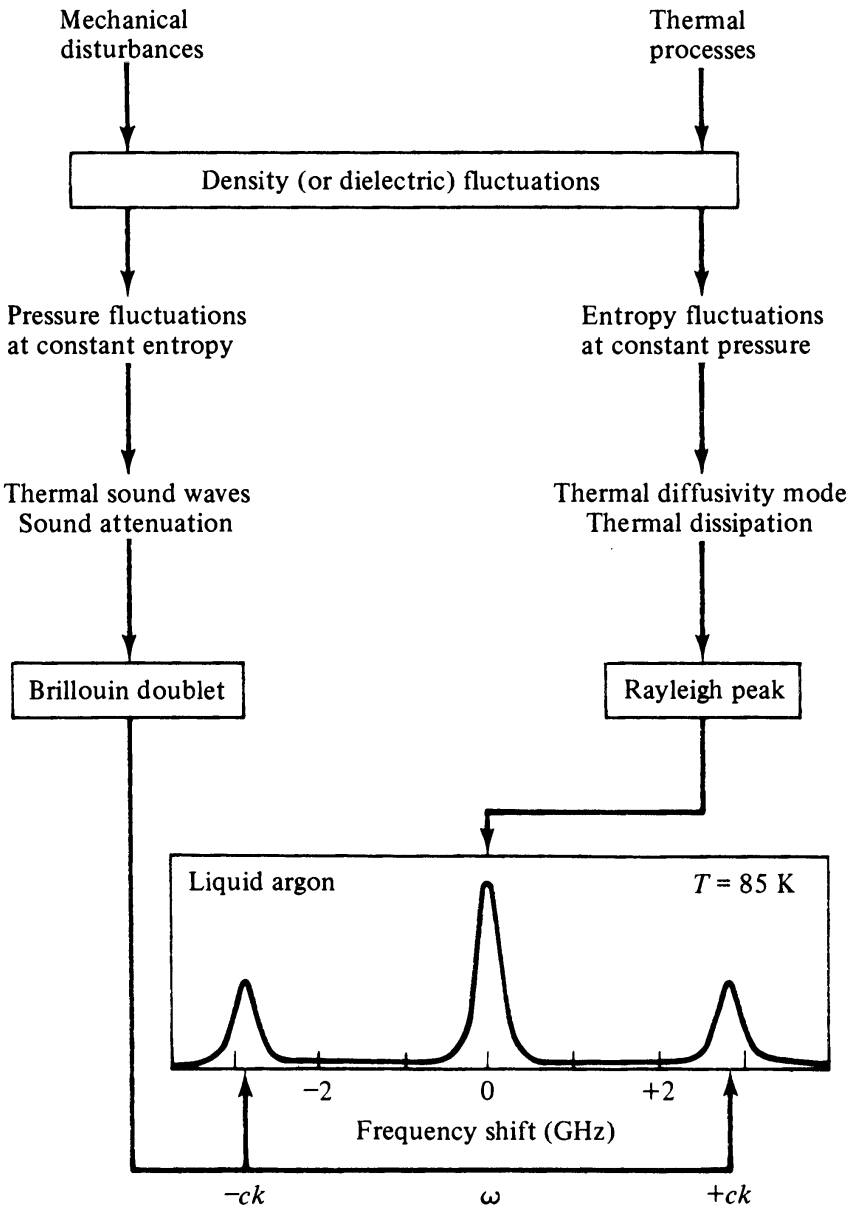


Figure 2.2: The Rayleigh-Brillouin spectrum arising from the dynamic structure factor in the hydrodynamic regime. The central peak (Rayleigh peak) arises from fluctuations at constant pressure and corresponds to the *thermal diffusivity (non propagating) mode.* The thermal diffusivity coefficient $D_T = \kappa_T/\rho_0 C_P$ can be get by the linewidth of the central peak, $D_T Q^2$. The two side-lorentzians are centered at $\pm c_0 Q$ and have width ΓQ^2. That is the Stokes and anti-Stokes component of the Brillouin-Mandelstam doublet which manifest the presence of density fluctuations at constant entropy and corresponds to the *longitudinal acoustic modes.* The experimental determination of their position and linewidth gives, respectively, the velocity of sound c_0 and Γ, which accounts for thermal diffusion and viscous dissipations. The amplitude of the last two terms in Eq. (2.33) is of several orders of magnitude smaller than the one of lorentzians. The effect is a slight pulling of Stokes and anti- Stokes peaks towards the central position, hardly detectable experimentally.

The ratio between the integrated intensities of the Brillouin peaks $2I_B$, and the Rayleigh peak, I_R, is called the *Landau-Placzek ratio*. By integrating the first three terms in Eq. (2.33) one obtains

$$\frac{I_R}{2I_B} = \gamma - 1 \tag{2.34}$$

which yelds a measure of the ratio between specific heats ($\gamma = C_P/C_V$). Other measurable quantities are the adiabatic sound velocity c_0, the thermal diffusivity, D_T, the thermal conductivity κ whenever C_P is known separately, the longitudinal kinematic viscosity ν_l where from the bulk viscosity η_B can be determined, which is not easily obtainable with other techniques. Whenever thermodynamic properties or transport coefficients can be obtainable independently, it is common procedure to take them as known parameters and to use Brillouin spectroscopy to investigate into velocity of sound and longitudinal kinematic viscosity, that become more difficult to know when the hydrodynamic conditions is abandoned for the arising of relaxation processes.

The damped harmonic oscillator (DHO) model

The Rayleigh-Brillouin spectrum describes the spectral density of simple fluids quite well in the hydrodynamic limit, in the central frequency region. Regarding the high-frequency tails of the measured spectrum, instead, the decrease is slower than that of a Lorentian function. In such a way that the second spectral moment diverges. This mismatch at high frequency is due to the fact that several assumptions and approximations have restricted the validity of the model to the regime of long times and low frequencies. Nevertheless, a good description of $S(Q,\omega)$ in the hydrodynamic regime has been be formulated under less strict approximations (Q^2 order terms are not neglected) [101], which is valid also at high frequencies and respects the convergence of the spectral moment up to the third order [16, 102]. In the tractation of Ref. [101] $S(Q,\omega)$ is represented by the spectrum of a damped harmonic oscillator (DHO) which oscillates at a frequency ω_0 and is damped by a factor $e^{-\Gamma}$:

$$\frac{S(Q,\omega)}{S(Q)} = \frac{1}{\pi}\frac{\Gamma\omega_0^2}{[\omega^2-\omega_0^2]^2+\omega^2\Gamma^2} \tag{2.35}$$

In this model, $\pm\omega_0$ approximately corresponds to the Brillouin peak position and Γ to the peak width at half maximum. This approach has been used to evaluate the speed of sound and the longitudinal kinematic viscosity.

2.4 Beyond the hydrodynamic limit: memory function, relaxing elastic modulus

The failure of hydrodynamics is expected, when going to describe fluctuations occurring on timescales and lengthscales comparable to, or smaller than, molecular collision time and interparticle distance. At high frequencies, the appearance of new modes is predictable, which mirror the existence of processes evolving in the liquid. See a qualitative illustration in Figure 2.3.

Nevertheless, the fact that inelastic X-rays and neutron scattering spectra show show the same features of light scattering spectra infers that the fundamental structure of hydrodynamic equations can be saved, beyond the hydrodynamic limit. As a matter of facts, the non-hydrodynamic behavior shows up quite smoothly. To describe the behavior of a liquid free from any timescale restriction the hydrodynamic approach may be generalized by keeping the same formalism used in the low frequency limit and reintroducing the frequency dependence into transport coefficients, in order to be able to take the response of the system into account at any frequency. Such a generalization includes hydrodynamics as its limiting case at low frequency.

It can be shown that an equation of motion for the normalized $F(Q,t)$ can be written in a generalized Langevin form [16, 102]

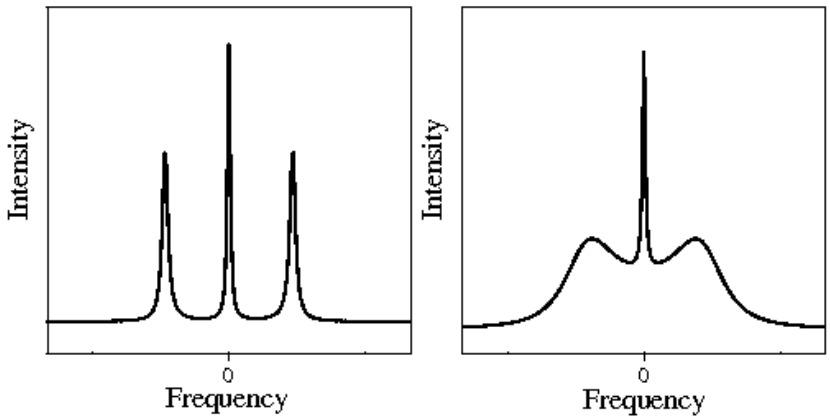


Figure 2.3: Qualitative appearance of a light scattering spectrum in the hydrodynamic regime (left) and with the presence of (in this case) a structural relaxation. New contributions to the spectrum appear, affecting the acoustic modes.

$$\frac{\partial^2 F(Q,t)}{\partial t^2} + \omega_0 F(Q,t) + \int_0^t dt' m_Q(t-t') \frac{\partial F(Q,t')}{\partial t'} = 0 \tag{2.36}$$

and, in the same way, the dynamic structure factor can be written as

$$S(Q,\omega) = I_0 \frac{Q^2}{\omega\rho} Im \left[\frac{1}{\omega^2 - \omega_0^2 - i\omega m^*(\omega)} \right] \tag{2.37}$$

where "Im" stands for imaginary part.

Equations Eqs. and have become now equations for the so-called second memory functions m [107], whose role is to express, at the time t, the effect of all the perturbations (relaxations) started before t. We are in practice transferring the problem from $F(Q,t)$ or $S(Q,\omega)$ to $m(t)$ or $m(\omega)$, with the advantage of a simpler -or even experimental- shaping of the processes involved in the dynamical region investigated. The memory function is meant hence to represent all the relaxations which will occur in a system over a certain dynamical and thermodynamical window.

An alternative description of $S(Q,\omega)$, completely equivalent to the formalism of the memory functions [108], is represented by the use the relaxing longitudinal elastic modulus M, defined as the ratio of the axial stress to axial strain in an unidirectional perturbation. In the limit of perfect elasticity, M is related to the speed of sound C by the relationship $M = \rho C^2$.

In the formalism of the relaxing modulus the dynamic structure factor is derived through the linearized equation of motion of density fluctuations $\rho_Q(t)$ which, in case of negligible thermal diffusion, becomes [108, 101]:

$$\ddot{\rho}_Q(t) + \left(\frac{\eta_L}{\rho} Q^2 \right) \dot{\rho}_Q(t) + \left(\frac{M_0}{\rho} Q^2 \right) \rho_Q(t) = 0 \tag{2.38}$$

Where η_L is the longitudinal viscosity, M_0 the adiabatic compressional modulus. The presence of relaxations can be accounted for by introducing a frequency dependent longitudinal modulus $M^*(\omega) = M'(\omega) + iM''(\omega)$. The same functionality of the memory function applies for $M^*(\omega)$, which has to be modeled ad-hoc for the system investigated and the frequency and thermodynamical domain involved. The spectrum of the density fluctuations is calculated through the fluctuation-dissipation theorem [100]:

$$S(Q,\omega) = \frac{I_0}{\omega} Im \frac{1}{\left[\frac{\omega^2 \rho}{Q^2} - M^*(\omega) \right]} \tag{2.39}$$

It is straightforward to connect the memory function $m^*(\omega)$ to the elastic modulus $M^*(\omega)$ through the respective expression of $S(Q,\omega)$. We obtain:

$$M^*(\omega) - M(\omega \to 0) = i\frac{\omega\rho}{Q^2}m^*(\omega) \tag{2.40}$$

In great part of the data analysis of the present work both the formalisms have been adopted and the fitting functions have been modeled taking care to respect Eq.(2.40). This has been done because IUVS was a new techniques and we aimed at the comparison to BLS and IXS results, techniques which traditionally have been adopting the two different formalisms [109, 19]. The results have been found to be equivalent so that in chapters 4 and 5 the analysis will be reported in terms of longitudinal elastic modulus only, as we are dealing with acoustic modes, for reasons of clarity.

We have mentioned that the choice of the proper shape of the memory function/elastic modulus is made "ad-hoc" for the system investigated. For this reason we return its discussion to chapter 4 relatively to water and to chapter 5 relatively to the solution LiCl-6H_2O.

2.5 Experimental determination of $S(Q,\omega)$

The dynamic structure factor can be measured by coherent light scattering experiments. A monochromatic ray of light impinges of the system, a non adsorbing, non conducting and non magnetic fluid, continuum with respect to the incoming wavelength. Indeed the wavelengths of light and UV, from 700 down to 100 nanometers are much larger than the intermolecular distances. The scattered intensity is analyzed (spatially separated according to ω into its $I(Q,\omega)$ spectral components) and then recorded by a detector posed at a distance much larger than the sample diameter. It then possible to retrieve $S(Q,\omega)$ from $I(Q,\omega)$ and to apply the formalisms of generalized hydrodynamic to retrieve the dynamic of the system. Under certain conditions, the same formalisms used for light (visible and UV) scattering can be applied to inelastic X-ray scattering too.

A theoretical description of light scattering has been developed on the basis of quantum field theory. Nevertheless, the major results differ little from a classical explanation [110, 111]. In the classical view point the system is schematized as the union of adjacent microscopical subregions, smaller than the cubic wavelength. The electrical charges in each subregion see the same electric field and gives its own dielectric response to the incoming radiation. All the electrical charges in a subregion are accelerated by the incoming radiation and re-irradiate at the same phase and amplitude. Subregions are optically different each other, because the dielectric response $\varepsilon(\mathbf{r},t)$ fluctuates in space and time. Hence, destructive interference in the non-forward direction is statistically forbidden. In this quasi-classic picture, light scattering is due to local fluctuations in the dielectric constant of the illuminated medium. [2]

In Figure 2.4) the essential diagram of a light scattering experiment is drawn [17]. An incident monochromatic light wave of angular frequency $\omega_i = 2\pi/\nu_i$, wave vector $\mathbf{k}_i$ and polarization $\mathbf{n}_i = 2\pi/\lambda_i$ is scattered by the sample in all directions. The *scattering angle*, θ, is defined between the incident (initial) direction and a selected outgoing (final) direction. The scattered radiation has different pulsation momentum and polarization, due to exchanges with the samples. As a single θ at experiment usually is selected, a single outgoing wave is collected, of pulsation $\omega_f = 2\pi/\nu_f$, wavevector $\mathbf{k}_f = 2\pi/\lambda_i$ and polarization $\mathbf{n}_f$.

The typical exchanged energy in light scattering is $\pm \mid \hbar\omega_i - \hbar\omega_f \mid$. It is a factor 10^{-6} of the incident energy. This fact calls for very high resolution power techniques. The momentum transfer Q is defined as $\mid \mathbf{Q} \mid = \mid \mathbf{k}_i - \mathbf{k}_f \mid$. Due to the very weak wavelength change in the scattering process, the initial and final wave vectors have comparable modulus $\mid \mathbf{k}_i \mid \approx \mid \mathbf{k}_f \mid$ and the main contribution

[2] In principle, when light impinges on a medium several phenomena may occur, whose relative dominance depends on the incident wavelength and on the electric and magnetic permittivity of the sample. In the geometrical optic approximation light may be transmitted, absorbed or reflected. From a physical optics viewpoint diffractions phenomena may occur. In the quantum optics regime, phenomena such as absorption, photoemission and resonances occur.

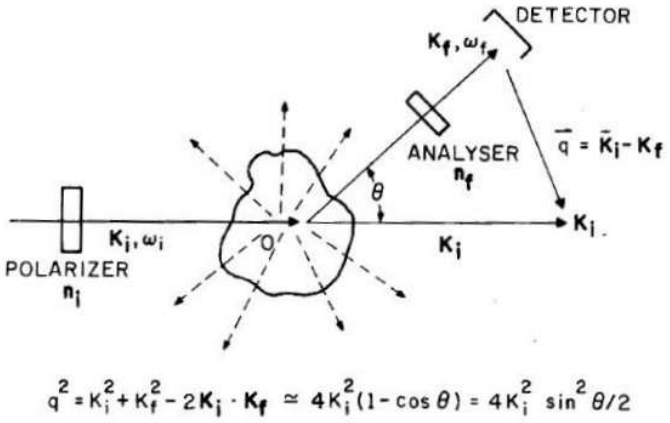


Figure 2.4: Schematization of a scattering experiment. Incident light (i) impinges on the sample and is scattered in all directions. Only the selected final light (f) arrives to the detector

to Q is due to the scattering angle. The momentum transfer is thus calculated according to the isosceles triangle formula as:

$$Q = \frac{4\pi n(\lambda, T)}{\lambda} sin\frac{\theta}{2} \tag{2.41}$$

This is the Bragg condition. It specifies the wave vector component of the dielectric constant fluctuation that will give rise to scattering at an angle theta. Since λ and θ are decided with the experiment, to measure Q the refractive index n of the investigated system must have been determined previously. In inelastic X-ray scattering is $n \approx 1$.

Detectors, as photomultipliers or CCD cameras, measure the intensity of light, not its electric field. The scheme in Figure 2.5 illustrates the general main features of an apparatus for measuring the power spectrum of a random fluctuating variable $A(t)$. The method applies for any fluctuating variable but we consider the case of our interest, where $A(t)$ is the outgoing electric field $E_f(t)$. It is there shown that the quantity measured in a light scattering experiment is $<\mid E_{TO} \mid^2>_T$:

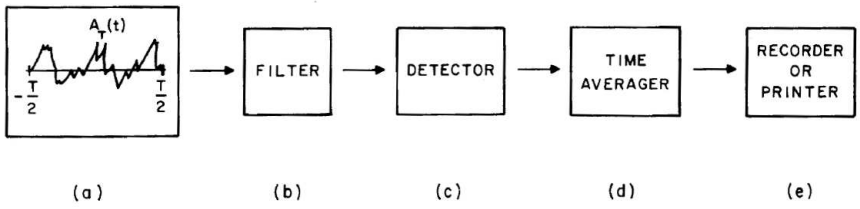


Figure 2.5: The fluctuating signal $E_T(t)$, measured for a period T (a), is passed through a filter (b) which allows a very narrow range of frequencies. The filter can be tuned on each frequency time by time or can be able to separate spatially the different pure spectral components, as for a diffraction grating. The signal that gets out the filter, E_{TO}, impinges on a detector (c) whose output is proportional to $\mid E_{TO} \mid^2$. The output of the detector is then averaged (d) over the recording interval T and the result $<\mid E_{TO} \mid^2>_T$ is recorded (e). Picture taken from [17].

It can be demonstrated [17] that in the long averaging time limit compared to the fluctuation mean time, $<\mid E_{TO} \mid^2>_T$ is proportional to the *spectral density* (or power spectrum) of the self correlation function of the outgoing electric field:

$$I_E(\omega_f) = \frac{1}{2\pi} \int_{-\infty}^{\infty} dt' e^{-i\omega_f t'} < E_f^*(t) E_f(t+t') > \tag{2.42}$$

Eq.(2.42) expresses an important starting statement. Our ultimate aim is to relate the spectral density $I_E(\omega_f)$ to the dynamic structure factor $S(Q, \omega_f)$.

2.5.1 Spectral density and dynamic structure factor

Due to vibrational, rotational and translational modes of the molecules in the sample, the local dielectric function $\epsilon(\mathbf{r}, t)$ fluctuates in time and space around its mean value ϵ_0. The fluctuations are defined by:

$$\epsilon(\mathbf{r}, t) = \epsilon_0 \mathbf{I} + \delta\epsilon(\mathbf{r}, t), \tag{2.43}$$

where $\mathbf{I}$ is the second rank unit tensor and $\delta\epsilon(\mathbf{r}, t)$ is the fluctuation tensor. Let the incident (i) electric field be a plane wave:

$$\mathbf{E}_i(\mathbf{r}, t) = \mathbf{n}_i E_0 e^{i(\mathbf{k}_i \mathbf{r} - \omega_i t)} \tag{2.44}$$

Classical electrodynamics [111] shows that the component (f) of the scattered field at large distance R from the scattering volume, having characterized polarization $\mathbf{n}_f$, propagation vector $\mathbf{k}_f$ and frequency ω_f is:

$$E_f(R, t) = \frac{E_0}{4\pi R \epsilon_0} e^{i[\mathbf{k_f} \cdot \mathbf{r} - \omega_i t]} \int_V d^3 r e^{i\mathbf{Q}\cdot\mathbf{r}} \mathbf{n}_f \cdot [\mathbf{k}_f \wedge \mathbf{k}_f \wedge [\delta\epsilon(\mathbf{r}, \mathbf{t}) \cdot \mathbf{n_i}]] \tag{2.45}$$

that is, the scattered field is proportional to the spatial Fourier transform of the dielectric function.

$$\delta\epsilon(\mathbf{Q}, t) = \int_V d^3 r e^{i\mathbf{Q}\cdot\mathbf{r}} \delta\epsilon(\mathbf{r}, t) \tag{2.46}$$

If we consider the matrix element $\delta\varepsilon_{if}$

$$\delta\varepsilon_{if}(\mathbf{Q}, t) = \mathbf{n}_i \cdot \delta\epsilon(\mathbf{Q}, t) \cdot \mathbf{n}_f \tag{2.47}$$

the electric field E_f in Eq. (2.45) can be simplified working out the vector cross product, as:

$$E_f(R, t) = -\frac{k_f^2 E_0}{4\pi R \epsilon_0} e^{i[k_f R - \omega_i t]} \delta\varepsilon_{if}(\mathbf{Q}, t) \tag{2.48}$$

The time correlation function of E_f can be calculated from Eq. (2.48). It follows that it is proportional to the time correlation function of $\delta\varepsilon_{if}(\mathbf{Q}, t)$

$$\langle E_f^*(R, 0) E_f(R, t) \rangle = \frac{k_f^4 |E_0|^2}{16\pi^2 R^2 \varepsilon_0^2} \langle \delta\varepsilon_{if}(\mathbf{Q}, 0) \delta\varepsilon_{if}(\mathbf{Q}, t) \rangle e^{-i\omega_i t} \tag{2.49}$$

By the combination of Eqs. (2.49) and (2.42)[3], we obtain a relationship between the spectral density of the light scattered and the self correlation function of the dielectric tensor fluctuations:

$$I_E(\mathbf{Q}, \omega_f, R) = \left[\frac{I_0 k_f^4}{16\pi^2 R^2 \epsilon_0^2} \right] \frac{1}{2\pi} \int_{-\infty}^{\infty} dt e^{i(\omega_i - \omega_f)t} \langle \delta\varepsilon_{if}(\mathbf{Q}, 0) \delta\varepsilon_{if}(\mathbf{Q}, t) \rangle \tag{2.50}$$

It is important to note: *(i)* the dependence of $I_E(\mathbf{Q}, \omega_f, R)$ on λ^{-4}. The higher the incident frequency, the brighter the scattering. This is also the reason for the blue color of sky and sea; *(ii)* the dependence of I_E on R^{-2} like for a spherical wave; *(iii)* I_E depends on ω_i and ω_f only through the difference $\omega = (\omega_i - \omega_f)$.

[3] We can assume $t = 0$ and $t' = t$ without loss of generality

The isotropic spectrum.

The energy-space distribution of the scattered intensity will depend on the molecular composition and motion of the investigated system, on the selected polarization, and on the angle of collection. In such a complicated situation, restrictions are of use. We will firs consider the case of an homogeneous and isotropic system in thermodynamic equilibrium. In this case the off-diagonal elements of the ϵ tensor are zero. The measured spectral density I_E can be put in relation to the mass density fluctuations by starting from the consideration that the dielectric constant ϵ_0 is a function of density and temperature. Its fluctuations can be expressed [17] as:

$$\delta\varepsilon(\mathbf{r},t) = \left(\frac{\partial\varepsilon}{\partial\rho}\right)_T \delta\rho(\mathbf{r},t) + \left(\frac{\partial\varepsilon}{\partial T}\right)_\rho \delta T(\mathbf{r},t) \tag{2.51}$$

Eq. (2.50) can be hence rephrased as $I_E(Q,\omega,R) = A(k_f,R)I_\varepsilon(Q,\omega)$ where:

$$A(k_f,R) = \frac{I_0 k_f^4}{16\pi^2 R^2 \epsilon_0^2} \tag{2.52}$$

and

$$I_\varepsilon(\mathbf{Q},\omega) = \frac{1}{2\pi}(\mathbf{n}_i\cdot\mathbf{n}_f)^2 \int_{-\infty}^{\infty} dt e^{-i\omega t}\langle\delta\varepsilon(\mathbf{Q},0)\delta\varepsilon(\mathbf{Q},t)\rangle \tag{2.53}$$

The substitution of Eq.(2.51) into Eq.(2.53) gives the spectrum

$$I_\varepsilon(\mathbf{Q},\omega) = (\mathbf{n}_i\cdot\mathbf{n}_f)^2\left(\frac{\partial\varepsilon}{\partial\rho}\right)^2_{T_0} S_{\rho\rho}(\mathbf{Q},\omega) +$$

$$+(\mathbf{n}_i\cdot\mathbf{n}_f)^2\left\{\left(\frac{\partial\varepsilon}{\partial\rho}\right)_{T_0}\left(\frac{\partial\varepsilon}{\partial T}\right)_{\rho_0}[S_{\rho T}(\mathbf{Q},\omega)+S_{T\rho}(\mathbf{Q},\omega)] + \left(\frac{\partial\varepsilon}{\partial T}\right)^2_{\rho_0} S_{TT}(\mathbf{Q},\omega)\right\} \tag{2.54}$$

where $S_{\rho\rho}(\mathbf{Q},\omega)$ is the spectral density of the correlation function of the mass density fluctuations $\langle\delta\rho^*(\mathbf{Q},t)\delta\rho(\mathbf{Q},t)\rangle$.

Analogously, $S_{\rho T}(\mathbf{Q},\omega)$ and $S_{T\rho}(\mathbf{Q},\omega)$ are the correlation functions of $\langle\delta\rho^*(\mathbf{Q},t)\delta T(\mathbf{Q},t)\rangle$ and $\langle\delta T^*(\mathbf{Q},t)\delta\rho(\mathbf{Q},t)\rangle$ respectively. $S_{TT}(\mathbf{Q},\omega)$ is the autocorrelation function of the temperature fluctuations $\langle\delta T^*(\mathbf{Q},t)\delta T(\mathbf{Q},t)\rangle$. The terms in the second row of Eq. (2.54) can be neglected in most liquids, as it is found experimentally that $(\partial\varepsilon/\partial T)_{\rho_0} \approx 0$.

In conclusion, for most applications the spectrum measured in a light scattering scattering experiment from an isotropic medium is found to be proportional to $S(Q,\omega)$ through the relationship:

$$I_E(\mathbf{Q},\omega,R) = \frac{I_0 k_f^4}{16\pi^2 R^2\epsilon_0^2}(\mathbf{n}_i\cdot\mathbf{n}_f)^2\left(\frac{\partial\varepsilon}{\partial\rho}\right)^2_{T_0} S_{\rho\rho}(\mathbf{Q},\omega) \tag{2.55}$$

The first term of Eq. (2.55) represents the measured spectrum. The dynamic structure factor of an isotropic system is hence measured directly from the intensity spectrum of the scattered light. If the incoming and final polarization are selected to be equal (for example vertical (V)) the result is maximized.

From Eq. (2.55) we also deduce that, in principle, there is no scattered light at a final polarization orthogonal to the incident polarization. As a matter of facts, it is found experimentally that such a contribution is nonzero even in the case of inert gases. This is due to collisions which deform the charge density, and occurs when the reversed investigated frequencies match the timescale of the collisions, that is 10^{-13}s. In practice, for an isotropic system it is possible to neglect the collisional contribution in the spectral range below 10 GHz.

2.5.2 Scattering geometries and non isotropic systems

When a system is not isotropic, the selection of the outgoing polarization will come into play for the determination of the dynamic structure factor. By this way, it is convenient to state scattering geometries concerning the polarization. In the laboratory system, the scattering plane, identified by $\mathbf{k}_i$ and $\mathbf{k}_f$, will be horizontal and the incident polarization will be vertical. The collected polarization will be selected either vertically (V) or horizontally (H). In any case of our interest the incident radiation was vertically polarized. The power spectra in the two configurations are called $I_{VV}(Q,\omega)$ and $I_{VH}(\omega)$, respectively. (see Fig.2.6).

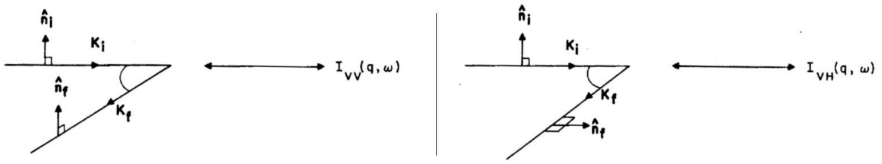


Figure 2.6: The so called VV (left) and VH (right) polarization selection configurations for a light scattering experiment. In our case the incident radiation is vertically polarized. The power spectra in the two configurations are called $I_{VV}(Q,\omega)$ and $I_{VH}(\omega)$, respectively.

If the scattering is purely isotropic, the measured spectrum in the VV condition ($I_E \equiv I_{VV}$) corresponds to the spectrum of the density fluctuations $I_{\rho\rho}$, the second term of Eq. (2.55): $I_{VV} = I_{\rho\rho}$ and $I_{VH} \approx 0$ will be negligible with respect to I_{VV}.

If the system is anisotropic, $I_{VV}(Q,\omega) \neq I_{\rho\rho}(Q,\omega)$. It has been shown that both $I_{VV}(Q,\omega)$ and $I_{VH}(\omega)$ are required to determine the spectrum of density fluctuations $I_{\rho\rho}(Q,\omega)$ through the relationship [17]:

$$I_{\rho\rho}(Q,\omega) = I_{VV}(Q,\omega) - \mathrm{r}^{-1} I_{VH}(\omega) \tag{2.56}$$

where r is the depolarization ratio whose value mirrors the degree of anisotropy and can be determined experimentally. The determination is needed of both $I_{VV}(Q,\omega)$ and $I_{VH}(\omega)$ and r to the knowledge of the $S(Q,\omega)$.

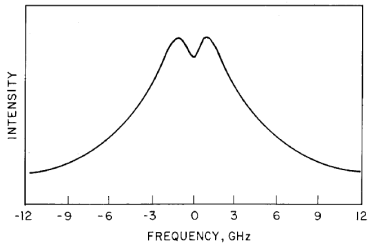


Figure 2.7: Aspect of a depolarized (VH or HV) light scattering spectrum

Depolarized light scattering in liquids at low frequencies is originated by three main causes [112]: shear modes (i.e. transverse acoustic modes at low temperatures) which is not detected in the backscattering geometry, orientational fluctuations which occurs when molecules have a degree of anisotropy and scattering induced by interactions, which always occurs.

Résumé du Chapitre 3

Ici nous décrivons l'instrumentation et les techniques expérimentales et utilisées au cours de ce travail. Après avoir passé en revue les principales techniques de diffusion inélastique de rayonnement, on discute des critères de choix de la technique la mieux appropriée dans une certaine gamme de température (ou de pression). Comme l'effort instrumental le plus important a été consacré à la réalisation des premières expériences sur la nouvelle ligne de lumière 10.2 IUVS du synchrotron Elettra, l'instrument de diffusion inélastique dans l'ultraviolet est décrit plus en détail. Nous avons aussi réalisé des expériences complémentaires de diffusion Brillouin dans le visible (BLS) et de diffusion inélastique des rayons X (IXS) à l'ESRF, pour disposer de spectres de référence pour l'IUVS et pour élargir la gamme dynamique. L'instrumentation correspondante est aussi décrite brièvement

Chapter 3

Inelastic ultra violet scattering and complementary techniques

Abstract

In this chapter the techniques and instrumentations utilized for the development of the present work are described. An overview is given of the main techniques for inelastic scattering of radiation and of the criterion for choosing the appropriate technique for a certain temperature (-pressure) regime. As the pioneering experimental task of the present work has been the performing of the first measurements at the new 10.2 IUVS beamline of Elettra synchrotron, the IUVS beamline is described in detail. We have also performed complementary experiments by Brillouin light scattering (BLS) and inelastic X-ray scattering (IXS) in order to acquire reference spectra for IUVS and enlarge the dynamical range. The respective instrumentations are also quickly described.

3.1 Inelastic scattering techniques

The autocorrelation function of the mass density fluctuations, $G(r,t)$ or, equivalently, its Fourier transform, the dynamic structure factor $S(Q,\omega)$, are the central quantities in the dynamical investigations of disordered systems. $S(Q,\omega)$ can be measured through inelastic scattering of radiation, as it is proportional to the intensity spectrum $I(Q,\omega)$ according to the relationship $I(Q,\omega)/Q^4 \propto S(Q,\omega)$) [16]. $G(r,t)$ can be measured by means of photon-correlation experiments [17]. The map in Fig.3.1 reports the regions of exchanged energy and momentum transfer competing to some inelastic scattering techniques. Each technique can access a dynamical region which is limited, by construction, by the energy resolution, the minimum and maximum incident wavelength, the achievable scattering angles and detector limitations. Furthermore, sample-dependent limitations have to be considered, due to absorption process.

The *best sensitivity condition* of an inelastic scattering technique to a relaxation process is achieved when the typical angular frequency probed by the technique, ω_P, is comparable to the reversed typical time of the process itself, $1/\tau_R$, that is, when the the relationship $\omega_P\tau_R \approx 1$ is satisfied. In general, the temperature excursion of $\tau_R(T)$ may cover several decades, as, for example in proximity of the structural arrest related to the glass transition. Moreover, different relaxation processes often occur over well separated timescales which are typically spread over decades. Hence, on one hand we have to choose the best sensitive technique to probe a certain process in a certain thermodynamic domain. On the other hand, a single technique will be never enough to map the whole time-temperature evolution of the all processes. As a matter of facts, a fully informative experimental approach will tile information from adjacent dynamical regimes got by means of complementary techniques.

Inelastic X-ray scattering is the technique of choice to study the dynamics evolving at high frequency on length scales close to the interparticle separation. In IXS the momentum transfer

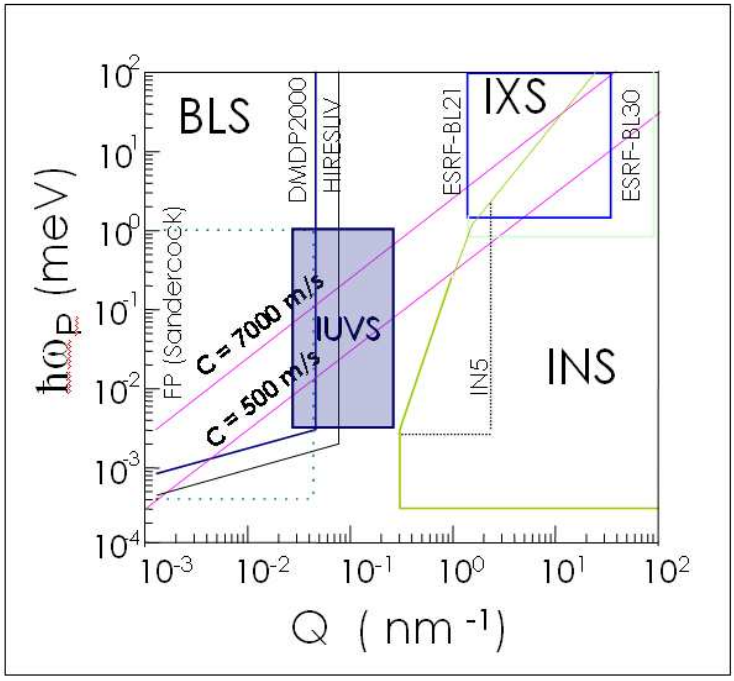


Figure 3.1: Map of the probed energy, $E = \hbar\omega_P$, and momentum transfer, Q, accessible by some techniques for inelastic scattering. BLS stands for Brillouin light scattering, IUVS for inelastic ultra violet scattering, IXS for inelastic X-ray scattering, INS for inelastic neutron scattering. Along the magenta diagonal lines the ratio $\hbar\omega_P/Q$ is constant and corresponds to the typical minimum and maximum speed of sound in condensed systems, 500 and 7000 m/s. By tradition, units of energy and momentum may switch from a technique to another. For example, it is worth reporting that for exchanged energy the following conversion is often applied : E[GHz] = E[μeV]/4.136

.

ranges from 1 up to 25 nm^{-1} (even more in opportune geometrical conditions) and the exchanged energy is of the order of 1 - some 100 meV. The development of IXS, in the nineties [], brought a considerable complement to neutron spectroscopies, which, historically, owned the field of investigation of atomic dynamics in condensed matter at momentum transfers and energies typical of collective motions. Indeed neutrons avail of a larger penetration depth than radiation, at an incident energy comparable to the probed energy and over a wider range of Qs. Nevertheless, the main limitation of neutron spectroscopy is the impossibility to measure sound modes whose speed is higher than the one of the probe ($\approx 1000/s$). This *kinematic limitation* is not relevant in crystalline samples, as the translational invariance allows the study of the acoustic excitations in high order Brillouin zones. In topologically disordered systems as liquids, glasses and gases the lack of long range periodicity makes any translation impossible. That becomes the domain of IXS. Photons of 0.1 nm wavelength and 12 Kev energy, are fast enough to excite high energy modes in disordered condensed matter. A resolving power of 10^7 is needed, which is achieved at the synchrotron radiation sources. Brillouin light scattering [17] is routinely used in the low momentum transfer region, from 10^{-3} up to $4 \cdot 10^{-2}$ nm^{-1}.

Previous inelastic scattering measurements of $S(Q,\omega)$ of water. Before the development of the IUVS beamline, IXS measurements of $S(Q,\omega)$ of liquid water between 273 and 473 K had been performed in the THz frequency regime 1 and 7 nm^{-1}, and by using pressure (1.5 kbar) to keep the density at $\rho \approx 1$ g/cm^3 [19, 91]. These measurements allowed the characterization of the structural relaxation of liquid water. When going to the supercooled state, though, the structural relaxation starts being too slow with respect to the inverse frequencies probed by IXS. At low temperatures the best sensitivity condition is not achieved anymore but the condition $\omega_P\tau_R \gg 1$ applies. On

the other hand, BLS measurements of $S(Q,\omega)$ of supercooled water at ambient temperature were performed, down to 251 K [20]. In this case, the dynamics of supercooled water was too fast for the technique to measure the structural relaxation ($\omega_P \tau_R \ll 1$). In principle, to measure the relaxation time of supercooled water by BLS, a much deeper supercooling degree would have to be realized, which is quite unlikely, due to the increasing probability of nucleation at lower temperature. In summary, previous IXS and BLS investigations of water dynamics have inferred that the relaxational dynamics of supercooled water could be probed in a so-called *mesoscopic* dynamical region, between those probed by BLS and IXS and at an incident wavelength that lies between the visible and the X-rays.

The development of the Inelastic ultraviolet scattering beamline in Elettra synchrotron [21, 22] has made it possible to determine $S(Q,\omega)$ in such a region, namely at exchanged energy between 10 μeV and 1 meV and 0.03 and 0.2 nm^{-1} momentum transfer. The pioneering experimental task of the present work has been the measuring of the dynamic structure factor of supercooled water by means of the new technique IUVS. Indeed water was the first system ever investigated by IUVS and the investigation has been performed by the present work. Since the IUVS beamline was new, we have have acquired also BLS reference measurements to check the calibration of the beamline. This procedure is recommendable in any case as it allows to double the extension of the investigated frequency domain, giving us access to 3 decades. The wider the frequency domain investigated, the more reliable is the determination of the relaxation shape. The results obtained by BLS and IUVS have been then successfully compared to results independently acquired in previous IXS investigations.

The dynamics of the LiCl-6H_2O solution has been investigated in a $\approx$ 270 K wide temperature domain by combining BLS, IUVS and IXS measurements. In such a large temperature domain, the relaxational dynamics of the solutions occupies five decades. Photon correlation spectroscopy (PCS) has been utilized to characterize the slower dynamics (micro to milliseconds).

3.2 The IUVS beamline in Elettra synchrotron

At a typical electron current of 200 mA, the IUVS beamline delivers on the sample a photon flux of $\approx 10^{12}$ photons/s in the 5 to 11 eV range, at a resolving power between 10^5 and 10^6. In figure 3.2 a 3D drawing of the beamline is shown.

Radiation Source: the figure-8 Undulator. The radiation source is a figure-8 undulator (see Fig. 3.3) whose length is maximized for the available space in the straight sections of the storage ring (4.5 m) [113, 114]. The figure-8 undulator has been constructed as an alternative to the standard vertical field device, with the main advantage of a much reduced on-axis power density, that is obtained with no penalty on the useful photon flux. Using a 32 mm period undulator with maximum deflection parameters $K_x = 3.4$ and $K_y = 9.4$, at the exit of a 600 $\times$ 600 mrad^2 pinhole, the total power of the synchrotron radiation is reduced down to about 20 W, while the first harmonic delivers $2{\cdot}10^{15}$ photons/s/0.1% BW. The energy of the first harmonic can be varied from a minimum of 4.7 eV to a maximum of 262 eV by varying the undulator gap between 19 and 248 mm, respectively.

The predicted spectrum of the figure-8 undulator and the power distribution are reported in Fig. 3.4. The radiation spectrum is composed of two sets of harmonics, conventionally defined by integer (i=1,2,3,etc) and half-integer (i=1/2,3/2,5/2,etc), indices and having alternatively horizontal (i=1,3,5,...) and vertical polarization direction. The angular distribution of the emitted power is peaked off-axis so that a suitable pinhole can filter-off most of the unwanted power, reducing the heat load on optics.

Filtering and collimation optics: Heat-load filter. The high order undulator harmonics of the undulator are cleaned by a low-pass filter made of two plane mirrors, one gold-coated, the other of plain silicon. **Mini Mono** is a small pre-cleaning monochromator that removes residual harmonic outgoing the heat-load filter, with a cutoff treshold of 14 eV. Radiation is dispersed by a spherical grating, which, properly orientated, reflects the desired wavelength to the exit slit. **Pre-focussing Mirror Chamber.** A silicon spherical mirror of radius 1.9047 m focalizes the radiation

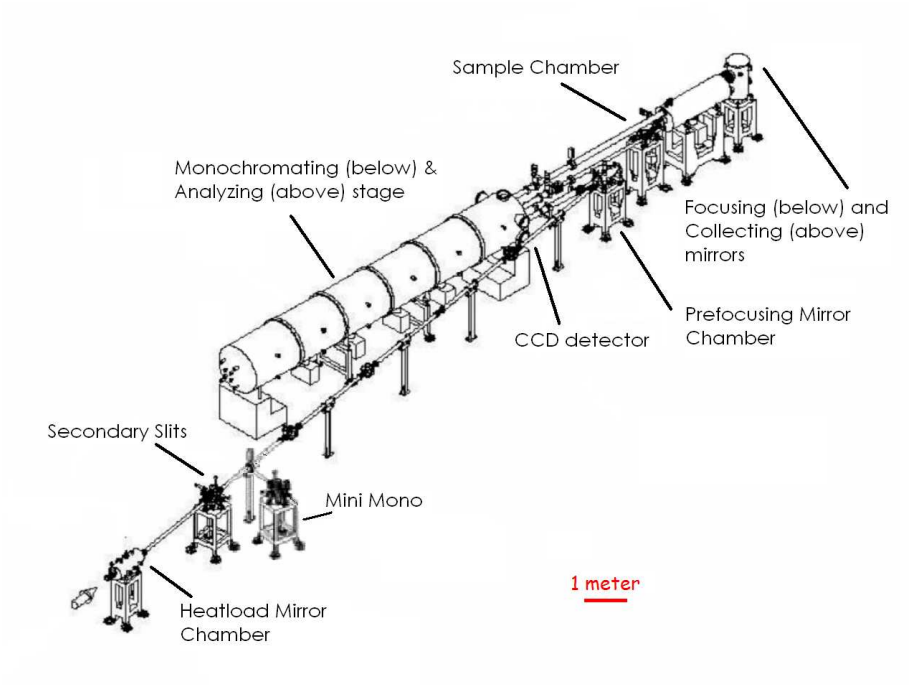


Figure 3.2: IUVS beamline at the Elettra synchrotron in Trieste. Adapted from www.elettra.trieste.it/experiments/beamlines/iuvs/schema.gif

coming from the undulator (36 meters far) onto the center of the monochromator entrance slit (1.8 meters far), with a 20:1 demagnification and with an incident angle of 85°.

Monochromator and Analyzer. Both monochromator and analyzer stages of IUVS beamline work according to the normal incidence monocromator (NIM) Czerny-Turner design [115]. Design and working principle are schematized in Fig. 3.5 for the case of monochromator: the incident radiation (A) is focused onto the entrance slit (B) and is collimated by a spherical mirror (C). The collimated beam is diffracted from a grating (D) and the dispersed beam is re-focussed by a second mirror (E) at the exit slit (F). Each wavelength is focussed to a different position at the plane of the slit F. The wavelength (G) transmitted through the slit F depends on the rotation angle of the grating D. The functionality of the analyzer is just the reverse.

The working principle of a NIM is represented in Fig. 3.6. The incoming radiation is reflected at a different "steps" of the blazed grating. For each wavelength, constructive interference is achieved when the difference in the optical path of the reflected rays is an integer multiple of the wavelength. With reference to the geometry drawn in Figure 3.6, the condition can be expressed as $m\lambda = d(sin\alpha + sin\beta)$. The IUVS monochromator grating is oriented to send the $m \approx 200$ order to the sample stage.

IUVS beamline is equipped by a blazed grating of Zerodur, coated with Al+MgF_2 to optimize the reflectivity for all the incoming wavelengths. The gratings are parallel to the the vertical plane and are 220 mm high by 420 mm wide, with 52 horizontal lines/mm. They give 40% efficiency in the 5-11 eV range. In figure 3.7 the side view of IUVS beamline monochromator and analyzer chamber is shown. The stages share the same chamber, kept in ultra high vacuum (10^{-8} mbar) to prevent power loss and noise due to air scattering. The monochromating stage is allocated in the lower plane, the analyzing stage occupies the upper level. The whole chamber is 8 meter long to match the best compromise between resolving power and mechanical stability.

Slits. IUVS beamline NIM chamber is equipped with four slits, two for the monochromating stage and two for the analyzer. Each slit is modeled rectangularly by four parallel blades, disposed on different planes to avoid diffraction. The monochromator entrance slit cuts the tails of the

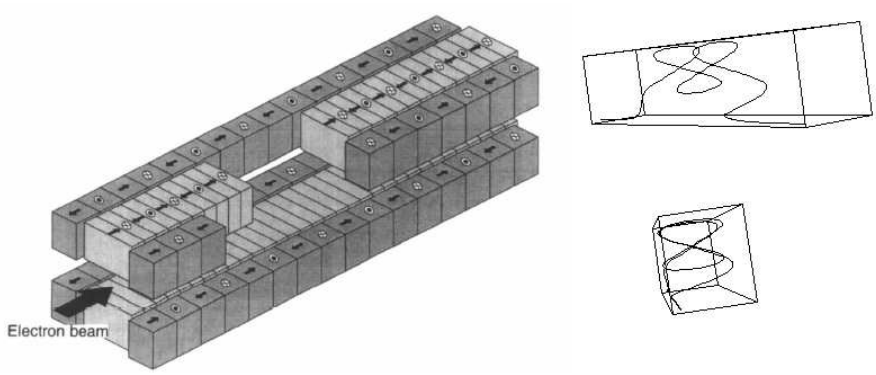


Figure 3.3: Schematic illustration of the figure-8 undulator (left) [113] and of the electron trajectory (right). The period length of the vertical undulator is twice as long as that of the horizontal undulator. The central row of magnets generates a vertical field and the side blocks generate a horizontal field at twice the periodicity. The resultant trajectory of the electrons projected on the plane orthogonal to the incoming direction is a *figure-of-eight*. (www.elettra.trieste.it/experiments/beamlines/iuvs)

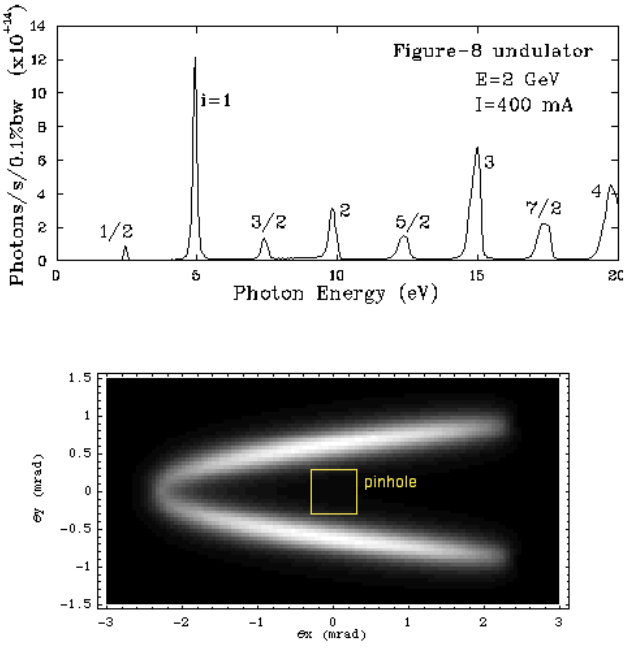


Figure 3.4: **Upper Panel:** predicted radiation spectrum at the minimum gap through a 0.6 x 0.6 mrad^2 pinhole. The higher harmonics are successively cut off above 14 eV. **Lower panel:**Power density angular distribution at the minimum gap.

incident radiation profile and lets the 99.7 % of intensity pass. The monochromator exit slit is used to clean the incident wavelength.

Energy resolution. The energy resolution of the beamline, ΔE, is determined by the resolving power of the grating and by the width of the exit slit and its distance from the grating. The contribution of the grating is can be calculated through the Rayleigh criterion [116] as the reverse

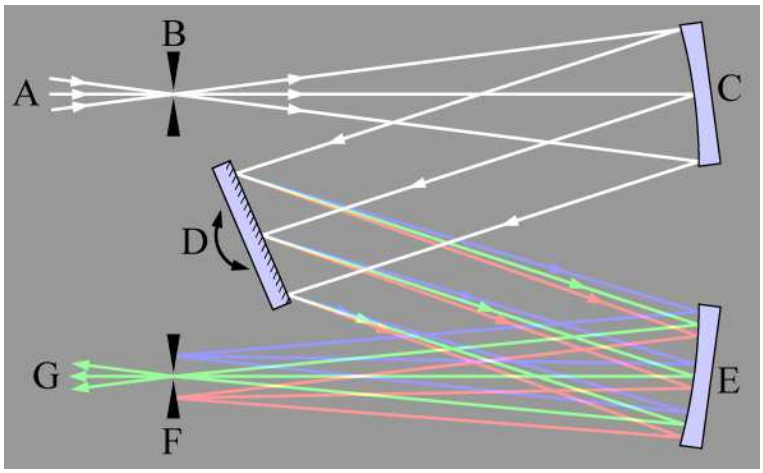


Figure 3.5: Normal incidence monochromator. the incident radiation (A) is focused onto the entrance slit (B) and is collimated by a spherical mirror (C). The collimated beam is diffracted from a grating (D) and the dispersed beam is re-focussed by a second mirror (E) at the exit slit (F). Each wavelength is focussed to a different position at the plane of the slit F. The wavelength (G) transmitted through the slit F depends on the rotation angle of the grating D. (Source: www.biocrawler.com)

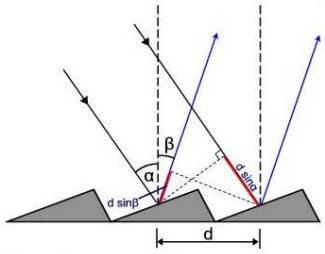


Figure 3.6: Blazed interference grating used in IUVS normal incidence monochromator and analyzer. The incoming radiation is reflected at a different "steps" of the blazed grating. Constructive interference is achieved when the condition $m\lambda = d(sin\alpha + sin\beta)$ is fulfilled, with m integer number and λ the wavelength.

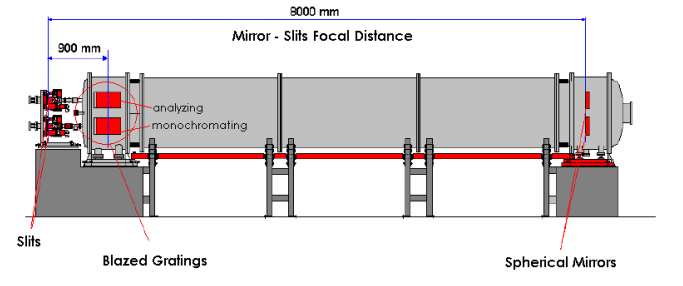


Figure 3.7: IUVS NIM monochromator and analyzer chamber. From a mechanical point of view the structures of monochromator and analyzer are the same. The two stages are located on parallel planes at low (monochromator) and up (analyzer) quotas in the chamber (Courtesy of A. Stolfa).

of the resolving power:

$$\left(\frac{\Delta E}{E}\right)_{Ray} = \frac{1}{mN} \tag{3.1}$$

where m is the refractive order and N the number of lines of the grating. In the case of IUVS ($m \approx 200$ and $N \approx 10^4$)this contribution is $\approx 10^{-7}$. The contribution to resolution due to slit width and distance is:

$$\left(\frac{\Delta E}{E}\right)_{slit} = \frac{\delta \cot\theta}{2F} \tag{3.2}$$

where δ is the slit opening, θ is the grating blaze angle and F is the focal length of the spherical mirror. With $\delta \approx 50$ μm, $F = 8$ m and $\theta = 69°$ we get a relative resolution of 10^{-6}. The total relative energy resolution of the beamline is given by the root sum squared of the two contributions, that is, 10^{-6}. That implies, for 5 - 10 eV incident energy, an absolute energy resolution of some μeV, that is, within few percent of the typical energy of the acoustic modes measured by IUVS. In figure 3.8 the experimental resolution function of IUVS is reported, measured on an isotropic copper scatterer. The spectrum can be approximated by a Lorentzian function, which is a good first order approximation of an Airy function, that describes the intensity profile of diffraction from a rectangular aperture [116]. The full width at half maximum of the measured curve gives the limit of the resolution, that is 18 μeV.

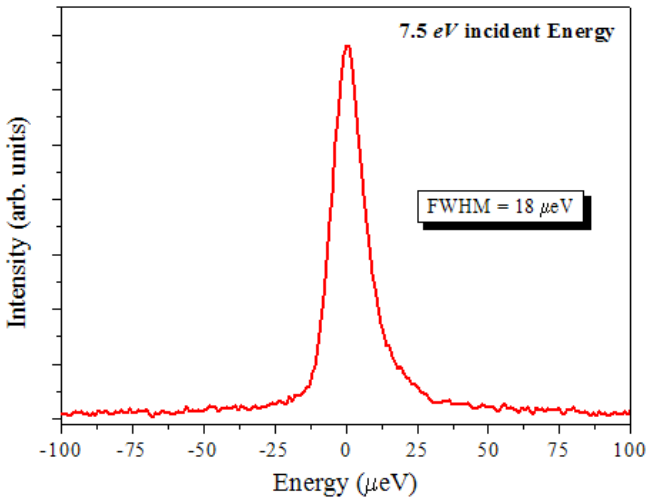


Figure 3.8: Energy resolution of the IUVS spectrometer measured with 7.5 eV energy photons. The spectrum has been obtained analyzing the isotropic scattering from a copper scatterer

Focusing mirror, Sample Chamber, Collection mirror. At the exit of the monochromator the beam is impinging on a spherical mirror, which focuses the radiation on the sample, with a spot size of $\approx 30 \times 100$ μm^2. A second spherical mirror is used to collect the radiation scattered from the sample and send it to the entrance slit of the analyzer unit.

Sample environment For experiments on liquids, rectangular cells of quartz are of use. Normal glass adsorbs the incoming beam. The sample holder is a rectangular brake of copper connected to an arm which can align the sample in the beam controlling along the X, Y and Z (beam axis) directions and along the rotation of the XZ plane around Y (see Fig. 3.9). The temperature of the arm can be controlled by a thermal bath (minimum cooling ≈ 246 K) or a Helium cryostat. Indium sheets are used for both thermal coupling and thermal dilatation matching.

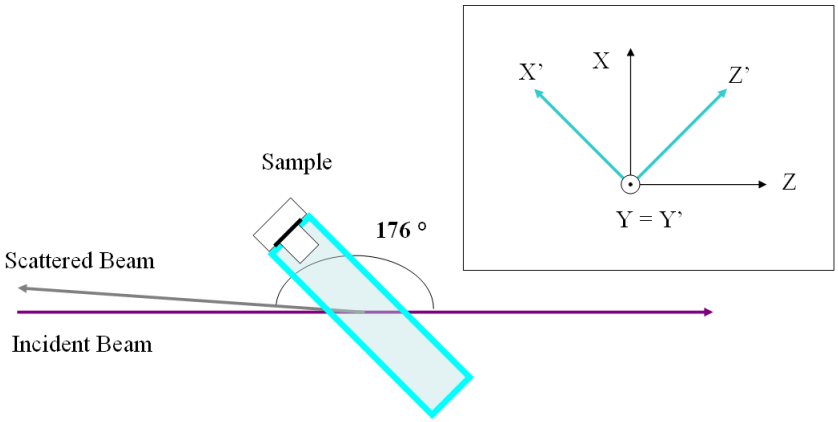


Figure 3.9: Relative position of the sample cuvette with respect to the beam in IUVS experiments. Z is direction of incoming beam. The scattered radiation is collected at 176° by the collecting mirror. XYZ are the lab axis coordinates; X'Y'Z' are the sample's. The 45° negative rotation of the sample, respect to Z, sends most of reflected light far away from the collecting mirror.

We have used the QS-111 Quartz SUPRASIL from Heraeus Quarzglas GmbH. see Fig. 3.10. The SUPRASIL standard identifies the quartz of highest purity and homogeneity, which gives transmission values of more than 80% between 200 nm and 2500 nm for an empty cell. Since this quartz is manufactured by flame hydrolysis of SiCl4 it is also called synthetic quartz. The sample chamber is kept in vacuum at 10^{-7}. Sample evaporation from the cuvette is prevented by a little viton o-ring inserted in a dent dug in the neck of the stopper and pressed by a screw (see Fig 3.10).



Catalogue Number: 111	
Material Color Code:	QS
Light Path:	10 x 10 mm
Volume:	3500 µl
Outer Dimensions:	
Height:	46 mm
Width:	12.5 mm
Depth:	12.5 mm
Inner Dimensions:	
Width:	10 mm
Base Thickness:	1.25 mm
Number of windows:	4

Figure 3.10: Quartz cuvettes from Hellma, suitable for IUVS experiments. The viton O-ring is inserted as a gasket around the stopper, which is pressed in order to prevent sample evaporation into the 10^{-7} **mbar** sample chamber.

Detector. The scattered radiation is detected by a peltier cooled CCD detector, which operates at 80°C with very low dark current (namely 3 el/pixel/hour). An example of acquired pattern is given in figure 3.11. The CCD chip has 2040 pixels in the dispersing direction (horizontal) and 512 in the other, which is proportional to the illuminated path in the sample. Pixels are wide 13,5 μm. The simultaneous collection of different energies allows much reduced time, with respect, i.e., to a photomultiplier. The typical statistically acceptable acquisition time varies between a minimum of 120 seconds (possibly replicable to get an average) to some tens minutes.

Radiation Source: 244 nm Laser. Alternatively to the synchrtotron source, IUVS beamline is equipped by a Lexel 95-SHG Argon Laser that is typically utilized at an incident power of 5 mW.

The UV laser beam is sent to the focussing chamber through an optional mirror that intercepts the path of the synchrotron radiation. In this case, all the beamline components as far as to the exit slit of the the monochromator included, are not contributing. The flux of the laser is 10^17 photons/s and the resolving power $E/\Delta E \approx 10^7$.

3.2.1 Calibration

Energy calibration. The correspondence between the horizontal pixel cardinality of the CCD and the energy exchanged in the scattering process can be calculated according to geometrical considerations. The calculated conversion between CCD pixel number ΔN and exchanged energy E is:

$$\Delta E[\mu eV] = 0.2786 \times E_{inc}[eV] \times \Delta N \tag{3.3}$$

where E_{inc} is the incident energy. Microelectronvolts (μeV) are the privileged unity for the exchanged energy, in IUVS.

Momentum Transfer
The momentum transfer is given by the relationship

$$Q = \frac{4\pi n(\lambda, T)}{\lambda} sin\frac{\theta}{2} \tag{3.4}$$

where λ is the incident wavelength, T the temperature, $n(\lambda, T)$ the refractive, θ is the scattering angle, that, in IUVS experiments, is typically 176° (almost backscattering).

Experimental Calibration. Test experiments have been perform to check the energy-momentum calibration of the new beamline. A simple experiment on crystalline quartz can show the validity of the relationships Eqs.(3.3) and (3.4). Quartz is a relaxation-free sample, and its Brillouin peaks only bring information about the acoustic modes. We have compared the sound velocity obtained by IUVS investigations to the values tabulated in [117].

We have measured the inelastic scattering spectrum at 6.67 and 7.63 eV incident energy, at 298 K. In figure 3.11 the full-chip CCD image of the acquisition at 6.67 eV is shown. The horizontal dimension is proportional to the energy dispersion, the vertical dimension is proportional to the spatial path of the UV beam into the sample. We have selected a region of interest (ROI) of the CCD image around the focus of the impinging beam, where the resolution is best. The selected ROI is a strip 36 pixels tall and 2048 pixels wide, as emphasized in the figure.

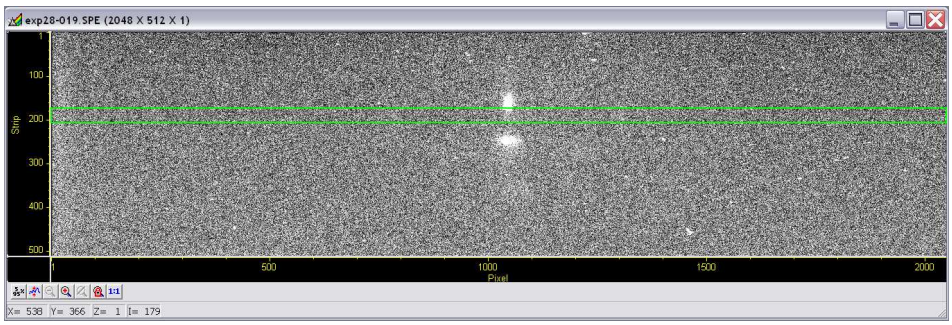


Figure 3.11: Full-chip image of CCD acquisition, at 6.67 eV incident energy and $T = 298$ K. The vertical dimension, 512 pixels long, mirrors the path of the UV beam into the sample. The two brighter spots are due stray reflections at the borders of the sample, The region of interest (ROI) is in the middle. The horizontal dimension of the chip is proportional to the exchanged energy. The rectangular selection identifies a ROI between 166 and 202 pixels in the vertical direction and 2048 pixels large, chosen around the beam focus.

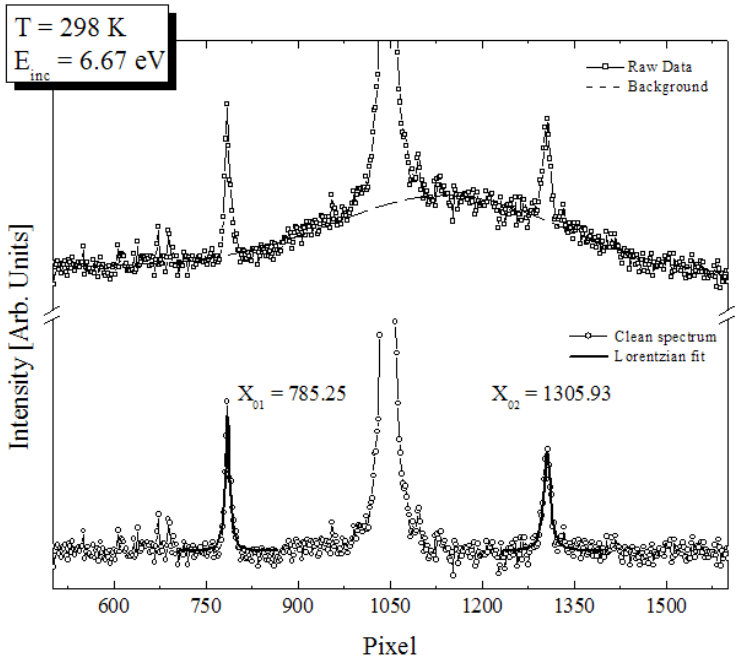


Figure 3.12: **Upper panel:** Open squares -intensity as a function of pixel number of the raw spectrum acquired in the selected ROI (see Fig. 3.11) at 298 K and 6.67 eV incident energy. Dashed line - background. **Lower Panel:** Open circles - the same spectrum with the background subtracted. Black lines - Lorentzian fits of the side peaks, from which the peak position is obtained: X_{01} = 785.25 and X_{02} =1305.93

Binning acquisitions in the ROI have been performed, where the counts have been summed along each vertical pixel stripes. The resulting raw intensity spectrum at 6.67 eV incident energy is shown in figure 3.12 as a function of CCD pixel number. The side peaks correspond to the acoustic modes of the crystal and have been modeled by Lorentzian functions to get the peak position. The spectrum has been symmetrized with respect to the incident energy by translation of the pixel axis by a shift $-(X_{01}+X_{02})/2$, where X_{01} and X_{02} are the Lorentzian peak positions.

The pixel-axis has been converted in μeV according to Eq. (3.3). The intensity spectrum is reported as a function of the exchanged energy in Figure 3.13.

In table 3.14 the parameters of this experiment are shown: the incident energy E_{inc}, the wavelength λ_{inc} (calculated as $1240/E_{inc}$), the momentum transfer Q, calculated through Eq. (3.4), where the value of n has been obtained in [118], the peak position in pixels and in μeV, calculated through Eq.(3.3). And finally, the speed of sound, calculated as $C = E/\hbar Q$ [119].

The value of C at the Q and temperature investigated reported in literature [117] is $\approx$ 6390 m/s, in good agreement with the values measured by IUVS.

3.2.2 Experimental possibilities

Inelastic ultraviolet scattering experiments with μeV energy resolution are routinely developed at the IUVS beamline of the Elettra Synchrotron. In the study of propagating collective excitations, this instrument bridges the energy-momentum gap existing between the low frequency (BLS) and high frequency (IXS) techniques.

Some publications, co-authored by the Author of the present manuscript, are mentioned in Appendix-A. Beyond water, the dynamics has been studied of glasses like SiO_2 and Glycerol. These work have been of secondary contribution from the part of this Author and are not reported

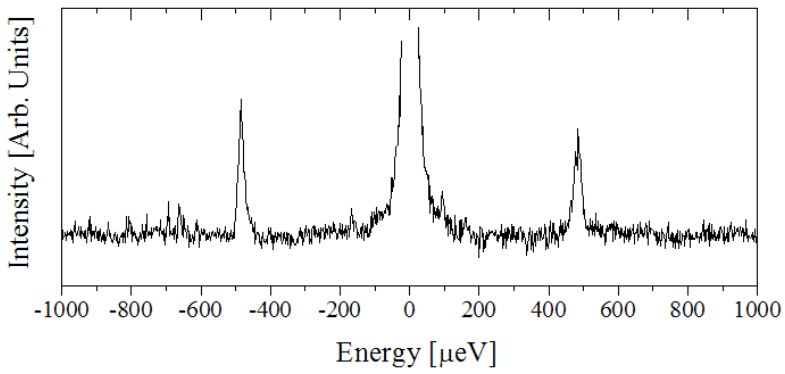


Figure 3.13: IUVS spectrum of quartz at 298 K and 6.67 incident energy, as a function of the exchanged energy. The spectrum has been symmetrized and the pixel-axis is converted to μeV according to Eq. (3.3)

E_{inc} [eV]	λ_{inc}[nm]	Q [nm-1]	n	PIX	E_0[eV]	C[m/s]
6.67	185.9	1.672	0.113	256	476	6400±30
7.63	162.5	1.770	0.137	271	576	6400±30

Figure 3.14: Parameters of IUVS experiments on crystalline quartz.

in the present manuscript.

Another interesting application of this instrument, allowed by the tunability of the incident photon energy, is the resonant scattering from electronic excitations. The scattering cross section for this process is expected to increase substantially and to allow the study of specific phenomena where the signal is usually very low. Among them and of particular importance is the scattering from surface waves, which gives information on the shear moduli the transverse dynamics of the system, a quantity that can be accessed experimentally only by indirect ways. The resonant Brillouin scattering would also open new possibilities not yet exploited in the usual light scattering experiments, as, for example, in the determination of the dynamics structure factors of specific species.

3.3 Brillouin light scattering experimental setup

Brillouin light scattering experiments have been performed at the Physics Department of Perugia University (Italy), in the laboratory of optical spectroscopies [120]. A picture of the setup is shown in Figure 3.15.

The core parts of this setup are the laser source, the sample holder with its thermalization chamber and the Fabry-Perot tandem interferometer (FPI) equipped by control and acquisition units. Steering mirror and focusing lenses optimize the optical path.

Two laser sources are available: an Innova300 Ar^+ laser, made by Coherent Inc., which operates at a power of $\approx$ 300 mW on a single mode of the 514.5 nm line, and a A Coherent DPSS 532 nm solid state which works at 100 mW. The laser beam is split into a reference and an incident beam. The reference beam is used to keep the merit factor maximized of the FPI resonant cavities. The setup is optimized for both the 90° and the 180° scattering angle geometries. In Fig. 3.15, the continuous line after the beam splitter identifies the path of the 180° geometry, while the dotted

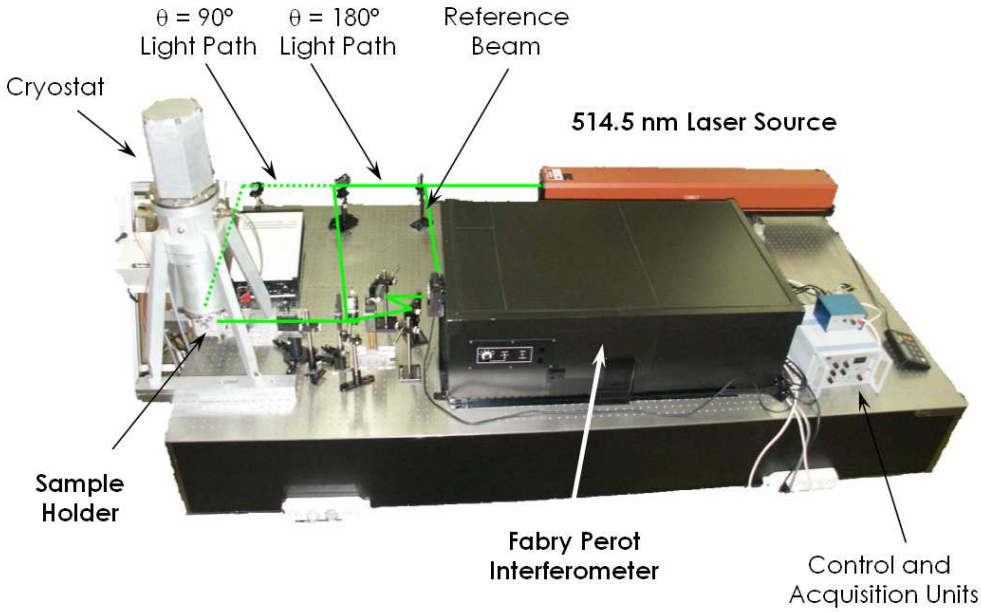


Figure 3.15: BLS setup of the Ghost Group in Perugia University. Description in the text

lines the one of the 90°. We have designed aluminum sample holders appositely to fit sample phials and thermalization systems. The sample holders have been realized by the departmental workshop of the university. We have used a Cryomech ST405 cryostat which can stabilize temperatures from 298 down to 30 K. The sample holder is kept in 10^{-7} mbars vacuum. An home-made feedback-equipped electric heater [121] is available for the higher temperatures up to 453 K. We have used the cryostat in the experiments on LiCl-6H_2O. As the cryostat vibrations may enhance the probability of water freezing, a vibration-free system has been appositely projected for water experiments, which is illustrated in figure 3.16. The sample holder is heated and cooled by a 51,4 W and 40x40x3,8 mm Melcor Peltier Cell, purchased by from RS Components. A copper plate connected to a thermal bath works as heat exchanger. To avoid thermal instability and condensation, the sample holder has been held into a glass bell jar, in 10^{-2} mbars static vacuum. The laser beam is vertically polarized. Vertical or horizontal polarization of the scattered radiation may be selected by a polaroid.

The scattered light is analyzed by a Sandercock-type (3+3)-pass Fabry-Perot interferometer charachterized by a finesse of about 100 and a contrast ratio greater than $5 \times 10^1 0$. [122]. At distances of 0.1 to 25 mm between the mirrors of the Fabry-Perot interferometer correspond investigated frequency domain, around the incident light, of some 100 GHz to 1 GHz. A photpmultiplier is used as a detector, which can work over 256, 512 or 1024 channels.

3.4 ID16 Beamline at the ESRF

The inelastic X-ray measurements have been performed at the ID16 beamline of the European Synchrotron Radiation Facility (ESRF) in Grenoble. This technique makes possible the study of phonon-like excitations at energy transfers between 1 and 500 meV and momentum transfers from 0.4 up to 160 nm^{-1}. Grossly speaking, this dynamical regions correspond to molecular correlation length of $2\pi/Q = 7$ nm to 20 $\AA$ and time evolutions of $h/\mathrm{E} = 10$ ps to 10 fs. A schematic lay-out of the beamline is given in Figure 3.17.

ID16 is an undulator beamline which avails of three insertion devices: two revolver undulators of 26 and 32 mm magnetic period and one of 35 mm magnetic period. The choice of the period is

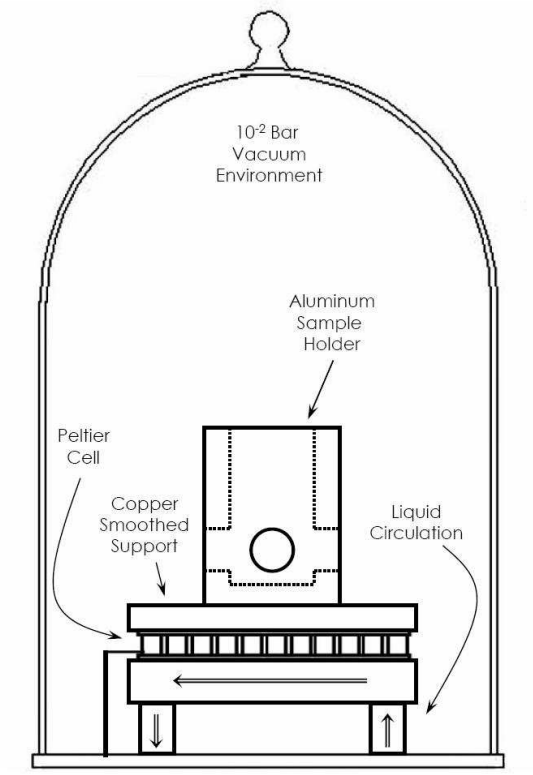


Figure 3.16: Vibrations-free sample holder environment utilized for BLS measurement on water samples.

the result of a compromise between the need of tunability within the working energy range between 5 and 25.7 KeV and flux maximization which is achieved by reducing the undulator period. The main monochromator consists of a flat perfect single crystal of silicon, operating at a Bragg angle of 89.98° and utilizing the Si(n,n,n,) reflection orders. This almost-backscattering geometry makes that the spectral angular acceptance is inclusive of the X-ray beam divergence. The choice for almost-backscattering configuration implies that the monochromator orientation is kept fixed and the energy scans are performed by varying the crystal lattice parameter through temperature control, which is performed with a precision of mK.

Two different spectrometers are operating at the ID16 beamline, that share the same sample goniometer and cannot hence be utilized simultaneously.

The horizontal spectrometer consists of a 7-meter arm which can rotate parallel to the horizontal plane and is equipped with five spherical crystal analysers. It can record spectra at five momentum transfers simultaneously. See Figure 3.18. By changing the arm angle, different series of five momentum transfers can be selected. This spectrometer is optimized for six preferred positions of the arm, which correspond to six (n,n,n)-reflections of the crystal analyzers, that is, to six values of n (n = 7,6,9,11,12,13). The horizontal spectrometer can select up to a maximum of ≈ 40 nm^{-1} momentum transfer. [1]

The analyzers operates through spherically shaped silicon crystals wich ensure an angular acceptance up to 4x10 mrad^2, found as a best-compromise between Q-resolution and signal maximization. As the realization of a spherical shape by mechanical bent would have introduced deformations, at the expenses of the intrinsic energy resolution, the analyzers have been constructed at the ESRF [124, 125] by gluing 12000 small crystals of 0.6x0.6x3 mm^3 size onto a spherical silicon

[1] The vertical spectrometer consists of a 3-meter arm rotating in the vertical plane and equipped with a single spherical crystal analyser. Due to the greated scattering agle analyzed, it and allows reaching much high momentum transfers with respect to the horizontal spectrometer. (up to 160 nm-1)

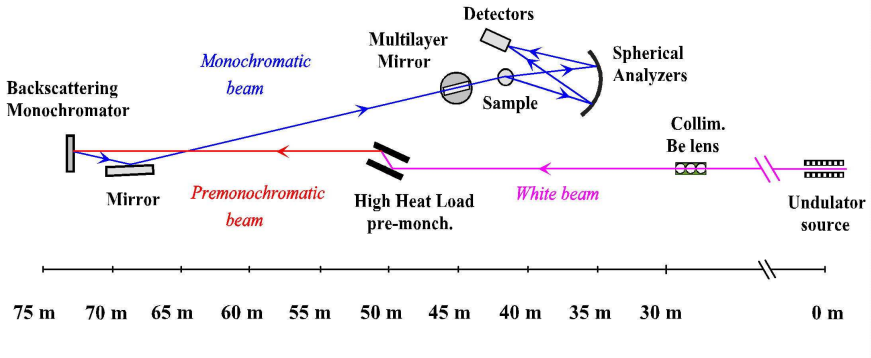


Figure 3.17: Density of water as a function of temperature

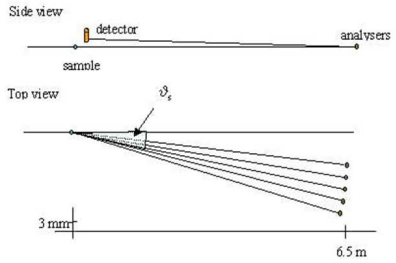


Figure 3.18: Side and top view of the horizontal spectrometer at ID16. The spectrometer collects the scattered radiation at five Qs simultaneously. The spectrometer is optimized for six preferred positions of the arm, which correspond to six (n,n,n)-reflections of the crystal analyzers, that is, to six values of n (n = 7,6,9,11,12,13) and can select up to a maximum momentum transfer of $\approx$ 40 nm^{-1}.

substrate whose radius fulfills the Rowland condition. This polygonal approximation yields an energy resolution of 0.9 meV utilizing the silicon (13,13,13) reflection order at 25704 eV.Temperature stability is extremely important for analyzer performance. A feedback temperature control sytstem ensures a maximum excursion of 6 10^{-4} °C over a 65 hours period.

The detector has been designed by Canberra-Eurisys for the IXS beamlines at the ESRF. The five individual silicon detectors as well as their pre-amplifiers are integrated on a single monolithic silicon chip, which is Peltier cooled in order to reduce the electronic background. Thanks to the increased thickness of the silicon detector with respect to the previous model, the signal losses even at the highest operating phonon energy of 25.7 keV remain modest (< 10 %).

Résumé du Chapitre 4

Ce chapitre présente les expériences réalisées sur l'eau pure liquide en phase normale et en phase surfondue, l'analyse des données et les résultats obtenus. Le facteur de structure dynamique a été mesuré, pour la première fois au moyen de la nouvelle technique de diffusion inélastique de l'ultraviolet (IUVS), à différents vecteurs de diffusion approchant $Q \approx 0.1$ nm^{-1} et jusqu'à 253 K. Dans l'étape de démarrage de l'instrument, la comparaison avec les techniques bien établies de BLS et d'IXS, qui donnent accès à des domaines complémentaires d'énergie et de vecteur de diffusion, a confirmé la faisabilité et la fiabilité des expériences d'IUVS. L'analyse simultanée des spectres de BLS et d'IUVS à l'aide d'un formalisme d'hydrodynamique généralisé à permis une caractérisation fine de la relaxation structurale. La comparaison du temps de relaxation et de l'exposant de d'étirement aux prédictions de la dynamique moléculaire confirme l'interprétation dynamique de la théorie MCT et plaide en faveur d'une origine dynamique de la divergence à T_S = 228 K, qui est voisine de la température critique to T_c de la théorie MCT. Ainsi un scénario de relaxation structurale est parfaitement capable de rendre compte de la dépendance en température et en longueur d'onde du phénomène de second son dans l'eau.

Chapter 4

Dynamics of supercooled Water in the mesoscopic region

Abstract

In this chapter the experiments performed on liquid and supercooled water, the elaborations and the results are reported and discussed. The dynamic structure factor of liquid and supercooled water has been measured by means of the novel synchrotron inelastic ultra violet scattering (IUVS) technique for the first time, at different momentum transfer values approaching $Q \approx 0.1$ nm^{-1} and down to 253 K. In the early stage of the IUVS beamline, the comparison to the well assessed techniques BLS and IXS, which explore complementary frequency-momentum domains, has confirmed the reliability and the feasibility of IUVS experiments. We have acquired BLS spectra which have been successfully utilized as a reference for the IUVS spectra. The simultaneous analysis of BLS and IUVS spectra in the framework of simple and generalized hydrodynamics[1] has allowed the characterization of the structural relaxation. The comparison of the relaxation time and stretching parameters to the predictions of molecular dynamics confirms the dynamic interpretation of MCT and plays in favor of the dynamical origin of the divergences in water at $T_S = 228$ K, which is quite close to T_c of MCT. The scenario of the temperature and momentum dependence of the speed of sound in water has allowed to assess undoubtedly the relaxational origin of the phenomenon of fast sound.

4.1 Introduction

The determination of $S(Q, \omega)$ has been performed for the experimental comparison to the molecular dynamics simulation of water, which agree with the expectations of MCT [11]. MCT attributes a dynamical origin to the apparent divergence of physical properties of water at $T_S \approx 228$ K. As pointed out in the previous chapters, explicit predictions about the structural relaxation have been formulated which may be directly compared to the results of inelastic scattering:

1. The structural relaxation is expected to decay like a stretched exponential function of time $\propto e^{-(t/\tau)^\beta}$. The equivalent function in the frequency domain is a Cole-Davidson function.

2. The temperature dependence of the structural relaxation time, τ, is predicted to follow a power law, $\tau(T) \propto (T - T_c)^{-\gamma}$. T_c is expected to be close to T_S and the power law exponent is predicted $\gamma \approx 2.7$.

3. The stretching exponent, β, is expected to be less then unity and to fall between 0.6 and 0.8, almost independently on temperature

[1] With the inclusion of the structural relaxation in the memory function. Some authors call this regime *molecular hydrodynamics*, while name generalized hydrodynamics the inclusion of the Q dependence.

Intrinsically related to the structural relaxation is the speed of sound. With respect to this, measuring the dynamics of supercooled water is expected to shed light on the dilemma about *fast sound*, as discussed in chapter 1, that is:

4. to discriminate between the hydrodynamic interpretation and the model of interaction-modes [92], which both are based on hypotheses in the dynamical region of the low Qs, where we can provide experimental evidences.

Last but not least a fifth challenge has been proposed:

5. to show the feasibility of the new IUVS technique and beamline and its and the uniqueness for the dynamics of supercooled water.

4.1.1 Remarkable Pre-requisites

In order to perform inelastic scattering experiments on supercooled water, three prerequisites are important: 1. to know the refractive index at the investigated Qs, 2. to know the UV absorption threshold which gives a limit to the minimum incident wavelength, 3. to prepare samples that reach the lowest supercooling possible.

1. Refractive index

The refractive index is fundamental to evaluate the momentum transfer Q, in the visible or ultraviolet range [2]:

$$Q = \frac{4\pi n(\lambda, T, \rho)}{\lambda} sin\frac{\theta}{2} \tag{4.1}$$

where λ is the incident wavelength, θ the scattering angle [3] and $n(\lambda, T, \rho)$ the refractive index, which depends on the incident wavelength, λ, the temperature and the density. It is very important that the determination of n is accurate as the dynamic structure factor and properties like the speed of sound and the sound absorption depend on Q.

The refractive index values of water have been obtained by applying the polynomial formula released by the International Association for the Properties of Water and Steam (IAPWS) [126], which interpolates a collection of values got from various experiments. In the table of Fig. 4.1 the IAPWS values of refractive index and momentum transfer are reported, concerned with all the incident wavelengths utilized in our experiments, at 335 K (maximum temperature investigated), 273 and 253 K (minimum temperature investigation). We have used values with an precision of $\pm 1 \times 10^{-4}$. The same values of table 4.1 are plotted in Fig. 4.2 as a function of incident λ. In figure 4.2 the neat increase in the refractive index marks the approach to an absorption threshold as a function of the decreasing wavelength.

2. Absorption threshold as a function of incident energy

The absorption spectrum of liquid water shows a steep rise in the range 6.5 to 8 eV [127]. Absorption becomes relevant against scattering at above 7.7 eV incident energy, that is, below 160 nm incident wavelength. At smaller wavelengths, the statistics of the collected spectra becomes dramatically poor.

3. Purity Standards for Water Samples

The heterogeneous nucleation is antagonist of water supercooling. In section **??** we have reported the results of decades of studies about the dependence of nucleation temperature on sample. In order to supercool water, the smallest possible samples of highest possible purity have to be used.

[2] or the X-rays, $n \approx 1$

[3] between the incident and the outgoing directions

λ [nm]	T [C]	T [K]	ρ [Kg/m^3]	n(λ, T, ρ)	θ [°]	Q [nm^{-1}]
184.52	61.85	335	982.233	1.4615	176	0.0995
194				1.4386	176	0.0931
200				1.4274	176	0.0896
226.5				1.3956	176	0.0774
244				1.3829	176	0.0712
514.5				1.3367	180	0.0327
514.5				*1.3367*	*90*	*0.0231*
532				1.3360	180	0.0316
532				*1.3360*	*90*	*0.0223*
184.52	0	273.15	999.843	1.4624	176	0.0995
194				1.4394	176	0.0932
200				1.4283	176	0.0897
226.5				1.3964	176	0.0774
244				1.3837	176	0.0712
514.5				1.3374	180	0.0327
514.5				*1.3374*	*90*	*0.0231*
532				1.3366	180	0.0316
532				*1.3366*	*90*	*0.0223*
184.52	-20	253.15	993.000	1.4632	176	0.0996
194				1.4402	176	0.0932
200				1.4291	176	0.0897
226.5				1.3972	176	0.0775
244				1.3845	176	0.0713
514.5				1.3382	180	0.0327
514.5				*1.3382*	*90*	*0.0231*
532				1.3374	180	0.0316
532				*1.3374*	*90*	*0.0223*

Figure 4.1: Refractive index values of water, $n(\lambda, T, \rho)$, at ambient pressure calculated by following the retrieval recipe given in [126], as a function of the incident wavelengths λ used in the present work and for three sampling values of temperature T (lowest and highest values investigated and 273 K). The density has been also taken into account [4]. The respective momentum transfer values, Q, have been calculated according to Eq. (4.1).

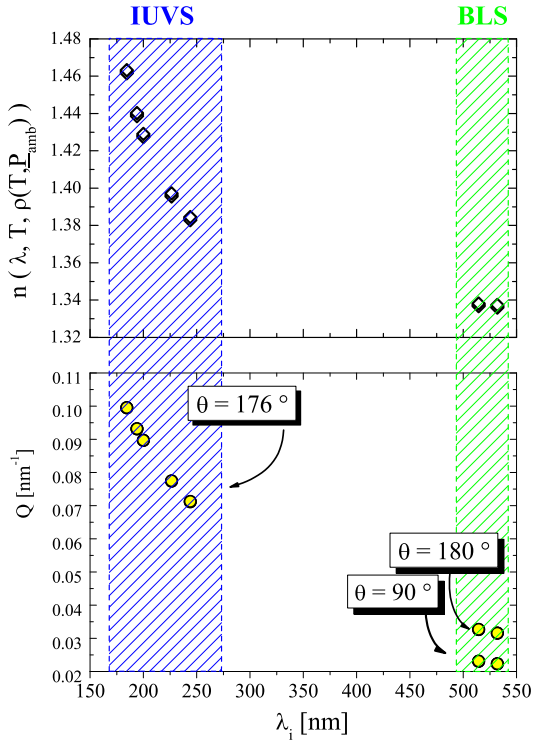


Figure 4.2: *Upper Panel:* Refractive index of water at ambient pressure, calculated following the recipe given in [126] and reported a function of incident wavelength. At each wavelength, points are inclusive of the temperature excursion. The preeminent dependence is, evidently, on lambda. The blue and green rectangles marked as "*IUVS*" and "*BLS*" individuate the regions competing to the techniques used. *Lower Panel:* Momentum transfer associated to the refractive index of upper panel, calculated through Eq. (4.1).

At present, the official classification of purity of water is tabulated by diverse organizations, including the American Society for Testing Materials (ASTM) [128], the National Committee for Clinical Laboratory Standards (NCCLS), the College of American Pathologists (CAP, the American Chemical Society (ACS) and the Europenan and US Pharmacopeia. Even though each organization utilizes its own denomination for the different types of water, it is generally agreed a classification into four classes, depending on electrical conductivity, resistivity and presence of seeding particles. In decreasing purity order, we can distinguish five classes, as represented in Table 4.3: Class I and class II water are used as reagents. Water of class III and IV is used for cleaning the glassery and as a starting reservoir to higher stages of purification. Beyond this classification, there is one more standard stated by the European and United States Pharmacopeias: the *Pharmacological Water*, which has the purity level of Ultrapure I class water, and, moreover, a very low concentration of endotoxins and pyrogens ($< 0{,}001$ EU/mL).

Class	Max. Conductivity (μS/cm @25 ° C)	Min. Resistivity (MΩ cm @25 ° C)	Silicates (mg/l)	Sodium (mg/l)	Chlorides (mg/l)	pH	TOC (ppb)
I - Ultrapure or Reagent	0.056	18.2	3	1	1	-	1 -15
II - Analytic	0.06 - 0.02	5 - 15	3	5	5	-	15 - 30
III - Laboratory	0.25	1 -4	500	10	10	-	30 - 50
IV - Laboratory	5	0.1 - 1	-	50	50	5 -8	-

Figure 4.3: Table of water classification released by ASTM [128].

4.1.2 An outline of the experiments

A summary of the most significative experiments is given in the table of Fig. 4.4. We have measured $S(Q,\omega)$ by means of IUVS between 343 and 253 K and at momentum transfer values around 0.1 nm^{-1}. The experiments have been performed at the 10.2 IUVS beamline at Elettra synchrotron. Q has been changed through the incident wavelength by changing the undulator gap. The scattering angle has been kept fixed at 176 °. We have also performed BLS measurements at $Q \approx 0.023$ and 0.033 nm^{-1}, to get a low frequency reference for the new IUVS beamline and to merge BLS and IUVS spectra and get information over a three decades frequency window, which has allowed the unambiguous extrapolation of the relaxation parameters. Since at low Qs ($Q \ll 1$ nm^{-1}) the structural relaxation does not depend on Q [16], the relaxation process is probed by IUVS and BLS is the same. BLS probes the relaxed regime and IUVS approaches the reversed relaxation time. BLS measurements have been performed down to 251 K. We have had care to replicate the temperatures investigated by IUVS in a wide set. We have collected spectra at both 90° scattering angle and backscattering, which correspond, respectively, to $Q \approx 0.023$ and 0.033 nm^{-1}.

In the grid of Fig. 4.4 the parameters relative to three best three series of IUVS spectra and two of BLS are summarized. Each series is characterized by the incident photon energy (wavelength) and the scattering angle. The *indicative* values of the refractive index $\langle n \rangle$ and of $\langle Q \rangle$ are reported [4]. Each series is identified by a symbol which will be used throughout all the graphs in this chapter. The energy resolution is also reported.

Source	E_i [eV]	λ_i [nm]	<n>	θ°	<Q [nm^{-1}]>	Resolution [μeV/GHz]	$T_{interval}$ [K]	Symbol	N° of temperatures
Synchrotron (UV)	6.72	184.52	1.462	176	0.099(5)	30 / 7.25	343 - 265		20
Synchrotron (UV)	6.20	200.00	1.428	176	0.089(6)	18 / 4.35	313 -269		9
Laser (UV)	5.08	244.00	1.383	176	0.071(2)	3.64 / 0.88	304 - 253		26
Laser (Ar+ GREEN)	2.41	514.50	1.337	180	0.032(7)	1.12 / 0.27	277 - 251		9
Laser (Ar+ GREEN)	2.41	514.50	1.337	90	0.023(0)	0.54 / 0.13	297 - 251		10

Figure 4.4: Outline of the experiments performed on water. Each row corresponds to a series of spectra, acquired at the conditions there specified. E_i is the incident energy, λ_i the incident wavelength, θ the scattering angle. The average refractive index $\langle n \rangle$ and momentum transfer $\langle Q \rangle$ are reported. The parentheses on the fourth digit mean an excursion of ± 1 with temperature. The energy resolution is shown, both in μeV and in GHz. The extremes of the temperature interval investigated are reported. The symbols will be used throughout the pictures of this chapter to indicate the respective series. In the last column, the number of temperatures at which spectra have been acquired is shown

We have also acquired eight triplets of isothermal spectra at three different Qs: at ≈ 0.023 and 0.032 nm^{-1} by BLS and at ≈ 0.1 nm^{-1} by IUVS. The eight temperatures investigated were between 298 and 253, every five degrees.

[4] The parentheses on the fourth digit mean an excursion of ± 1 with temperature. In the folloqing, when n or Q are mentioned, reference will be made to their indicative values. Data analysis has revealed to be sensitive to the fourth digit of $Q(\lambda, T, \rho)$. Nevertheless, throughout the text, the fourth digit if not needed will be omitted without any approximation.

4.2 IUVS: experiments and spectra

4.2.1 The samples

The purest samples, which offer the maximum degree of supercooling, is pharmacological water. Sample preparation was done under conditions of very high cleanliness, under the hook of the class-100 cleanroom of Lilith nanofabricarion beamline at Elettra Synchrotron.[5] Water was poured by means of sterilized syringes into never used QS-111 cuvettes[6]. Water from Galenica Senese froze at 253 K. Water from Nova Argentia and Reagent Water 99.99 % from Sigma-Aldrich froze between 263 and 261 K.

4.2.2 IUVS with synchrotron radiation; $Q = 0.099$ nm^{-1}

In figure 4.5 a selection is shown of one of the very first series of IUVS spectra of water, from the synchrotron source. The incident energy in this series was 6.72 eV, the momentum transfer $Q = 0.099$ nm^{-1}, the highest and the lowest temperatures 343 and 265 K. The central line is theoretically due to the Rayleigh peak [17] but Since in water $C_P/C_V \approx 1$, the intensity of this peak is very weak and what we measure is basically due to the reflection on the sample cell. The side peaks are the Stokes and the antiStokes Brillouin peaks [17]. Their broadening is evident as a function of decreasing temperature. In figure 4.5 the instrumental resolution function is compared to the antiStokes peak of the spectrum at 305 K. One can observe that the width of the peak is larger than the instrumental resolution. The broadening is a mark of the entrance, in the frequency window, of a relaxation process whose timescale is comparable to the reverse frequency of the probed modes. The FWHM of the resolution function is, in this series, 30 μeV.

4.2.3 IUVS with synchtrotron radiation; $Q = 0.089$ nm^{-1}

The subsequent experiments have been done at 6.2 eV incident energy and $Q \approx 0.089$ nm^{-1}, at optimized resolution (18 μeV) and increased statistics. At this energy the absorption of water is already much reduced. In Fig. 4.6, the full-chip CCD image is displayed of the acquisition made at 298 K. The region of interest (ROI) where both the spectrum and the background have been acquired, is evidenced as a green rectangle. The raw spectrum and background are shown in the upper panel of Fig. 4.7, in terms of CCD counts as a function as a function of pixels. The acquisition time was 30 minutes for both the contributions. The background has been acquired at the monochromator exit slit, with beam on and sample chamber excluded by the shutter. It is due to spurious reflections onto optical elements and to CCD electrical noise. The motors of the gratings have been turned off, during the measurements, as their noise also affects the spectra. In the lower panel of Fig. 4.7 the same spectrum is reported after background subtraction.

The complete series at $Q = 0.089$ nm^{-1} is shown in Fig. 4.8.The increase of quality with respect to the first series is evident. The broadening of Brillouin peaks is appreciable as a function of the decreasing temperature. The linewidth of side peaks is not resolution limited.

[5] In a class-100 cleanroom less than 100 particles whose diameter is greater than 0.5 μm are present in a cubic foot of air.

[6] As we tested that commercial glassy phials of pharmacological water can be supercooled at least down to 253 K, twe contacted pharmacological companies to ask for a special production in sealed in quartz SUPRASIL. All the companies, though, could only propose to us exaggerate quantities at prohibitive costs.

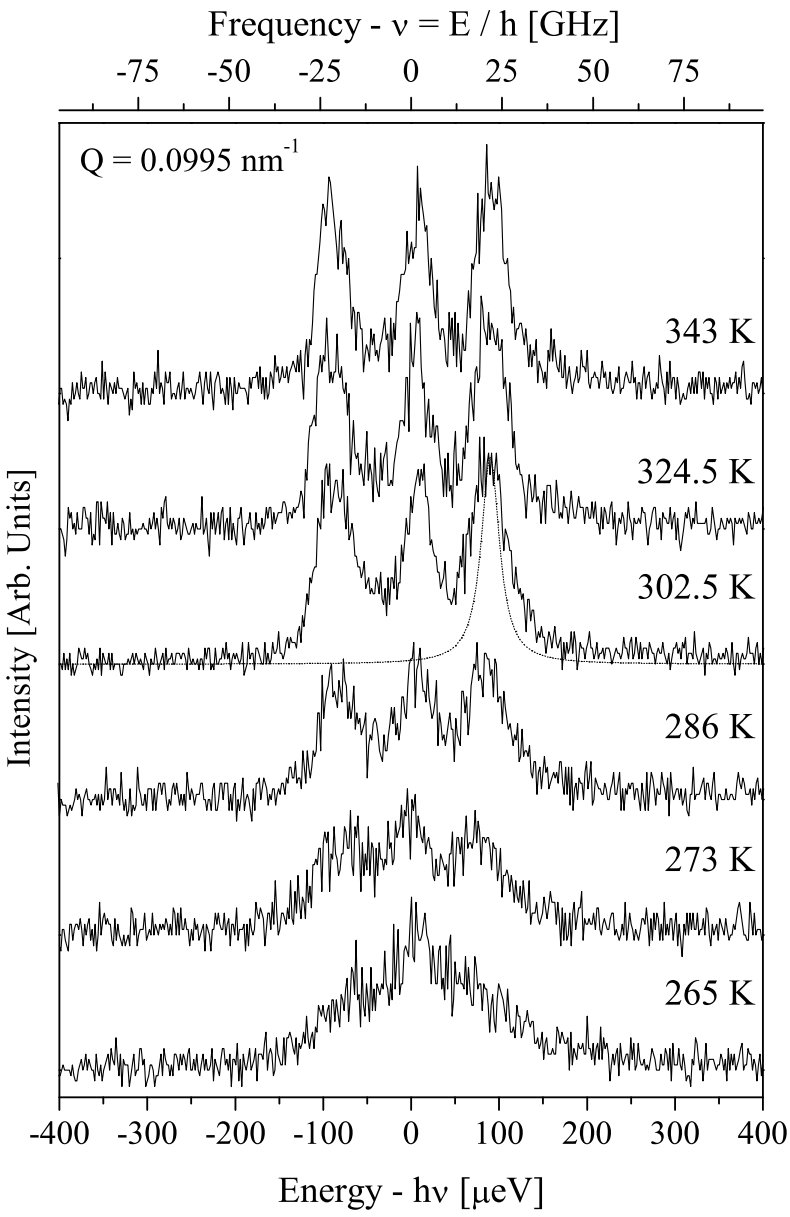


Figure 4.5: Spectra among first inelastic UV scattering spectra of liquid and supercooled water, taken at 6.72 eV incident photon energy and 0.099(5) nm^{-1} momentum transfer, at the indicated temperatures, including both the highest and the lowest limits reached in the experiments. The overall instrumental resolution function is superimposed on the spectrum at 302.5 K, shifted and aligned with the Antitokes Brillouin line.

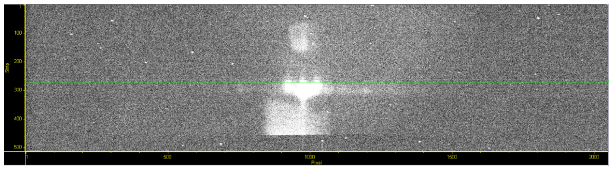


Figure 4.6: CCD full image of the IUVS spectrum of water at 298 K and 6.2 eV incident radiation. The vertical axis is proportional to the space, in the sample, crossed by incident beam. The horizontal dimension is proportional to the energy dispersion. The intense spot are due to reflections on the cuvette surfaces.

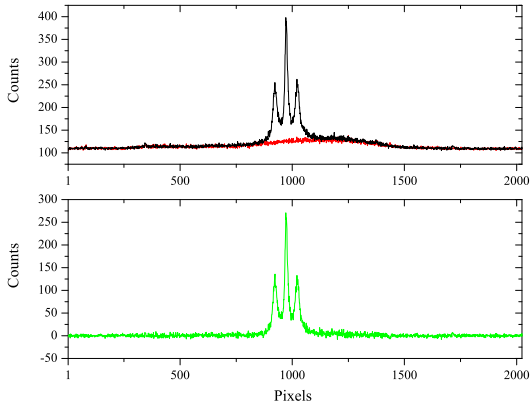


Figure 4.7: *Upper panel:* IUVS spectrum of water at 298 K and $Q = 0.089$ nm^{-1} acquired in a 30 minutes binning acquisition of the ROI selected in 4.6. The background, got in the same ROI, is also shown in red. *Lower panel:* Same spectrum after background subtraction.

4.2.4 IUVS with laser; $Q = 0.071$ nm^{-1}

A series of spectra by the $\lambda = 244$ nm UV laser source completes the scenario of IUVS experiments on water. In figure 4.9 a selection of spectra is shown. This series includes lowest supercooling temperature we could reach (253 K). The incident energy is more distant from the absorbance threshold of water and also the transmission coefficient of the cuvette quartz is higher. Moreover the photon flux is 100 times higher than for the synchrotron source. The signal to noise ratio of these spectra is very high. The energy resolution is also better, 3.6 μ eV. The broadening of Brillouin peaks shows its greatest entity in this series, which marks the closest approach ever reached to the relaxation of supercooled water.

4.2.5 About the energy resolution

The resolution function of IUVS beamline is an Airy function, whose first harmonic approximation is a Lorentzian function. To measure it, one can focalize the beam on a copper surface and acquire the quasi-Lorentzian spectrum from copper surface reflection. Another method is to extract the resolution directly from the central peak of a spectrum at a temperature high enough that the structural relaxation is far. Indeed this is possible because Rayleigh peak of water is weak and the central peak comes from the reflection on the cell surface.[7] Both procedures have been adopted and they have shown to be equally reliable to data analysis.

[7] It is common practice in inelastic X-ray scattering to characterize the contribution of the empty cell so that it can be subracted. In IUVS and BLS this is not possible as the different refractive index makes such a comparison not possible.

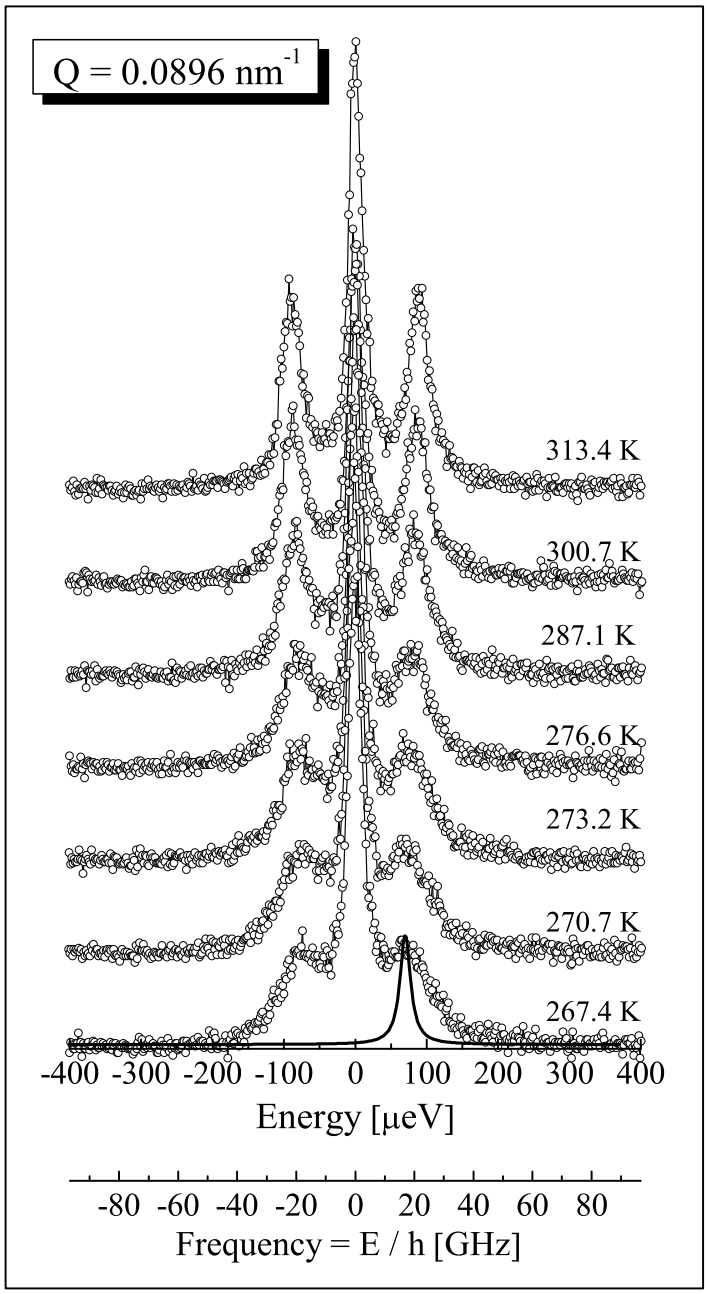


Figure 4.8: Series of IUVS spectra of water acquired at 6.2 eV incident energy and $Q = 0.089$ nm^{-1}. The temperature has been varied between 313 and 267 K. The resolution function is also shown as a bold continuous line.

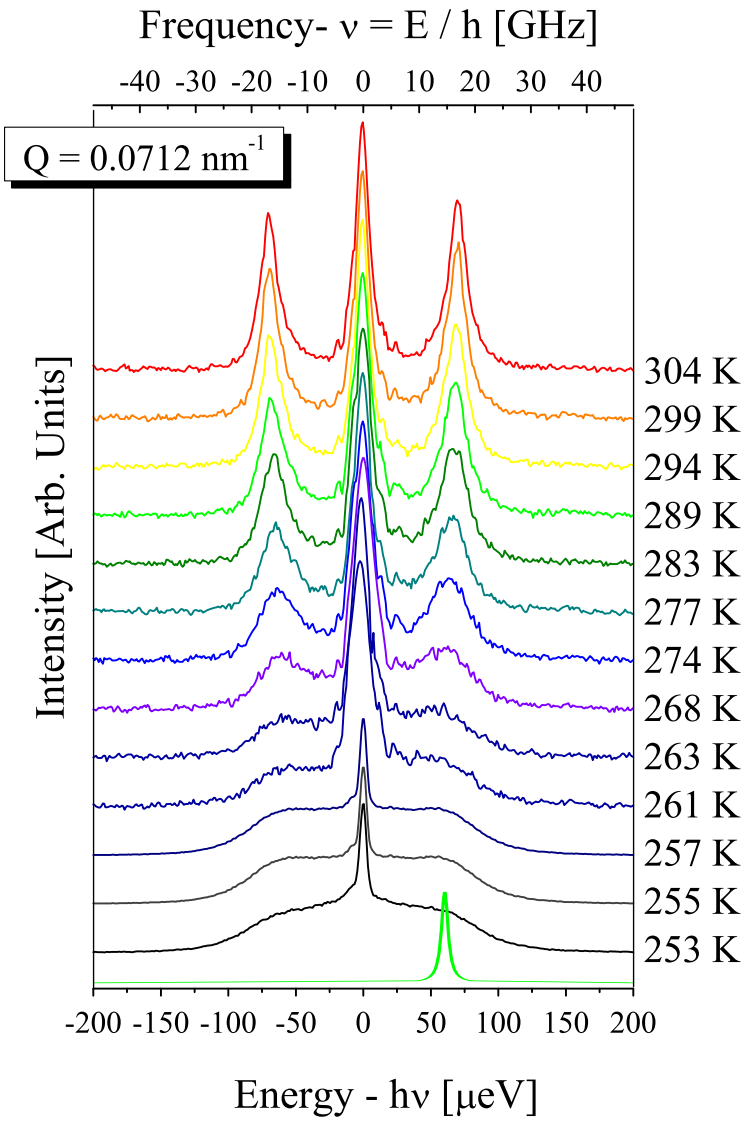


Figure 4.9: IUVS spectra of water by UV laser source. Aquisition temperature has been varied from 304 to 253 K and it is specified on the side. The incident energy of the UV laser is 5.081 eV. $Q \approx 0.071$ nm^{-1}. $T = 253$ K is, actually, the lowest supercooling limit of water that we could reach in IUVS experiments. It is evident the neat broadening of Brillouin peaks and the shift of the peak position on cooling the system. The peak position themselves are smaller, compared to those found in spectra acquired by synchrotron. The resolution function, whose FWHM is 3.6 μ eV, is also shown for comparison, as a small peak below antiStokes side.

4.2.6 Attempts with quartz capyllaries

To reach a deeper supercooling we have tried to reduce the volume of water samples by using quartz capillaries got from GLAS Technik & Konstruktion [129]. We have used 1 and 0.7 mm diameter capillaries, 80 mm long, with 0.01 mm wall thickness. We have been limited in the minimum diameter by the beam size (150 microns wide spot in IUVS and 30 microns in BLS) and by the stray light from the capillary walls, which becomes dominant when the volume is too small. The capillaries were filled by following the same procedure than for cuvettes, and sealed by rubber or by hydrogen flame, firing far from water and very quickly. To avoid dominant stray light from the capillary wall as well as to guarantee heat conduction, we have immersed the capillary filled by water in a quartz cuvette filled by glycerol, which was a reflective index intermediate between water and quartz.

An example of the acquired spectra is given in figure 4.10. Two spectra are shown, taken at $Q = 0.072$ nm^{-1}. The beam source is the UV laser. The Brillouin peaks at lower energy belong to water, those at higher energy to glycerol. Decreasing the temperature, the peaks of water shifts towards lower energy and start broadening, while the peaks of glycerol move in the opposite direction. We had to recognize that the use of capillaries *(i)* did not result in any gain of freezing point, with respect to cuvettes, as the freezing temperature was 263 K for 1 mm diameter tubes and 259 K for 0.7 mm diameter, and *(ii)* implies that two systems have to be studied, as the spectra require the careful subtraction of glycerol contribution.

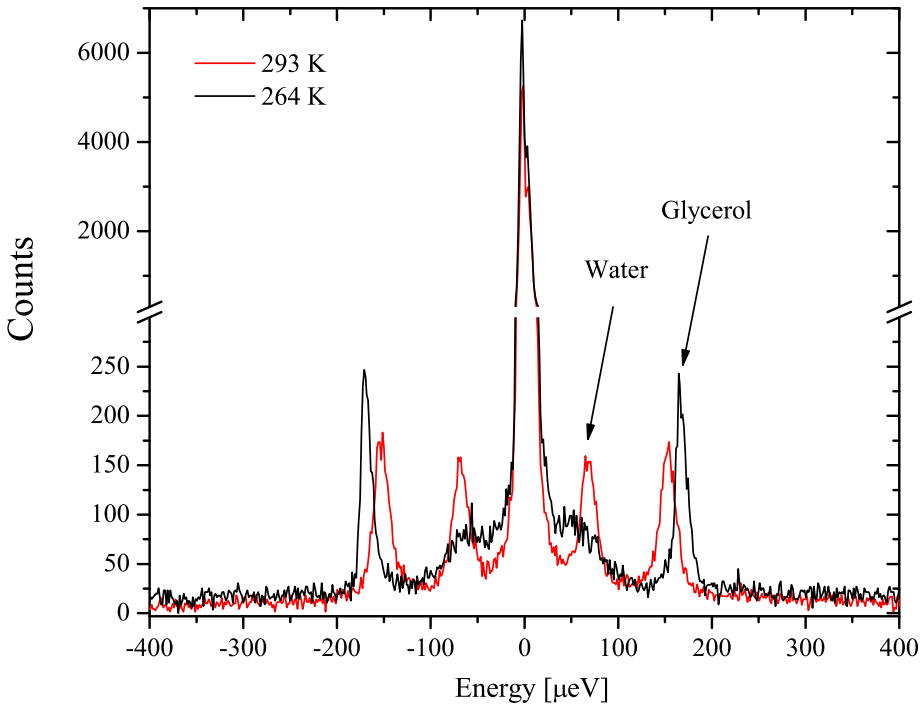


Figure 4.10: Example of IUVS spectra acquired by sample of water in 1 mm capillary immersed in glycerol environment. Incident energy was 5.08 eV and $Q \approx 0.071$ nm^{-1}. Phonon peak of both substances are evident in the spectra, as well as the inverse shifting trend as a function of decreasing temperature.

4.3 BLS experiments and spectra

The Brillouin light scattering measurements have been performed in the laboratory of the Group of High resolution Optical Spectroscopy and related Techniques (GHOST) in Physics Department of Perugia University.

4.3.1 Samples

For visible light we could use normal glass sample holders. We purchased sealed cylindrical phials of injectable water, got in pharmacy. We have tested the freezing of a number of phials got from different companies, before use. The most satisfactorily have been those by Galenica Senese [130], which have reached the supercooling limit of 251 K, low enough to our purpose of partnering the IUVS spectra. It is notworthy that the supercooling gain offered by the sealed phials is only 2 K with respect to the home made sample preparation of IUVS samples. The roundness of the phials does not affect particularly the experiments in the backscattering geometry. More care had to be taken in the alignment of the sample in the 90° geometry. In this case the scattering angle has been carefully controlled for refractive deviations by performing measurements at around 290 -300 K and checking the coincidence of the apparent sound velocity obtained by the BLS spectra to the adiabatic sound velocity measured by ultrasonics technique.

4.3.2 BLS Spectra

In backscattering configuration ($Q \approx 0.032nm$), series of I_{VV} and I_{VH} have been acquired. The isotropic spectrum, $I_{\rho\rho}$ can be calculated according to the relationship

$$I_{\rho\rho}(Q,\omega) = I_{VV}(Q,\omega) - \mathrm{r}^{-1} I_{VH}(\omega) \tag{4.2}$$

where r^{-1} is the normalizing factor. We have spanned a total frequency window of 800 GHz by investigating three partially overlapping free spectral ranges (FSR). We have used three mirror distances of the FPI interferometer, 7, 2 and 0.5 mm, which approximately correspond to FSR of 11, 100 and 800 GHz, respectively. The 11 GHz FSR avails of better resolution (130 GHz) and is ideal for sharp detection of acoustic peaks. In the 800 GHz FSR we have measured the high frequency tail of the spectrum. The resolution (270 GHz) is not high enough to measure the phonon peaks correctly in this case. An intermediate FSR is needed to append the extremes with continuity.

In figure 4.11 the three I_{VV} and I_{VH} spectra of water acquired at 273 K are shown, limitedly to the positive frequencies.

The central line is not shown. The spectra have been purged from the spurious peaks: the ghost peaks of the FPI cavities have been removed. The acoustic peak of the phial glass, located at about 30 GHz, has also been subtracted from the I_{VV} spectrum. An VV contribution to I_{VH}, due to not 100% efficiency of the polarizer, has been subtracted in correspondence of the acoustic peak. These corrections, applied to all our measurements, result in very accurate spectra. Before appending the three contributions, the dark count has been subtracted from each part, normalized to number of counts [8]. The composition of the spectra in figure 4.11 relies on the fact that the $I_{\rho\rho}$ spectrum of water tends to zero at high frequencies (for BLS, at frequencies higher than 40 GHz). This implies that the high frequency tails of the VV and VH spectra will coincide. The spectra have thus been composed through an initial multiplicative rescaling which has lead the long frequency tails of VV an VH over each other. The other contribution have followed by continuity.

It is evident in Figure 4.11 that the VH contribution is negligible with respect to the VV scattering. We have found that this remains the same at all the investigated temperatures (see Fig. 4.17).The light scattering spectrum of water is purely isotropic.

[8] The dark count, the photomultiplier photon counts with no laser light sent to the in-pinhole, was 0.00181 counts/scan.

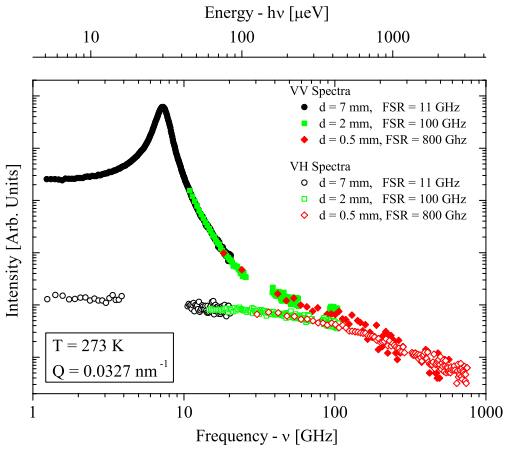


Figure 4.11: I_{VV} and I_{VH} spectra of water at 273 K and $Q = 0.032$ nm^{-1}. The contributions at three FSR's are indicated in the legend, together with the mirror distances used. The spectra have been purged by spurious non-sample contributions and have been appended over each other, after proper background subtraction.

The $I_{\rho\rho}$ spectrum at 273 K and $Q = 0.032$ nm^{-1}, calculated through Eq. (4.2), is shown in figure 4.12. Other BLS spectra are reported in the following sections, together with IUVS measurements.

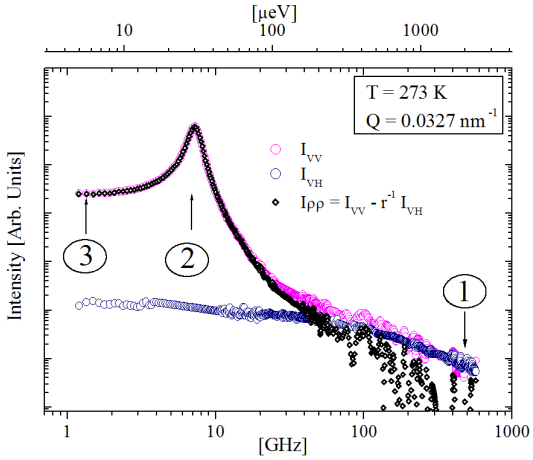


Figure 4.12: The antiStokes peak of the isotropic spectrum of water at 273 K and $Q = 0.032$ nm^{-1}, calculated according to Eq. (4.2). To our purposes, $I_{\rho\rho}$ coincides with I_{VV}. Regions 1, 2, 3 identify, respectively, frequency domains much higher than, around and much lower than the acoustic peak position.

4.4 Data analysis

We have analyzed the BLS and IUVS spectra in the framework of generalized hydrodynamics. As the scattering from water is mainly isotropic, the measured intensity is proportional to $S(Q,\omega)$ ([17], see Chapter 2), according to Eq. (2.55):

$$I_E(\mathbf{Q},\omega,R) = \frac{I_0 k_f^4}{16\pi^2 R^2 \epsilon_0^2}(\mathbf{n}_i \cdot \mathbf{n}_f)^2 \left(\frac{\partial\varepsilon}{\partial\rho}\right)^2_{T_0} S_{\rho\rho}(\mathbf{Q},\omega) \tag{4.3}$$

The derivation of the interpretative line shape for the $I_{\rho\rho}(Q,\omega)$ spectrum in the framework of hydrodynamic [16, 17, 102] has been discussed in Chapter 2. The *full spectrum* lineshape, whose frequency extremes being virtually $\pm\infty$ and corresponding in practice to the extinction of $I_{\rho\rho}(Q,\omega)$, is formulated in a general shape, inclusive of possibly occurring relaxation process:

$$I\rho\rho(Q,\omega) = \frac{I_0}{\omega}\frac{M''(\omega)}{[\omega^2\rho/Q^2 - M'(\omega)]^2 + [M''(\omega)]^2} \tag{4.4}$$

where $M^*(\omega) = M'(\omega) + iM''(\omega)$ is the generalized longitudinal acoustic modulus. Its real part $M'(\omega)$ is related to the speed of sound while the imaginary part $M''(\omega)$ is related to sound absorption. The occurrence of relaxation processes is taken into account in the frequency dependence of M^*. [9]

An approximate and very informative preliminary analysis has been performed before dealing with the full spectrum, limitedly within each of the three frequency regions identified in figure 4.12: (1) frequency domains much higher than, (2) around the and (3) much lower than the position of the longitudinal acoustic peak, ω_{LA}.

4.4.1 Region 1. - $\omega \gg \omega_{LA}$: the high frequency tail of the spectrum

We have discussed this region in section 4.3.2: at high frequency the isotropic spectrum decays rapidly to zero. That makes it possible the multiplicative rescale of the high frequency tails of I_{VV} and I_{VH}, to determine $I_{\rho\rho}$

4.4.2 Region 2. - $\omega \approx \omega_{LA}$: classical acoustic analysis with the DHO model

At frequencies close to the LA peak, the spectrum of Eq. (4.4) can be approximated to

$$I_{LA}(Q,\omega) = I^0_{LA}\frac{\Gamma_{LA}\omega^2_{LA}}{[\omega^2_{LA} - \omega^2]^2 + [\omega\Gamma_{LA}]^2} \tag{4.5}$$

where $\omega = 2\pi\nu$ is the pulsation and ω_{LA} and Γ_{LA} approximately correspond to the frequency position and to the full width at half maximum (FWHM) of LA peaks. ω_{LA} and Γ_{LA} are related to the elastic modulus by the equations

$$M'(\omega_{LA}) = \rho C(Q,T) = \rho\omega^2_{LA}/Q^2 \tag{4.6}$$

$$M''(\omega_{LA}) + \omega_{LA}\eta_L = \rho\omega_{LA}\Gamma_{LA}/Q^2 \tag{4.7}$$

Moreover these parameters are related to the sound velocity $C(Q,T)$ and to the longitudinal kinematic viscosity $\nu_L(Q,T)$ by the relationships:

[9] We recall that the generalization of hydrodynamics through the elastic moduli formalism is equivalent to memory functions approach. In the early stage of this work we have adopted both formalisms, to check the continuity to BLS and IXS techniques which by tradition avail of different formalisms. In this manuscript the analysis is reported in terms of elastic moduli only, for reasons of clarity.

$$C(Q,T) = \frac{\omega_{LA}(Q,T)}{Q^2} \tag{4.8}$$

and

$$\nu_L(Q,T) = \frac{\eta_L(Q,T)}{\rho(T)} = \frac{\Gamma_{LA}(Q,T)}{2\pi Q^2} \tag{4.9}$$

The DHO analysis is in principle very simple and gives back an immediate snapshot of the temperature dependence of sound velocity and of longitudinal kinematic viscosity, which, can be compared with the results of ultrasound spectroscopies limitedly to the relaxed regime. ω_{LA} and Γ_{LA}.[10]

Least chi-squares Levemberg-Marquardt minimization of DHO model has been performed around the LA peaks of all the spectra acquired by IUVS and BLS. As a results of this analysis we have obtained $\omega_{LA}(Q,T)$ and $\Gamma_{LA}(Q,T)$. The fitting lineshape is the convolution of Eq. (4.5 with the proper instrumental resolution $R(\omega)$ funciton, plus a lorentzian term almost constant, of width Γ_c, which takes the central peak into account:

$$I_{fit}(Q,\omega) = I_{LA}(Q,\omega) \bigotimes R(\omega) + \frac{A}{\omega_c + \Gamma_c^2} \tag{4.10}$$

In figure 4.13 a selection of IUVS spectra acquired at $Q = 0.071$ nm^{-1} is shown, with fitting lines 4.10 superimposed. DHO model is a good approximation to IUVS spectra down to about 260 K. At lower temperatures it starts failing, as one can appreciate in the bottom right panel, where the extra broadening of the peaks cannot be accounted for. This gives an evidence of the expected failure of simple hydrodynamics of supercooled water at $Q \approx 0.1$ nm^{-1}. In the following sections the spectra will be completely accounted for in a generalized hydrodynamic approach which takes the structural relaxation of water into account.

In Figure 4.14 the BLS and IUVS spectra of supercooled water at the lowest temperature investigated by these techniques ($\approx$ 250 K), are compared, with DHO fit superimposed. The picture shows that simple hydrodynamics still holds for supercooled water in the BLS regime, $Q = 0.0326$ nm^{-1}, but needs to be be generalized at $Q \approx 1$ nm^{-1}. This confirms the expected sensitivity of inelastic ultra violet scattering to the relaxational dynamics of supercooled water.

Where the DHO approximation is no longer valid, it is still possible to measure accurately the peak positions ω_{LA} through the density current [16]:

$$J_{\rho\rho}(Q,\omega) = \frac{\omega}{Q^2} I_{\rho\rho}(Q,\omega) \tag{4.11}$$

The maximum of $J_{\rho\rho}(Q,\omega)$ corresponds to $\omega_{LA}(Q,T)$ [16].

The best-fitting parameters, $\omega_{LA}(Q,T)$ and $\Gamma_{LA}(Q,T)$, are illustrated in Fig. 4.15. The apparent speed of sound $C(T)$ and the longitudinal kinematic viscosity $\nu_L(T)$ have been calculated by ω_{LA} and Γ_{LA} through Eqs. 4.8 and 4.9. The results are reported in figures 4.33 and 4.31, respectively.

[10] It is worth noting that this kind of analysis is being developed since the very first experiments of light scattering in the 60's, which did not still avail of tandem interferometers. The frequency position and the width of LA peaks feel negligibly the distortion due to overlapping of different interferometers orders.

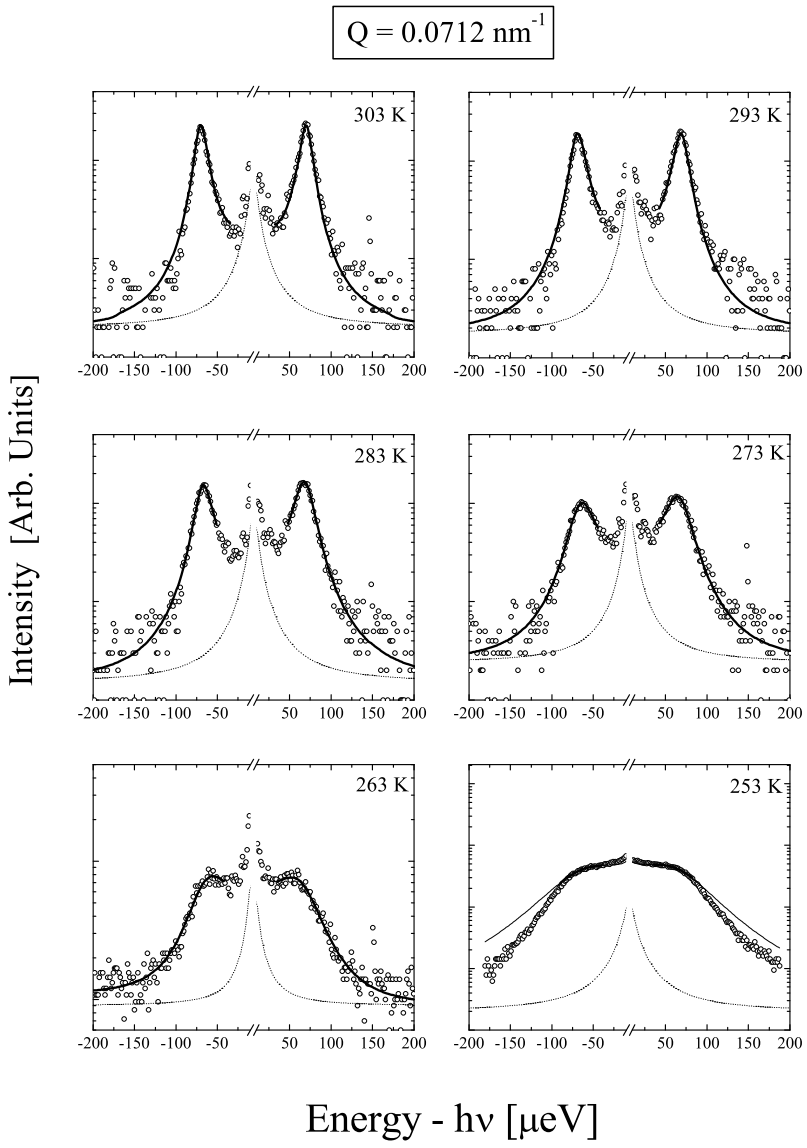


Figure 4.13: IUVS spectra (dots) at $Q = 0.071$ nm^{-1} and temperatures between 303 and 253 K, from upper left to bottom right. Fitting lines by Eq. (4.10) are superimposed (solid lines). The contribution of the central peak is shown as dash line). DHO fit, performed around a narrow frequency region of the acoustic peak, actually describe well the spectra to a wider region. Below $\approx$ 260 K DHO approximation starts failing. In the bottom right panel the failure is evident.

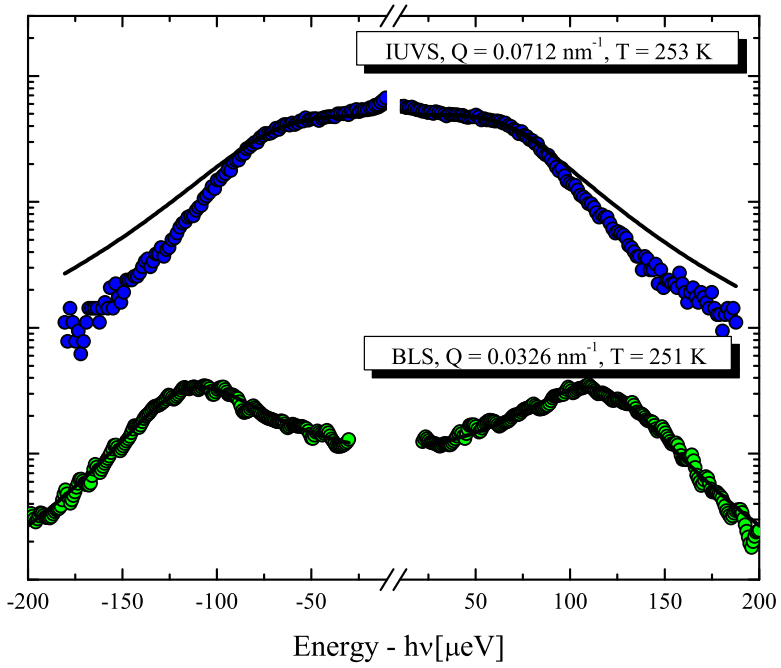


Figure 4.14: IUVS (blue dots) and BLS (green dots) spectra at the lowest temperatures reached by the respective experiments. The solid lines are the best-fit of Eq.(4.10) around the acoustic peaks, prolonged to all the range. This picture shows that simple hydrodynamics still holds for supercooled water at $\approx 250K$ and $Q = 0.0326\ nm^{-1}$ but it needs to be generalized at the same temperatures and $Q \approx 1\ nm^{-1}$, in the dynamic regime spanned by IUVS, to take the relaxational processes into account. Indeed, the deviation from the DHO approximation in IUVS spectra, on cooling the system, mirrors the occurrence of the structural relaxation which introduces new spectral components in the experimental window. The process is characterized by a relaxation time which matches the reciprocal angular frequency of the acoustic modes probed by IUVS ($\omega\tau \approx 1$). At the same temperature, the relaxation is too fast with respect to the modes probed by BLS. In the light scattering regime at 251 K, the dynamics of water is completely relaxed.

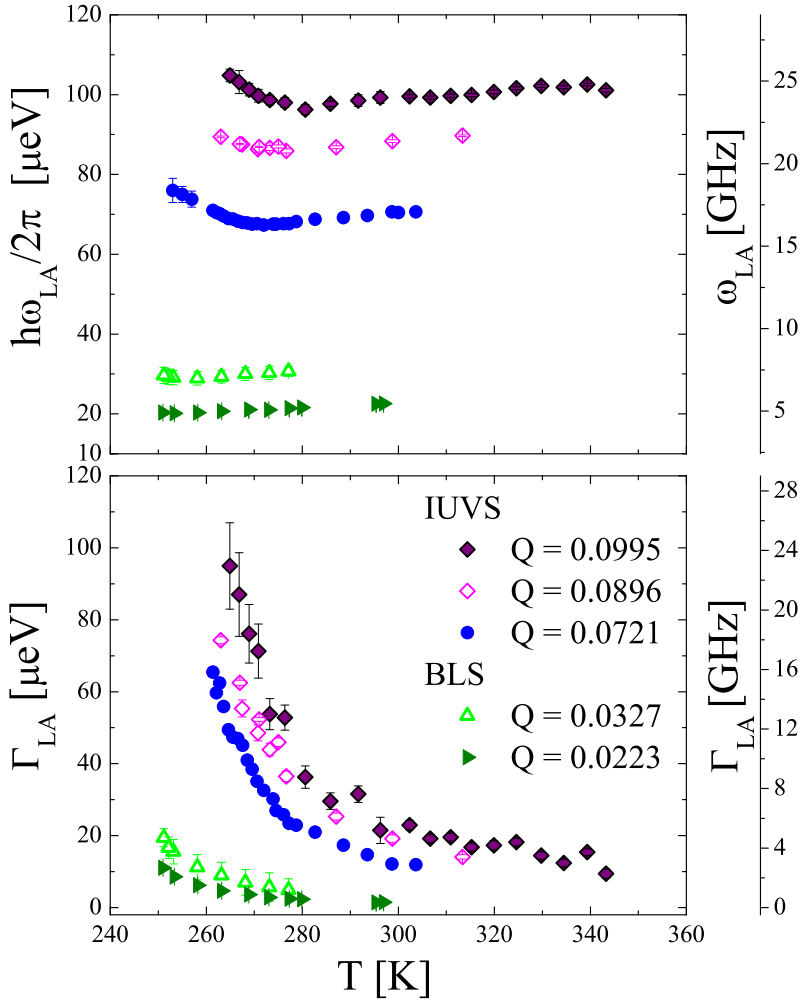


Figure 4.15: Fitting parameters $\omega_{LA}(T)$ (upper panel) and $\Gamma_{LA}(T)$ obtained from DHO analysis through Eq. (4.10). Each color corresponds to a series of experiment as specified in Table 4.4, which identify the Q-th longitudinal acoustic mode. Each point corresponds to a spectrum. Momentum transfer values are specified in figure's legend.

4.4.3 Region 3. - $\omega \ll \omega_{LA}$: accurate joining of IUVS and BLS spectra

In the regime ($Q \ll 1$ nm^{-1}), the longitudinal elastic modulus $M^*(\omega)$ does not depend on Q [16]. As the modulus is expected to be extended over some decades of frequency, a very informative procedure which allows to characterize $M^*(\omega)$ consists in joining together BLS and IUVS spectra acquired at the same temperature. This procedure extends to more than 3 decades the frequency window over which $M^*(\omega)$ can be investigated. We have acquired eight triplets of isothermal spectra at three different Q: $Q_1 \approx 0.023$ and $Q_2 \approx 0.032$ nm^{-1} by BLS and at $Q_3 \approx 0.1$ nm^{-1}, by IUVS. The eight temperatures investigated have been between 298 and 253, every five degrees. The isothermal spectra have been joined each to the others through the low frequency limit ($\omega \ll \omega_{LA}$) of the complex susceptibility $\chi''(\omega)$, which is related to the isotropic spectrum through the Fluctuation-Dissipation theorem [100]:

$$\chi''(Q,\omega) = I_0 \omega I_{\rho\rho}(Q,\omega) \tag{4.12}$$

In the low frequency limit $\chi''(\omega)$ does not depend on Q. This can be immediately realized by leading Eq. (4.12) to the low frequencies and provided that the contribution $\omega\eta_l$ of the longitudinal viscosity η_l contributes negligibly to $M^{''}(\omega)$, as in the case of water. We obtain:

$$\underset{\omega \ll \omega_{LA}}{\chi''(Q,\omega)} = \underset{\omega \ll \omega_{LA}}{I_0 \omega I_{\rho\rho}(Q,\omega)} = \frac{M''(\omega)}{M'(\omega)^2 + M''(\omega)^2} \tag{4.13}$$

which implies that, at a given temperature, the products $\omega I_{\rho\rho}(Q,\omega)$ at different Q must coincide. We have purged the spectra of the stray light which affects the central line. To do that we have simulated the Rayleigh peak, and quantified the remaining part. It was not surprising that the Rayleigh peak is negligible, since $\gamma = 1$ (See Section**??**). For every temperature three $\chi''_{Q_i}(\omega)$ have been calculated, for i = 1,2,3. The low frequency tails of $\chi''_{Q_1}(\omega)$, $\chi''_{Q_3}(\omega)$, $\chi''_{Q_3}(\omega)$ have been multiplied arbitrarily until coincidence. In figure 4.16 the susceptibilities at 253 K and $Q = 0.0712$, 0.0327 and 0,0230 nm^{-1} are shown, after the rescale.

The re-multiplication of rescaled $\chi''(Q,\omega)$ by ω gives back triplets of isothermal isotropic spectra, cleaned from stray light and set in opportune relative intensity. The antiStokes peaks of a selection of triplets is reproduced in figure 4.17. Our measurements are informative from 300 MHz to 300 GHz.

The spectra of each triplet have been analyzed simultaneously through a full-spectrum function in the framework of generalized hydrodynamics. This is discussed in the next section.

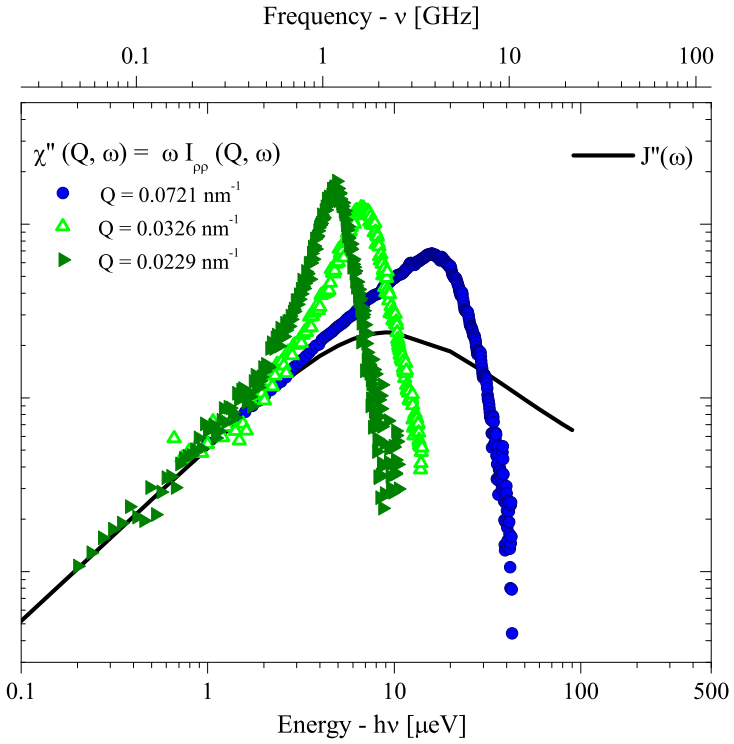


Figure 4.16: Imaginary part of susceptibility $\chi''(\omega)$ at $T = 253$ K and at Q's indicated in the legend. $\chi''(\omega)$ has been calculated from the corresponding measured isotropic spectra according to the Fluctuation Dissipation theorem, Eq. (4.12). By multiplicative rescale, the low frequency tails of χ'' have been lead to coincidence, as in the low frequency regime χ'' does not depend on Q. For sake of completeness, the imaginary part, $J''(\omega)$, of the complex longitudinal compliance $J^*(\omega) = 1/M^*(\omega)$ is also shown. In the low frequency limit ($\omega \ll \omega_{LA}$) χ'' and J'' coincide. This can be realized by substituting J^* in Eq. (4.13). We obtain that at low frequency $\underset{\omega \ll \omega_{LA}}{\chi''(Q,\omega)} = \underset{\omega \ll \omega_{LA}}{J''(\omega)}$. We outline that $J''(\omega)$ has been calculated *after* the full-spectrum analysis (discussed in the next section)

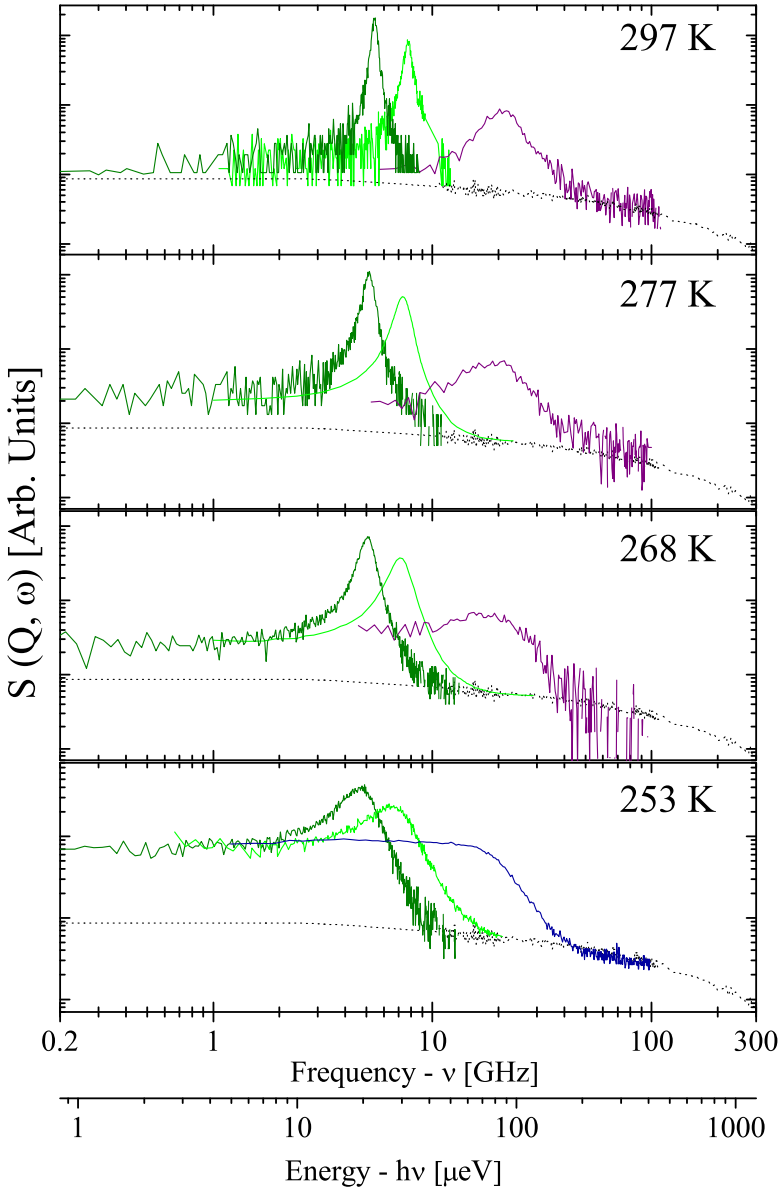


Figure 4.17: antiStokes side of I_{VV} and I_{VH} spectra at 297, 277, 268, and 253 K and Q = 0,0230, 0.0327, 0.0896 nm^{-1} (except for T = 253 K, where the Q = 0.0712 nm^{-1} spectrum is shown), in both the VV (solid lines) and VH (dotted lines) polarization configurations. Spectra in each triplet have been purged from stray light contribution and rescaled over each other, as described in the text.

4.4.4 Full-spectrum joint analysis

When relaxations become prominent in the Rayleygh-Brillouin spectrum, there is a progressive but continuous detachment from the pure hydrodynamic regime which can be formally generalized by the use of memory function [16], or equivalently including the frequency dependence in the longitudinal elastic modulus [101], which both include the effects of the relaxations, that is processes through which the energy of the acoustic modes is dissipated. The elastic modulus has to to be chosen properly, ad-hoc for the processes occurring in the dynamical window investigated. In our spectral window the dynamics of water is mainly affected by three kind of dissipative processes [19]: (1) the instantaneous processes, (2)the thermal relaxation and (3) the structural relaxation. The analysis with the full-spectrum lineshape model of Eq.(4.4) has been performed, first of all, of the triplets of spectra acquired at the same temperature and different Q by IUVS and BLS (some of them in Fig. 4.17).

Instantaneous Relaxation

In molecular fluids, microscopic relaxations can dissipate part of the energy of the acoustic waves through intramolecular degrees of freedom. In water, the only intramolecular degree of freedom is represented by fast intramolecular vibrations. The fast dynamics has been taken into account by adding including a term $\omega\eta_\infty$ to the imaginary part of the longitudinal elastic modulus [101]. The value of η_∞, $(3.1 \pm 0.4)10^{-3} cm^2/s$, has been taken from Ref.[19] and kept fixed throughout data elaborations.

Thermal Relaxation

Thermal diffusion processes dissipate energy at a typical time $\tau_T = 1/(D_T Q^2)$, with $D_T = \kappa/(\rho C_V)$, where κ is the thermal conductivity, ρ the density and C_V the specific heat at constant volume [16]. This thermal relaxation into account, in time domain, is [16, 102]: $\approx \omega_0^2[\gamma-1]e^{-\gamma D_T Q^2 t}$ where $\gamma = C_P/C_V$, the ratio of constant pressure vs constant volume specific heat. As in water $C_P \approx C_V$, the thermal relaxation is supposed to be negligible with respect to the experimental resolution. Indeed, the we have evaluated hD_TQ^2 which is, for IUVS Qs ≈ 0.76 much smaller than the experimental resolution. It has not been possible to resolve the thermal relaxation neither by IUVS nor by BLS.

The Structural Relaxation

The structural relaxation plays a preeminent role since it is related to the cooperative processes by which the local structure, after being perturbed by an external disturbance or by a spontaneous fluctuation, rearranges toward a new equilibrium position. This relaxation is intimately related to the many-body effects which differentiate liquids from, e.g., diluted gases, and can be considered as a sort of fingerprint of the liquid state. The phenomenology of structural relaxation -or *viscoelasticiy*- has been introduced since a long time [131, 132, 133] to interpret the experimental results concerning the frequency dependence of the sound velocity in ultrasound and light scattering regime [134, 135, 136]. In particular, the very strong frequency and temperature dependence of the sound velocity in glass forming systems near the glass transition are well explained in terms of structural relaxation [40]. More recently this approach has been successfully employed to interpret the dispersive behavior of longitudinal modes in the Thz range [137].

As discussed in Chapter 1, the MCT prediction for the long time limit behavior of the density autocorrelation function $F(Q,t)$, that is, for the structural relaxation, is a stretched exponential behavior, $\propto e^{-(t/\tau)^\beta}$ where τ is the characteristic time and β is the stretching parameter, predicted to be less than unity.

An analytical Fourier transform which translates the stretched relaxation from time to frequency domain does not exist. Nevertheless, it has been stated, based on the comparison of a number of experiments and interpolations, that the Cole-Davidson lineshape in the frequency domain is

a good interpolation for those processes that in the time domain are represented by a stretched exponential decay [138] : $\approx \frac{\Delta}{[1+i\omega\tau]^{\beta}}$ where Δ is the relaxation amplitude.

We have used the full spectrum lineshape in Eq. (4.4):

$$I\rho\rho(Q,\omega) = \frac{I_0}{\omega}\frac{M''(\omega)}{\left[\omega^2\rho/Q^2 - M'(\omega)\right]^2 + \left[M''(\omega)\right]^2} \tag{4.14}$$

with

$$M^*(\omega) = M_\infty + i\omega\eta_\infty + \Delta M^*(\omega) \tag{4.15}$$

and

$$\Delta M^*(\omega) = \frac{M_0 - M_\infty}{(1 + i\omega\tau_{CD})^{\beta_{CD}}} \tag{4.16}$$

Defining

$$tg(\phi) = \omega\tau \tag{4.17}$$

we obtain the real part of the modulus

$$M'(\omega) = M_\infty + \frac{M_0 - M_\infty}{\left[1 + (\omega\tau)^2\right]^{\beta/2}} cos(\beta\phi) \tag{4.18}$$

and the imaginary part

$$M''(\omega) = -\frac{M_0 - M_\infty}{\left[1 + (\omega\tau)^2\right]^{\beta/2}} sin(\beta\phi) + \omega\eta_\infty \tag{4.19}$$

A Levemberg-Marquardt chi-squared minimization algorithm has been used to optimize simultaneously three fitting functions $I(Q_1,\omega)$, $I(Q_2,\omega)$, $I(Q_3,\omega)$, one to each spectrum, with the constraint that parameters which define the structural relaxation are common. This is possible because in the low Q regime, the relaxation does not depend on Q [16, 19]. The i-th component of fitting function (with i = 1, 2, 3)reads

$$I(Q_i,\omega) = I_0 i[R_i(\omega) \otimes S(Q_i,\omega)] \tag{4.20}$$

Where $I_0 i$ is an intensity factor, $R_i(\omega)$ is the resolution function of the i-th spectrum which is produced as convolution with $S(Q_i,\omega)$. $S(Q,\omega)$ has been modeled as in Eq. (4.4) with real part as in Eq. (4.18) and imaginary part as in Eq. (4.19).

In the joint- analysis three parameters have been left free, which characterize the structural relaxation, τ, β and c_∞, and, of course, the intensity. The central peak has been modeled with an additive Lorentzian function as the thermal relaxation is negligible with respect to the instrumental

resolution and it is only stray light. The adiabatic sound velocity c_0 has been kept fixed to the values measured in [139] throughout all the data analysis.

A sample of the quality of the fit is shown in Fig. 4.18 where the fitting lines of the joint analysis with Eq. (4.20) are shown, superimposed to the triplets acquired at 273 K and 253 K (the lowest reached in this work) and joined each other according to the absolute rescale described in the previous section.

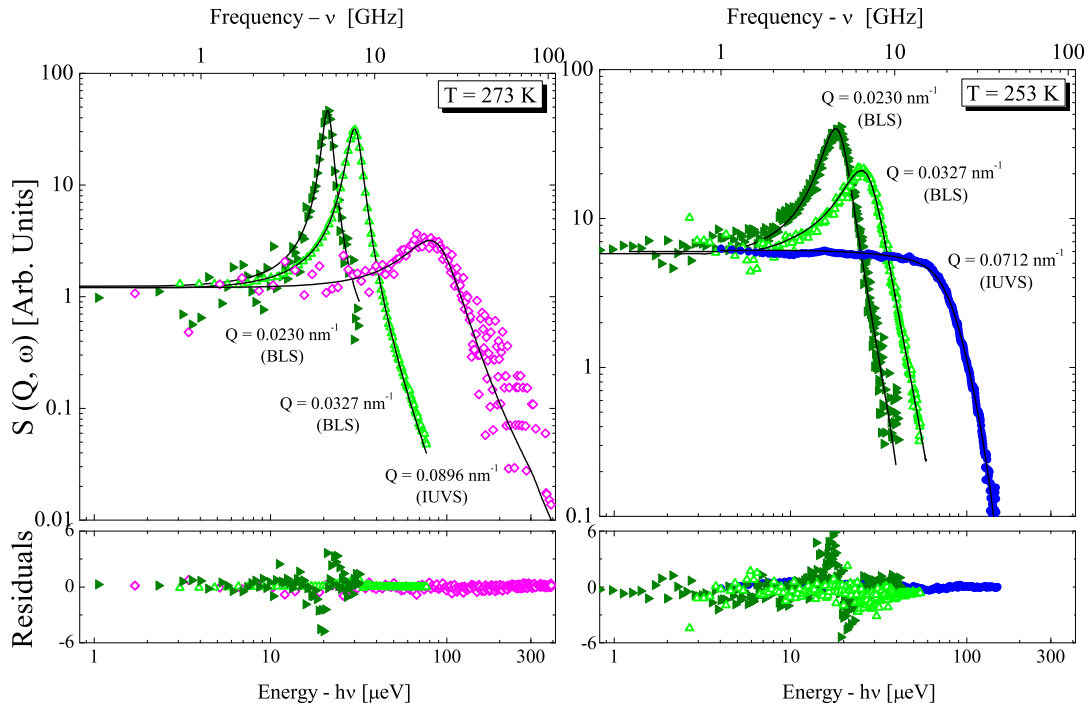


Figure 4.18: AntiStokes peaks of two isothermal triplets of spectra, with fitting lines superimposed resulting from joint analysis. *Left panels*: spectra acquired at 273 K and $Q = 0.023$, 0.033 nm^{-1} (by BLS) and 0.0896 (by IUVS) with fit superimposed and residuals on the bottom. The respective frequency axis ν [Ghz] is reported in the upper axis. *Left panels*: same scenario as for left panels, but at different temperature, T = 253 K, and a different Q probed by IUVS : 0.0712 nm^{-1}.

The fitting parameters obtained are shown and discussed in the next sections. In section 4.5.3 we report and discuss the relaxation time and the stretching parameter. In section 4.5.4 we report and discuss the speed of sound $C(T)$ measured by both DHO analysis and the values of c_∞ obtained by the full spectrum analysis.

4.4.5 Full-spectrum analysis of single IUVS spectra

IUVS spectra with no same-temperature BLS partner have been fitted by constraining the relaxation stretching parameter β within the range obtained by the joint analysis, to avoid the correlations between parameters which may occur in a reduced frequency window. A set representative for the temperature domain investigated and the fit quality is shown in figure 4.19. No BLS spectrum has been analyzed by full-spectrum formalism because the DHO approximation is already satisfactory, for water, down to the lowest temperature investigated. In the present investigation BLS spectra are mostly concerned with the completely relaxed regime of water.

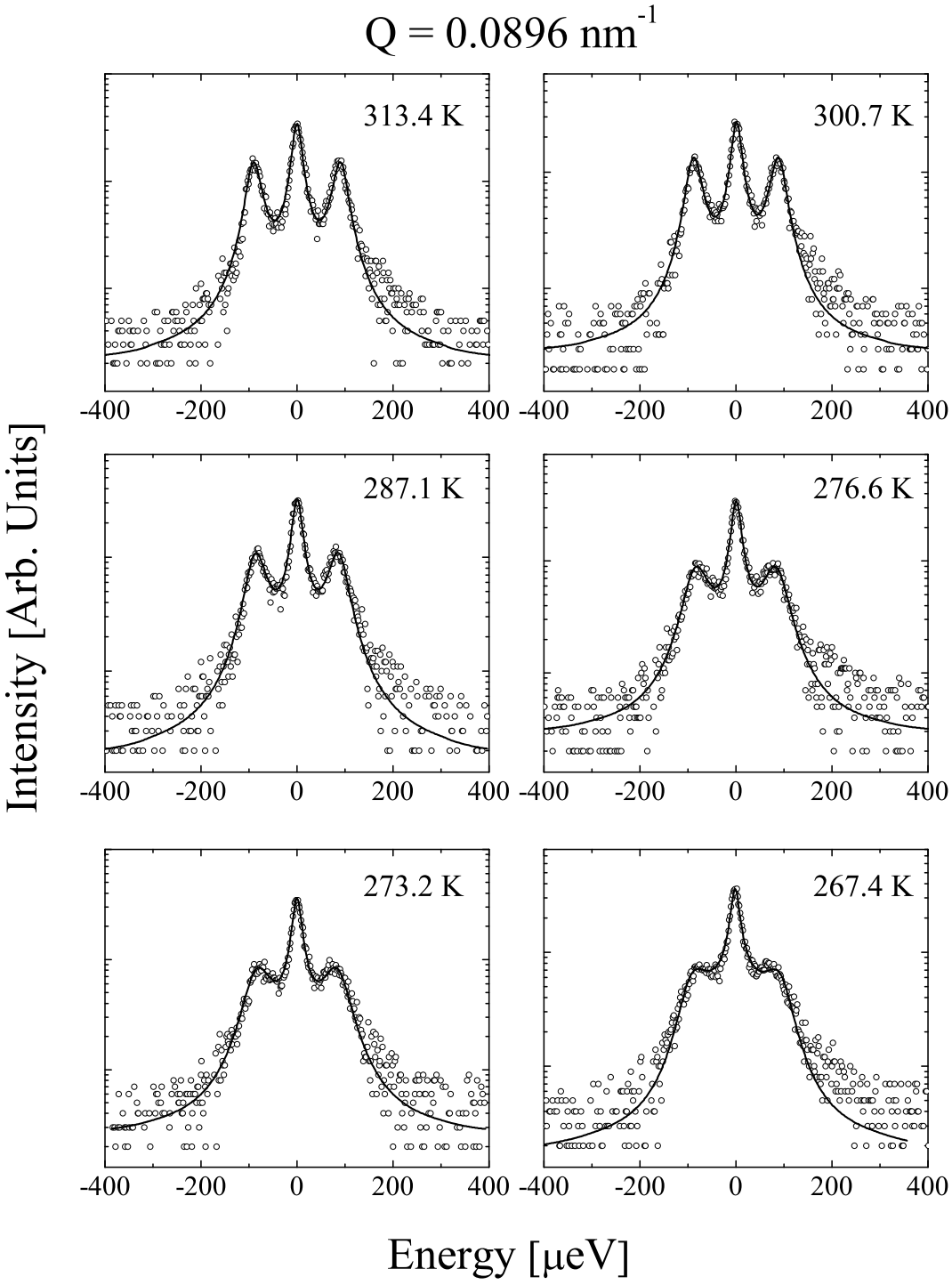


Figure 4.19: IUVS spectra at $Q \approx 0.089\ nm^{-1}$ and temperatures indicated. The fitting lines are superimposed, evaluated according to the full spectrum lineshape of Eq. (4.4) in the generalized hydrodynamic regime which takes the structural relaxation into account.

4.5 Results and Discussion

4.5.1 Best fit parameters and the structural relaxation

In figure 4.20 the real and imaginary part of the relaxing longitudinal elastic modulus $M'(\omega)$ and $M''(\omega)$ of water at 253 K are reconstructed by the using in Eqs. (4.18) and (4.19) the fitting parameters c_0, c_∞, τ and β obtained by the full-spectrum analysis described in the previous sections. The role of the parameters in the relaxation is also indicated in the figure: the limiting values of the speed of sound c_0 and c_∞ are related to the low and high frequency tails of $M'(\omega)$. The stretching parameter β is the slope of the high frequency side of $M''(\omega)$ in the bi-logarithmic scale. The relaxation time, τ, corresponds, approximately, to the reciprocal frequency position of the maximum of $M''(\omega)$.

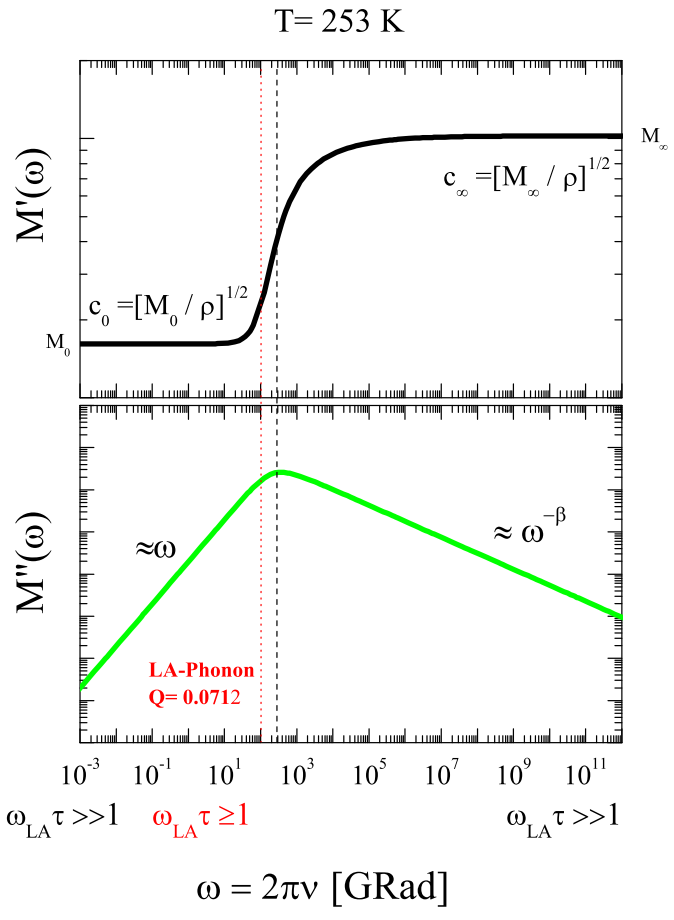


Figure 4.20: Frequency dependent (relaxing) longitudinal elastic modulus at T = 253, drawn from Eqs. (4.18) and (4.19) using the best-fit parameters of the full-spectrum analysis reported in Table 4.21. The relation between the parameters and the frequency regions of the relaxation is specified.

The values of the best-fitting parameters of the joint analysis are reported in the table of Figure 4.21.

T[°C]	T[K]	c_0 [m/s]	c_∞ [m/s]	τ_{CD} [ps]	β_{CD}	$\tau_{CD} \times \beta_{CD}$ [ps]
4	277.15	1419	3226 ± 100	0.17 ± 0.20	0.48 ± 0.10	0.082 ± 0.097
0	273.15	1405	3614 ± 100	1.29 ± 0.20	0.43 ± 0.1	0.551 ± 0.155
-5	268.15	1390	3107 ± 150	2.25 ± 0.20	0.51 ± 0.2	1.124 ± 0.105
-10	263.15	1350	3198 ± 80	3.94 ± 0.20	0.37 ± 0.17	1.436 ± 0.400
-15	258.15	1307	3210 ± 160	4.85 ± 0.30	0.43 ± 0.12	2.074 ± 0.502
-20	253.15	1270	3190 ± 120	5.96 ± 0.80	0.38 ± 0.14	2.262 ± 0.888

Figure 4.21: Best-fit parameters characterizing the structural relaxation of water down to 253 K, resulting from the joint analysis with the formalism of the longitudinal elastic modulus.

4.5.2 Sensitivity of IUVS technique

In Figure 4.22 the normalized real and imaginary part of the longitudinal elastic modulus $M'(\omega/2\pi)$ and $M''(\omega/2\pi)$ of water at 304 K (upper panel) and at 253 K (lower panel) are compared to the same-temperature antiStokes peak of the IUVS spectra measured at $Q \approx 0.072$ nm^{-1}.

The figure shows that the best sensitivity condition ($\omega\tau \approx 1$) of IUVS to the structural relaxation of supercooled water has been progressively approached upon supercooling. The magenta frame in Figure 4.22 emphasizes the frequency window, larger than three decades, experimentally accessed by our experiments by merging same-temperature BLS and IUVS spectra. We have direct access to the low frequency tail of the relaxation, that is, to the adiabatic sound velocity c_0. At low temperatures, also the stretched side of $M''(\omega)$, which is characterized by the stretching parameter β, enters the probed window. The figure accounts for the need for joint analysis in the determination of c_∞, which is not measurable directly at any of the investigated temperatures but has to be extrapolated by the fitting procedure: the indetermination on c_∞ has been considerably reduced by the direct access to the low and central frequencies of the relaxation process.

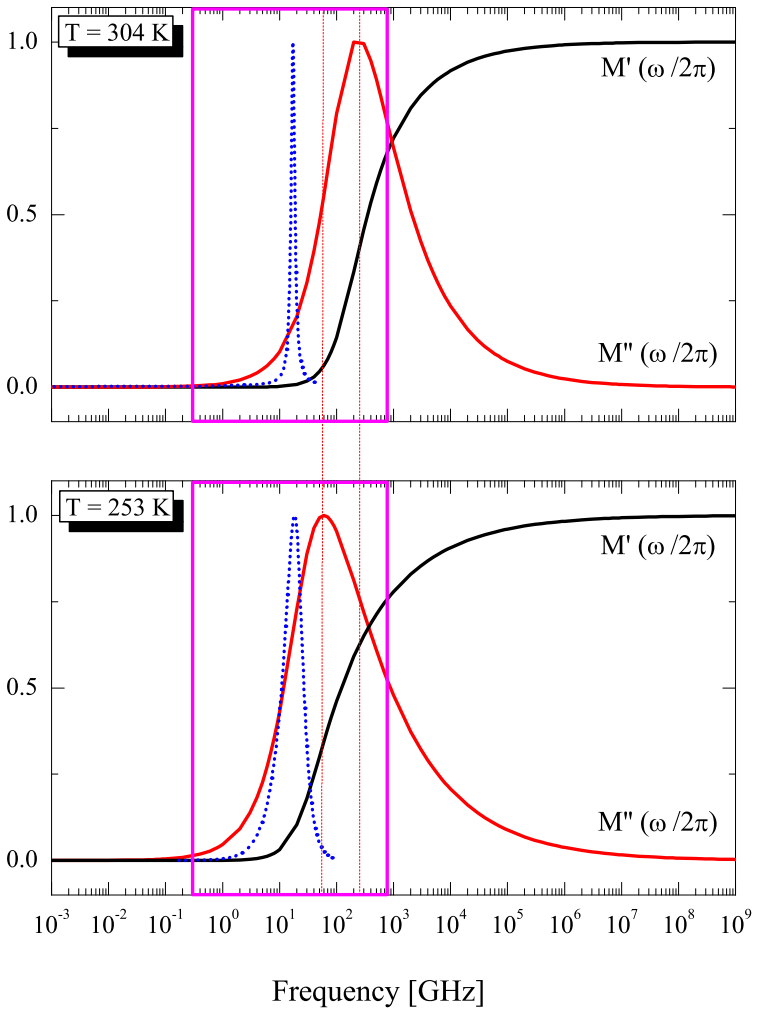


Figure 4.22: Real part $M'(\omega/2\pi)$ (black curves) and imaginary part $M''(\omega/2\pi)$ (red curves) of the normalized longitudinal elastic modulus, at 304 K (upper panel) and 253 K (lower panel), obtained by the joint analysis of IUVS and BLS spectra in the framework of generalized hydrodynamics. The antiStokes peak of the corresponding IUVS spectra, acquired at $Q \approx 0.1$ nm^{-1} and 304 K (upper panel) and 253 K (lower panel) is also reported (blue dotted lines). The magenta framework, in both panels, includes the frequency region that we have accessed experimentally. The vertical red lines mark, at the two temperatures, the frequency at which the maximum occurs of M'' which corresponds, approximately, to the reciprocal relaxation time. The best sensitivity condition of IUVS to the structural relaxation of supercooled water, discussed in Chapter 3, is progressively achieved upon supercooling.

4.5.3 Structural relaxation time and strength. Comparison to molecular dynamics simulations

The structural relaxation times of water, τ_{CD}, of Table 4.21, are displayed in figure 4.23 as a function of temperature. Our results are compared to the congruent relaxation times independendly evaluated in the formalism of longitudinally elastic modulus from IXS measurements [19]. A satisfactory continuity between the two datasets is obtained, which confirms the reliability of the new IUVS measurements and of the method adopted.

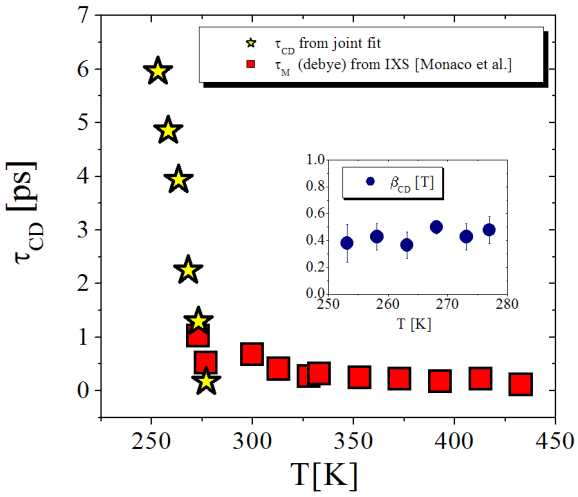


Figure 4.23: Stars: Structural relaxation times of water, τ_{CD}, obtained by full spectrum joint analysis of BLS and IUVS spectra in the formalism of relaxing longitudinal elastic modulus described in Section 4.4.4. Squares: longitudinal modulus relaxation times independently obtained by IXS at higher temperatures and frequencies [19]. Inset: stretching parameter of the longitudinal relaxing modulus as a function of temperature.

Compliance and the time domain

To compare our results to the predictions of molecular dynamics simulations described in Chapter 1, we have transformed the relaxation times obtained in the frequency domain into the corresponding values in time domain, according to the *Detailed comparison of William Watts and Cole Davidson functions* of C. P. Lindsey and G. D. Patterson, described in Ref. [138].

The time domain exponential decay found for the long-time limit of the structural relaxation by MD simulations is the so-called Kohlrausch-Williams-Watts (KWW) function:

$$\phi(t) = e^{-\left(\frac{t}{\tau_{KWW}}\right)^{\beta_{KWW}}} \tag{4.21}$$

The stretched KWW function can be considered the superposition of single exponential decays [138]:

$$e^{-\left(\frac{t}{\tau_{KWW}}\right)^{\beta_{KWW}}} = \int_0^\infty e^{(-t/\tau)} \rho_{KWW}(\tau) d\tau \tag{4.22}$$

where $\rho_{KWW}(\tau)$ is the distribution function. As a *relaxation time* of this decay is meant the average relaxation time of the distribution, $\langle \tau_{KWW} \rangle$, which is given by [138]:

$$\langle \tau_{KWW} \rangle = \frac{\tau_{KWW}}{\beta_{KWW}} \Gamma \left(\frac{1}{\beta_{KWW}} \right) \tag{4.23}$$

where Γ is Euler Gamma function.

If the relaxation is simply exponential ($\beta_{KWW} = 1$), an analytical Fourier transform relates $\phi(t)$ to the respective compliance, which has the Debye form:

$$\frac{J(\omega) - J_\infty}{J_0 - J_\infty} = \frac{1}{1 + i\omega\tau_J} \tag{4.24}$$

In the case of a stretched relaxation, it has been shown, in a numerical and comparative way based on a number of experiments [138], that the Fourier transform of the KWW function $\phi(t)$ is the complex Cole-Davidson compliance:

$$J(\omega) = J_\infty + \frac{J_0 - J_\infty}{[1 + i\omega\tau_J]^{\beta_J}} \tag{4.25}$$

whose real and imaginary parts, $J'(\omega)$ and $J''(\omega)$, are given by:

$$J'(\omega) = J_\infty + \frac{J_0 - J_\infty}{[1 + (\omega\tau_J)^2]^{\beta_J/2}} \cos(\beta_J \arctan(\omega\tau_J)) \tag{4.26}$$

and

$$J''(\omega) = \frac{J_0 - J_\infty}{[1 + (\omega\tau_J)^2]^{\beta_J/2}} \sin(\beta_J \arctan(\omega\tau_J)) \tag{4.27}$$

where $0 < \beta_J \leq 1$. Also in this case $J(\omega)$ is represented as a superposition of Debye processes, in which $\beta_J = 1$, which evolve over a distribution of relaxation times, $G(\tau)$

$$\frac{J(\omega) - J_\infty}{J_0 - J_\infty} \int_{-\infty}^{+\infty} \left(\frac{1}{1 + i\omega\tau} \right) G(\tau) dln\tau \tag{4.28}$$

$G(\tau)$ is zero for the relaxation times $\tau \geq \tau_J$. In the formalism of compliance, the average relaxation time, $\langle \tau_J \rangle$ is given by

$$\langle \tau_J \rangle = \tau_J \beta_J \tag{4.29}$$

Both functions, $\phi(t)$ and $J(\omega)$ are characterized by a relaxation time and a stretching parameter. The stretching parameter gives an evaluation of the non-exponential character of the relaxation function and of the broadness of the relaxation times distribution. The meaning of the relaxation time is not equivalent in the two distributions. In time domain, τ_{KWW} is the time at which the decrease is $1/e$. In frequency domain, τ_J is the maximum value of relaxation time. An analytical relationship between the τ and β of two domains does not exist, but a numerical correspondence has been stated numerically [138]:

$$\beta_{KWW} = \begin{cases} 0.970\beta_J + 0.144 & \text{if } 0.2 \leq \beta_J \leq 0.6 \\ 0.683\beta_K + 0.316 & \text{if } 0.6 \leq \beta_J \leq 1 \end{cases} \tag{4.30}$$

and

$$\tau_{KWW} = \tau_J(1.184\beta_J - 0.184) \tag{4.31}$$

We have calculated the complex compliance from the longitudinal acoustic modulus $M^*(\omega)$, as: $J^*(\omega) = 1/M^*(\omega)$. We have then evaluated the compliance relaxation time, τ_J, and the stretching parameter, β_J, by a fitting procedure. The parameters are reported in table 4.24 and displayed in figure 4.25

T[°C]	T[K]	τ_J [ps]	β_J	$\tau_J \times \beta_J$ [ps]
4	277.15	4.62 ± 0.40	0.73 ± 0.13	3.372 ± 0.162
0	273.15	5.31 ± 0.40	0.73 ± 0.14	3.886 ± 0.156
-5	268.15	8.48 ± 0.70	0.78 ±0.13	3.886 ± 0.156
-10	263.15	13.2 ± 1.5	0.66 ± 0.14	6.605 ± 0.153
-15	258.15	17.5 ± 1.5	0.73 ± 0.14	8.967 ± 0.186
-20	253.15	21.5 ± 2.0	0.69 ± 0.12	14.840 ± 0.172

Figure 4.24: Relaxation times, τ_J, stretching parameter β_J and average relaxation times $< \tau_J > = \tau_J \beta_J$ of liquid and supercooled water calculated in the formalism of the longitudinal compliance.

In figure 4.25 $\tau_J(T)$ and $\beta_J(T)$ obtained in the present work are reported, together with the corresponding values previously evaluated by IXS [19] at higher frequencies and temperatures. The average time $< \tau_J > = \tau_J \beta_J$ and β_{KWW}, calculated according to 4.30, are also shown.

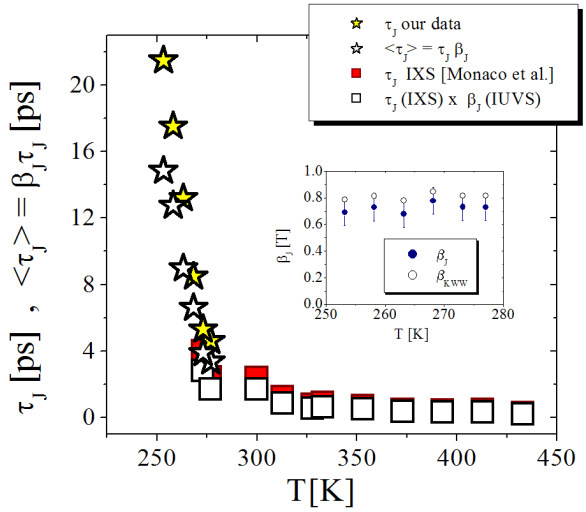


Figure 4.25: Relaxation times, τ_J, of liquid and supercooled water evaluated in the frequency domain in the formalism of the longitudinal compliance, obtained in this work by the joint analysis of the spectra obtained by IUVS and BLS at low frequencies (yellow stars) and at higher frequencies and temperatures by IXS [19] (red squares). The white symbols are the corresponding average values, $< \tau_J > = \tau_J \beta_J$. Inset: stretching parameter of the frequency dependent compliance.

Time domain and comparison to molecular dynamics simulations

We have evaluated the structural relaxation time in time domain, τ_{KWW}, according to Eq. (4.31), the relaxation stretching β_{KWW} according to Eq. (4.30) and the average relaxation time $< \tau_{KWW} >$ according to Eq. (4.23). The values are reported in Table 4.26.

T[°C]	T[K]	τ_{KWW} [ps]	β_{KWW}	$< \tau_{KWW} >$ [ps]
4	277.15	3.14 ± 0.02	0.81±0.01	3.51
0	273.15	3.62 ± 0.02	0.81±0.01	4.05
-5	268.15	6.26 ± 0.03	0.84±0.01	6.82
-10	263.15	8.19 ± 0.05	0.78±0.01	9.45
-15	258.15	11.90 ± 0.10	0.81±0.01	13.30
-20	253.15	13.60 ± 0.10	0.78±0.01	15.60

Figure 4.26: Relaxation times and stretching of water in the liquid and supercooled state, evaluated in the time domain.

We have finally obtained a set of values congruent to those predicted by of molecular dynamics simulations (MD). In Figure 4.27 the fit of MCT power law $\propto 1/(T - T_c)^{\gamma}$ to the values of $< \tau_{KWW} >$ is shown. We have fitted the MCT lineshape on our results and those from IXS [19] at once. In the optimization we have found $T_c = 220 \pm 10$ K and $\gamma = 2.5 \pm 0.8$, in good agreement with the MCT fit of MD data (Chapter 1).

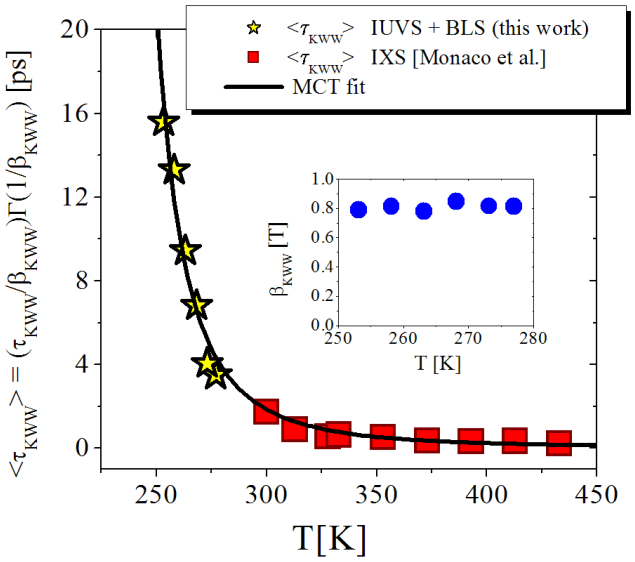


Figure 4.27: Average relaxation times $< \tau_{KWW} >$ as a function of temperature. Yellow stars result from the combined analysis of our IUVS and BLS. Red squares have been obtained by applying the Lindsey-Patterson procedure to the IXS results of Ref. [19]. The continuous line is the best-fit power law of MCT theory. The best-fitting parameters $T_c = 220 \pm 10$ and $\gamma = 2.5 \pm 0.8$ are in good agreement with MCT applied to the results of molecular dynamics simulations [11]. The stretching parameter β_{KWW} is reported in the inset. It has an a temperature independent value of ≈ 0.8.

In the inset of Fig. 4.27 the stretching parameter β_{KWW} it is also displayed. We have found an almost temperature independent value $\beta_{KWW} = 0.8 \pm 0.1$, in good agreement with the findings of molecular dynamics simulations at low Qs

We have hence given the first experimental evidence obtained by inelastic scattering techniques for a dynamic interpretation of water singularities, based on MCT theory. From this point of view, water seems to behave as many other glass formers. Indeed the validity of MCT adds a piece of information to the IXS experiments, which were performed at high temperatures and constant density. In these investigations [19] a Debye function was enough for shaping the structural relaxation and the temperature dependence of the relaxation time was Arrhenius, $\tau = \tau_0 exp(E_a/K_B T))$ [140], with an activation energy of $E_a = 3.8$ KCal/mol.

We have checked that a Debye lineshape is not suitable to fit the structural relaxation of water as the correlation of the parameters would give $c_\infty \approx 2000$ m/s, too low with respect to the direct DHO evaluation of IXS spectra. We have also checked that a single Arrhenius law is not enough to fit the whole collection of relaxation times. This is shown in figure 4.28. The temperature dependence of the structural relaxation time of glass-forming systems is usually described by the Vogel-Fulcher-Tamman equation (VFT) [141] $\tau = \tau_0 exp(A/T - T_0))$, where τ is expected to diverge at T_0. In the particular case $T_0 = 0$ the Arrhenius equation is obtained. The VFT equation applies to the structural relaxation of intermediate and fragile glasses while an Arrnenius behavior is typical of the structural relaxation of strong glasses and of secondary relaxations. A deep comparison to the VFT model has quite broad implications which lie beyond the targets of the present work. Nevertheless we have fitted the VFT equation to our dataset to make a comparison. We have found difficult to obtaine a unique convergence of the VFT optimization on our dataset. As we experienced a strong correlation between the parameters, the value of T_0 was been constrained between 136 and 228 K, the range in which the glass transition temperature of water is inferred by various authors. In figure 4.28 the obtained VFT line is shown, for which $T_0 = 136 \pm 50$ K.

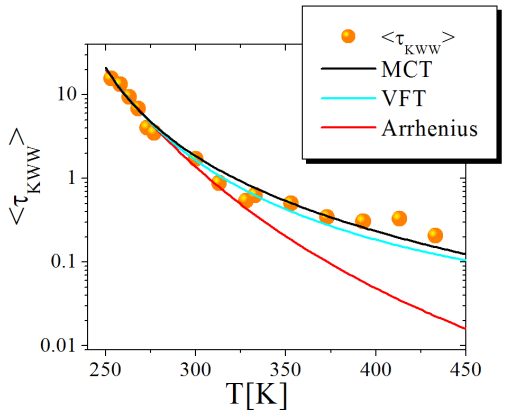


Figure 4.28: Arrhenius and VFT lineshape fit to the structural relaxation times of water. A single Arrhenius lineshape cannot fit the whole collection of relaxation times.

For sake of completeness the τ_{KWW} obtained all IUVS spectra fitted singularly is reported in Figure 4.29. There is a general agreement, within the error bar, with the MCT predictions already found.

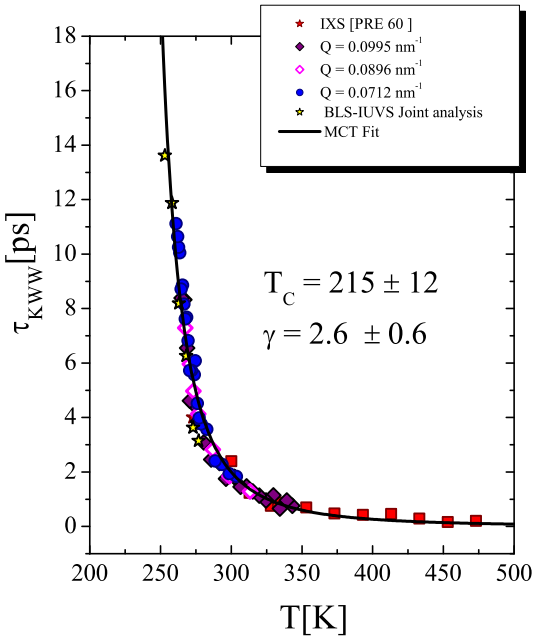


Figure 4.29: The whole collection of relaxation times obtained by fitting IUVS spectra singularly.

Comparison to viscosity

In Figure 4.30 the Arrhenius plot of the relaxation times, $log(1/\tau_{KWW}(T))$ as a function of $1000/T$, is shown. The shear and longitudinal viscosities are also shown, rescaled over the relaxation times. Shear viscosity values have been found in [4] and longitudinal kinematic viscosity has been measured in the present work, at lower temperatures -see Figure 4.31- while high temperature values have been measured in [19]. A phenomenological fractional-Debye-Stokes-Einstein scaling law between viscosities and relaxation times applies $\tau \propto \eta^n/T$ where the fractional exponent is $n = 1.2$ for the shear viscosity and $n = 1.3$ for the longitudinal viscosity.

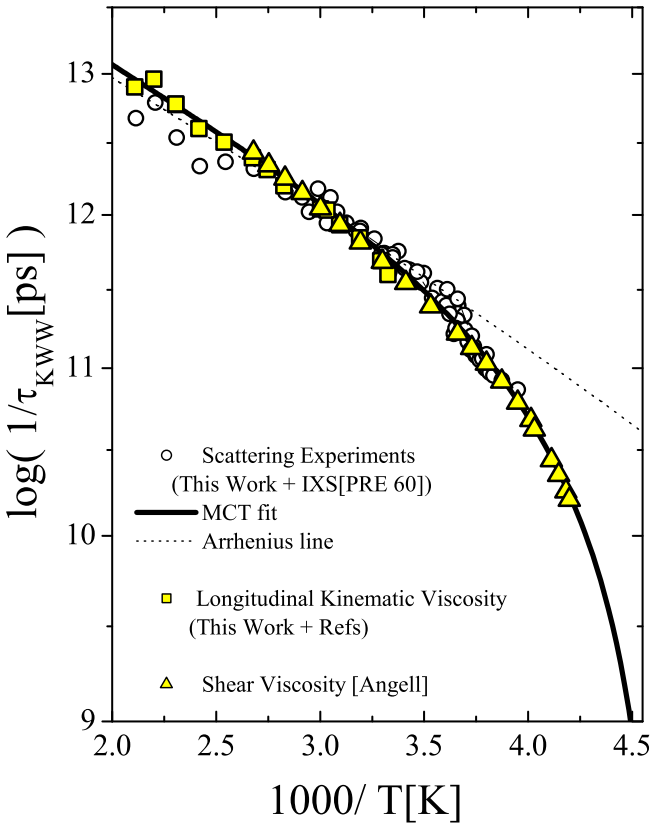


Figure 4.30: Arrhenius plot of structural relaxation time, shear viscosity and longitudinal kinematic viscosity.

The longitudinal shear viscosity values calculated in the present work by DHO analysis are reported in Figure 4.31:

When a supercooled liquid approaches the glass transition, its viscosity increases of several decades in a few degrees. The temperature ratio at which this happens, defined its fragility. In the Angell-plot in Figure 4.32 (Adapted from Ref. [35]) the viscosity of water is compared to that of many aqueous solutions, including LiCl - $6H_2O$, and SiO_2.

In this plot, only SiO_2 shows a linear Arrhenius trend, the others systems deviate and are more or less fragile. Indeed, fragility is defined as the entity of such a deviation, as $\varphi = d\lg_1 0(\tau)/d(T_g/T)$ [145]. Water, on a scale where T_g is assumed to be 136 K, behaves as a fragile glass former, with the eccentric behavior, with respect to other systems, of a power law for the viscosity.

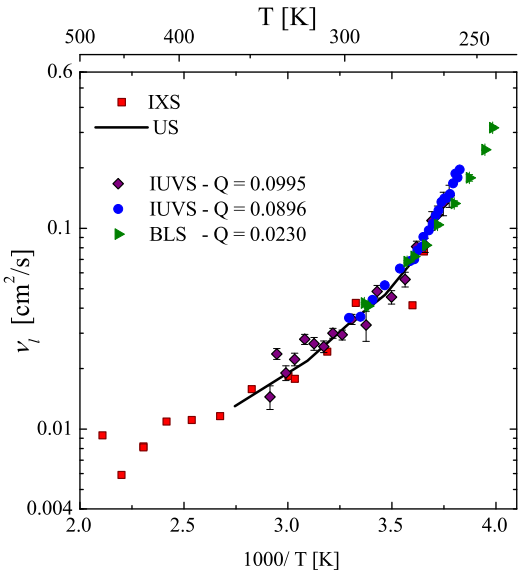


Figure 4.31: Angell plot of the longitudinal kinematic viscosity of water η_l/ρ, evaluated in this work by the DHO analysis.

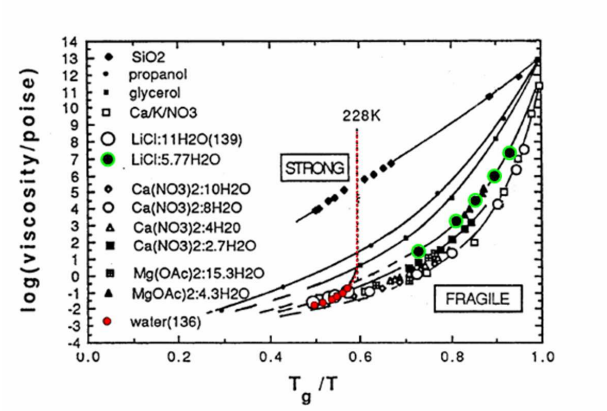


Figure 4.32: Angell plot of viscosity of water and various aqueous solutions. Picture from [35].

4.5.4 Sound velocity and the debate about *fast sound*

The whole information brought by the present work about the sound velocity in water has been collected and resumed in Figure 4.33.

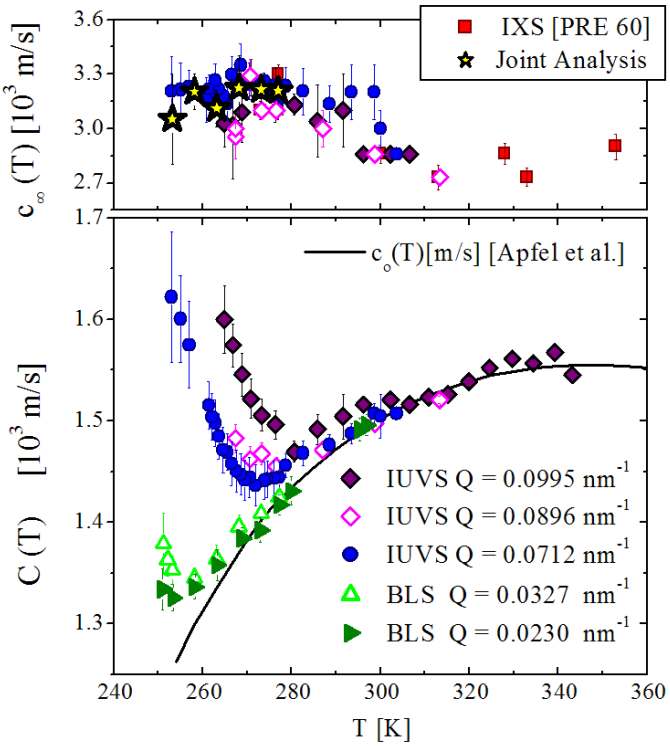


Figure 4.33: **Upper panel:** High frequency limit of sound velocity, $c_\infty(T)$, obtained by the analysis of IUVS spectra in the framework of generalized hydrodynamics. The results from the joint-fitting of IUVS and BLS spectra are reported as stars. As full diamonds are reported results from the $Q = 0.099$ nm^{-1} series; as open diamonds, from the $Q = 0.089$ nm^{-1} series and, as circles, from the series at $Q = 0.071$ nm^{-1}. The red squares indicate the results from IXS [19] which have been used as a reference for the spectra at high temperatures ($T > 300$ K), where the values of c_∞have been constrained within a 200 m/s error bar to the results of IXS. **Lower panel:** The full line represents the low frequency limit of sound velocity as a function of temperature, $c_0(T)$, got from ultrasonic measurements [89]. c_0 has been kept fixed in the full-spectrum fits. The apparent sound velocity, $C(Q,T)$ evaluated through the DHO model or by the maximum density of current of spectra is reported, for the Qs investigated. We observe the sharp departure from the ultrasonic behavior at ≈ 300 K for $Q = 0.099$ nm^{-1} (IUVS, full diamonds), at ≈ 284 K for $Q = 0.089$ nm^{-1} (IUVS, open diamonds), at ≈ 280 K for $Q = 0.071$ nm^{-1} (IUVS, open circles), at ≈ 265 K for $Q = 0.032$ nm^{-1} (BLS, half full circles), and at ≈ 269 K for $Q = 0.023$ nm^{-1} (BLS, full circles).

The determination of c_∞ in the dynamical window where the relaxation of water occurs has been a striking point of this work. The joint analysis has allowed the determination of uncorrelated values of c_∞ (reported as stars). In the upper panel of Fig. 4.33 the values of $c_\infty(T)$ are shown, calculated from the real part of the elastic modulus as $c_\infty(T) = [M_\infty/\rho]^{1/2}$. We got $c_\infty = 3200 \pm 100$ m/s, almost constant in the whole range of temperature and not depending on Q. At temperatures higher than 300 K we have constrained c_∞ around the values obtained by IXS in the $1 \div 8$ nm^{-1} regime [19], within an error bar of 200 m/s. The consistency of our results with the values of c_∞ measured independently and directly by IXS [80], testifies *(i)* the reliability of the measurements

performed at the IUVS beamline and *(ii)* that the speed of sound measured at high frequency corresponds to the relaxation-free limit of sound modes, as universally observed in glass-forming materials.

In the lower panel, the behavior of the adiabatic sound velocity c_0 is reported as a function of temperature. The values of $c_0(T)$ have been taken from [89] and kept fixed in the fits. The value of the apparent speed of sound $C(T)$ is also shown, for all the investigated values Q. $C(T)$ has been calculated from the position of the DHO model peaks, as $C(Q,T) = \omega_{LA}(Q,T)$ from the peak position of spectra, or from the density current where the DHO cannot apply. The incipit of a transition of $C(T)$ from c_0 to c_∞ is evident, even if stopped by freezing at about 1600 m/s. Moreover, in the figure is also appreciated that the detachment from the adiabatic regime begins at lower temperatures for lower Q.

The features resumed in figure 4.33 are universally observed in glass forming systems when the transition from the relaxed to the unrelaxed regime takes place, driven by the occurrence of the structural relaxation process. Such a phenomenology is summarized in figure 4.34, where the general behavior of the apparent speed of sound is sketched, qualitatively, as a function of momentum transfer, Q, and temperature T.

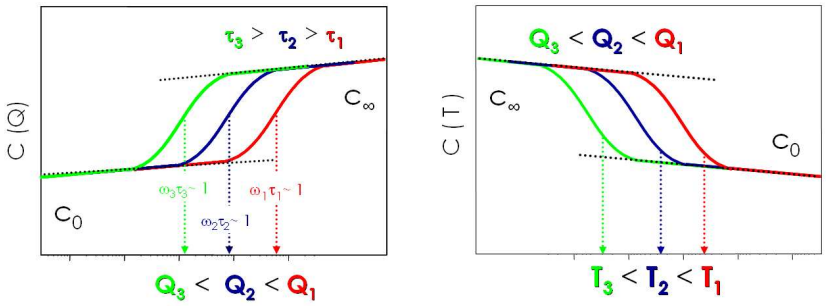


Figure 4.34: **Left panel:** A schematic representation of the apparent speed of sound as a function of Q and for different values of the relaxation time τ. As pointed out in Chapter 3, the relaxation time can be measured by inelastic scattering when it is comparable to the reversed frequency of the Q-th acoustic mode excited by the incident radiation (best-sensitivity condition). As a consequence, the higher is Q, the smaller will be the probed τ. Far from the relaxation, at lower frequencies the system is completely relaxed and the speed of sound is c_0 (adiabatic). At higher frequencies the system is unrelaxed and the speed of sound is c_∞. **Right panel:** A schematic representation of the apparent speed of sound as a function of temperature for different values of Q. On decreasing the temperature, the structural relaxation time will become, typically, larger. This inverts the order of the curves represented in the left panel: at high temperature, the structural dynamics is faster and can be investigated by high frequency techniques, like IXS, while we will use low frequency techniques like BLS to measure the slow dynamics at low temperatures. This explains the detachment of $C(T)$ from c_0, reported in Fig. 4.33, which occurs at lower temperatures for lower Q. We can infer that, if freezing did not intervene, we could observe in water the whole transition from c_0 and c_∞.

In Figure 4.35, the speed of sound measured at 293 K by IUVS and BLS is reported, for comparison, together with the published data, measured by IXS at the same temperature. The value is very close to c_0

The transition between c_0 and c_∞ observed in Figs. 4.33 and 4.35, can attributed to the structural relaxation. The physical mechanism responsible for the transition is the rearrangement of the long range molecular displacement correlations, when the thermodynamic conditions make it start introducing spectral components in the frequency window of the acoustic modes.

When fluctuations are applied (or spontaneously occur) on a timescale much longer than the structural relaxation time τ, the liquid is in a completely relaxed state, the vibrational and re-

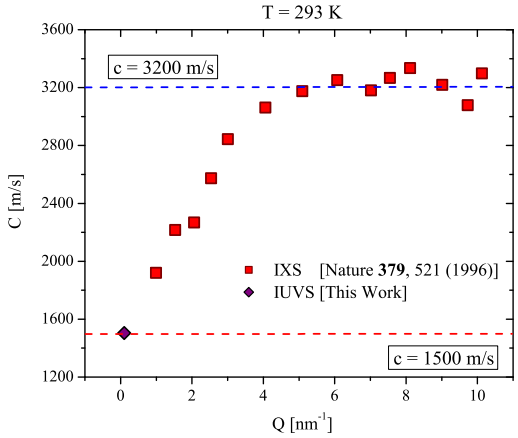


Figure 4.35: Sound velocity at 293 K as a function of momentum transfer. The value measured by IUVS at $Q \approx 0.99$ nm^{-1} and the published, data measured by IXS, are reported for comparison. The trend shows the continuity of the results, as a function of Q.

laxational degrees of freedom are in thermodynamical equilibrium, and the predictions of the hydrodynamics theory can be applied. In the opposite limit, when the density fluctuations are much faster than with respect to τ, the vibrational degrees of freedom cannot exchange energy with the relaxational ones. In this case, the constituent particles behave as if they were displaced from their equilibrium positions (that slowly change with time as dictated by the relaxational dynamics) by the vibrational degrees of freedom: in this sense, the collective dynamics of the liquid is seen as solid-like.

Several investigations performed at high frequencies by IXS and inelastic neutron scattering (INS) have clearly revealed the presence of longitudinal and transverse modes in water [80, 91, 92], which are obviously far from the experimental capabilities of the low frequency techniques IUVS and BLS which we have appositely utilized to perform investigations in a regime where the acoustic modes are decoupled from the transverse component.

Nevertheless, a comparison is of order to the interpretation given in [92] by the *interaction-model* introduced in Chapter 1. This model provides a very good fitting of a large collection of sound velocity values at $Q > 1$ nm^{-1} and ambient temperature. It is based on the interaction between the dispersive the non-dispersive modes, which is hypothesized with maximum strength at $Q \approx 1$ nm^{-1} and linear Q-dependence in the low-Q dynamical region [92], i.e., just where we can provide experimental evidences while the high frequency techniques like IXS and INS cannot.

We have calculated the speed of sound in water at 300 and 237 K, according to the interaction-model, by simply substituting $Q = 0{,}0994$ nm^{-1} and the temperature values in the equations provided by the authors in [92]. In figure 4.36 the results are shown as orange squares, together with the values of $C(T)$ we have measured at $Q \leq\approx 1$ nm^{-1} and already displayed in figure 4.33.

The discrepancy is evident between the values, together with an apparently parallel trend to the data of c_0, while a trend parallel to the curve at $Q = 0.0994$ nm^{-1} could be expected, in case of a systematic error in the calculation of $C(T)$. This mirrors the complete absence of any relaxational dynamics in the hypotheses of the interaction-model. With respect to this, we can conclude that generalizes hydrodynamics provides a complete interpretation of the phenomenology of water dynamics, while the hypotheses of the interaction model only apply in the limit of high frequency. Indeed, we can still speak of "modes interaction" in water, as in other liquids, provided

that this interaction is driven by the structural relaxation [91]. For these reasons, we have proposed to abandon the use of the term *fast-sound* [25], which recalls a propagation mechanism through lighter atoms of gas mixtures, and to retrieve the original *high-frequency sound* denotation of c_∞, appropriate to unambiguously identify the relaxational origin of free density fluctuations in water.

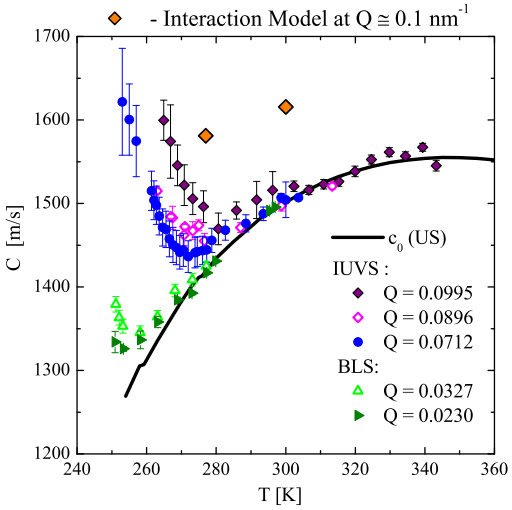


Figure 4.36: Comparison of the predictions of the model of interaction-modes [92] (orange squares) to our measured data.

Résumé du Chapitre 5

Ce dernier chapitre est consacré à la discussion des résultats obtenus danse l'étude expérimentale de la solution $LiCl,6H_2O$. Nous avons mesuré le facteur de structure dynamique dans les phases liquides et vitreuses, de 353 K à 80 K, au moyen de la diffusion inélastique de la lumière visible, de l'ultraviolet et des rayons X, soit entre 1 GHz et 10 THz, ainsi que par spectroscopie de corrélation de photons entre 0,01 Hz et 20 kHz. Nos résultats à haute température montrent un seul processus de relaxation dont les caractéristiques sont très similaires à ce qui est observé dans l'eau pure. Par contre en abaissant la température en dessous de 220 K, une température qui n'est pas loin de la température T_S de divergence de l'eau, le mode de relaxation se divise en deux processus : une relaxation structurale ($\alpha-$) et une relaxation secondaire ($\beta-$). À l'approche de la transition vitreuse, l'amplitude de la relaxation $\alpha-$ augmente aux dépens de la relaxation $\beta-$ qui disparaît progressivement.

Chapter 5

Dynamics of the LiCl-6 H_2O Solution from 1 GHz to 10 THz

Abstract

In this chapter the experiments performed on the the LiCl - $6H_2O$ solution, the elaborations and the results are reported and discussed. We have measured the dynamic structure factor in the liquid and glassy phases by means of inelastic scattering of radiation in the visible, UV and X-ray range, between 1 GHz and 10 THz, and by means of photon-correlation spectroscopy, between 0.01 Hz and 20 KHz. The measurements have been performed between 353 K and 80 K. Our data show that a single relaxation process exists at high temperature, which has features similar to those of the single relaxation of pure water. Upon cooling the system below $\approx$ 220 K, which is not far from the diverging temperature T_S of water, this single mode starts to differentiate two processes, a structural ($\alpha-$) and a secondary ($\beta-$)relaxation. As the temperature is decreased, the relaxation is the vanishing continuation of the single, high-temperature process, while the onset of the $\alpha-$relaxation occurs at the expense of the $\beta-$process.

5.1 The LiCl - 6 H_2O Solution

The rich phenomenology of static and dynamic properties of aqueous solutions has been attracting the interest of scientists, especially at temperatures below the homogeneous crystallization temperature of water, 235 K, where entropy increases its power and subtle structural effects due to hydrogen bonding take places by changing the thermodynamic scenario [4]. Also at ambient temperature electrolyte aqueous solutions are fascinating, being wide concerned with human life: important chemical reactions in human body involve ionic substances in aqueous environment, e.g. membrane permeability and neuronal signaling [147]. LiCl-$R$$H_2O$ aqueous solutions (being R the molar ratio solvent/solute) have been the subject of extensive investigations of structural [148, 149] dynamic [150, 26, 151] and thermodynamic [152] properties. Indeed, the presence of ions profoundly affects the structure of the liquid: for $R \leq 6$ it has been shown the glassy state is attained by increasing the network of H-bonds among the hydration shells of ionic clusters, in addition to strengthening of ion-solvent interactions [153].

The $R = 6$ solution owns the peculiarity of avoiding crystallization in the whole temperature range down to the (calorimetric) glass transition temperature $T_g \sim 135$ K [150]. The wide domain of metastability has allowed a detailed study of structure [154] and dynamics [150] of this system: evidence has been given of important structural modifications occurring around the peritexy temperature of the penta-hydrate, $T_p = 202$ K -which has been identified as the vanishing melting temperature of the $R = 6$ solution; the formation of hydrogen bonds organized in tetrahedral short-range coordination typical of water has been inferred to originate as temperature is decreased across T_p.

The structural or α-relaxation process of LiCl-6H_2O measured by Neutron Spin Echo (NSE) at high temperature seems to obey a scaling law comparable to that of viscosity while, at low temperature (< 200 K), some difficulties arose in comparing NSE spectra to mode coupling theory (MCT) [74], as the data could not be scaled any more over viscosity and the critical temperature predicted by MCT could not be identified [150]. In addition to the α-relaxation, the presence of a local β-relaxation, not evidenced by NSE, has been inferred by NMR, dielectric and muon spectroscopies in the temperature range from 130 K to 220 K [155].

The coexistence of $\alpha-$ and $\beta-$ relaxations may considerably complicate the analysis of density fluctuations spectra, especially if measured in narrow spectral regions. Aqueous LiCl solutions have been investigated by Brillouin Light Scattering (BLS) [156] in the limited frequency region of few GHz around the Brillouin peaks. From a single-relaxation hydrodynamic analysis, an unexpected Arrhenius behavior for the relaxation time has been inferred. In the same work, a MCT analysis of the data has evidenced a qualitative agreement but a significant quantitative disagreement with the predictions of the theory. Impulsive stimulated light scattering (ISS) measurements [157, 158] have also been performed to determine the frequency-dependent longitudinal elastic modulus in the MHz-GHz frequency region. Approaching the liquid-to-glass transition, the divergence of the α-relaxation has been observed together with a hint of an MCT $\beta-$region. A MCT analysis of the temperature behavior of such a region has given an unphysical value of the critical temperature of the system; a more detailed analysis of ISS data was not possible, because the spectral region where β-relaxation is decoupled from $\alpha-$ one and located above the upper frequency limit of this technique.

The scenario described above is still calling for unambiguous settlement of the dynamical properties of the $R = 6$ solution. An important limit to our knowledge comes from the fact that the different relaxation processes have been revealed by the use of different physical observables which can be sensitive to different microscopic dynamics, hard to be quantitatively compared the one to the other. With respect to this, a more comprehensive investigation of the dynamics of density fluctuations is highly desirable in order to shed light onto the interplay between the $\alpha-$ and $\beta-$ relaxations and their correlations to structural modifications occurring at the development of the short range order.

Due to the 200 K wide range of metastability of this solution, more than one technique is needed to characterize the whole entirety of its relaxational dynamics. In order to get a homogeneous description over a broad frequency range, we measured the dynamic structure factor, $S(Q, \omega)$, of LiCl - 6H_2O by means of three techniques for inelastic scattering of radiation which probe contiguous frequency domain: we availed of the recently developed inelastic ultra-violet scattering (IUVS) technique [21], as well as of inelastic X-ray scattering (IXS) [159], complemented by traditional Brillouin light scattering (BLS) and photon correlation spectroscopy (PCS) measurements [160].

5.2 Experiments

Anhydrous Lithium Chloride 99,99% was purchased from Sigma-Aldrich. The solutions were prepared under glove box nitrogen environment. As the mixing reaction is exothermic enough to cause significant evaporation of the solvent evaporation, the process was let to occur into a sealed container until the solution returned to ambient temperature. Before the measurements, the solutions were micro-filtered.

Photon-correlation experiments

Photon correlation spectroscopy (PCS) measurements were performed in the temperature range between 139 K and 153 K. A Coherent DPSS 532 solid state laser was used to generate a 100 mW, 532-nm incident light beam. The time fluctuations of the 90 scattered radiation were analyzed by a Brookhaven BI9000T photon correlator, at VV polarization. A selection of spectra is displayed in Fig. 1, which shows the noticeable evolution of the relaxation time over 4 decades in this narrow temperature range, a typical immediate sign of the slowing down of structural relaxation associated to the glass transition.

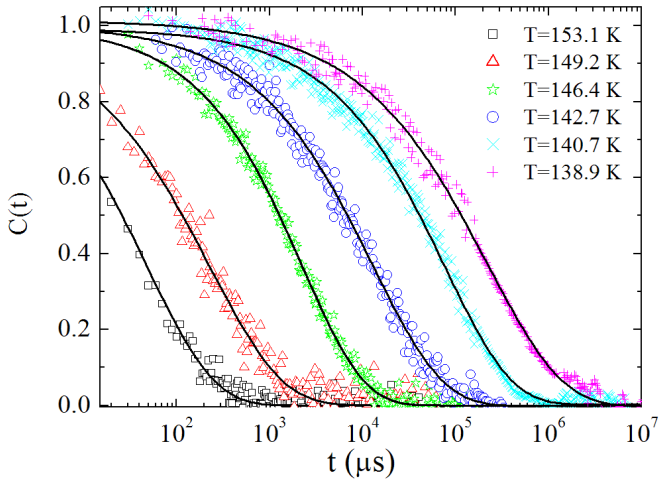


Figure 5.1: Photon correlation polarized spectra of LiCl - $6H_2O$ acquired over a five decades time domain, at the reported temperatures. Solid lines are the best fits obtained using the normalized function $C(t) = [exp(-t/t_K)^{\beta}]^2$, with β kept almost constant around 0.6, according to indications given in Ref. [150]. Relaxation times are reported in Fig. 5.9. The flex position of the spectra, approximately proportional to the reciprocal relaxation time, shows a shift of four decades in a 15 K narrow temperature range, typical sign of the blocking of relaxational dynamics associated to the glass transition.

Inelastic scattering experiments

The coherent dynamic structure factor $S(Q, \omega)$ of LiCl-$6H_2O$ was measured by means of three different spectrometers to cover the frequency range between 1 GHz and 10 THz. In utilizing three different instruments, we took care to get triplets of same-temperature spectra that can be joined to cover a 4-decades frequency range.

At lower frequencies we availed of the Brillouin light scattering (BLS) technique, at a total resolution of 350 MHz. The source was a 532 nm single mode laser delivering a power of 200 mW. The spectra were collected by a Sandercock-type 3+3 pass tandem Fabry-Pérot interferometer. Polarized spectra (VV) were recorded in the backscattering geometry for temperatures ranging from 358 K down to 82 K. Temperature variations were kept within ±0.1 K. The momentum transfer,

Q, varied between 0.0330 and 0.0331 nm^{-1} in the spanned temperature range. Depolarized (VH) measurements were also performed in order to obtain the isotropic spectrum $I_{\rho\rho}$, according to the procedure illustrated in Figure 5.2for three selected temperatures and described in details in Ref. [109].

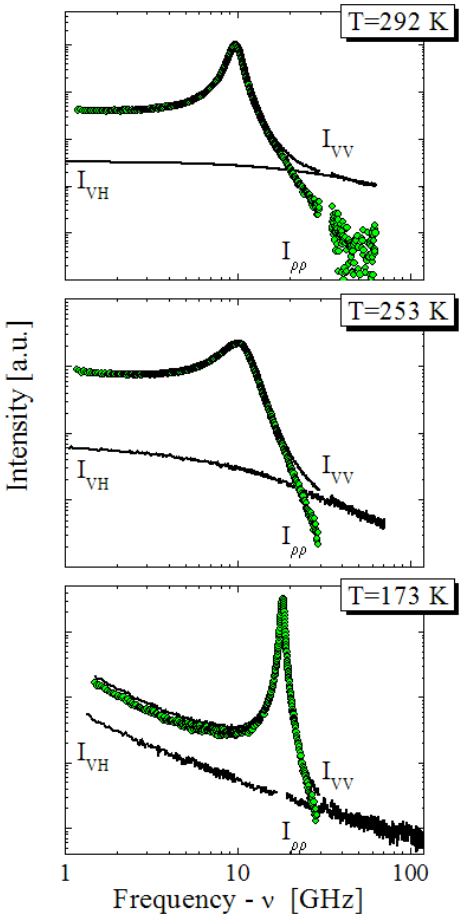


Figure 5.2: Log-Log plot of I_{VV}, I_{VH} and $I_{\rho\rho}$ (circles) BLS spectra at three different temperatures. The isotropic spectra $I_{\rho\rho}$ are obtained by subtracting the appropriate anisotropy contribution from the polarized spectrum: $I_{\rho\rho} = I_{VV}$ - r^{-1} I_{VH}. It is evident in the figures that the I_{VH} contribution is, actually, negligible.

We observe in Figure 5.2 that the contribution from the anisotropic scattering can be neglected, in agreement with the absence of strong rotation-translation couplings in LiCl-6H_2O Brillouin spectra [161]. As a consequence, $I_{\rho\rho}$ is a good approximation to the coherent dynamic structure factor $S(Q,\omega)$ of this sample. The measurements at intermediate frequencies were performed at the Inelastic Ultra-Violet scattering (IUVS) beamline at the Elettra Synchrotron light laboratory in Trieste [21], at temperatures ranging from 338 K down to 86.5 K. The source was a 488 nm single mode second harmonic generator Lexel Ar^+ laser whose frequency is doubled by an intracavity system equipped with nonlinear beta-Barium Borate single crystals. The energy resolution was 3.6 micro-eV and the momentum transfer was varying between 0.0744 and 0.0750 nm^{-1} in the spanned temperature range. The scattered light was analyzed by an 8 m long Czerny-Turner normal incidence spectrograph. The temperature range was the same as in BLS measurements.

A selection of IUVS spectra is shown in Figure 5.3.

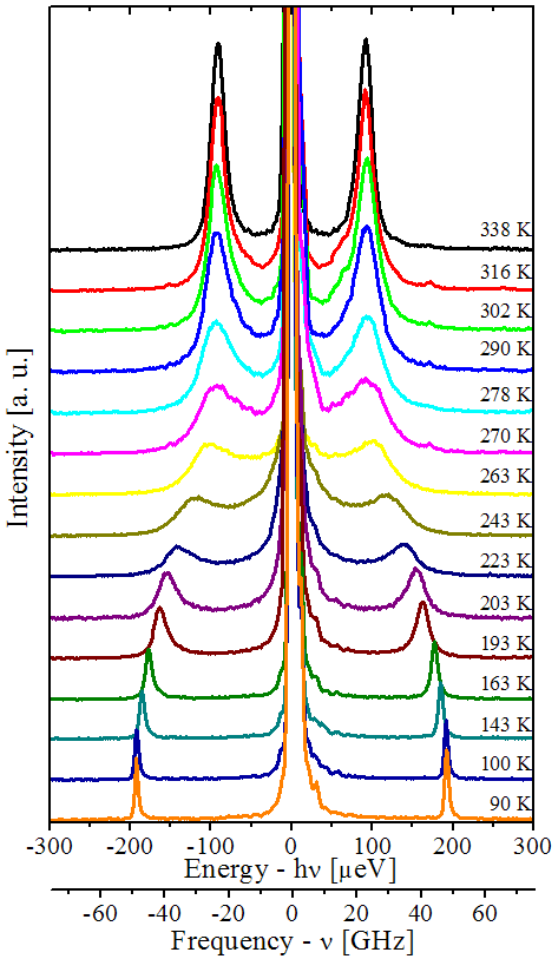


Figure 5.3: Selection of inelastic ultra-violet scattering spectra, acquired at the temperatures reported on the side. Momentum transfer changes between 0.0744 and 0.0750 nm^{-1}. Inelastic peak position, proportional to sound velocity, is evidently increasing as a function of decreasing temperature. Peak width increasing and decreasing on cooling the system is due to the appearance and outgoing of extra-modes related to relaxation processes evolving on the timescale of the probed acoustic modes.

The spectra in the THz frequency regime were obtained by Inelastic X-ray Scattering (IXS) at the ID16 beamline of the European Synchrotron Radiation Facility (ESRF)[159]. The monochromator and analyzer crystals were operating at the Si(11 11 11) reflection in an extreme backscattering configuration corresponding to an incident photon energy of 21.75 keV and a total energy resolution of 1.5 meV. Due to the limited beamtime availability, we measured $S(Q, \omega)$ at three selected temperatures only, 292, 253 and 173 K, with a momentum transfer ranging from 2 to 15 nm^{-1}. In Fig. 5.4 the IXS spectra are shown, together with the anti-Stokes peaks of spectra acquired at the same temperatures by means of BLS and IUVS techniques.

5.3 Analysis and Results

According to the generalized hydrodynamics theory [108, 101], the spectrum of light scattered by the density fluctuations in a fluid can be modeled as:

$$I\rho\rho(\omega) = \frac{I_0}{\omega} \frac{M''(\omega)}{\left[\omega^2\rho/Q^2 - M'(\omega)\right]^2 + \left[M''(\omega)\right]^2} \tag{5.1}$$

where $Q = 4\pi n/\lambda sin(\theta/2)$ is the momentum transfer - with n the refractive index, λ the incident wavelength, θ the scattering angle. ρ is the mass density. $M^*(\omega) = M'(\omega) + iM''(\omega)$ is the generalized longitudinal acoustic modulus, whose real part $M'(\omega)$ is related to the speed of sound in the and the imaginary part $M''(\omega)$ is related to the sound absorption. The spectrum is characterized by two side peaks due to the inelastic scattering of incoming radiation from thermally activated longitudinal acoustic modes, whose position and width depend on $M'(\omega)$ and $M''(\omega)$, respectively, as can be realized from Eq. 5.1.

For a given scattering experiment, that is, for a given value of Q, the spectrum quickly decays to zero at frequencies higher than that of the Brillouin peak, that is for $\omega \gg Q(M'/\rho)^{1/2}$. As a consequence, the only way to investigate a broad frequency domain is to vary the incident wavelength, that is, to avail of different techniques. In Fig. 5.4, the IXS spectra are presented (right panels), together with the Brillouin peaks of BLS and IUVS spectra taken at the same temperature (left panels). Joined together, the spectra cover a frequency domain of about four decades: the Brillouin peaks are found between 10 and 100 GHz in BLS and IUVS spectra and at about 1 THz in the IXS case. BLS and IUVS Brillouin peaks of spectra at three temperatures are joined to corresponding-temperature IXS spectra. One observes that spectra totally cover about four decades; peaks occur between 10 and 100 GHz in BLS and IUVS spectra and at about 1 THz in IXS case.

The frequency dependent complex modulus $M^*(\omega)$ takes the acoustic attenuation and dispersion into account, as relaxations. In liquids and glasses the relaxation scenario is quite complex and broadly extended over frequency. A glass-forming liquid usually exhibits a structural, or $\alpha-$relaxation, whose typical time parallels the viscosity with an increase of decades in few degrees towards the glass transition temperature T_g, where the relaxation itself undergoes a blockage. One or more faster processes ($\beta-$,$\gamma-$, ...) are usually present, which may survive below T_g. A general expression for $M*(\omega)$, which formally includes the whole information about relaxations, is:

$$M^*(\omega) = M_\infty + i\omega\eta_\infty + \Delta M^*(\omega) \tag{5.2}$$

where $M_\infty = \rho c_\infty^2$ is called the unrelaxed modulus c_∞ the unrelaxed sound velocity and η_∞ the unrelaxed viscosity, which represents the acoustic damping by all the relaxation processes that take place at frequencies too high to be accessed by the experiment.

$\Delta^* M(\omega)$, the relaxing part of the modulus, can be expressed by one or more phenomenological relaxation laws, each one being generally related to a temperature depending charachteristic time (*relaxation time*) and expressing the variation in $M^*(\omega)$ with respect to the frequency ω of the traveling acoustic wave.

Relaxations in glass forming liquids typically are characterized by a power law distribution of relaxation times. In the frequency domain, they are often modeled by using a Cole-Davidson relaxation function [163] :

$$\Delta M^*(\omega) = \frac{M_0 - M_\infty}{(1 + i\omega\tau_{CD})^{\beta_{CD}}} \tag{5.3}$$

where τ_{CD} is the characteristic relaxation time and β_{CD} is a stretching parameter which ranges between 0 and 1. The average typical time of the relaxation is $\langle\tau\rangle = \beta_{CD}\tau_{CD}$ [163].

It is generally true that the characteristic time of a relaxation increases, as the temperature decreases. At a fixed temperature, a relaxation process will affect the modulus $M^*(\omega)$ only in the limited frequency range comparable to the reverse relaxation time. At the lower or the higher frequencies, two limiting conditions may be attained, called the *relaxed* and the *unrelaxed* regimes [164].

The system is in its relaxed regime when ω is small with respect to τ^{-1} (the $\omega\tau \ll 1$ condition) i.e., when its dynamic is fast enough to answer to the exciting probe without delay. This occurs when the temperature is sufficiently high or the exciting frequency is sufficiently low. The opposite case, the unrelaxed regime, occurs when ω is large with respect to τ^{-1} ($\omega\tau \gg 1$) and is verified at low temperature or high probing frequency. Since the system cannot relax fast enough to follow the acoustic excitations, the values obtained are called unrelaxed. In both these limiting conditions, the spectrum of Eq. 5.1 is properly approximated by that of a damped harmonic oscillator[138, 16](DHO),

$$I(\omega) = I_0 \frac{\Gamma\omega_0^2}{[\omega^2 - \omega_0^2]^2 + [\Gamma\omega]^2} \tag{5.4}$$

where ω_0 and Γ correspond to the frequency position and linewidth of the Brillouin peaks, respectively. In terms of elastic modulus, the relaxed condition is expressed by the relationship $M^*(\omega) = M_0 + i\omega\eta_L$, where $M_0 = \rho c_0^2$ is the relaxed modulus, c_0 is the relaxed adiabatic sound velocity and $\eta_L = (M_\infty - M_0)\langle\tau\rangle + \eta_\infty$ is the relaxed longitudinal viscosity. In this limit, the following two relationships hold: *(i)* between the frequency of the Brillouin peak and the relaxed modulus $\omega_0 = q(M_0/\rho)^{1/2} = qc_0$ and *(ii)* between the peak linewidth and the longitudinal viscosity: $\Gamma = \eta_L q^2/\rho$. In the unrelaxed limit $M^*(\omega) = M_\infty + i\omega\eta_\infty$, $\omega_0 = q(M_\infty/\rho)^{1/2} = qc_\infty$, and $\Gamma = \eta_\infty q^2/\rho$. As regards LiCl6$H_2$O, the IXS technique probes the dynamics at frequencies so high that the values obtained are always unrelaxed. For IXS data, the DHO model is sufficient to extract all the valuable information from the spectra.

Regarding IUVS and BLS data, since one or more relaxations affect the spectra window (see Fig. 5.3), the full-spectrum modeling described by Eqs. (5.1) (5.2), (5.3) is required for a complete description of the spectra. This modeling provides typival time, stretching parameter, and amplitude of the relaxation(s). Nevertheless, Eq. 5.4 still gives approximate values of $M^*(\omega)$ at frequencies around the Brillouin peaks, and a first glance at the dynamics of the system, with fingerprints such as the temperature behavior of the apparent velocity of sound and of the longitudinal apparent kinematic viscosity, as discussed in the following. Last but not least, the proofs of consistency of limiting values c_0, c_∞, η_L, η_∞, with results by other techniques (like ultra-acoustics or ISS) are of fundamental importance. Spectra analysis by DHO model is appropriate to this purpose.

In the intermediate frequency region between the two limits, Eq. (5.3) is a good approximation for a relatively narrow spectral region around the inelastic peaks. Important fingerprints of the system, such as temperature behavior of apparent velocity of sound and of longitudinal apparent kinematic viscosity may be deduced from DHO analysis.

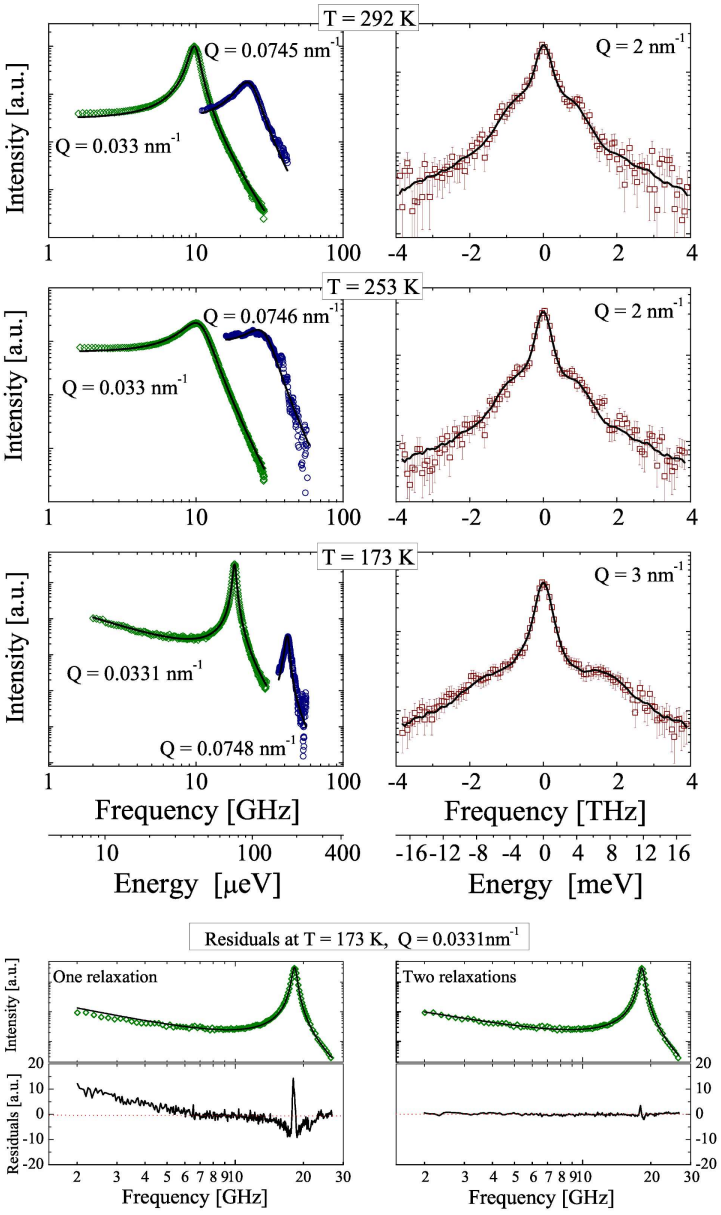


Figure 5.4: **Upper panels:** Brillouin spectra acquired at the temperatures of 292, 253, and 173 K by different inelastic scattering techniques: light scattering (green diamonds), ultraviolet scattering (blue circles),and x-ray scattering (red squares). In the left panels, only the Stokes inelastic peaks are reported. The lineshape equation (5.1), convoluted with appropriate experimental resolution, has been fitted to each triplet of spectra. This procedure takes into account the presence of one (at 292 and 253 K) or two (at 173 K) stretched relaxation processes. The fitting lines are superimposed over the measured spectra, with the transferred momentum Q also indicated. The obtained fit parameters are reported in the tables in Fig. 5.7 and 5.8 and illustrated in Fig. 5.5 (c_∞), Fig. 5.9 ($\langle\tau\rangle = \beta_\tau$), and Fig. 5.12 (comparison to the pure solvent). Tiling the spectra has made it possible to cover a frequency window of four decades. That makes it feasible to adjust all relaxation parameters at once, with a considerable reduction in correlation among them. **Bottom panels:** Fit results and residuals by single-relaxation (left) and two-relaxations models (right) of the BLS spectrum at 173 K. In order to account for the low frequency region of the spectrum, a secondary relaxation has to be included in the analysis.

5.3.1 Acoustic Analysis

We fit Eq. (5.4) convoluted with appropriate experimental resolution around the Brillouin peaks of all measured BLS, IUVS and IXS spectra. We obtained $\omega_0(T)$ and $\Gamma(T)$ at each temperature. The apparent velocity of sound $C(T)$ is related to peak position through the relationship

$$C(T) = \frac{\omega_0(T)}{Q} \tag{5.5}$$

In Fig. 5.5, $C(T)$ is reported as a function of temperature. Figure 5.5 evidences the transition from the relaxed to the unrelaxed regime in LiCl-6H_2O. Both the limits have been attained by BLS and IUVS experiments and an evident dispersion occurs of $C(T)$ between c_0 and c_∞, from high to low temperature, respectively. The dispersion reveals the presence of relaxational dynamics evolving on a timescale which approaches the reciprocal probed frequency, $1/\omega_0$, of the acoustic modes. Indeed, that is also the reason why the relaxations affects BLS data at a lower temperature than IUVS data. As previously mentioned, due to the very high frequency acoustic modes probed by IXS, the respective velocity dispersion occurs at higher temperatures than those investigated and, $C(T)$ matches $c_\infty(T)$, in the whole temperature range explored. In Fig. 5.5, the literature data from ISS (Ref. [158]) are also reported: limiting values c_0 and c_∞ are consistent with our investigations.

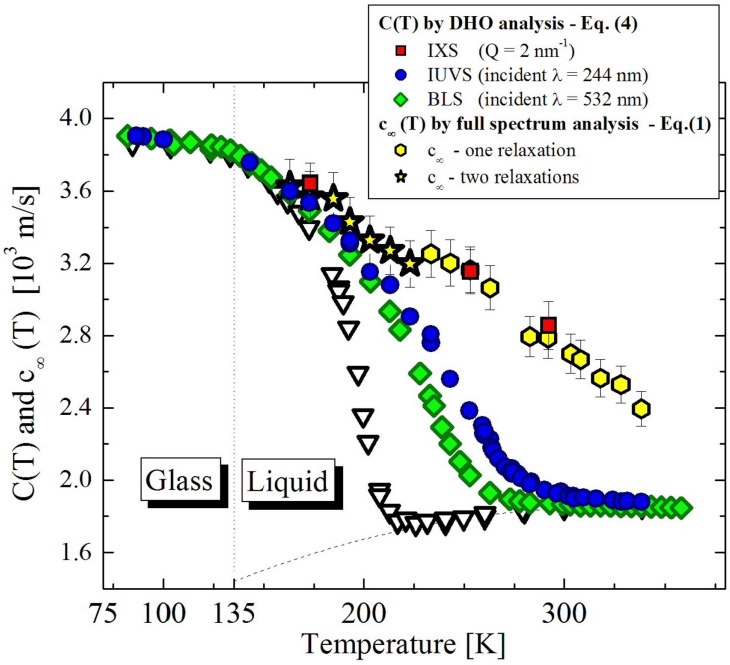


Figure 5.5: Temperature dependence of the apparent sound velocity, $C(T)$, in the LiCl-6H_2O solution, measured in this work by means of BLS (green diamonds), IUVS (blue circles) and IXS (red squares), obtained by Eq. (5.5). For sake of comparison, literature data are also reported: $C(T)$ in glassy phase, measured by IXS (open squares) [162] and $C(T)$ measured by ISS (Ref. [158])(open triangles). The high frequency limiting values $c_\infty(T)$ obtained by joint analysis in this work are shown, as yellow hexagons and stars: at above $\sim$ 220 K only one relaxation is sufficient to model the spectra (hexagons); below $\sim$ 220 K two relaxations are needed to give a satisfactorily description of the spectra (stars). Values of $c_\infty(T)$ are also reported in the tables of Figs. 5.7 and 5.8. The interpolation of the low frequency limit values $c_0(T)$is also shown, as dashed line and is got from Ref. [158]. The vertical dotted line in correspondence of T_g = 135 K indicates the transition between liquid and glassy phase.

In Fig. 5.6 the longitudinal apparent kinematic viscosity η_l/ρ calculated from DHO linewidths as

$$\frac{\eta_l}{\rho} = \frac{\Gamma}{Q^2} \tag{5.6}$$

is reported as a function of temperature.

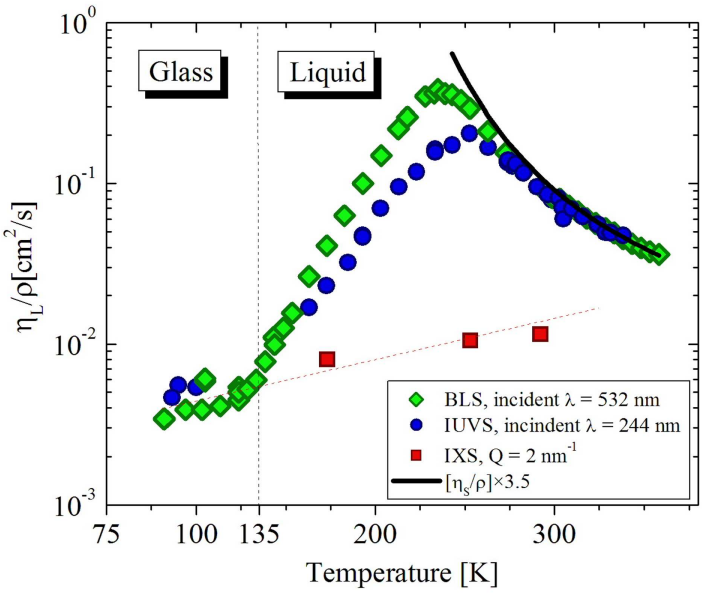


Figure 5.6: Temperature dependence of the apparent longitudinal kinematic viscosity of LiCl - H_2O, as obtained by BLS (green diamonds), IUVS (blue circles), IXS (red squares). The values have been calculated through Eq. (5.6). The linear dotted line on IXS data is a guide to the eye. The kinematic shear viscosity η_S/ρ from Ref. [163] has been multiplied by the ad-hoc constant factor 3.5 in order to match η_L/ρ at high temperatures. It is reported as a black thick line. The vertical dotted line in correspondence of T_g = 135 K marks the separation between the liquid and the glassy phase.

The values of $\eta_l/\rho(T)$ obtained by BLS and IUVS spectra exhibit maxima which correspond to the dispersion in sound velocity, at temperatures where the relaxational dynamics mostly affects the longitudinal acoustic modes. The Γs of IXS spectra are related to the unrelaxed longitudinal kinematic viscosity through the relationship $\Gamma/Q^2 = \eta_\infty/\rho$. The values obtained by IXS have an almost constant temperature dependence in the whole range investigated: 8x10^{-3} ¡ η_∞/ρ¡ 10^{-2} cm^2/s. For each temperature, the value of η_∞ has been kept fixed, in the full-spectrum analysis (see next Section).

It is interesting to compare η_L to the shear viscosity, η_s, which has been measured at low frequencies. Above 250 K, $\eta_s(T)$ exhibits a temperature dependence proportional to that of $\eta_L(T)$, with an almost constant ratio η_L/η_s = 3.5. In Fig. 5.6, η_s/ρ x 3.5 is also reported. This ratio is related to longitudinal acoustic absorption and classical absorption α_{cl}, through the relationship $\alpha/\alpha_{cl} = 3/4\ \eta_L/\eta_s$ [164]. In LiCl-6H2O we obtain α/α_{cl} = 2.6. According to Pinkerton's classification of liquids [164], an α/α_{cl} ratio between 1 and 3 is typical of associated liquids, while values greater than 3 are typical of Kneser liquids, where secondary relaxation channels are active for the dissipation of acoustic energy. According to this classification, LiCl-6H_2O at high temperature is an associated liquid with a value of α/α_{cl} not far from 3, the value of pure water [164].

5.3.2 Full Spectrum Hydrodynamic Analysis

The intermediate regime between the relaxed and the unrelaxed limits is highly informative because the characteristic time and shape of the relaxation processes evolving in the system are embedded in this spectral region [101]. In figures 5.5 and 5.6 we observe a clear deviation from the relaxed and unrelaxed regimes, between 338 and 163 K. In this temperature range we performed the analysis of the full-spectrum analysis by fitting equation (5.1), convoluted with the appropriate experimental resolutions, to the spectra. We used a LevenbergMarquardt minimization algorithm. The elastic modulus was modeled according to Eq. (5.2), using a ColeDavidson expressionEq. (5.3)for the relaxing part. We found indications for the Cole-Davidson relaxations in LiCl-6H2O in previous investigations [157, 158].

In Fig. 5.4, the joint-fit lines of three triplets of spectra are reported. Spectra acquired at same temperatures by different techniques were analyzed simultaneously. Throughout all the data analysis, η_∞ was fixed to the values we measured by IXS and c_0 to measured values or extrapolated by ISS [158] (see Figs. 5.5 and 5.6). Above $\approx$ 220 K, a single-relaxation model was sufficient to describe the spectra and three parameters $c_\infty(T)$, $\tau_{CD}(T)$, and $\beta_{CD}(T)$ were left to vary freely. The best-fitting values are reported in the table of Fig. 5.7 and plotted in Fig. 5.5 ($c_\infty(T)$) and and Fig. 5.9 ($\langle\tau(T)\rangle = \tau_{CD}(T)\beta_{CD}(T)$).

T [K]	τ_{CD} [ps]	β	c_0 [$\cdot 10^3$ m/s]	c_∞ [$\cdot 10^3$ m/s]
233	27.7±0.5	0.41±0.04	1.76	3.25±0.13
243	18.9±0.4	0.38±0.04	1.78	3.20±0.13
253	11.6±0.4	0.38±0.04	1.79	3.17±0.13
263	12.0±0.2	0.30±0.04	1.80	3.06±0.12
283	6.8±0.2	0.39±0.04	1.83	2.79±0.11
292	6.1±0.2	0.37±0.04	1.84	2.78±0.11
303	5.8±0.2	0.32±0.02	1.84	2.70±0.11
308	5.0±0.2	0.34±0.02	1.84	2.67±0.11
318	4.6±0.1	0.36±0.02	1.85	2.56±0.10
328	4.0±0.1	0.36±0.02	1.85	2.53±0.10
338	0.4±0.1	0.37±0.02	1.85	2.39±0.10

Figure 5.7: Best fit parameters of the joint analysis with the single-relaxation lineshape Eq. (5.3) in the fitting function, Eq. (5.1).

Below $\approx$ 220 K we found a progressive inadequacy of the single-relaxation modeling. Indication for a possible additional feature had been given in previous works, [156, 157, 158, 108], where a single-relaxation model had been postulated. With respect to these works, the joint analysis by means of BLS, IUVS, and IXS is performed over a broader frequency range and can give insight into a splitting of the $\alpha - \beta$ relaxations and into the nature of the β-relaxation itself. To take two processes into account, we used the sum of two ColeDavidson relaxation functions, in place of Eq. (5.3),

$$\Delta M^*(\omega) = \frac{M_0 - M_i}{(1 + i\omega\tau_\alpha)^{\beta_\alpha}} + \frac{M_i - M_\infty}{(1 + i\omega\tau_\beta)^{\beta_\beta}} \tag{5.7}$$

where M_i is the intermediate value of the modulus, $\tau_\alpha(\tau_\beta)$ and $\beta_\alpha(\beta_\beta)$ are are, respectively, the relaxation time and the stretching parameter of the $\alpha - (\beta-)$ relaxation. On lowering the temperature below $\sim$220 K, the $\alpha-$ relaxation progressively exits our experimental spectral window, becoming too slow for being measured. For this reason fixed the values of τ_α and τ_β (see table in Fig. 5.8) to those previously obtained by ISS, which are compatible with elastic modulus formalism approach [157, 158]. We assessed such compatibility by means of PCS measurements (see Fig. 5.9)

The optimization was performed using four free parameters: $\tau_\beta(T)$, $\beta_\beta(T)$, $c_i(T)$ - being $M_i = c_i^2/\rho$ - and $c_\infty(T)$. The results are reported in the table in Fig. 5.8 and in Fig. 5.5 ($c_\infty(T)$) and Fig. 5.9 ($\langle\tau_\beta\rangle = \tau_\beta\beta_\beta$ and $\langle\tau_\alpha\rangle = \tau_\alpha\beta_\alpha$).

T [K]	τ_β [ns]	β_β	τ_α [ns]	β_α	c_0 [$\cdot 10^3$ m/s]	c_i [$\cdot 10^3$ m/s]	c_∞ [$\cdot 10^3$ m/s]
163	4.87±0.09	0.49±0.02	2787	0.3	1.56	2.98±0.09	3.63±0.15
173	2.27±0.09	0.41±0.04	179	0.3	1.59	2.87±0.09	3.56±0.14
183	0.93±0.02	0.42±0.04	23.6	0.3	1.63	2.90±0.09	3.54±014
193	0.23±0.02	0.56±0.04	4.00	0.3	1.66	2.56±0.08	3.43±0.13
203	0.089±0.002	0.63±0.04	1.14	0.3	1.69	2.39±0.07	3.34±0.13
213	0.058±0.002	0.55±0.02	0.360	0.3	1.72	2.22±0.07	3.27±0.13
223	0.036±0.002	0.55±0.02	0.142	0.3	1.73	2.22±0.06	3.20±0.13

Figure 5.8: Best fit parameters of the joint analysis with the double-relaxation lineshape equation (5.7) in the fitting function, Eq. (5.1).

The change between one and two relaxation regimes occurs smoothly on cooling the system between 223 and 213 K. At these temperatures, the spectra can be fitted by including either one or two relaxations, with no significant changes in the final value of χ^2. However, as the use of two relaxations gives a smoother temperature dependence of parameters, only the results from this last kind of analysis is reported here. An indicative splitting temperature is identified to be ≈ 220 K. At lower temperatures, the spectra cannot be fitted anymore by means of a single-relaxation model. This is accounted for by the residuals, e.g. at 173 K. In the bottom panels of Fig. 5.4 the residuals clearly infer that taking into account two relaxation better describes the spectra.

In Fig. 5.5 the values of $c_\infty(T)$ are reported. An increasing trend as a function of decreasing temperature is found, as in other glass formers [165, 166]. The values found by full-spectrum analysis are consistent with the results obtained independently by the DHO analysis of IXS spectra. The total variation is between 2400 m/s and 3600 m/s. The characteristic times of both relaxations are displayed as a function of reversed temperature in Fig. 5.9 together with literature data.

The $\beta-$relaxation times follow an Arrhenius law with activation energy $E_a \approx 23$ kJ/mol. It is worth noting that the same activation energy can be obtained from literature data [155]. By a constant multiplicative factor of ≈ 6, which compensates for different origin, the $\beta-$relaxation times of literature are brought to coincide with our results (see Fig. 5.9). This fact is compatible with the possibility that the same $\beta-$process is perceived by different observables. The amplitudes of the relaxations are reported as a function of temperature in Fig. 5.10

The amplitude of the single relaxation above ≈ 220 K is $\Delta_1 = (M_\infty - M_0)/\rho$. Below this temperature, the relaxation amplitudes are $\Delta_\alpha = (M_i - M_0)/\rho$ and $\Delta_\beta = (M_\infty - M_i/\rho)$. Since the amplitude is proportional to the energy dissipated by the sound modes through the relaxation processes, the trends in Fig. 5.10 show that the onset of the $\alpha-$relaxation occurs as a splitting, to the expense of the $\beta-$process, which starts weakening upon cooling.

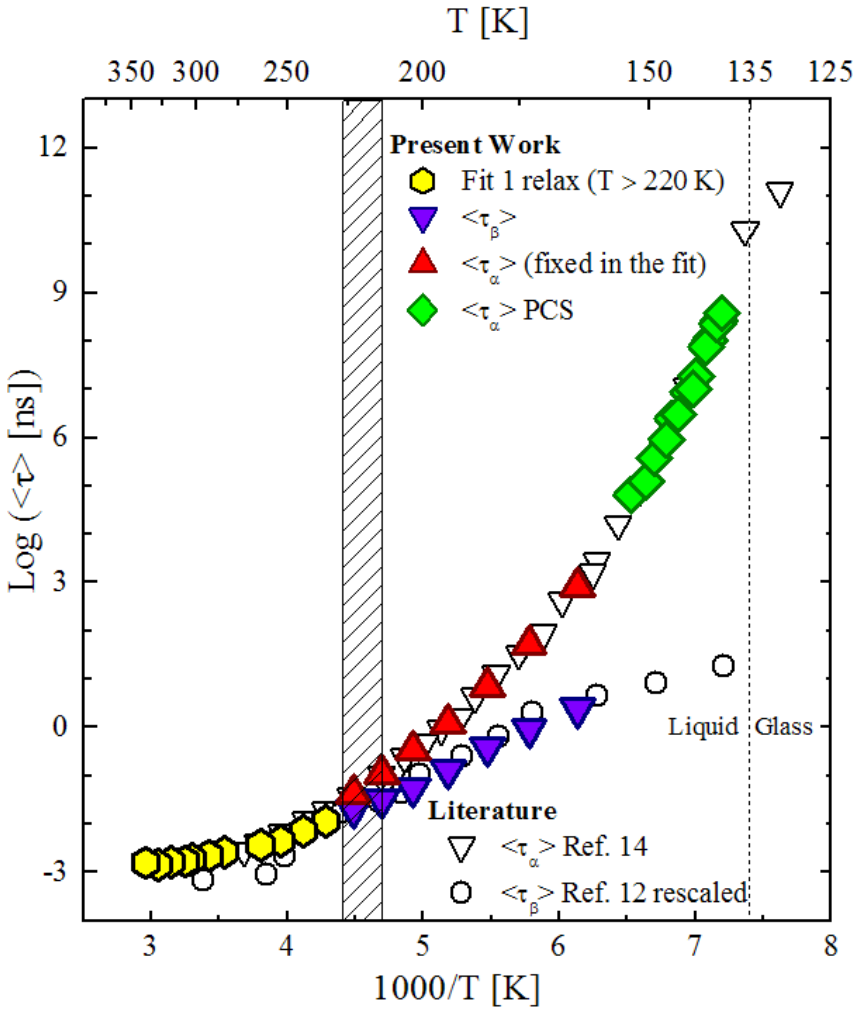


Figure 5.9: Arrhenius plot of the relaxation times in the LiCl-6 H_2O solution. Colored symbols are from the present work, black and white from the literature. The average times of the single-relaxation which dominates the dynamics at higher temperatures (T $>\sim$ 220 K) are reported as yellow hexagons. Below $\sim$ 220 K, two relaxations ($\alpha-$ and $\beta-$) are needed for Eq. (5.1) to fit the spectra: the β-relaxation times are reported in violet top-down triangles and the α-relaxation times as top-up red triangles. The shaded rectangle highlights the splitting region. Since the α-relaxation times above $\sim$ 220 K exit the frequency window probed by inelastic scattering techniques, they have been constrained, during the analysis, to the values measured by ISS (open top-down triangles) [157]. The $\alpha-$relaxation times at low temperatures, measured by PCS, are also reported (green diamond), confirming that the physical description of relaxation is equivalent as in ISS, and that ISS is a reliable source of information to complete our low frequency data. The $\beta-$ relaxation times obtained by various techniques [155], are reported as open circles, after having been re-scaled by a multiplicative factor of 6 over our results, since those techniques probe different observables. The vertical dotted line in correspondence of T_g = 135 K marks the separation of liquid and glassy phase.

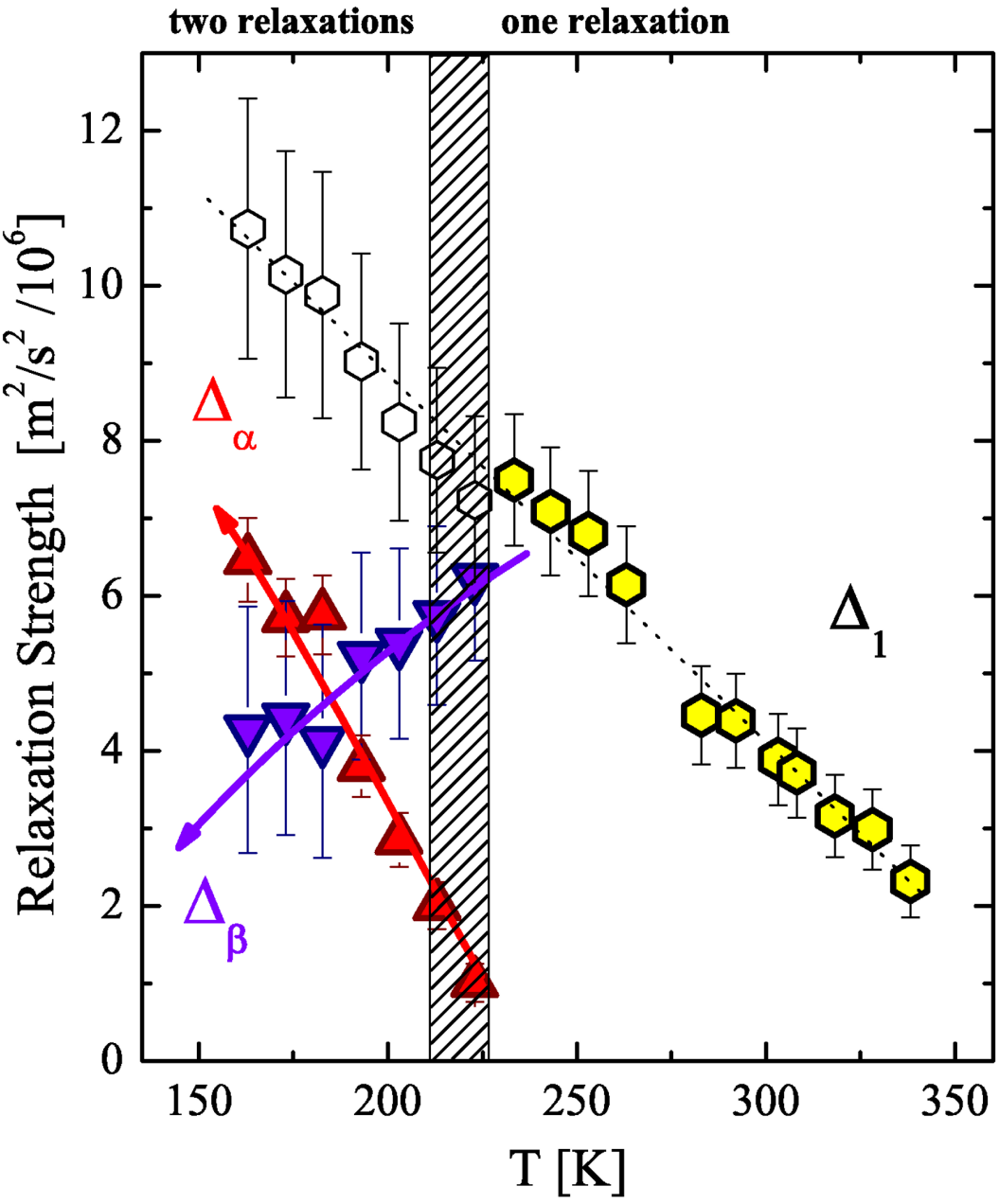


Figure 5.10: Temperature dependence of the relaxation strengths. At high temperature, there is a single relaxation process whose strength, $\Delta_1 = (M_\infty - M_0)/\rho$ is reported as yellow hexagons. Below $\sim$ 220 K the onset of the $\alpha-$process appears, with an increase in the the amplitude $\Delta_\alpha = (M_i - M_0)/\rho$ (red top-up triangles), while the $\beta-$relaxation amplitude $\Delta_\beta = (M_\infty - M_i)/\rho$, fades (violet top-down triangles). The sum of the amplitudes (open hexagons) continues the trend of the single high-temperature process, after the splitting. The shaded rectangle highlights the splitting region and the straight lines are guides for the eyes.

5.4 Discussion

The temperature dependence of the relaxation strengths in LiCl - $6H_2O$ reveals the development of $\alpha-$ and $\beta-$ relaxations. The $\beta-$ process is the low-temperature continuation of the single high-temperature process, while the $\alpha-$ process has its onset from the $\alpha - \beta$ splitting

The $\beta-$relaxation of LiCl-$6H_2O$ is of so-called L-type [167], characterized by amplitude decrease on cooling. Such a feature is common to materials like d-Sorbitol [168], Toluene and 1-Propanol [169] in random copolymers of poly(*n*-butyl methacrylate-*stat*-styrene) [170], and some epoxy systems [142].

From a theoretical point of view, an onset of $\alpha-$ from $\beta-$ process had been predicted for the rotational relaxations in solutions of small molecules in supercooled fluids [171], qualitatively similar to the one we have found here. It is also worth noting that the behavior we have found resembles coupling phenomena between *soft lattice modes* and *relaxation modes* of lower frequency reported on approaching structural phase transitions in crystalline solids [172]. Herein also, the strength and the relaxation time of the lower frequency process both increase critically, at the expense of the pre-existing mode whose amplitude and frequency keep decreasing slowly. Indeed, the nature and interplay of $\alpha-$ and $\beta-$ relaxations in glass-forming systems is a largely debated topic. A great impulse to the study of secondary processes and of their connection with the glass transition has been recently given by experimental studies performed as a function of pressure. It has been determined that secondary relaxations can be divided into two wide classes [173, 174, 175].

1. Processes that do not shift toward lower frequencies on increasing the pressure, related to local motion arising from intramolecular degrees of freedom, without interplay with the glass transition.

2. Processes which shift with pressure increase, sensitive to changes in the specific volume and entropy, as the $\alpha-$relaxation. For these processes, a good agreement was found with the predictions of the coupling-model [173]. They typically decouple from the $\alpha-$relaxation at a time longer that 10^{-6} s. This second kind of process is called JohariGoldstein (JG) relaxation [176].

There are indications from literature [155] that the $\beta-$relaxation of LiCl-$6H_2O$ solutions is intimately related to the $\alpha-$relaxation, following the predictions of the coupling-model which is able to give a consistent explanation of the presence of $\alpha-$ and $\beta-$ relaxations and the temperature dependence of their characteristic times.

On the other hand, there are some critical points arising from our results, which discourage the interpretation of the $\beta-$process either in terms of the coupling model or as a $\beta_{JG}-$ relaxation. In fact, the stretching parameter of the coupling model, obtained in [155], should approach 1 at high temperature, but neither previous ISS nor our data give evidence of this limiting value. Moreover, in the liquid phase, the $\beta-$relaxation of LiCl6H2O is very fast, reaching a characteristic time of about 10^{-10} s at the splitting region instead of 10^{-6} s, more typical of the JG relaxations. This $\beta-$relaxation is not only the natural continuation of the high-temperature relaxation (Figs. 5.9 and 5.10) but it also exhibits an apparent activation energy of about 23 kJ/mol below the $\alpha-$-$\beta-$ splitting (between 220 and 163 K), a value compatible with the breaking and formation of a single hydrogen bond and with a JG secondary relaxation [176]. The temperature dependence of the activation energy of the $\beta-$ relaxation for lower temperatures, and particularly around the glass transition [155], is instead unusually low for a glass former [176] ($\approx 2RT_g$) and typical of many non-JG secondary relaxations. For these, a minimal model has been suggested [177, 178], consisting on localized motions in an asymmetric double well potential. Moreover, a peculiarity of LiCl6H2O that distinguishes it from systems with $\alpha-$-$\beta_{JG}-$ splitting, is the onset of the $\alpha-$-relaxation close to the splitting and to the melting temperature. Other cases where similar behavior was observed include ibuprofen [179], poly (phenyl glycidyl ether)-coformaldehyde (PPGE)[180] and di-glycidyl ether of bisphenol A (DGEBA)[142], where two crossover regions were found, characterized by the splitting of relaxation processes. The high temperature crossover, called γ-crossover, is located at $T_c(\gamma) \approx (1.4 - 1.5)Tg$ and at a relaxation time $\tau_c(\gamma) \approx 10^{-10}$s, i.e., close to that we find for LiCl6H2O. In all these cases, the fast secondary process was not a $\beta_{JG}-$ relaxation.

An additional hypothesis about the origin of the secondary relaxation may come from recent theories and experimental results concerning the dynamics and phase diagram of water and of dilute ion solutions at low temperatures and high pressures. Considerations are drawn in the section of general conclusions, where the solution is compared to the pure solvent, revealing interesting coincidences.

Concerning the nature of the β-relaxation, further investigation is required to understand whether it is a JG-type relaxation, intimately related to the glass transition, a relaxation due to molecular degrees of freedom or it is connected to the liquid-liquid phase transition hypothesized for water and LiCl solutions near the homogenous nucleation temperature. In order to discriminate among these three possibilities, measurements as a function of pressure are scheduled in our laboratories.

Conclusions (Français)

Depuis des décennies, l'étonnant diagramme des phases stables et métastables de l'eau reste l'objet de nombreuses questions non résolues. La phase liquide surfondue est séparée de la phase vitreuse (glace amorphe) par un intervalle de température qualifié de *no man's land* qui s'étend sur une centaine de degrés et dans lequel il est impossible d'éviter la cristallisation. Dans la phase liquide surfondue, plusieurs caractéristiques thermodynamiques de l'eau présentent des comportements critiques. Toutes ces variations anomales peuvent être décrites par des lois de puissance divergeant à une température $T_S \approx 228$ K qui se situe dans le no *man's land*. Malgré de nombreuses tentatives théoriques et expérimentales, il nous manque encore une description cohérente, capable d'expliquer l'ensemble des propriétés observées. Les simulations de dynamique moléculaire indiquent, pour l'eau, un gel de la relaxation structurale à une température $T_c = 220$ K, qui est en accord avec les prédictions de la théorie de couplage de modes (MCT).

Dans ce travail, nous avons cherché à comparer nos résultats expérimentaux dans l'eau liquide et surfondue aux approches numériques de dynamique moléculaires et à celle de la theorie de couplage de modes. Nous avons mesuré le facteur de structure dynamique entre 343 K et 251K à différents vecteurs de diffusion, Q, dans la gamme 0,02 - 0,1 nm^{-1}, en utilisant, pour la première fois la technique de diffusion inélastique de la lumière ultraviolette (IUVS). La mesure des propriétés dynamiques de l'eau surfondue a en effet constitué un des premiers objectifs majeurs de la nouvelle ligne de lumière IUVS du synchrotron Elettra de Trieste. Pour calibrer ces résultats par rapport à une référence, avons aussi mesuré le facteur de structure dynamique par diffusion Brillouin (BLS) dans le domaine visible. L'une des originalités de ce travail est l'analyse simultanée des spectres d'IUVS et de BLS, obtenus, à la même température, donnant accès à une fenêtre de fréquence couvrant trois décades qui permet une comparaison plus fine aux prédictions des modèles théoriques.

Nous avons caractérisé la relaxation structurale de l'eau liquide et de l'eau surfondue en utilisant un formalisme de module élastique complexe (et de fonction mémoire) qui donne une évaluation précise du temps de relaxation moyen, de sa distribution, de la vitesse du son et de ses limites à haute fréquence et à basse fréquence. La comparaison de ces résultats à ceux des précédentes mesures de diffusion inélastique des rayons X (IXS) montre une bonne cohérence d'ensemble qui conforte l'interprétation du *second son* dans l'eau par un mécanisme de relaxation structurale. Les temps de relaxation déduits des expériences sont en bon accord avec les simulations de dynamique moléculaire et avec la théorie MCT. Nous avons trouvé un comportement en exponentielle étirée pratiquement indépendante de la température et une dépendance en loi de puissance qui diverge non loin de $T_c = 220$ K, et non loin de la température critique o ù les propriétés thermodynamiques et de transport semblent aussi présenter un comportement anomal.

L'analyse de nos résultats s'appuie sur l'idée d'un gel des fluctuations de densité à longue portée susceptible d'expliquer l'augmentation de la densité moyenne et la viscosité de cisaillement augmentant avec le temps de relaxation structurale. En fait, la théorie MCT peut être considérée comme une approximation au premier ordre d'un processus plus complexe dans lequel la transition cinétique apparaît comme un artefact qui disparait lorsque le couplage avec les quantités de mouvement des particules est pris en compte. La température T_c conserve la signification d'un

changement de régime entre deux comportements dynamiques. Au dessus de T_c, les effets de *hopping* sont négligeables et la théorie MCT simplifiée permet d'interpréter la dynamique lente. Par contre, en dessous de T_c, ni la théorie, ni les expériences ne fournissent d'information sur le comportement attendu.

Une voie indirecte pour aborder ce sujet est l'étude des solutions LiCl-RH$_2$O, avec R le rapport molaire de l'eau au sel. Pour $R = 6$ la solution reste amorphe jusqu'à basse température avec une transition vitreuse à T_g =135 K, proche de celle de l'eau pure. Nous avons mesuré le facteur de structure dynamique de cette solution par diffusion inélastique dans les domaines visible, UV et rayons-X de 1 GHz à 10 THz ainsi que par spectroscopie de corrélation de photons de 0.01 Hz à 20 KHz. L'étude d'une telle gamme de fréquence a permis d'analyser la dynamique entre 353 K and 80 K, un domaine de température dans lequel la solution passe continuement de la phase liquide à la phase vitreuse. Comme dans le cas de l'eau pure, l'analyse simultanée des spectres BLS, IUVS and IXS montre, à haute température, un simple processus de relaxation qui se divise, en dessous de 220 K, en deux mécanismes distincts : une relaxation structurale et une relaxation secondaire, cette dernière étant dans le prolongement du comportement à haute température. D'autres études sont en cours pour essayer de comprendre la nature de cette relaxation secondaire.

Au delà des propriétés spécifique de cette solution aqueuse, il est intéressant de comparer sa relaxation à haute fréquence à celle de l'eau pure. On observe des similitudes qui sont montrées sur la 5.11 : les vitesses du son non relaxées, c_∞, et les temps de relaxation τ des deux systèmes ont des valeurs assez proches à haute température. Lors du refroidissement la dynamique de l'eau commence à ralentir avant celle de la solution et dans l'intervalle de température autour de 220 K, la dynamique relaxationnelle de l"eau présente un divergence de type MCT alors que celle de la solution se divise en deux modes.

Selon de récents résultats théoriques et expérimentaux concernant la dynamique et le diagramme de phase de solutions iniques diluées à basse température et à haute pression, la séparation dynamique que nous observons pourrait être connectée avec une hypothétique transition liquide-liquide d'une phase homogène vers un mélange d'eau pure à basse densité (LDL) et d'eau à haute densité encapsulant le chlorure de lithium (HDL+LiCl). L'existence d'une telle transition dans les solutions d'halogénures alcalins avait été proposée dans les années 60 par by C. A. Angell et coll. [181] et elle a été récemment invoquée en regard de l'une des configurations possibles du diagramme de phase de l'eau à basse température [3].

La présence de quantités modérées d'ions Li^+ et Cl^- pourrait avoir l'effet de déplacer, dans le plan $p - T$, la ligne de transition liquide-liquide de l'eau pure tandis qu'une grande partie des ions se concentrerait dans la phase HDL dès l'apparition de la transition. Mishima and Stanley [3] ont recennment proposé ce modèle à deux fluides pour l'interprétation de nouvelles données calorimétriques des solutions diluées de LiCl [182], en s'appuyant aussi sur des simulations [183] et des résultats expérimentaux sur la phase vitreuse [184]. Les phases LDL et HDL+LiCl seraient alors le pendant des phases amorphes de haute densité (HDA) et basse densité (LDA) trouvées dans l'eau [185],[186].

L'existence de deux phases liquides (LDL et HDL) qui se sépareraient en dessous d'un second point critique (220 K, 100 MPa) pourrait expliquer les anomalies de l'eau à pression atmosphérique en termes de précurseurs de la transition à deux liquides. Décider cependant si le rôle joué par les ions Li^+ et Cl^- serait de déplacer l'équilibre entre les deux phases rencontrées dans l'eau pure ou s'il faut faire appel à une phénoménologie complètement différente, requiert des investigation supplémentaires.

Perspectives

Ce travail pionnier a été réalisé à pression atmosphérique et la poursuite des expériences de diffusion inélastique de l'ultraviolet (IUVS) s'étend maintenant à d'autres domaines de la thermodynamique. Des études de l'eau surfondue sous pression ont été réalisées par IUVS [187] et elles confortent

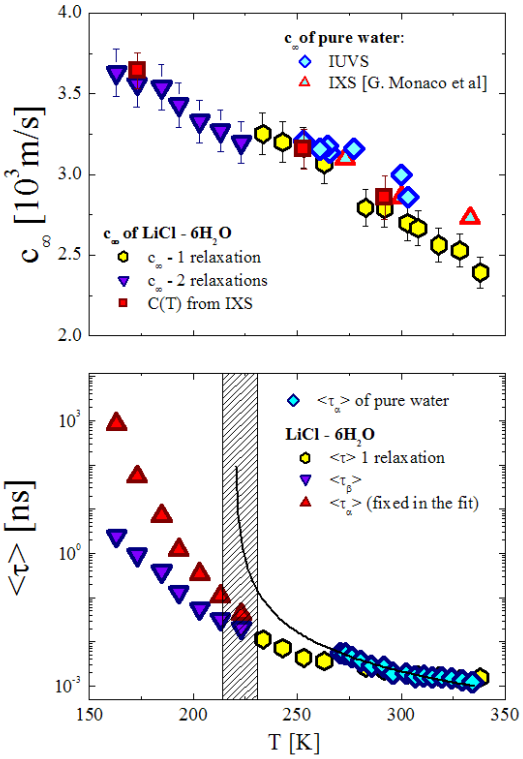


Figure 5.11: Comparaison entre les paramètres de relaxation dans l'eau pure et dans la solution LiCl-6H_2O. (a) Les valeurs limites haute fréquence de la vitesse du son dans la solution et dans l'eau pure (losanges cyans) sont voisines dans toute la gamme de température. (b) Les temps de relaxation moyens de l'eau pure (losanges cyans) sont représentés avec l'extrapolation prédite par la théorie du couplage de modes (ligne noire continue). Le domaine de température hachuré représente la région o ù l'eau présente un singularité et o ù apparaît le dédoublement de la relaxation structurale dans la solution LiCl-6H_2O.

l'hypothèse d'une transition de phase liquide-liquide [55, 56, 58]. Des études de la solution LiCl-$6H_2O$ on aussi été réalisées par IUVS sous pression en vue d'une comparaison avec l'eau [188].

Très récemment l'existence, dans l'eau, d'un point critique liquide-liquide a été déterminé par dynamique moléculaire à T ≈220 K et P ≈ 100 MPa [189], comme prédit par des travaux antérieurs [190]. Le point critique termine la ligne de Widom qui sépare les phases liquides de haute et de basse densité [62]. Dans le même travail, les auteurs ont aussi trouvé un second point critique (T = 230 K et P = -120 MPa) dans une solution à 0,67 Mol. de NaCl, suggérant que l'effet des ions ets de déplacer le diagramme de phase. Ce travail de simulation accrédite l'utilisation de solutions ionique de plus en plus diluées pour explorer le *no-man's land* de l'eau.

À présent, on cherche encore des expériences capables de discriminer entre les différentes interprétations des propriétés de l'eau et il manque à la communauté scientifique une vision unifiée de la phénoménologie de ce liquide. Avec ce travail nous espérons avoir apporté des éléments de connaissance et de méthodologie permettant de mieux comprendre cette substance fascinante qui a en commun avec notre vie d'être loin d'une compréhension totale.

Conclusions

The eccentric phase diagram of the stable and metastable states of water is a long backdated puzzle. The supercooled and glassy phases at ambient pressure are separated by a *no-man's land* where crystallinity is impossible to avoid, in bulk samples. In the supercooled phase, the absolute value of some transport and thermodynamic properties of water experiences an enormous increase, anomalous with respect to the behavior of most liquids in the same thermodynamic conditions. All these properties can be interpolated by a power law which diverges towards a temperature value, $T_S \approx 228$ K, which is located just into the *no-man's land*. Theoretical and experimental efforts of scientists have been devoted along decades to understand the origin of such a puzzling phase diagram and the apparent divergences. Due to the experimental impracticability of the no-man's land, a coherent unified picture able to explain the complete scenario of water properties is still far from being settled. Molecular dynamics simulations (MD) of water dynamics have given indication for the arrest of the structural relaxation at a temperature $T_c \approx 220$ K, in agreement with the interpretation of mode coupling theory (MCT), which had been originally formulated for the description of the glass transition.

In this work we have aimed at an experimental comparison to the dynamical viewpoint expressed by MD and MCT, through the investigation of the dynamical properties of water in its liquid and supercooled phases. We have measured the dynamic structure factor of superpure water between 343 and 251 K, at different Qs in the 0.02 - 0.1 nm^{-1} range, by using for the first time the technique of inelastic ultraviolet scattering (IUVS) which had been inferred, by previous studies, to be a unique tool, among other scattering techniques, to measure the dynamical properties of the supercooled state of water. The IUVS beamline of the Elettra synchrotron in Trieste was just ending its commissioning when this work begun. As a non negligible part of this work, we have aimed at showing, for the first time ever, the feasibility of IUVS measurements.

In addition, we have performed reference measurements in the relaxed regime of water dynamics by means of Brillouin light scattering (BLS). The qualifying point of our investigation has been the simultaneous analysis of spectra acquired at same temperature and different momentum transfers by IUVS and BLS, which has given access to a three decades wide frequency windows, reducing the indeterminacy which occurs in a narrow range.

We have characterized the structural relaxation of liquid and supercooled water in the formalism of the relaxing elastic modulus (and memory functions) and obtained an accurate evaluation of its features, i.e. the relaxation times and stretching, the apparent speed of sound and the limiting speeds of sound. The comparison of our results to previous measurements independently obtained by inelastic X-ray scattering (IXS) has shown a good continuity which has proved the reliability of the new-built beamline IUVS. The values of speed of sound, acquired at different momentum transfers thanks to the tunability of the synchrotron source, have shown the typical visco-to-elastic transition between the relaxed and unrelaxed frequency regimes, providing discriminating evidences in favor of the relaxational interpretation of the phenomenon of *fast-sound*.

The experimentally determined relaxation times and stretching parameters are in good agreement with the predictions of molecular dynamics simulations and mode coupling theory. We have found a stretched relaxation shape, almost temperature independent and slightly less than unity, and a power-law temperature dependence of the relaxation time, which diverges not far from T_S

$\approx T_c \approx 220$ K, where thermodynamic and transport properties of water are also inferred to diverge.

Our work infers a critical arrest in the long range density fluctuations of water, which explains the increase of the derivatives of the density. The shear viscosity increases with the structural relaxation time. Actually the ideal MCT can be considered a first order approximation in a more complex scheme where the kinetic transition is an artifact of the approximations involved and disappears when couplings with particle momenta are taken into account. The concept of T_c retains the meaning of a crossover temperature between two different dynamic behaviors and the prediction of the ideal MCT can be used to interpret the slow dynamics above T_c, when hopping effects are negligible. Unfortunately neither MCT theory nor the experiments give us information about the temperatures below T_c

An indirect route to a deeper supercooling of water is the investigation of progressively diluted aqueous solutions. The LiCl-RH$_2$O solutions, where R is the water to salt molar ratio, offer an interesting phase diagram with a maximum degree of supercooling for $R \approx 6$ and 4, whose T_g =135 K is close to the one of water. As a first step in this kind of approach, we have measured the dynamic structure factor of the R= 6 solution by means of inelastic scattering of radiation in the visible, UV and X-ray range, from 1 GHz to 10 THz and by means of photon-correlation spectroscopy, from 0.01 Hz to 20 KHz. The investigation of such a large frequency domain is necessary to follow the dynamics over the broad temperature range between 353 K and 80 K in which this solution passes from the hot liquid phase down to the supercooled and glassy phase. As in the case of water, the joint analysis of BLS, IUVS and IXS spectra in the relaxing modulus formalism has allowed the characterization of the relaxational dynamics of the R= 6 solution.

Our data show that a single relaxation process, which, at high temperatures, has features similar to those of the single relaxation of pure water, starts to differentiate into two relaxations, structural ($\alpha-$) and secondary ($\beta-$), upon cooling below $\sim$ 220 K. On cooling the system below this temperature, the relaxation strengths reveal an uncommon behavior with respect to most glass forming systems: the β relaxation is the continuation of the single process existing at high temperature and an onset occurs for the α- from the β-process. Studies are still under progress to understand the nature of this secondary relaxation.

Beyond the characterization of the solution itself, it is interesting to compare its relaxational properties to the ones of the pure solvent. Some coincidences are found, and reported in Figure 5.12: the unrelaxed sound velocities, c_∞, and the relaxation times τ of pure water and solution are quite close at high temperatures. On cooling, the dynamics of water starts slowing down, with respect to that of the solution. In the temperature range around 220 K the MCT power law of water diverges and the relaxational dynamics of the LiCl-6H$_2$O solution splits into two processes.

According to recent theories and experimental results concerning the dynamics and phase diagram of water and of dilute ion solutions at low temperatures and high pressures, the dynamical splitting that we observe could be possibly connected with the onset of the hypothetical liquid-liquid phase transition from the homogeneous liquid phase to a mixture of a low-density liquid pure water (LDL) and a high-density liquid water, encapsulating LiCl salt (HDL+LiCl). The existence of this transition in alkali halide aqueous solutions was proposed in the sixties by C. A. Angell and co-workers [181], supported by several authors across years and ultimately related to one of the possible conformations of the water phase diagram at low temperature [3].

The presence of moderate quantities of Li^+ and Cl^- ions could have the effect of shifting the liquid-liquid transition line of pure water to a different locus in the $p-T$ plane and the large part of the ions should move to the HDL phase as soon as the liquid-liquid transition occurs. Mishima and Stanley [3] have proposed this two-fluid model for the interpretation of new calorimetric data of dilute LiCl solution [182], relying also on simulations [183] and experimental work on LiCl solutions glasses [184]. LDL and HDL+LiCl would be, in this framework, the liquid counterparts, for LiCl

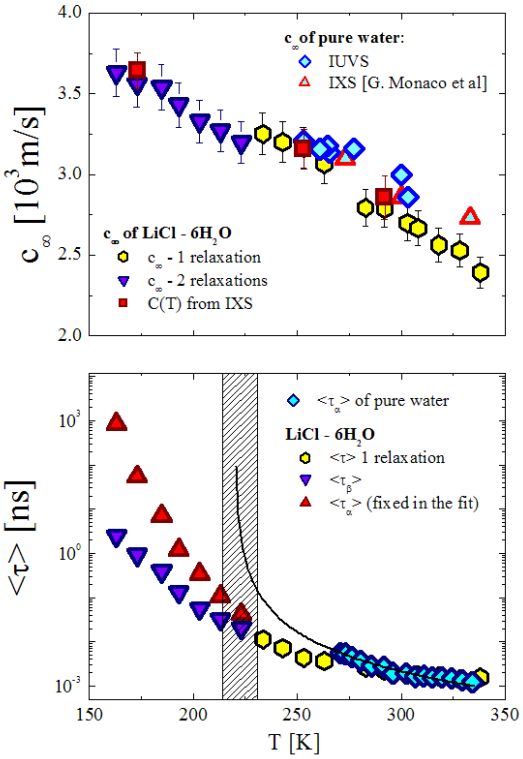


Figure 5.12: Comparison between the LiCl6H_2O solution and pure water relaxation parameters. (a) The limiting high frequency sound velocity of the solution and of pure water (cyan diamonds) are close to each other over the whole measured temperature range. (b) The average relaxation times of water (cyan diamonds) have been found to be interpolated by a diverging power law according to the previsions of mode coupling theory (bold black line). The slanted lines indicate the temperature region region where water has a singularity and the relaxation dynamics of LiCl6H_2O a splitting and the onset of the structural relaxation.

solutions, of the high and low density amorphous phases found in water (HDA [185] and LDA [186]), respectively.

The existence of two liquid phases, LDL and HDL, which separate below the second critical point (220 K, 100 MPa), could explain water's anomalies at ambient pressure in terms of the beginning of the two liquids transition. Whether the main role played by LiCl is that of perturbing the equilibrium between two species also present in pure water or that of introducing a completely new phenomenology, requires further investigations.

Lively trends

This pioneering work has been lead at ambient pressure. The prosecution of inelastic ultraviolet scattering experiments is now embracing a much wider and highly informative thermodynamic domain. Studies of supercooled water have been lead by IUVS under pressure [187], which support the liquid-liquid phase transition hypothesis [55, 56, 58]. IUVS experiments have also been performed on LiCl-6H_2O [188] as a function of pressure, aiming at the future comparison to water, to ascertain the physical origin of water anomalies .

Very recently, the existence of the liquid-liquid critical point in water has been found by molecular dynamics simulations [189] at T $\approx$ 220 K and P $\approx$ 100 MPa, as predicted by earlier works [190]. The critical point emanates the Widom line [62] which separates the low density liquid and the high density liquid phases [55, 56]. In the same work the authors have also found the second critical point in the 0.67 Mol/Kg solution of NaCl, at T = 230 and P = -120 MPa and suggested that the effect of ions is a shift of the phase diagram. This computational work strongly accredits the use of progressive dilution of ionic solutions in the experimental approach to the *no-man's* land of water.

At present, experiments able to clearly discriminate between different interpretations do not exist and the scientific community is still looking for an unified picture of the phenomenology of water. With the present work, I wish we have provided an useful piece of information and methodology towards the understanding of this fascinating substance, which is as common to our lives as far from our full comprehension.

Bibliography

[1] Thales the Milesian, as reported by Aristoteles in *Metaphysica*, Book I , 3, 983 b6, 8-11, 350 B.C. .

[2] G. W. Robinson, S-B. Zhu, S. Stingh, M. W. Evans, *Water in Biology, Chemistry and Physics, Experimental Overwievs and Computational Methodologies*, World Scientific, Singapore 1996.

[3] O. Mishima and H. E. Stanley, *Nature* **396**, 329 (1998).

[4] C. A. Angell, in *Water, a Comprehensive Treatise Vol. 7, Water and Aqueous Solutions at Subzero Temperatures*, edited by F. Franks, printed by Plenum Press, New York 1982.

[5] O. Mishima, *Nature* **384**, 546 (1996).

[6] C. A. Angell, *Science* **319**, 582 (2008).

[7] P. G. Debenedetti, *J. Phys.: Condens. Matter* **15**, R1669R1726 (2003).

[8] W. Götze, in: J.P. Hansen, D. Levesque, J. Zinn-Justin, Les Houches (Eds.), *Liquids, Freezing and the Glass Transition*, Session LI, 1989, North-Holland, Amsterdam, 1991.

[9] P. Gallo, F. Sciortino, P. Tartaglia and S-H Chen, *Phys. Rev. Lett.* **76** 2730 (1996).

[10] F. Sciortino, P. Gallo, P. Tartaglia, and S. H. Chen, *Phys. Rev. E* **54**, 6331 (1996).

[11] F. Sciortino, L. Fabbian, S-H Chen, Piero Tartaglia, *Phys. Rev. E* **56**, 5397 (1997).

[12] F. W. Starr, M.-C. Bellissent- Funel, and H. E. Stanley, *Phys. Rev. Lett.* **82**, 3629 (1999).

[13] F. W. Starr, F. Sciortino, and H. E. Stanley, *Phys. Rev. E* **60**, 6757 (1999);

[14] L. Fabbian, A. Latz, R. Schilling, F. Sciortino, P. Tartaglia, and C. Theis, *Phys. Rev. E* **60**, 5768 (1999).

[15] W. Götze and A. Sjögren, *Transp. Theory Stat. Phys.* **24**, 801 (1995).

[16] J. P. Boon and S. Yip in *Molecular Hydrodynamics*, Mc Grew Hill (1980).

[17] B.J. Berne and R. Pecora, *Dynamic Light Scattering*, John Wiley & Sons, New York (1976).

[18] F. Sette, M. H. Krish, C. Masciovecchio, G. Ruocco, G. Monaco, *Science* **280**, 5369 (1998).

[19] G. Monaco, A. Cunsolo, G. Ruocco and F. Sette, Phys. Rev. E **60**, 5505 (1999).

[20] A. Cunsolo and M. Nardone, *J. Chem. Phys.* **105**, 3911 (1996).

[21] C.Masciovecchio, D. Cocco, A. Gessini, *AIP Conf. Proc.* **705**, 1190 (2004).

[22] C. Masciovecchio, A. Gessini, S. C. Santucci, *J. non Crys. Sol.* **352**, 5126 (2006).

[23] C. Masciovecchio, S. C. Santucci, A. Gessini, S. Di Fonzo, G. Ruocco, and F. Sette, *Phys. Rev. Lett.* **92**, 255507 (2004).

[24] S. C. Santucci, S. Di Fonzo and C. Masciovecchio; *Jnl. of El. Spec. and Rel. Phen.* **144**, 941 (2005).

[25] S. C. Santucci, D. Fioretto, L. Comez, A. Gessini and C. Masciovecchio, *Phys. Rev. Lett.* **97**, 225701 (2006).

[26] J. Dupuy, J. F. Jal, B. Prevel, A. Aouizeratelarby, P. Chieux, A. J. Dianoux, and J-F Legrand, *Journal De Physique IV* **2(C2)** 179 (1992).

[27] S. C. Santucci, L.Comez, F. Scarponi, G. Monaco, R. Verbeni, J-F Legrand, C. Masciovecchio, A. Gessini and D. Fioretto, *J. Chem. Phys.* **131**, 154507 (2009).

[28] Calorimetry at Surfaces Using High-Resolution Core-Level Photoemission: S. C. Santucci *et al. Phys. Rev. Lett.* **93**, 106105 (2004).

[29] F. Franks, *Biochemistry and Biophysics at Low Temperatures*, Cambridge University Press, Cambridge (1985).

[30] P. G. Debenedetti and H. E. Stanley, *Physics Today* **56**,40 (2003).

[31] P. G. Debenedetti, *Metastable Liquids*, Princeton University Press (1986).

[32] S-H Chen, F. Mallamace, C. Y. Mou, M. Broccio, C. Corsaro, A. Faraone, and L. Liu, *P. Natl. Acad. Sci. USA* **29**, 12974 (2003).

[33] G. P. Johari, A. Hallbrucker and E. Mayer, *Nature* **330**, 552 (1987).

[34] V. Velikov, S. Borick and C. A. Angell *Science* **294**, 2335 (2001).

[35] C. A. Angell, *Chem. Rev.* **102**, 2627 (2002).

[36] A. Nagoe, Y. Kanke and M. Oguni, *J. Phys. Condens. Matter* **22**, 365105 (2010).

[37] J. Swenson and J. Teixeira, *J. Chem. Phys* **132**, 014508 (2010).

[38] S. Sastry, P. G. Debenedetti, F. Sciortino and H. E. Stanley *Phys. Rev. E* **53**, 6144 (1996).

[39] C. A. Angell and H. Kanno *Science* **193** 1121 (1976); S. J. Henderson and R. J. Speedy *J. Phys. Chem.* **91**, 3062 (1987).

[40] E. Donth, *The Glass Transition, Relaxation Dynamics in Liquids and Disordered Materials*, edited by Springer-Verlag, Berlin, 2001.

[41] M. D. Ediger, C. A. Angell, S. R. Nagel *J. Phys. Chem.* **100**, 13200 (1996).

[42] I. Kohl, L. Bachmann, A. Hallbrucher, E. Mayer and T. Loerting, *Phys. Chem. Chem. Phys.* **7**, 3210 (2005)

[43] E. F. Burton and W. F. Oliver, *Proc. R. Soc. Lond. A* **153**, 166 (1936).

[44] E. Mayer, in *Hydrogen Bond Networks*, eds. M-C Bellissent-Funel and J-C Dore, Kluwer Academic, Dordrecht 1994.

[45] P. Brüggeller, and E. Mayer, *Nature* **288**, 569 (1980).

[46] J. Dubochet and W. A. McDowall, *J. Microsc.* **124**, RP3-RP4 (1981).

[47] O. Mishima, L. D. Calvert and E. Whalley, *Nature* **310**, 393 (1984).

[48] R. J. Hemley, L. Chen, and H. Mao, *Nature* **338**, 638 (1989).

[49] F. Sciortino et al., *Phys. Rev. E* **52**, 6484 (1995).

[50] J. S. Tse and M. L. Klein, *Phys. Rev. Lett.* **58**, 1672 (1987).

[51] R. J. Nelmes, J. S. Loveday, Th. Straessle, C. L. Bull, M. Gutherie, G. Hamel and S. Klotz, *Nat. Phys.* **2**, 414 (2006).

[52] R. J. Speedy and C. A. Angell, *J. Chem. Phys.* **65**, 851 (1976).

[53] R. J. Speedy, *J. Chem. Phys.* **86**, 982 (1982).

[54] D. E. Hare and C. M. Sorensen, *J. Chem. Phys.* **84** 5085 (1986).

[55] P. H. Poole, F. Sciortino, U. Essmann and H. E. Stanley, *Nature* **360**, 324 (1992).

[56] P. H. Poole, F. Sciortino, U. Essmann and H. E. Stanley, *Phys. Rev. E* **48**, 3799 (1993).

[57] E. G. Ponyatovskii, V. V. Sinitsyn and T. A. Pozdnyakova, *JEPT Lett.* **60**, 360 (1994).

[58] P. H. Poole, F. Sciortino, T. Grande, H. E. Stanley, and C. A. Angell, *Phys. Rev. Lett.* **73**, 1632 (1994).

[59] S. S. Borick, P. G. Debenedetti and S. Sastry, *J. Phys. Chem.* **99**, 3781 (1995).

[60] C. T. Moynihan, *Two species/nonideal solution model for amorphous/amorphous phase transitions*, Mater. Res. Soc. Symp. Proc. **455**, 411 (1997).

[61] C. F. Tejero and M. Baus, *Phys. Rev. E* **57**, 4821 (1998).

[62] G. Franzese and E. H. Stanley, *J. Phys Condens. Matter* **19**, 205126 (2007).

[63] G. A. Appignanesi, J. A. Rodriguez Fris and F. Sciortino, *Eur. Phys. J. E* **29**, 305 (2009).

[64] H. E. Stanley and J. Teixeira, *J. Chem. Phys.* **73**, 3404 (1980).

[65] H. E. Stanley, *J. Phys. A: Math. Gen.* **12**, L329 (1979).

[66] R. L. Blumberg, G. Shlifer and H. E. Stanley*J. Phys. A: Math. Gen.* **13**, L147 (1980).

[67] Y. Xie, K. F. Ludwig, G. Morales, D. E. Hare and C. M. Sorensen, *Phys. Rev. Lett.* **71**, 2050 (1993).

[68] S. S. Borick, P. G. Debenedetti, and S. Sastry, *J. Phys. Chem.* **99**, 378 (1995).

[69] S. Sastry, P. G. Debenedetti, F. Sciortino, and H. E. Stanley, *Phys. Rev. E* **53**, 6144 (1996).

[70] P. G. Debenedetti, *Nature* **392**, 127 (1998).

[71] L. P. N. Rebelo , P. G. Debenedetti and S. Sastry, *J. Chem. Phys.* **109**, 626 (1998).

[72] T. M. Truskett, P. G. Debenedetti, S. Sastry, and S. Torquato, *J. Chem. Phys.* **111**, 2647 (1999).

[73] H. J. C. Berendsen, J. R. Grigera and T. P. Straatsma, *J. Phys. Chem.* **91**, 6269 (1987).

[74] W. Götze, L. Sjögren, *Rep. Prog. Phys.* **55**, 241 (1992).

[75] W. Götze, *J. Phys. Cond. Matter* **11**, A1 (1999).

[76] M. H. Cohen and D. Turunbull *J. Chem. Phys.* **31** 1164(1959)

[77] W. Götze, *Aspect of structural glass transitions*, Les Houches Session LI, 1989, Elsevier 1991.

[78] D. R. Reichman and P. Charbonneau, *Ann. Rev. of Phys. Chem.* **56**, 157 (2005).

[79] S. Corezzi, Ph.D. Thesis, *The role of configurational entropy in the liquid-glas transition* Università degli Studi di Perugia, 2002.

[80] G. Ruocco and F. Sette, *J. Phys.: Condens. Matter* **11** R259 (1999).

[81] A. Rahman and F. H. Stillinger, *Phys. Rev. A* **10**, 368 (1974).

[82] J. Teixeira, M. C. Bellissent-Funel, S. H. Chen, B. Dorner, *Phys. Rev. Lett.* **54**, 2681 (1985).

[83] G. Jacucci, M. Ronchetti and W. Schirmacher, *J. Physique Coll.* **8**, C8, 385 (1984); J. Bosse, G. Jacucci, M. Ronchetti, W. Schirmacher, *Phys. Rev. Lett.* **57**, 3277 (1986).

[84] W. Montfrooij, P. Westerhuijs, V. O. de Haan, and I. M. de Schepper, *Phys. Rev. Lett.* **63**, 544 (1989); M. Alvarez, F. J. Bermejo, P. Verkerk, B. Roessli, *Phys. Rev. Lett.* **80**, 2141 (1998).

[85] E. Enciso, N.G. Almarza, M.A. Gonzalez, F.J. Bermejo, R. Fernandez-Perea, F. Bresme, *Phys. Rev. Lett.* **81**, 4432 (1998).

[86] M. Sampoli, U. Bafile, E. Guarini and F. Barocchi, *Phys. Rev. Lett.* **88**, 085502 (2002).

[87] F. Sette, G. Ruocco, M. Krish, U. Bergmann, C. Masciovecchio, V. Mazzacurati, G. Signorelli and R. Verbeni, *Phys. Rev. Lett.* **75**, 850 (1995).

[88] M. A. Ricci, D. Rocca, G. Ruocco and R. Vallauri, *Phys. Rev. Lett.* **61**, 1958 (1988).

[89] J. C. Bacri and R. Rajaonaris, J. Phys. Lett. (Les Ulis) **40** , 2404 (1979); V. A. Del Grosso and C. W. Mader, *J. Acous. Soc. Am.* **52**, 1442 (1972); W. Wagner and A. Pruß, *J. Phys. Chem. Ref. Data* **31** , No. 2, p. 387 (2002).

[90] F. Sciortino and S. Sastry, *J. Chem. Phys.* **100**, 3881 (1994).

[91] E. Pontecorvo, M. Krish, A. Cunsolo, G. Monaco, A. Mermet, R. Verbeni, F. Sette and G. Ruocco, *Phys. Rev. E* **71**, 011501 (2005).

[92] C. Petrillo, F. Sacchetti, B. Dorner, and J.-B. Suck, *Phys. Rev. E* **62**, 3611 (2000); Sacchetti, J.-B. Suck, C. Petrillo, and B. Dorner, *Phys. Rev. E* **69**, 061203 (2004).

[93] R. Torre, P. Bartolini, R. Righini, *Nature* **428**, 296 (2004).

[94] W. Götze and M. Sperl, *Phys. Rev. Lett.* **92**, 105701 (2004).

[95] C. Despretz, *Ann. de Chimie et de Phys.* **70**, 23 (1837), *C. R. Acad. Sci., Paris* **4**, 124 (1837).

[96] L. C. de Coppet, *Ann. Chim. et Phys.* **6**, 275 (1875).

[97] G. E. Walrafen, *J. Chem Phys.* **40**, 3249 (1964).

[98] H. E. Moran Jr., *J. Phys. Chem.* **60**, 1666 (1956).

[99] G. Vuillard and J. J. Kessis, *Bull. Soc. Chem. Fr.* **336**, 2063 (1960).

[100] R. Kubo, *Rep. on Progr. Phys.* **29**, 255 (1966).

[101] J. Montrose, V. A. Solovyev, and T. A. Litovitz, J. *Acoust. Soc. Am.* **43**, 117 (1968).

[102] U. Balucani and M. Zoppi, "*Dynamics of the liquid state*", Clarendon Press, Oxford (1994).

[103] R. Bansal and K.N. Pathack, *Phys. Rev. A*, **9**, 2773 (1974).

[104] R. Bansal and K.N. Pathack, *Phys. Rev. A*, **11**, 724 (1975).

[105] R. Bansal and K.N. Pathack, *Phys. Rev. A*, **15**, 2519 (1977).

[106] R. Bansal and K.N. Pathack, *Phys. Rev. A*, **15**, 2531 (1977).

[107] R. Zwanzig, in *Lectures in Theoretical Physics*, edited by W. Brittin (Wiley-Interscience, New York, 1961), Vol. **3**, pp. 106141; H. Mori, *Prog. Theor. Phys.* **33**, 423 (1965).

[108] N. J. Tao, G. Li and H. Z. Cummins, *Phys. Rev. B* **45**, 686 (1992).

[109] D. Fioretto, L. Comez, G. Socino, L.Verdini, S. Corezzi, P. A. Rolla, *Phys. Rev. E* **59**, 1899 (1999).

[110] A. Einstein, *Ann. Phys.* **33** 1275 (1910)[English translation in *Colloid Chemistry*, J. Alexander ed., Vol. **I**, 323-339, New York (1929)].

[111] L. D. Landau and E. M. Lifshitz, *Electrodynamics of Continuous Media*, Addison Wesley, Reading, Mass. (1960).

[112] H. Z. Cummins, G. Li, W. Du, R. M. Pick and C. Dreyfus, *Phys. Rev. E* **53**, 896 (1996).

[113] T. Tanaka, H. Kitamura, *Nucl. Instr. and Meth. in Phys. Res. A* **364**, 368 (1995); T. Tanaka, H. Kitamura *J. Synchrotron Rad.* **3**, 47 (1996).

[114] B. Diviacco, R. Bracco, D. Millo, and D. Zangrando, in *Proceedings of the Eighth European Particle Accelerator Conference* (European Physical Society, Paris, 2002), p. 2610.

[115] M. Czerny and A. F. Turner, *Z. Phys.* **61**, 792 (1930).

[116] F. A. Jenkins and H. E. White, *Fundamentals of Optics*, McGraw Hill, 1957.

[117] H. Y. Hao and H. J. Maris, *Phys. Rev. B* **63**, 224301 (2001).

[118] *CRC handbook of Chemistry and Physics*, Ed. David R. Lide, 79 ed, 1999.

[119] N.W. Ashcroft and N.D. Mermin, *Solid State Physics*, Thomson/Brooks, 1976.

[120] See Group Website *http://ghost.fisica.unipg.it/*

[121] Filippo Scarponi, Ph.D. Thesis: *Collective Dynamics of λ Transition in Sulfrum*, Università degli Studi di Perugia, 2005.

[122] F. Nizzoli and J. R. Sandercock, in *Dynamical properties of Solids*, ed. by G. Horton and A. A. Maradudin (North-Holland, Amsterdam) 1990; http://www.jrs-si.ch/

[123] R. Verbeni, F. Sette, M. Krisch, U. Bergmann, B. Gorges, C Halcoussis, K. Martel, C. Masciovecchio, J. F. Ribois, G. Ruocco, H. Sinn, *J. Synchrotron Radiat.* **3**, 64 (1996).

[124] C. Masciovecchio, U. Bergmann, M. Krisch, G. Ruocco, F. Sette and R. Verbeni, *Nucl. Instrum. Meth. B* **111**, 181 (1996).

[125] C. Masciovecchio, U. Bergmann, M. Krisch, G. Ruocco, F. Sette and R. Verbeni, *Nucl. Instrum. Meth. B* **117**, 339 (1996).

[126] *Release on the Refractive Index of Ordinary Water Substance as a Function of Wavelength, Temperature and Pressure* by The International Association for the Properties of Water and Steam (IAPWS), Erlangen, Germany September 1997; and references therein.

[127] R. Onaka and T. Takahashi, *J. Phys. Soc. of Japan* **24**, 548 (1968).

[128] Standard Specifications for Reagent Water D1193-99 Vol. 11.01, page 104, in Annual Book of ASTM Standards 2000.

[129] GLAS Technik and Konstruktion, by Müller and Müller OHG, Germanenweg 13 c, D-14621 Schönwalde-Glien b. Berlin. Telefon: (0 33 22) 40 02 04.

[130] See website http://www.galenicasenese.it/

[131] J. Frenkel and J. Obraztsov, *J. Phys. URSS* **3**, 131 (1940); *J. Exptl. Theor. Phys. URSS*, **9**, 1081 (1939).

[132] J.J. Markham, *J. Acoust. Soc. Am.* **22**, 628 (1951).

[133] L. Hoff, *J. Acoust. Soc. Am.* **23**, 12 (1951).

[134] G. D. Patterson, G. R. Alms and C. P. Lindsey, *J. Chem. Phys.* **69**, 4802 (1978).

[135] G. Fytas, C.H. Wang, D. Lilge and Th. Dorfmüller, *J. Chem. Phys.* **75**, 4247 (1981).

[136] M.G. Sceats and J.M. Dawes, *J. Chem. Phys.* **83**, 1298 (1985).

[137] T. Scopigno, G. Ruocco and F. Sette, *Rev. Mod. Phys.* **77**, 881 (2005).

[138] C. P. Lindsey and G. D. Patterson, *J. Chem. Phys* **73**, 3348 (1980).

[139] J. C. Bacr and R. Rajaonaris, *J. Phys. Lett. (Les Ulis)* **40**, 2404 (1979); V. A. Del Grosso and C. W. Mader, *J. Acoust. Soc. Am.* **52**, 1442 (1972); W. Wagner and A. Pru, *J. Phys. Chem. Ref. Data* **31**, 387 (2002).

[140] C. J. F. Boettcher and P. Bordewijk in *Theory of Electric Polarization*, Elsevier, 1973.

[141] H. Vogel, *Physik Z.* **22**,645 (1921).

[142] S. Corezzi, E. Campani, P. A. Rolla, S. Capaccioli, D. Fioretto, *J. Chem. Phys.* **111**, 9343 (1999).

[143] I. Kohl, L. Bachmann, E. Mayer, A. Hallbrucker, T. Loerting, *Nature* **435**, E1 (2005).

[144] K. Hofer, E. Mayer, G. P. Johari, *J. Phys. Chem.* **95**, 7100 (1991).

[145] C. A. Angell, J. Non-Cryst. Solids **131**, 13 (1991).

[146] E. A. Jagla, *J. Phys. Cond. Matt.* **11**, 10251 (1999).

[147] H. Lodish, A. Berk, P. Matsudaira, C.A. Kaiser, M. Krieger, M. P. Scott, S. Lawrence Zipursky, J. Darnell in *Molecular Cell Biology - 5th ed.*, W. H. Freeman and Company (2004). ISBN 0-7167-4366-3.

[148] S. Bouazizi, S. Nasr, *J. Mol. Struct.* **837**, 206 (2007).

[149] I. Harsányi, L. Pusztai, *J. Chem. Phys.* **122**, 124512 (2005).

[150] B. Prével, J. Dupuy-Philon, J. F. Jal, J-F Legrand, P. Chieux, *J. Phys.: Condens. Matter* **6**, 1279 (1994).

[151] J. Colombani, J. Bert, and J. Dupuy-Philon, *J. Chem. Phys.* **110**, 8622 (1999).

[152] J. Pátek, J. Klomfar, *Fluid Phase Equilib.* **250**, 138 (2006).

[153] J. Dupuy-Philon, J. F. Jal, B. Prével, *J. Mol. Liquids* **64**, 13 (1995).

[154] B. Prével, J. F. Jal, J. Dupuy-Philon, A. K. Soper, *J. Chem. Phys.* **103**, 1886 (1995).

[155] P. O. Maurin, *J. Chem. Phys.* **109**, 10936 (1998).

[156] N. J. Tao, H. Z. Cummins, *Phys. Rev. B* **43**, 5815 (1991).

[157] I. C. Halalay and K. A. Nelson, *Phys. Rev. Lett.* **69**, 636 (1992).

[158] I. C. Halalay and K. A. Nelson, *J. Chem. Phys.* **97**, 3557 (1992).

[159] Up-to-date website: http://www.esrf.eu/UsersAndScience/Experiments/HRRS/ID16/

[160] L. Comez, D. Fioretto, H. Kriegs W. Steffen, *Phys. Rev. E* **66**, 032501 (2002).

[161] R. Pick, private communication.

[162] C. Masciovecchio, G. Ruocco, F. Sette, M. Krisch, R. Verbeni, U. Bergmann, M. Soltwisch, *Phys. Rev. Lett.* **76**, 3356 (1996).

[163] C. T. Moynihan, N. Balitactac, L. Boone, and T.A. Litovitz, J. Chem. Phys. 55, 3013 (1971).

[164] K. F. Herzfeld and T. A. Litovitz, *Absorption and Dispersion of Ultrasonic Waves* Academic Press, London (1965).

[165] G. Monaco, D. Fioretto, L. Comez and G. Ruocco, *Phys Rev. E* **63**, 061502 (2001).

[166] L. Comez, D. Fioretto, F. Scarponi. G. Monaco, *J. Chem. Phys.* **119**, 6032 (2003).

[167] C. Hansen, R. Richert, *Acta Polymerica* **48**, 484 (2003).

[168] H. Wagner and R. Richert, *J. Phys. Chem. B* **103**, 4071 (1999).

[169] A. Kudlik, C. Tschirwitz, S. Benkhof, T. Blochowicz, E. Rössler, *Europhys. Lett.* **40**, 649 (1997).

[170] S. Kahle, J. Korus, E. Hempel, R. Unger, S. Höring, K. Schröter, E. Donth, *Macromol.* **30**, 7214 (1997).

[171] D. Kivelson and S. A. Kivelson, *J. Chem. Phys.* **90**, 4464 (1989).

[172] J. Hlinka, T. Ostapchuk, D. Nuhnyy, J. Petzelt, P. Kuzel, C. Kadlec, P. Vanek, I. Ponomareva, and L. Bellaiche, *Phys. Rev. Lett.* **101**, 167402 (2008).

[173] K. L. Ngai, S. Capaccioli, *J. Phys.: Condens. Matter* **20**, 244101 (2008).

[174] K. Kaminski, E. Kaminska, M. Paluch, J. Ziolo and K. L. Ngai, *J. Phys. Chem. B* **110**, 25045 (2006).

[175] S. Hensel-Bielowka, M. Paluch and K. L. Ngai , *J. Chem.Phys.* **123**, 014502 (2005).

[176] G. P. Johari and M. Goldstein, *J. Chem. Phys.* **53**, 2372 (1970).

[177] J. C. Dyre and N.B. Olsen, *Phys. Rev. Lett.* **91**, 155703 (2003).

[178] K. Grzybowska , A. Grzybowski , J. Ziolo, S. J. Rzoska and M. Paluch, *J. Phys.: Condens. Matter* **19**, 376105 (2007).

[179] A. R. Brás, J. P. Noronha, A. M. M. Antunes, M. M. Cardoso, Andreas Schönhals, F. Affouard, M. Dionísio, and N. T. Correia, *J. Phys. Chem. B* **112**, 11087 (2008).

[180] S. Corezzi, M. Beiner, H. Huth, K. Schröter, S. Capaccioli, R. Casalini, D. Fioretto, E. Donth, *J. Chem Phys.* **117**, 2435 (2002).

[181] C. A. Angell and E. J. Sare, *J. Chem. Phys* **49** (10), 4713 (1968).

[182] O. Mishima, *J. Chem. Phys.* **123**, 154506 (2005).

[183] D. Paschek, *Phys. Rev. Lett.* **94**, 217802 (2005).

[184] Y. Suzuki and O. Mishima, *Phys. Rev. Lett.* **85**, 1322 (2000).

[185] O. Mishima, L. D. Calvert and E. Whalley , *Nature* **314**, 76 (1985).

[186] E. F. Burton and W. F. Oliver, *Proc. R. Soc. Lond. A* **153**, 166 (1936).

[187] F. Bencivenga, A. Cimatoribus, A. Gessini, M. G. Izzo and C. Masciovecchio, *J. Chem. Phys.* **131**, 144502 (2009).

[188] S. Saccani, F. Bencivenga, A. Gessini and C. Masciovecchio, in press on *J. Non-Crys. Solids* (2010).

[189] D. Corradini, M. Rovere and P. Gallo, *J. Chem. Phys.* **132**, 134508 (2010).

[190] O. Mishima and H. E. Stanley, *Nature* **392**, 164 (1998).

[191] S. Sastry, *Nature* **398**, 467 (1999).

Appendix A

Publications

This work has lead to the following publications on scientific journals:

1. Structural Relaxation in Liquid Water by Inelastic UV Scattering: C. Masciovecchio, S. C. Santucci, A. Gessini, S. Di Fonzo, G. Ruocco, and F. Sette, *Phys. Rev. Lett.* **92**, 255507 (2004).

2. Inelastic Ultraviolet Scattering from High Frequency Acoustic Modes in Glasses: C. Masciovecchio, A. Gessini, S. Di Fonzo, L. Comez, S. C. Santucci, and D. Fioretto; *Phys. Rev. Lett.* **92**, 247401 (2004).

3. Infinite frequency sound velocity in liquid water by inelastic UV scattering: S.C. Santucci, S. Di Fonzo and C. Masciovecchio; *Jnl. of El. Spec. and Rel. Phen.* **144**, 941 (2005).

4. Ultraviolet Brillouin scattering as a new tool to investigate disordered systems: C. Masciovecchio, A. Gessini, S. C.Santucci, *J. non Crys. Sol.* **352**, 5126 (2006).

5. Is there any Fast Sound in Water? S.C. Santucci, D. Fioretto, L. Comez, A. Gessini and C. Masciovecchio, *Phys. Rev. Lett.* **97**, 225701 (2006).

6. Onset of the alpha-relaxation in the glass-forming solution LiCl-6H_2O revealed by Brillouin scattering techniques: S. C. Santucci, L.Comez, F. Scarponi, G. Monaco, R. Verbeni, J-F Legrand, C. Masciovecchio, A. Gessini and D. Fioretto, *J. Chem. Phys.* **131**, 154507 (2009).

Not reported here, a contribution has been given by the Author of the present manuscript to the experiments and elaborations performed on glasses at the same laboratories mentioned before. The results have lead to the following publications:

7. Crystal-Like Nature of Acoustic Excitations in Glassy Ethanol: A. Matic, C. Masciovecchio, D. Engberg, G. Monaco, L. Börjesson, S. C. Santucci, R. Verbeni, *Phys. Rev. Lett.* **93**, 145502 (2004).

8. Brillouin Ultra Violet Scattering on Vitreous Silica: G.Baldi, S.Caponi, L.Comez, S. Di Fonzo, D. Fioretto, A. Fontana, A. Gessini, C. Masciovecchio, M. Montagna, G. Ruocco, S. C. Santucci and G. Viliani; *J. of Non-Crys. Solids* **351**, 1919 (2005).

9. Evidence for a new nano-scale stress correlation in silica glass: C. Masciovecchio, G. Baldi, S. Caponi, L.Comez, S. Di Fonzo, D. Fioretto, A. Fontana, A. Gessini, M. Montagna, G. Ruocco, S. C. Santucci, F. Sette and G. Viliani, *Phys. Rev. Lett.* **97**, 035501 (2005).

Parallel to this work, the elaboration of an experiment of X-ray photoemission spectroscopy (XPS), developed by the Author of the present manuscript, has brought to a prototypical method to perform surface calorimetry. The results are published in:

10. Calorimetry at Surfaces Using High-Resolution Core-Level Photoemission: S. C. Santucci, A. Goldoni, R. Larciprete, S. Lizzit, M. Bertolo, A. Baraldi, and C. Masciovecchio, *Phys. Rev. Lett.* **93**, 106105 (2004).

In the following, *Highlights articles* published at Synchtrotron radiation sources are listed:

1. Calorimetry at Surfaces Using High-Resolution Core-Level Photoemission: S. C. Santucci, A. Goldoni, R. Larciprete, S. Lizzit, M. Bertolo, C. Masciovecchio; Elettra Hilights 2002-2003.

2. Inelastic Ultra Violet Beamline at Elettra: C.Masciovecchio, A. Gessini, S. Di Fonzo, A. Stolfa, S. C. Santucci; Elettra Hilights 2002-2003.

3. Dynamics of Disordered Systems by Inelastic Ultra Violet Scattering: C. Masciovecchio, A. Gessini, S. Di Fonzo, S. C. Santucci, L. Comez, D. Fioretto; Elettra Hilights 2003-2004.

4. Crystal-like nature of Acoustic Excitations in Glassy Ethanol: A. Matic, C. Masciovecchio, D.Engberg, G. Monaco, L. Börjesson, S. C. Santucci, R. Verbeni; ESRF Highlights 2004.

5. Classical elastic theory failure in glasses: C. Masciovecchio, S. Di Fonzo, A. Gessini, D. Fioretto, L. Comez, S. C. Santucci, G. Baldi, S. Caponi, A. Fontana, G. Viliani; Elettra Hilights 2005-2006.

Appendix B

Extra: Core-level photoemission spectroscopy proposed as surface calorimetry.

B.1 Motivation

Developed in parallel to the present work, the elaboration of an experiment of synchrotron X-ray photoemission spectroscopy (XPS) has lead to the proposition of a method to perform surface calorimetry. This method relies on the phonon broadening of bulk and surface photoemission peaks. Since phonon modes are nevertheless concerned with the present work and also in virtue of the interesting results obtained (published in [1]), this extra-topic is attached here.

B.2 Abstract

The experimental determination of thermodynamic properties of two dimensional objects like surfaces and interfaces is a not trivial task. On the other hand, the explosive growth of research and development about low-dimensioned objects, arouses the need of tools for probing such properties. We propose a method, based on core-level photoemission spectroscopy, for obtaining quantitative evaluation of the internal energy of both crystal bulk and surface, distinctively and simultaneously. Our measurements, performed on Lithium (110) from 22 K up deeply into the liquid phase, clearly reveal two phase changes: the known liquid-to solid transition and the surface melting, occurring 50 K below the known melting point.

B.3 Introduction

Thermodynamics has been providing a well-founded knowledge of specific heats and phase diagrams of elements since the XIXth century. Calorimetry can detect first order phase transitions occurring in a macroscopic sample of a substance. During the last decades, the running of research and technology towards miniaturization has moved much attention onto low-dimensional systems, like micro- and nano-structures and crystalline surfaces and interfaces (See Ref. [2]). As a crystalline surface, we mean the very external layer of atoms, a region of extreme discontinuity in the crystal. The interest about these systems is twofold. Firstly, technological: the specific heat of low-dimensioned systems is very important when physical growing and chemical reactions are involved. Secondly, from a more general point of view, the knowledge of the internal energy of crystal surfaces should be helpful in answering some puzzling questions about the microscopic mechanism of the solid to liquid transition.

Indeed, that melting is initiated at the surface and then is extended to the bulk, is a 100 years old speculation [3, 4] which had to wait a long time for experimental tools having enough energy and space resolution and for more powerful calculation tools. Nowadays, many progresses have been done about this topic [5]. An accredited idea is that the occurrence or not of premelting is related to the surface orientation. Experimental evidences have revealed premelting in (110) and (100) surfaces of fcc crystals and premelting absence in the (111) ones [6, 7, 8]; simulations have lead to the same results [9, 10], and theories have been formulated for a microscopic interpretation [11, 12]. Calculations predict surface melting for each low-index orientation of Vanadium [13] and in alkali clusters [14].

In this work, we have quantified the phonon broadening of the bulk and surface photoemission peaks of Li(110) (bcc). We have provided the first experimental evidences for surface premelting in an alkaline metal. We have therefore proposed to extend the relationship between the phonon broadening of bulk peak and the specific heat, to the case of surface, as a method to measure the internal energy of the surface itself.

B.4 Experiments

Photoemission spectroscopy is a technique highly sensitive to both bulk and surface contribution simultaneously, which can be performed in the solid and in the liquid phases, as it does not require long-range order. We measured the photoemission lineshapes of the 1s level of bulk and surface atoms of Li(110), in a wide temperature from 22 K up to 553 K, well above the melting transition (T_M= 453 K [15]) .

Our experiments were performed in the ultra-high-vacuum (base pressure $< 5\text{x}10^{-11}$ mbar) experimental chamber of the SuperESCA beamline at the Elettra Synchrotron. Li(110) films were grown in situ onto a clean Ni(100) crystal kept at 22 K. Li 1s-level photoemission spectra were obtained with photon energy of 94 eV, collecting the photoelectrons at 40° from normal emission. The total energy resolution was set to 80 meV. Lithium was chosen because its vapor pressure is low enough to allow the existence of the liquid phase in vacuum. Moreover, Lithium is representative of the simple metals class and it is a good test case for theoretical approaches to the dynamics of the solid-to-liquid transition.

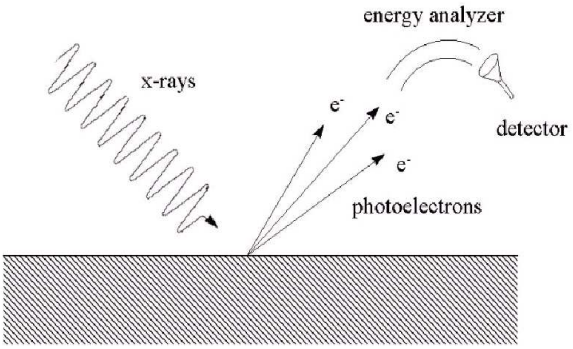


Figure B.1: Schematic diagram of an XPS experiments: X-rays is incident on the sample. Electrons are photoemitted at a kinetic energy which depends on both incident energy and angle.

B.5 The XPS spectra

A selection of the acquired spectra is shown in Fig. B.5, as a function of temperature. The sharper line, at lower binding energies, is the photoemission peak of bulk atoms. The broader one, at higher binding energies, is the photoemission peak from the surface [16]. Without any kind of analysis, the progressive broadening of both lines is immediately evident with the increasing temperature;

this is the well-known, phonon-broadening phenomenon and is due to electron-phonon coupling [17, 27]. The progressive shift of binding energies (approximately corresponding to peak maxima) towards higher values is also evident with increasing temperature.

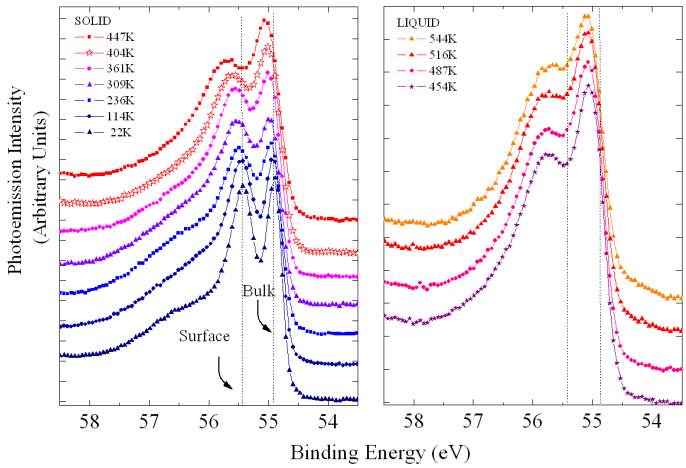


Figure B.2: Selection of the acquired XPS spectra of Li(110). Left panel: solid phase. Right panel: liquid phase. 22 K is the minimum temprature investigated, 544 K is the maximum temperature at which the liquid held. In both panels, the vertical dotted lines mark the position of bulk and surface peak at 22 K, as a reference for the binding energy temperature shift. A third contribution is present at high binding energies, due to lithium oxidation. It has been characterized and subtracted in data analysis.

B.6 Fits: phonon broadening and binding energy

Phonon broadening and binding energy of bulk and surface have been characterized through a standard best-fitting of the Doniach-unjic (DS) lineshape Eq.(B.1):

$$DS(\varepsilon) = \frac{\Gamma(1-\alpha)cos\left(\frac{\pi\alpha}{2} + (1-\alpha)tan^{-1}\left(\frac{\varepsilon - E_b}{\gamma/2}\right)\right)}{((\varepsilon - E_b)^2 + (\gamma/2)^2)^{(1-\alpha)/2}} \tag{B.1}$$

Here, ε is the energy of the photoemitted electrons, α is the asymmetry index and γ is the Lorentzian width, which is related to the core-hole lifetime. α and γ are temperature independent parameters and have been fixed to the values of Ref. [16] ($\alpha = 0.22 \pm 0.01$ in the bulk, $\alpha = 0.30 \pm 0.01$ in the surface and $\gamma = 0.45 \pm 0.1$ meV). E_b is the binding energy.

The phonon broadening, W, has been taken into account by convoluting Eq.(B.1) with a Gaussian function whose full width at half maximum is W [16, 19]. [1]. The fitting lineshape of a single peak is:

$$F(\varepsilon) = \int d\varepsilon' DS(\varepsilon') e^{-\left(\frac{2.773(\varepsilon - \varepsilon')^2}{W^2}\right)} \tag{B.2}$$

The total fitting function adopted is the sum of three[2] lineshapes Eq. (B.2), one per each peak, plus a background line which has been taken proportional to the spectrum integral. Since the binding energies of bulk and surface peaks are well distinguishable, we could perform a simultaneous characterization of the respective peaks in the whole temperature range.

[1] The broadening has been corrected for the instrumental resolution (80 meV, temperature independent).

[2] A third peak has been introduced in the low temperature spectra to reproduce the small oxide contribution at higher binding energy.

An example of the quality of the fitting procedure is given in Figure B.3. In the upper panel, the fitting function (red line) is superimposed to the spectrum acquired at at 114 K (black dots). Single peak contributions of bulk, surface, oxide and the background used are also shown. The spectrum corrected by subtracting the oxide peak is also shown as open circles. The residuals in the lower panel attest the reliability of the analysis.

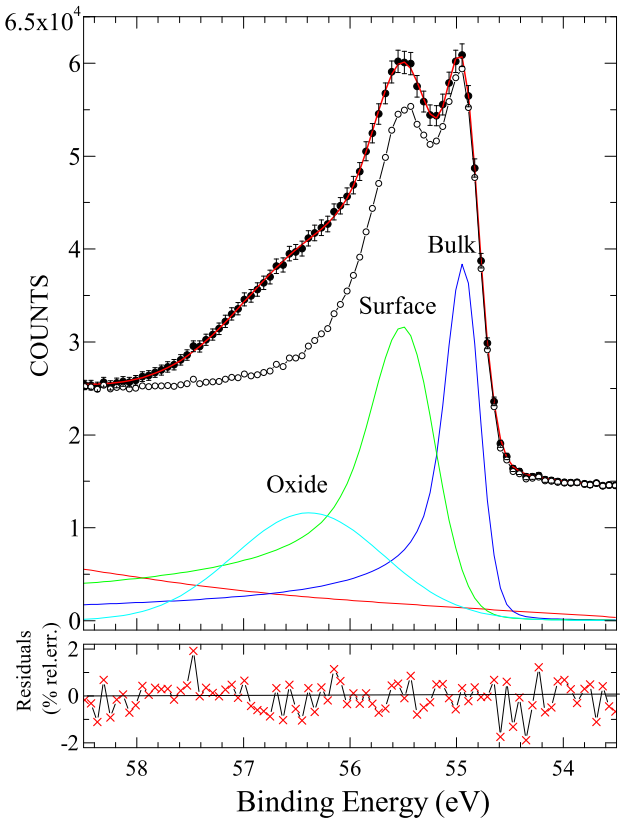


Figure B.3: **Upper Panel.** Black dots: XPS spectrum at 114 K with the fitting line superimposed. The colored peaks represent the three contributions calculated according to Eq.(B.2). The background used is shown as a red line. Open dots: same spectrum corrected for the oxidation peak. **Lower Panel.** Residuals.

The temperature depending parameters obtained by the fits are shown in Fig. B.4. In the left panel, the squared phonon-broadenings, $W^2(T)$, of surface and bulk peaks are reported. In the right panel, the binding energies are shown. The globally monotonic increase of these parameters is affected by two abrupt anomalies, one at T^*= 404 K and the other at the melting point T_M= 453 K, 50 K above. Figure B.4 implies the thermodynamic phases of our system: up to 404 K both surface and bulk are solid. At 404 K the surface seems to undergo premelting, while the bulk does not show any change (this will be discussed in the last section). At 453 K, the known melting transition occurs. The surface is affected, as well, because it feels a liquid background. A stronger proof for this representation is given in the following, when internal energies and latent heats are considered in detail.

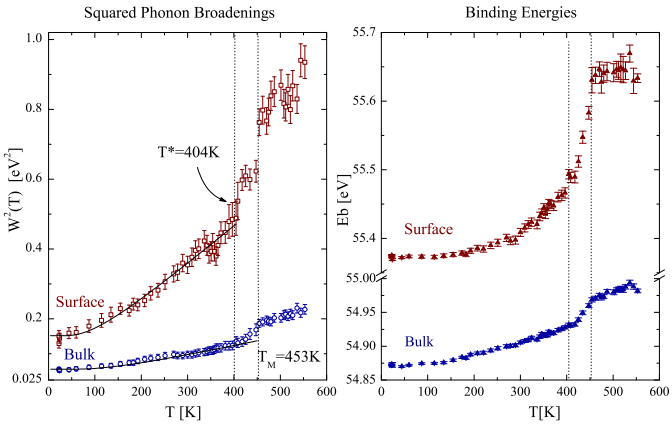


Figure B.4: **Left Panel:** Squared phonon contribution W^2 to the linewidths of surface and bulk peaks. The corresponding best-fitting lines (Overhauser function) of core-level phonon broadening theory are superimposed as solid lines: Eq.(B.3) for the bulk and Eq. (B.9) for the surface. **Right Panel:** binding energies of bulk peak (blue triangles) and surface peak (red triangles). Dramatic changes occur in the slope at T^*= 404 K and T_M= 453 K. In the following, these changes are shown to be related to phase transitions.

B.7 Analyisis of the bulk peak

The temperature dependence of phonon broadening of a photoemission peak, as theorized by L. Hedin and A. Rosengren [20] is given by the equation (also known as the Overhauser formula)

$$W^2(T) = W_0^2 \left[1 + 8 \left(\frac{T}{\theta_D} \right)^4 \int_0^{\theta_D/T} dx \frac{x^3}{e^x - 1} \right] \tag{B.3}$$

where $\theta_D$is the Debye temperature and W_0 is the zero-temperature phonon width. We have tested this equation on the bulk phonon broadening data up to the melting point (see the black line in the left panel of Fig. B.4).

The integral fitting function, with the second integration extreme as a variable, has been appositely written as a part of this work: the Riemann definition of integrals has been adopted and the division of the interval thickened until the stability was obtained, that is, when the integral value did not depend anymore on further thickening and on the fact that the value of the fitting function was calculated in the middle of the intervals or on an extreme. A Levemberg-Marquardt algorithm was utilized to perform the minimization.

The parameters obtained are $W_0^2 = 0.051 \pm 0.006$ eV^2 and $\theta_D = 470 \pm 25$ K, in good agreement with the values estimated by experiments performed in a reduced temperature range (78-280 K [15]), and with the Debye temperature inferred from the phonon dispersion of Lithium [22]. In this work, the Overhauser equation, Eq. (B.3), has been compared for the first time to Li(110) spectra below 78 K. Indeed, previous measurements of phonon broadening, had been performed down to 78 K [16], a temperature where the effective bending of the $W^2(T)$ curve towards the zero point energy is not yet evident and a simple linear fit of phonon broadening data is also suitable.

Indeed, Eq. (B.3) for phonon broadening is quite similar to the Debye equation for the internal energy $U(T)$ [23]:

$$U(T) = \frac{9RT^4}{\theta_D^3} \int_0^{\theta_D/T} dx \frac{x^3}{e^x - 1} \tag{B.4}$$

where R is the gases constant and $\theta_D = 442$ K is the Debye temperature. The internal energy $U(T)$ can been calculated by the specific heat C_P through integration, according to:

$$U(T) = \int C_P(T)dT \tag{B.5}$$

In figure B.5 the measured specific heat of Lithium at constant pressure, C_P, is shown as a function of temperature, from a few K up to the liquid phase. [21]. The melting transition is evident in the discontinuity at 440 K.

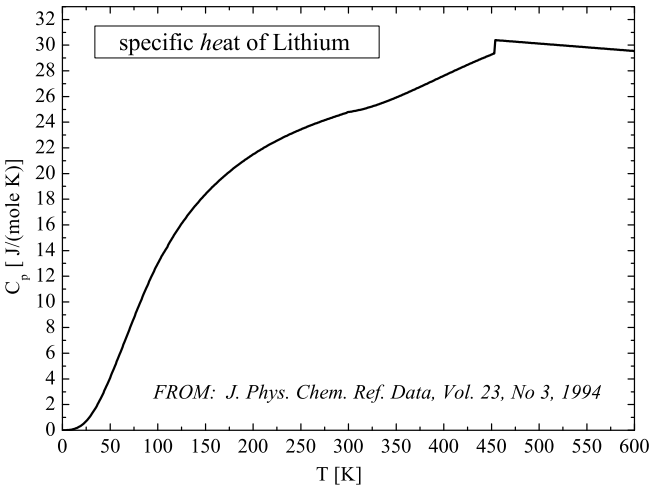


Figure B.5: Specific heat of Lithium at constant pressure [21]

We have calculated the internal energy associated to C_P through Eq. (B.4). The result is shown in Fig. B.6

The internal energy shows a temperature trend quite similar to that found in phonon broadening -(Fig. B.4). Indeed, comparing Eq.(B.3) to Eq.(B.4), we have obtained an equation which links photoemission to calorimetry:

$$U(T) = -\frac{9R}{8}\theta_D + \frac{9R}{8}\frac{\theta_D}{W_0^2}W^2(T) \tag{B.6}$$

Eq.(B.6) implies that the internal energy $U(T)$ may be calculated through the determination of the temperature-depending phonon broadening of the XPS peak of bulk[3]. Eq. (B.6) suggests a "non calorimetric way to calorimetry", performed through XPS measurements. If this correspondence is effectively verified, the immediate development will be the extension of this method to the case of surface, where standard calorimetry is hardly applicable.

In Fig. (**??**) we show the good correspondence expressed by the statement of Eq.(B.6): the internal energy obtained by integration of the specific heat (Eq. (B.4 applied to the data in Fig. B.5) is reported as a continuous line. As blue dots, the internal energy is shown calculated by substituting the results of the present XPS experiment into Eq.(B.6). The agreement is actually very good.

The binding energies of core electrons are also affected by phonon broadening. A linear relationship can be established between the bulk binding energy and the internal energy [25, 26, 27]. One finds:

$$U(T) = \frac{3BV_0}{\gamma A}\Delta E_b \tag{B.7}$$

[3]the Debye formula is derived for bulk.

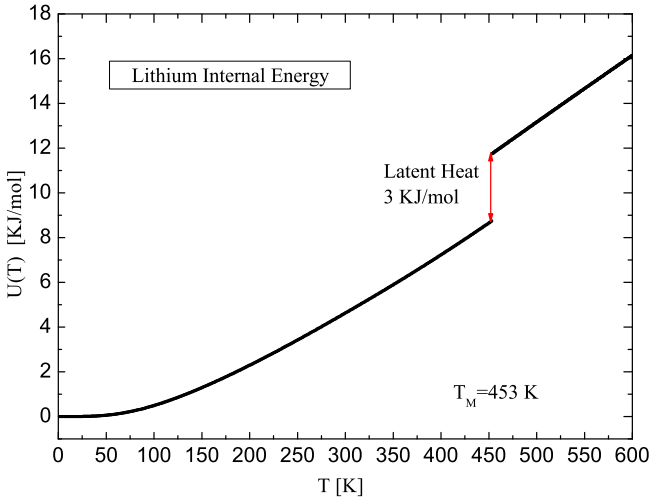


Figure B.6: Internal energy $U(T)$ calculated by integrating $C_P(T)$

where $A = 4.3eV$, $B = 11.6$ GPa is the bulk modulus $\gamma = 0.8$ is the Grüneisen parameter and $V_0 = 1.810^{-6}m^3$. The internal energy calculated through Eq.(B.7) is shown in Fig. B.7 as green triangles. In this case also, the agreement with the standard calorimetric data is good.

One might be surprised by the fact that this analysis, performed in the solid phase, leads to a good agreement also in the liquid. The comparison of phonon dispersion relations of crystalline [22] and liquid [24] phase, though, implies that the Debye temperature, the fundamental parameter of this comparison, does not change after the melting. In figure B.8 the dispersion relations of solid (left panel) and liquid (right panel) lithium are shown. From the well known relationship $\hbar\omega_D = K_B\theta_D$ [27] and since 1meV = 4.136 THz one can deduce that $\theta_D \approx 440$ K in both the solid and the liquid phase.

B.8 From bulk to surface

The good agreement of internal energy of bulk lithium measured by XPS and by standard calorimetry, suggests the intrinsic "calorimetric capabilities" of the XPS technique, which, once supported by an appropriate comprehensive theory and by a significant number of test cases, could become irreplaceable when dealing with surfaces or miniaturized parts which cannot be investigated by standard calorimetric methods. In the following we propose a prototypical extension of this method to the surface which gives successful results in the case of Li(110).

B.9 Analysis of the surface peak

To develop a calorimetric method for surfaces based on XPS measurements, a formula similar to Overhauser equation (B.3), able to describe the surface phonon broadening, has to be stated. Moreover, in analogy with the XPS bulk calorimetry expressed by Eq.(B.6), it is reasonable to assume that such a surface-Overhauser equation will be equivalent to the theoretical Debye formula which expresses the internal energy of a surface, that is [23]:

$$U_S(T) = \frac{4RT^3}{(\theta_D^{(S)})^3}\int_0^{\theta_D^{(S)}/T} dx \frac{x^2}{e^x - 1} \tag{B.8}$$

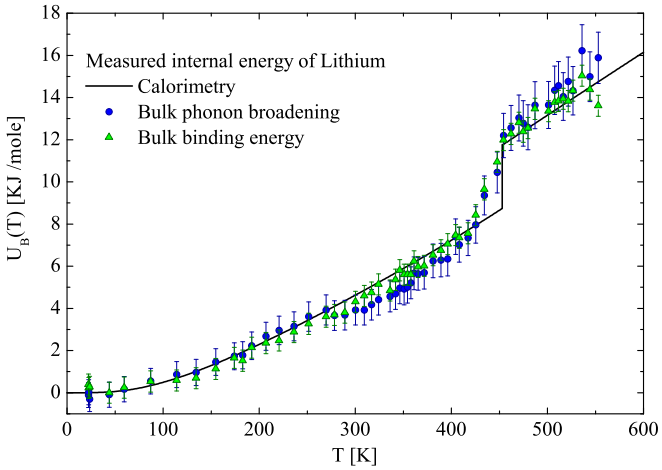


Figure B.7: Internal energy of Lithium as a function of temperature, measured by calorimetry (solid line) and obtained by the phonon broadening W of the XPS bulk peak through Eq. (B.6) (blue circles) and the binding energies through Eq. (B.7) (green triangles)

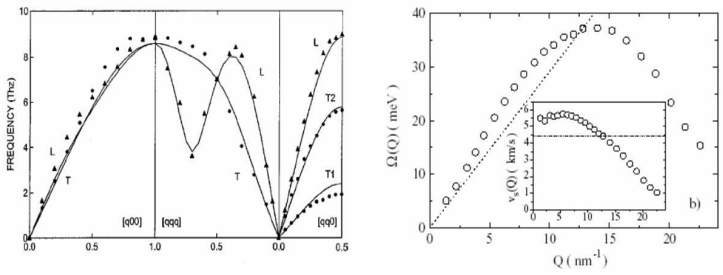


Figure B.8: Phonon dispersion curves of solid [22] (left panel) and liquid Lithium [24].

where $\theta_D^{(S)}$ is Debye temperature of surface.

Following the work of Hedin and Rosengren [20], we have formulated an expression for the temperature dependence of the phonon broadening of the XPS surface peaks, $W_S(T)$:

$$W_S^2(T) = W_{0S}^2 \left[1 + c_S \left(\frac{T}{\theta_D^{(S)}} \right)^3 \int_0^{\theta_D^{(S)}/T} dx \frac{x^2}{e^x - 1} \right] \tag{B.9}$$

where W_{0S} is the zero-point energy, θ_D is the Debye temperature of the surface and c_s has to be determined experimentally. The Debye temperature of the surface, $\theta_D^{(S)}$, is a property of the system, which has been extrapolated by the phonon dispersion curves of the Li(110) surface [28] reported in Fig. B.9. The Debye formula $\hbar\omega_D = K_B\theta_D$, with $\omega_D = 8.4$ THz, has given a value $\theta_D = 409$ K.

The Overhauser equation (B.9) has been fitted over the squared phonon broadening parameters $W_S^2(T)$ calculated by the surface XPS peaks. In the left panel of Fig. B.4 the optimized function is reported, as a line over surface data, attesting the good quality of the fit. In the fitting procedure $\theta_D^{(S)}$ has been kept fixed at 409 K. The analysis has given, as best fitting parameters, an asymptotic value $W_{0S}^2 = 0.152 \pm 0.006$ eV^2 and $c_S = 6 \pm 1$.

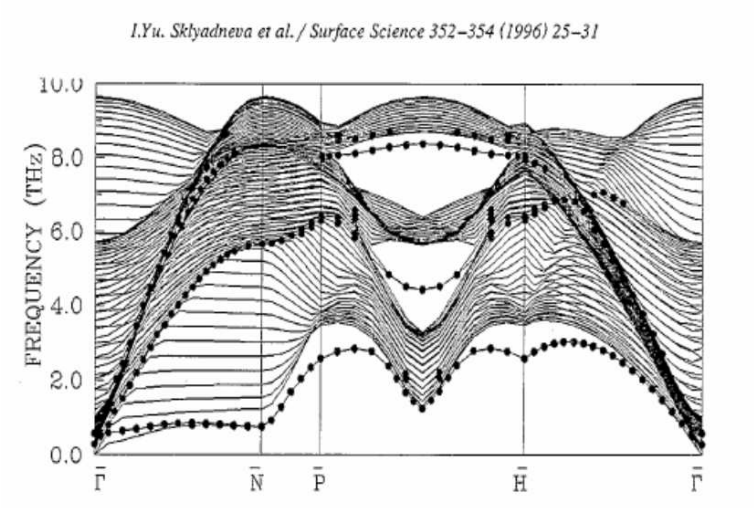


Figure B.9: Phonon dispersion curves of a Li(110) film from Ref. [28]

The relationship between the Overhauser equation (B.9) and the Debye equation (B.8) for the surface XPS peak becomes:

$$U_S(T) = -\frac{4R}{6}\theta_D^{(S)} + \frac{4R}{6}\frac{\theta_D^{(S)}}{W_{0S}^2}W_S^2(T) \tag{B.10}$$

In Fig. B.9 the surface internal energy $U_S(T)$ obtained by substituting our experimental data $W_S(T)$ of figure in Eq.(B.10) is shown (dots). The surface internal energy calculated through the Debye equation (B.8) is also reported (solid line). For comparison, the $U(T)$ of bulk is also displayed (dotted line).

Two evident discontinuities occur in $U_S(T)$ which correspond to temperature driven phase transitions. As already noted, the transition at 453 K corresponds to the bulk melting. The latent heat discontinuity of ≈ 3 kJ/mole, is the same than that observed in the bulk. This confirms that Eq. (B.10) gives a quantitative estimation of $U_S(T)$.

The jump occurring at 404 K can be observed only in the surface data: it corresponds, therefore, to a surface phase transition. Being it a first-order singularity and considering that the latent heat released of ≈ 2 kJ/mole scales on the bulk value with a ratio of 2/3, in accord with the respective dimensionality, we associate this phase transition to a surface melting.

B.10 Conclusions

1. High-resolution (80 meV) X-ray photoemission spectroscopy experiments on Li(110) have been performed from 22 K up to 550 K. This is the first XPS investigation of Li(110) lead in the liquid phase and below 78 K.

2. Our experiments have been performed at temperatures low enough to give the experimental proof for a low temperature asymptotical bending of the Overhauser prediction of temperature dependent phonon broadening of photoemission lines.

3. This work provided also the first experimental evidence for the surface premelting in a bcc crystal, whose occurrence had been only predicted, before, by computer simulations on Vanadium [13]. The systematic collection of experimental evidences in other metals is strongly suggested, since the natural interest of scientists is the statement and the interpretation of general criteria for melting [29].

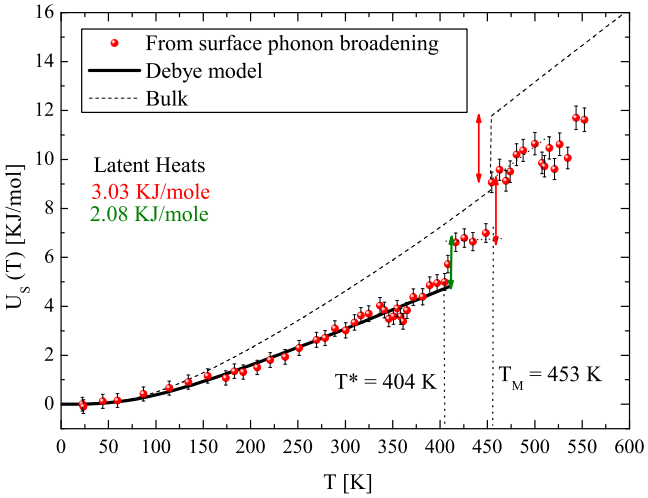


Figure B.10: Bold black line: internal energy of Li(110) surface as a function of temperature, calculated according to the Debye equation (B.8), and θ_D obtained by the surface phonon dispersion curves. calculated according to the Eq.(B.10) from the phonon broadening values $W_S^2(T)$ of the surface peak reported in Fig. B.4. The theoretical Debye formula expressing the surface internal energy, Eq.(B.8), is shown as a black thick line. The internal energy of bulk (Fig. B.6) is also reported, for comparison, as black dashed line. At $T^* = 404$ K premelting occurs, with latent heat 2.08 KJ/mole. At $T_M = 453$ K Lithium is completely melted. The length of vertical arrows in correspondence of phase transitions is equal to latent heats.

4. A prototypical method to perform surface calorimetry, based on XPS measurements, has been proposed as the extension of XPS-based calorimetry for the bulk, as also formulated and checked accurately in the present work. To be adjusted, the surface calorimetry needs that experiments are lead on more metals, as well as the evidence of irrefutable matching points with other well assessed techniques.

5. Surface critical phenomena may be studied by low energy electron diffraction, which is the technique of choice to obtain the order of the phase transition and the critical exponent [25], but long-range order is needed. The present methodology based on high-resolution core-level photoemission offers the unique characteristic to measure quantitatively the internal energy of surface atoms in topologically disordered state, like the liquid phase.

6. The more objects are miniaturized, the more their surface becomes important. This kind of investigation could be extended to any two-dimensional ordered or disordered array of atoms and molecules (for example organic monolayers) adsorbed on substrates or, more specifically, to nanostructures with large surface to bulk ratio (like nanotubes and nanodots), which play a fundamental role in nanotechnological applications, and which may not be studied by low energy electron diffraction. Surface calorimetry should be of fundamental importance to low-dimensioned systems, like nanostructures and layers for heterogeneous catalysis.

Bibliography

[1] Calorimetry at Surfaces Using High-Resolution Core-Level Photoemission: S. C. Santucci *et al. Phys. Rev. Lett.* **93**, 106105 (2004).

[2] Various Authors, *Surf. Sci.* Vol **500**, (2002).

[3] G. Tammann, *Z. Phys. Chim. Phys.-Chim Biol.* **68**, 205 (1910).

[4] J. Frenkel, Kinetik Theory of Liquids (Clarendon, Oxford, 1946) pp. 425-6.

[5] J. D. Dash, *Rev. Mod. Phys.* **71**, 1737 (1999).

[6] J. W. M. Frenken, J. F. Van Der Veen, *Phys. Rev. B* **34**, 7506 (1985).

[7] E. T. Chen, R. N. Barnett, U. Landmann, *Phys. Rev. B* **41**, 439 (1990).

[8] W. Theis, K. Horn, *Phys. Rev. B* **51**, 7157 (1995).

[9] H. Hkkinen, U. Landman, *Pys. Rev. Lett.* **71**, 1023 (1993).

[10] T. S. Rahman, Z. J. Tian, J. E. Black, *Surf. Sci.* **374**, 9 (1997).

[11] R. Lipowsky, *Phys. Rev. Lett.* **49**, 1575 (1982).

[12] A. Trayanov, E. Tosatti, *Phys. Rev. B* **38**, 6961 (1988).

[13] V. Sorkin, E. Polturak, J. Adler, Phys. *Rev. B* **68**, 174103 (2003).

[14] A. Aguado, *Phys. Rev. B* **63**, 115404-1 (2001).

[15] C. B. Alcock, M. W. Chase, V. P. Itkin, *J. Phys. Chem. Rev. Data* **23**, 385 (1994).

[16] D.M. Riffe, G. K. Wertheim, *Phys Rev. B* **61**, 2303 (2000).

[17] L. Hedin, X-ray spectroscopy (McGraw Hill, New York, 1974) pp227-283.

[18] G. D. Mahan, *Phys. Rev. B* **21**, 4791 (1980).

[19] S. Doniach, M. unjic, *J. Phys. C* **3**, 285 (1969).

[20] L. Hedin, A. Rosengren, *J. Phys. F: Metal Phys.* **7**, 1339 (1977).

[21] C.-O. Almbladh, A. L. Morales, *J. Phys. F* **15**, 991 (1985).

[22] J. K. Freericks, S. P. Rudin, A. Y. Liu, *Physica B* **425** 284-288 (2000).

[23] D. L. Goodstein, States of Matter, (Dover Publications Inc., New York, 1985) p.159.

[24] T. Scopigno et Al., *Europhys. Lett.* **50**, 189 (2000).

[25] D. M. Riffe, G. K. Wertheim, D. N. E. Buchanan, P. H. Citrin , *Phys. Rev. B* **45**, 6216, (1992).

[26] D. E. Gray, American institute of Physics Handbook (McGraw Hill, New York, 1972) pp. 4-126.

[27] N. W. Ashcroft, N. D. Mermin, Solid State Physics, (Saunders College Publishing, New York, 1976) pp. 492-495.

[28] I. Yu. Sklyadneva, E. V. Chulkov, A. V. Bertsch, *Surf. Sci.* **25**, 352-354 (1996).

[29] V. Lubchenko, *J. of Phys. Chem. B* **110**, 18779 (2006).

Dynamical properties of water and of the LiCl-6H_2O solution, investigated by inelastic scattering of light and synchrotron radiation.

Abstract:

The eccentric phase diagram of the stable and metastable states of water is a long backdated puzzle. Several theories have been proposed to explain the apparent divergenges of thermodynamic and transport properties of supercooled water but an unified picture is still lacking, basically because the divergence temperature is located below the nucleation temperature, in the so-called no-man's land. We have lead an experimental approach to the relaxational properties of liquid and supercooled water, measured by means of inelastic scattering of ultraviolet synchrotron radiation for the first time and also light scattering. By analyzing the spectra in the formalism of memory functions we have found a good agreement with previous molecular dynamics simulations and with mode coupling theory, which attributes to the singularities of water a dynamical origin. We have also made a first step into the no-mans land by investigating the dynamics of the LiCl-6H_2O solution. Indeed, the progressive dilution of aqueous solutions can be an indirect method to obtain information about the pure solvent below its homogeneous nucleation temperature. We have lead inelastic scattering experiments of light and synchrotron ultraviolets and X-rays. We have found that, on cooling the solution, a single relaxation process, which at high temperatures owns features similar to those of the structural relaxation of pure water, starts splitting into a structural and a secondary relaxations. The splitting occurs at around the temperature where the properties of water seem to diverge. According to recent theories and experiments about the dynamics and phase diagram of water and of dilute ion solutions at low temperatures and high pressures, the dynamical splitting that we observe could be possibly connected with the onset of the hypothetical liquid-liquid phase transition at pressures much higher than those investigated.

KEYWORDS: water, LiCl-6H_2O solution , glass transition, ultraviolet, synchrotron radiation, X-rays, inelastic scattering, dynamics of liquids and glasses.

Propriétés dynamiques de l'eau et de la solution LiCl-6H_2O, étudiées par diffusion inélastique du rayonnement synchrotron et de la lumière visible.

Résumé:

Le diagramme des phases stables et métastables de l'eau reste une énigme depuis des décennies. De nombreuses interprétations ont été proposées pour expliquer les divergences apparentes de certaines propriétés thermodynamiques et de transport, de l'eau surfondue. Mais une description unifiée manque encore, essentiellement parce que la température où apparaissent diverger ces propriétés est située en dessous de la température limite de cristallisation, dans une région, qualifiée de no-man's land, entre l'eau surfondue et la glace amorphe. Nous avons, pour la première fois, mesuré les propriétés dynamiques de l'eau liquide et surfondue par diffusion inélastique du rayonnement synchrotron ultraviolet et par diffusion de lumière visible. En analysant les spectres obtenus à l'aide d'un formalisme de fonction mémoire, nous avons trouvé un bon accord avec les simulations de dynamique moléculaire et avec la théorie du couplage de modes, qui attribue une origine dynamique aux singularités observées dans le no-man's land de l'eau. Nous avons aussi mesuré la dynamique de la solution LiCl-6H_2O par diffusion inélastique de la lumière visible et du rayonnement synchrotron dans la gamme des ultraviolets et des rayons X. Cette investigation est un premier pas dans le no man's land de l'eau par parce que la dilution progressive de solutions aqueuses constitue une méthode indirecte pour obtenir des informations sur l'eau pure en dessous de la température de nucléation homogène des cristaux. Nous avons observé au cours du refroidissement de la solution, une relaxation, qui possède des caractéristiques similaires à celles de la relaxation structurale de l'eau pure, mais qui se divise en une relaxation structurale et une relaxation secondaire, autour de la température où les propriétés de l'eau pure semblent diverger. Selon des expériences et des théories récentes et sur la dynamique et le diagramme de phase de l'eau et des solutions ioniques diluées à basse température et à pression élevée, la séparation des dynamiques que nous observons pourrait éventuellement être reliée au début d'une hypothétique transition de phase liquide-liquide qui apparaît à des pressions beaucoup plus élevées que celles étudiées.

MOT-CLES: eau, solution LiCl-6H_2O, transition vitreuse, ultraviolets, synchrotron, rayons-X, diffusion inélastique, propriétés dynamiques des liquides et des verres.